

الجمهورية الجزائرية الديمقراطية الشعبية
République Algérienne Démocratique et Populaire
وزارة التعليم العالي والبحث العلمي
Ministère de l'Enseignement Supérieur et de la Recherche Scientifique

Université Mohamed Khider BISKRA
Faculté des Sciences Exactes et des
Sciences de la Nature et de la Vie
Département: Sciences de la Matière
Réf:.....



جامعة محمد خيضر بسكرة
كلية العلوم الدقيقة و علوم
علوم الطبيعة و الحياة
قسم علوم المادة
المرجع:.....

Thèse présentée en vue de l'obtention du diplôme de doctorat LMD:

Spécialité : physique

Intitulé :

Exploration et étude des nouvelles générations des verres des oxydes lourds à base d'antimoine pour la photonique

Présentée par :

GUESMIA Nesrine

Soutenue publiquement le : **31/10/2022**

Devant le jury composé de :

SOLTANI Mohamed Toufik	Professeur	U.M.K. Biskra	Président
HAMZAOUI Majda	M.C	U.M.K. Biskra	Rapporteur
BAAZOUZI Mourad	M.C	U.M.K. Biskra	Examineur
SAHNOUNE Foudil	Professeur	U. M'sila	Examineur
HERAIZ Menad	Professeur	U. M'sila	Examineur

الجمهورية الجزائرية الديمقراطية الشعبية
Democratic and Popular Republic of Algeria
وزارة التعليم العالي والبحث العلمي
Ministry of Higher Education and Scientific Research

University Mohamed Khider BISKRA
Faculty of Exact Sciences and Science
of Nature and Life
Department of Material Sciences
Ref:.....



جامعة محمد خيضر بسكرة
كلية العلوم الدقيقة و علوم
علوم الطبيعة و الحياة
قسم علوم المادة
المرجع:.....

Thesis Presented to obtain the degree of Doctorate LMD

Specialty: physics

Entitled:

Exploration and study of new generations of antimony-based heavy oxide glass for photonics

Presented by:

GUESMIA Nesrine

31/10/2022

Jury:

SOLTANI Mohamed Toufik	Professor	U.M.K. Biskra	President
HAMZAOUI Majda	M.C	U.M.K. Biskra	Supervisor
BAAZOUZI Mourad	M.C	U.M.K. Biskra	Examiner
SAHNOUNE Foudil	Professor	U. M'sila	Examiner
HERAIZ Menad	Professor	U. M'sila	Examiner

Dedication

Dedicate First and foremost, I would like to sincerely and deeply thank my God (Allah), who gave me the will and the courage to realize my dream, my thesis.

I express my deep gratitude to my parents and my sisters for their encouragement and support.

I dedicate this work: To the two people closest to my soul and heart, My Dear Parents who have sacrificed their entire Life to support me and encourage me to achieve my dreams and ambitions. You will always remain in my heart. To my dear sisters *Kouda, Kanane* and *Kiba*. You are the best. To all my big family.

To my friends and colleagues *Beghdadi Lina, Rezgui Sayah, Lakhedar Sek, Kanane boden, massouda, Soumaya, Kabiba* and *Imen, Zahra Charife, Hadjer Dardora, Souhaila, Nabila, Kafida...etc.* For all the good times we spent together and all the help you gave me.

Thanks

I would like to express my deep gratitude to the **Laboratory of Photonic Physics and Multifunctional Nanomaterials**, Department of Physics, University of Med Khaider Biskra, and everyone present in it who played a great role in enabling me to carry out this work.

First of all, I would like to thank Dr. **Majda Hamzaoui** for mentoring and guiding me over the past five years, and for her invaluable help and meeting most of my needs and, if necessary, for purchasing with her own money during the research internship. I would also like to thank Dr. **Majda Hamzaoui** for supervising this thesis. I must also thank her for his intellectual approach and especially for the support and trust he gave me by integrating me into her research team.

Also, I would like to thank Professor **M. T. Soltani** for accepting me in his laboratory as well as for his invaluable help during my research internships.

I am very grateful to all the members of the jury:

Professor **M. T. Soltani**, University of Biskra, for the honor he did me by agreeing to chair the jury for this thesis.

Pr. **Sahnoune Foudil** and Pr. **Heraiz Menad** University. M'sila as examinateur and Dr. **Mourad Baazouzi** at the University of Biskra for the interest they showed in my work by accepting to be examiners.

I sincerely thank the following people for their help:

- In the field of mechanic, optic and photoluminescence: Pr. Chala Abdel wahed, Saihe, Pr. Hachani and Pr. Saide Rahmen.
- In the field of Raman spectroscopy, Pr. D. de Ligny, Institute of Glass and Ceramics, University of Erlangen-Nuremberg, Germany

I would like to associate in my thanks all those, colleagues and friends with whom I was able to collaborate throughout the realization of this work:

Lina, Saihe, Lakheder, Hanane, Soumaia, Imen, Hadjer, Zahra, Nabila Hafida, Souhaila, Masseurda, Zainebe...etc. May they all find here the expression of my sincere friendships. Without forgetting all those who, by their friendly presence and their sympathy enabled me to carry out this work.

Last but not least, my strongest thanks go to my lovely parents, and my beautiful sisters; Houda, Hanane and Hiba.

TABLE OF CONTENTS

Contents.....	I
List of figures.....	V
List of tables.....	IX
General Introduction.....	1

Chapter I: Generals on the glass

I.1 Introduction.....	7
I.2 Glass definition.....	8
I.3 Glass production.....	8
I.4 Glass transition.....	9
I.5 Glass formation.....	11
I.5.1 Formative elements.....	12
I.5.2 Modifier elements.....	12
I.5.3 Intermediate elements.....	13
I.6 General characteristics of glass chemical compositions.....	14
I.6.1 Antimony oxide Sb_2O_3	14
I.6.2 Tungsten trioxide WO_3	16
I.6.3 Phosphate.....	17
I.6.3.1 Tetrahedra Q^3	18
I.6.3.2 Tetrahedra Q^2	18
I.6.3.3 Tetrahedra Q^1	19
I.6.3.4 Tetrahedra Q^0	20
I.7 Rare earth ions.....	20
I.7.1 Samarium ions.....	20
I.7.2 Effect of RE doping on the glass structure.....	23
I.8 Photonic applications.....	23

Chapter II: Experimental technique of characterization glasses

II.1 Introduction.....	29
II.2 Characterization techniques.....	30
II.3 Thermal characteristics.....	30
II.3.1 Experimentation equipment.....	32
II.4 Physical and mechanical properties.....	34

II.4.1 Density.....	34
II.4.1.1 Experimentation equipment.....	34
II.4.2 Elastic properties.....	34
II.4.2.1 Experimental apparatus	36
II.4.3 Micro-hardness	37
II.4.3.1 Experimentation equipment.....	38
II.5 Optical and structural characteristics.....	38
II.5.1 UV-Vis and IR spectroscopy.....	38
II.5.2 Optical characteristics.....	40
II.5.2.1 Experimentation equipment.....	41
II.5.2.2 Determination of the forbidden band width (E_g) and the Urbach energy (E_u).....	42
• Determination of the forbidden band width.....	42
• Determination of the Urbach energy.....	43
II.5.3 Infrared spectroscopy (FTIR).....	44
II.5.3.1 Experimental equipment.....	46
II.6 Fluorescence spectroscopy.....	47
II.6.1 Experimental equipment.....	48
II.7 Raman spectroscopy.....	49
II.7.1 Experimental equipment.....	51

Chapter III: Physical properties of glasses on the ternary system Sb_2O_3 - WO_3 - $NaPO_3$

III.1 Introduction.....	55
III.2 Production of glass.....	56
III.2.1 Choosing a crucible.....	56
III.2.2 Starting materials.....	56
III.2.3 Synthesis.....	56
III.3 Vitreous domains.....	59
III.3.1 Binary systems.....	59
III.3.1.1 The $(100-x) Sb_2O_3-xWO_3$ and $(100-x) NaPO_3-xWO_3$ binary systems.....	59
III.3.1.2 In the binary system $(100-x) Sb_2O_3 - x NaPO_3$	60
III.3.2 The ternary system.....	60
III.4 Physical characteristics.....	64
III.4.1 Density, molar volume, oxygen molar volume and oxygen packing density.....	64
III.5 Thermal properties by DSC.....	69

III.6 Elastic properties.....	74
III.6.1 Elastic modulus experiment.....	74
III.6.2 Elastic moduli and Poisson's ratio by Makishima-Mackenzie's theory.....	76
III.7 Micro- Hardness.....	84
III.8 Conclusion	85

Chapter IV: Optical and structural studies of SWN glasses

IV.1 Introduction.....	89
IV.2 Optical characteristics.....	89
IV.2.1 Band gap energy and Urbach energy.....	89
IV.2.2 Calculation of optical properties.....	95
IV.3 Structural properties.....	102
IV.3.1 Number of network bonds (n_b) and average cross-link density ($\overline{n_c}$).....	102
IV.3.2 Average interionic separations($\langle d_{P-P} \rangle$) and the single bond strength B_{M-O}	103
IV.3.3 IR and ATR spectroscopy.....	105
IV.3.3.1 IR spectra (1,5-8 μ m).....	105
IV.3.3.2 ATR spectra (1600-400 cm^{-1}).....	107
IV.3.4 Raman spectroscopy.....	110
IV.4 Conclusion.....	115

Chapter V: Physical and spectroscopy studies of Sm⁺³ ions doped SWN glasses

V.1 Introduction.....	122
V.2 Experimental synthesis.....	123
V.3 Physical properties.....	123
V.4 Mechanical properties.....	122
V.4.1 Theoretical elastic modulus.....	127
V.4.2 Experiment elastic modulus of SWNSm glasses.....	128
V.5 Thermal properties.....	129
V.6 Structural properties.....	130
➤ IR spectroscopy.....	130
➤ ATR analyze.....	131
V.7 Optical absorption.....	134
V.8 Photoluminescence (PL) study.....	138
V.8.1 Excitation spectra.....	138

V.8.2 Emission spectral.....	140
V.8.3 Cross-relaxations and energy transfer mechanism in Sm ³⁺ ions.....	141
V.8.4 Emission lifetime analysis.....	142
V.9 CIE chromaticity coordinates.....	144
V.10 Conclusion.....	145
General conclusion.....	151

LIST OF FIGURES

Figure I.1: Schematic representation in 2D of the ordered structure of a silica crystal (a), and of a disordered structure of a silica glass (b).....	8
Figure I.2 : The interaction of physical states.....	9
Figure I.3: Thermodynamic variation of the specific volume $V(H)$ as a function of temperature T ; characterization temperatures.....	10
Figure I.4: A two-dimensional glass network of composition A_2O_3 (after Zachariasen 1932).....	12
Figure I.5: Two-dimensional schematic representation of the structure of a $(Si_2O - Na_2O)$ glass.....	13
Figure I.6: The role played by the different constituents of glass (soda-lime): Si, former, true modifier Na, Ca, charge compensator, Al, intermediate.....	14
Figure I.7: The structures of: (a) α - Sb_2O_3 , senarmontite, (b) β - Sb_2O_3 , valentinite, and (c) α - Sb_2O_4 , cervantite.....	15
Figure I.8: Crystal structure of tungsten oxide WO_3	16
Figure I.9: Schematic representation of phosphate groups and their denomination in terms of Q^n	17
Figure I.10: (A) Emission spectra, (B) excitation spectrum, and (C) energy level diagram of Sm^{3+} ions in $LiPbAl$ glass with cross-relaxation channels.....	22
Figure I.11: The proposed model for the structure of Sm^{3+} doped $Li_2O-SrO-B_2O_3$ glass.....	23
Figure I.12: Some of photonic applications.....	24
Figure II.1: Difference characterization techniques used in our work.....	30
Figure II.2: Differential Scanning Calorimeter (DSC) device labsys evo 1600°C.....	30
Figure II.3: Schematic diagram of the DSC.....	31
Figure II.4: Spectra of DSC.....	31
Figure II.5: DSC devise operation principal used in our work.....	33
Figure II.6: Scale equipped with a hydrostatic weighing device (OHAUS Adventurer AX type).....	34
Figure II.7: The different types of propagation wave in a homogeneous and infinite medium.....	35

Figure II.8: Pulse-Echo device equipment: Immersion transducer with an Olympus Model 5800RP generator, coupled to a 20GHz oscilloscope (HAMEG type).....	37
Figure II.9: Zwich/Roell (Indentec) micro-hardness tester.....	37
Figure II.10: The Vickers test principle.....	38
Figure II.11: Transparency domains of the three main families of oxide, halide and chalcogenide glasses.....	39
Figure II.12: Typical UV-Visible spectrophotometer operating.....	40
Figure II.13: Typical operating principle of a transmittance spectrophotometer in the UV-Vis and NIR range.....	41
Figure II.14: Variation of the absorption coefficient as a function of photon energy.....	42
Figure II.15: Determination of the energy gap.....	43
Figure II.16: Variation of $\ln(\alpha)$ as a function of $h\nu$	44
Figure II.17: Some vibrations mode.....	45
Figure II.18: a) FT-IR spectrometer Spectrum Two. b) Perkin Elmer spectrophotometer UATR techniques.....	46
Figure II.19: Device operation principle Spectrometer: Perkin Elmer Spectrum Two.....	47
Figure II.20: Diagram of the principle of photoluminescence phenomenon.....	47
Figure II.21: Schematic of the spectrofluorimeter equipment used for recording excitation, emission, and lifetime spectra.....	48
Figure II.22: Dispersion mechanisms of Stokes, Rayleigh and Anti-Stokes.....	50
Figure II.23: Schematic of an upright Raman microscope.....	51
Figure II.24: Microscope connected to an IHR 320 Horiba monochromator with a UV-VIS CCD camera.....	51
Figure III.1: Elaboration assembly from our glass.....	58
Figure III.2: The vitreous domain of the studied binary systems.....	59
Figure III.3: Glass domain of our ternary system $\text{Sb}_2\text{O}_3\text{-NaPO}_3\text{-WO}_3$	60
Figure III.4: The variation of ρ and V_m with the content of NaPO_3 in $(90-x) \text{Sb}_2\text{O}_3\text{-}10\text{WO}_3\text{-}x\text{NaPO}_3$ glasses.....	67
Figure III.5: The variation of ρ and V_m with NaPO_3 content in glasses $(80-x) \text{Sb}_2\text{O}_3\text{-}20\text{WO}_3\text{-}x\text{NaPO}_3$	68
Figure III.6: The variation of V_o and OPD with the content of NaPO_3 in AN glasses.....	68
Figure III.7: The variation of V_o and OPD with NaPO_3 content in BN glasses.....	69
Figure III.8: DSC curves of glass samples in the $(90-x) \text{Sb}_2\text{O}_3\text{-}x \text{NaPO}_3\text{-}10\text{WO}_3$ ternary system.....	70

Figure III.9: DSC curves of glass samples in the ternary system $(80-x) \text{Sb}_2\text{O}_3 - x\text{NaPO}_3 - 20\text{WO}_3$	70
Figure III.10: Evolution of T_g and ΔT for $(90-x) \text{Sb}_2\text{O}_3-10\text{WO}_3-x\text{NaPO}_3$ glass samples.....	71
Figure III.11: Evolution of T_g and ΔT for $(80-x) \text{Sb}_2\text{O}_3-20\text{WO}_3-x\text{NaPO}_3$ glass samples.....	71
Figure III.12: Experimental moduli of elasticity of AN glasses containing NaPO_3	78
Figure III.13: Theoretical moduli of elasticity of AN glasses containing NaPO_3	79
Figure III.14: The theoretical moduli of elasticity of BN glasses containing NaPO_3	80
Figure III.15: Experimental moduli of elasticity of BN glasses containing NaPO_3	81
Figure III.16: Poisson's ratio of $(90-x) \text{Sb}_2\text{O}_3-10\text{WO}_3-x\text{NaPO}_3$ glasses as a function of fractal bond connectivity.....	82
Figure III.17: Poisson's ratio of $(80-x) \text{Sb}_2\text{O}_3-20\text{WO}_3-x\text{NaPO}_3$ glasses as a function of fractal bond connectivity.....	82
Figure III.18: Theoretical and experimental Poisson's ratio of $(90-x) \text{Sb}_2\text{O}_3-10\text{WO}_3-x\text{NaPO}_3$ glasses as a function of NaPO_3 (mol%).....	83
Figure III.19: Theoretical and experimental Poisson's ratio of $(80-x) \text{Sb}_2\text{O}_3-20\text{WO}_3-x\text{NaPO}_3$ glasses as a function of NaPO_3 (mol%).....	83
Figure III.20: Values of temperature of glass transition, Young modulus and micro-hardness of AN glasses.....	84
Figure IV.1: Transmittance spectra in the UV-visible, and NIR ranges of the $(90-x) \text{Sb}_2\text{O}_3-10\text{WO}_3-x \text{NaPO}_3$ ternary system.....	90
Figure IV.2: Transmittance spectra in the UV-visible, and NIR ranges of the $(80-x) \text{Sb}_2\text{O}_3-20\text{WO}_3-x \text{NaPO}_3$ ternary system.....	90
Figure IV.3: Plot of $(\alpha hv)^{1/2}$ versus hv curve to estimate the band gap ($E_{g \text{ indirect}}$) of AN glasses.....	91
Figure IV.4: Plot of $(\alpha hv)^{1/2}$ versus hv curve to estimate the band gap ($E_{g \text{ indirect}}$) of BN glasses.....	91
Figure IV.5: Plot of $(\alpha hv)^{1/2}$ versus hv curve to estimate the band gap ($E_{g \text{ direct}}$) of AN glasses.....	92
Figure IV.6: Plot of $(\alpha hv)^{1/2}$ versus hv curve to estimate the band gap ($E_{g \text{ direct}}$) of BN glasses.....	92
Figure IV.7: $\ln(\alpha)$ as a function of hv for AN glasses to estimated E_u values.....	93
Figure IV.8: $\ln(\alpha)$ as a function of hv for BN glasses to estimated E_u values.....	94

Figure IV.9: Variation of n , R_m and α_m against NaPO_3 % content of AN glasses.....	98
Figure IV.10: Variation of n , R_m and α_m against NaPO_3 % content of BN glasses.....	99
Figure IV.11: ATR transmittance spectrum of the raw materials ((a) Sb_2O_3 , (b) NaPO_3 and (c) WO_3) in the region $1500\text{-}400\text{ cm}^{-1}$	105
Figure IV.12: IR transmittance spectra of AN glasses in the region $1,5\text{-}8\mu\text{m}$	106
Figure IV.13: IR transmittance spectra of BN glasses in the region $1,5\text{-}8\mu\text{m}$	106
Figure IV.14: ATR absorption spectra of AN glasses in the region ($1600\text{-}400\text{cm}^{-1}$).....	109
Figure IV.15: ATR absorption spectra of BN glasses in the region ($1600\text{-}400\text{cm}^{-1}$).....	109
Figure IV.16: Raman absorption spectra of system $(90\text{-}x)\text{ Sb}_2\text{O}_3\text{-}10\text{WO}_3\text{-}x\text{NaPO}_3$ with x varying from 10 to 80 glasses.....	110
Figure IV.17: Deconvolution analysis of the Raman spectra of AN glasses.....	111
Figure IV.18: Suggested of structural of SWN glasses with high concentration of NaPO_3	113
Figure V.1: The photos of SWNSm glasses with Sm^{3+} ions vary from 0,15 to 0,75 mole %.....	123
Figure V.2: Density and molar volume of $(40\text{-}x)\text{ Sb}_2\text{O}_3\text{-}10\text{ WO}_3\text{-}50\text{ NaPO}_3\text{-}x\text{ Sm}_2\text{O}_3$ glasses.....	124
Figure V.3: DSC curves of $(40\text{-}x)\text{ Sb}_2\text{O}_3\text{-}10\text{ WO}_3\text{-}50\text{NaPO}_3\text{-}x\text{Sm}_2\text{O}_3$ glasses.....	129
Figure V.4: The value of transition temperature of SWNSm glasses.....	129
Figure V.5: IR transmittance spectra of SWNSm glasses in the region $1,5\text{-}8\mu\text{m}$	130
Figure V.6.a: ATR spectra of SWNSm glasses in the range $4000\text{-}400\text{cm}^{-1}$	131
Figure V.6.b: Deconvolution analysis of the ATR spectra of SWNSm glasses.....	132
Figure V.7: The structural suggests of SWNSm glasses.....	133
Figure V.8a: UV-Vis region absorption spectrum of SWNSm0,30 sample.....	135
Figure V.8b: NIR region absorption spectrum of SWNSm glasses.....	136
Figure V.9: Plot of $(\alpha h\nu)^{1/2}$ vs $h\nu$ curve to estimate the $E_{g\text{ indirect}}$ of SWNSm0.30 glasses.....	137
Figure V.10: Plot of $\text{Ln}(\alpha)$ vs $h\nu$ curve to estimate the E_u of SWNSm0.30 glasses.....	137
Figure V.11: Excitation spectra of Sm^{+3} doped SWN glasses.....	139
Figure V.12: Schematic energy level diagram for the Sm^{+3} : SWNSm glasses.....	139
Figure V.13: Emission spectra of Sm^{+3} doped SWN glasses.....	140
Figure V.14: The cross-relaxation channels involved in Sm^{+3} ions in SWNSm glasses.....	141
Figure V.15: Decay (lifetime) curves of SWNSm glasses.....	143
Figure V.16: The CIE coordinates of SWNSm glasses.....	144

LIST OF TABLE

Table I.1: Physical constants of inorganic constituents.....	14
Table I.2: Electronic configuration of samarium ions.....	21
Table III.1: starting materials of the $\text{Sb}_2\text{O}_3\text{-WO}_3\text{-NaPO}_3$ ternary system.....	56
Table III.2: Composition, density ρ , characteristic temperature, thermal stability ΔT and the color of samples of glasses from the $\text{Sb}_2\text{O}_3\text{-WO}_3\text{-NaPO}_3$ ternary system.....	61
Table III.3: The theoretical density (ρ_{theo}), experimental density (ρ_{exp}), molar volume (V_m), molar volume of oxygen (V_o) and oxygen packing density (OPD).....	65
Table III.4: The theoretical density (ρ_{theo}), experimental density (ρ_{exp}), molar volume (V_m), molar volume of oxygen (V_o) and oxygen packing density (OPD).....	66
Table III.5: Acoustic impedance (Z), Thermal expansion coefficient (α_p) and Debay temperature (θ_D).....	74
Table III.6: Physical and experimental elastic properties of the ternary system (90-x) $\text{Sb}_2\text{O}_3\text{-xNaPO}_3\text{-10WO}_3$	75
Table III.7: Physical and experimental elastic properties of the ternary system (80-x) $\text{Sb}_2\text{O}_3\text{-xNaPO}_3\text{-20WO}_3$	76
Table III.8: Molecular weight, Density, packing factor of oxide and dissociation energy per unit volume of Sb_2O_3 , WO_3 and NaPO_3	77
Table III.9: Theoretically calculated compositional and elastic properties of AN glasses based on the Makishima-Mackenzie theory.....	79
Table III.10: Theoretically calculated compositional and elastic properties of BN glasses based on the Makishima-Mackenzie theory.....	80
Table IV.1: Electronegativity, Refractive index, Optical basicity and ionic polarizability of oxides (α_{O-2}) values of Sb_2O_3 , WO_3 and NaPO_3 oxide.....	95
Table IV.2: Some physical calculated properties of the (90-x) $\text{Sb}_2\text{O}_3\text{-10WO}_3\text{-xNaPO}_3$ glasses (AN series).....	96
Table IV.3: Some physical calculated properties of the (80-x) $\text{Sb}_2\text{O}_3\text{-20WO}_3\text{-xNaPO}_3$ glasses (BN series).....	97
Table IV.4: Values of average cross-link density (\bar{n}_c) and number of bonds per unit volume (n_b) of glasses in the AN and BN glass samples.....	102
Table IV.5: The value of coordination number, CN, single bond strength, B_{M-O} of Sb_2O_3 , WO_3 and P_2O_5 oxide.....	103

Table IV.6: Average phosphore-phosphore separation, single bond B_{M-O} , $\alpha(OH)$ and OH content (ppm) of AN and BN glasses.....	104
Table IV.7: Assignment of the ATR transmittance bands ($1600-400\text{ cm}^{-1}$) of AN and BN glasses.....	108
Table IV.8: Assignment of the Raman absorption bands ($10-1400\text{ cm}^{-1}$) of AN glass.....	114
Table V.1: Glass composition in mole %, density (ρ), Molar volume (V_m), oxygen packing density (OPD), oxygen molar volume (V_o), Young modulus (E_i) and Poisson's ratio (ν_t).....	124
Table V.2: The number density of Sm^{3+} ions (N), the inter-nuclear distance (r_i), polaron radius(r_p), field strength (F), number of bonds per unit volume (n_b) and cross-link density (\bar{n}_c) and the average antimony–antimony separation($d_{(Sb-Sb)}$).....	125
Table V.3: Various physical and optical properties of SWNSm glasses.....	127
Table V.4: Molecular weight, density, packing factor of oxide, dissociation energy per unit volume of Sb_2O_3 , WO_3 , $NaPO_3$ and Sm_2O_3	128
Table V.5: The experimental elastic properties of the SWNSm glasses.....	128
Table V.6: Assignment of the ATR transmittance bands ($4000-400\text{ cm}^{-1}$) of SWNSm glasses.....	134
Table V.7: The transition of Sm^{+3} and assignment wavelength correspond to the excited states from the ground states $^6H_{5/2}$ to various excited states.....	135
Table V.8: The transition of Sm^{+3} and assignment wavelength correspond to the excited states from the ground states $^6H_{5/2}$ to various excited states.....	138
Table V.9: The CIE –chromaticity diagram of Sm^{+3} doped SWN glasses.....	144

General introduction

General introduction

From windows to screens for electronic devices and fiber optics, oxide glasses have been used in a variety of applications [1]. They are used in a wide variety of fields, such as glazing (windows), domestic utensils (glasses etc.), eyeglasses or lighting.

Antimony oxide glasses are suitable for laser sources and optical amplification in telecommunications because they have low phonon energy (600 cm^{-1}) [2, 3], high refractive index [4, 5], high thermal and chemical stability, and superior corrosion resistance. Antimony oxide glasses have large transmittance windows of around $0,4\text{-}6\text{ }\mu\text{m}$ and a near-infrared transmission cut-off of up to $8\text{ }\mu\text{m}$. Antimony oxide has been added to a variety of glass compositions due to its various applications [5-7]. The strong third-order nonlinearity of antimony-borate or antimony-phosphate glasses has been demonstrated, making them particularly attractive for all-optical switching, 3D optical storage, and holographic data storage [8-11].

Phosphate glasses have many advantages over traditional silicate and borate glasses due to their better physical characteristics, such as high coefficients of thermal expansion, low melting and softening temperatures, and high ultraviolet and far infrared transmission [12]. They are also the materials of choice for high-power laser applications. Many phosphate glasses are susceptible to crystallization or devitrification during processing or when used in applications requiring prolonged exposure to high temperatures. In recent years, much research has been conducted to improve the physical characteristics and chemical endurance of phosphate glasses, such as their low chemical durability and high hygroscopicity, by inserting a variety of glass formers and modifiers into the phosphate glass network, such as TiO_2 , V_2O_5 , Al_2O_3 , WO_3 , MoO_3 , Cr_2O_3 , Ta_2O_3 , Sb_2O_3 , etc [13, 14]. We would also like to note that, aside from its use in optical devices, phosphate glasses can also be used for biomedical applications [15].

Since antimony oxide is included, greater chemical stability and some physical qualities are provided because pure phosphate glasses are unstable. Enhancements in photosensitivity, AC conductivity, and nonlinear optical (NLO) characteristics are all found in antimony phosphate. So, we can say that the addition of different heavy metal oxides to phosphate glasses, such as antimony oxide, makes them suitable for NLO devices [15, 16].

Franco et al., [17] also showed that the incorporation of WO_3 in $\text{Sb}_2\text{O}_3\text{-SbPO}_4\text{-WO}_3$ glasses improves thermal stability and increases the glass transition temperature (T_g), and a photosensitive response under laser irradiation [18] and affects the redox behavior of the different oxidation states of tungsten W^{6+} , W^{5+} or W^{4+} .

As a result, tungsten oxide is widely employed in smart windows, anti-glare mirrors, non-emissive displays, optical recording devices, semiconductor gas sensors, and non-linear optics [19].

The electro-chromic and photochromic characteristics of tungsten oxide WO_3 have also been extensively researched [20, 21]. The concept of this effect is based on the ability of the element to vary its degree of oxidation and therefore its color under stimulation. It is a reversible phenomenon. As a result, several research studies on the characterization of amorphous WO_3 films formed on glass substrates have been conducted [22]. Extension of WO_3 to the vitreous network optimizes chemical stability and resistance to devitrification, as well as the ability to add a third, fourth, or even fifth component to the mixture [23].

In reality, large modulus of elasticity is still desirable in the fabrication of thinner, stiffer substrates for thin-film electronics or smart phone displays, among other applications. Elasticity is a material characteristic that is used to explain a variety of physical properties of vitreous materials, including thermal shock resistance and fracture toughness. Thus, when a material is charged with a specific force value, it produces an atom displacement, which results in a reaction in the form of strain, which gives a broad perspective on the mechanical behavior of the material [12].

Glass-doped RE ions can be helpful in the manufacturing of photonic devices such as lasers, optical broadband amplifiers, fiber lasers, LEDs, planar waveguides, small microchip lasers, etc. Sm^{3+} is one of the RE ions that can activate other RE ions to create luminescence in the visible and near-infrared (NIR) spectrum. Additionally, because of their strong orange/red emission light, Sm^{3+} -doped glasses are highly sought after for applications in high density optical storage, undersea communication, color displays, and visible solid state lasers. Generally, the emission spectra of Sm_2O_3 doped glasses show four emission peaks at 565, 602, 648 and 709 nm, which correspond to the $^4\text{G}_{5/2} \rightarrow ^6\text{H}_{5/2}$, $^6\text{H}_{7/2}$, $^6\text{H}_{9/2}$ and $^6\text{H}_{11/2}$ transitions, respectively. The highest emission transitions at $^4\text{G}_{5/2} \rightarrow ^6\text{H}_{7/2}$ are allowed magnetic dipole (MD) and electric dipole (ED) transitions [23-25].

General introduction

The thesis is structured into five chapters, starting with a general introduction.

- ✚ The first chapter is devoted to general notions about glasses. Its purpose is to give an overview of these materials, their properties, their structures and their photonic applications.
- ✚ In the second chapter, we present the details of the experimental techniques used in this work.
- ✚ Throughout the third chapter, we present a description of the experimental conditions for the synthesis of glasses of the $\text{Sb}_2\text{O}_3\text{-WO}_3\text{-NaPO}_3$ system. Thus, we have explored new antimonite glasses in the ternary system based on the association of antimony oxide with phosphate and tungsten oxides. Two series of AN and BN samples were chosen to highlight the effect of the incorporation of NaPO_3 oxides with several physical properties. Thermal characteristics are carried out by differential scanning calorimetry to determine the characteristic temperatures of these glasses and to follow the evolution of the thermal properties and stability according to the vitreous compositions. Elastic, mechanical and other characteristics were also carried out.
- ✚ The fourth chapter gathers the structural studies of these glasses by the use of infrared vibrational spectroscopy FTIR, Raman and the optical properties (such as transmittance spectrum in the fields of UV-Vis and NIR region, E_g and E_u , etc.).
- ✚ The fifth chapter is devoted to the study of the photoluminescence properties of the Sm^{3+} ion in the SWN glassy matrix. This study takes into account the effect of the concentration of the Sm^{3+} ions on the physical, thermal, structural, optical and PL (excitation and emission spectrum in the UV-Vis region and decay curves (lifetime)) properties of the SWNSm glasses.

Finally, the thesis is closed with a general conclusion, which highlights all the most significant results of this work.

References

1. Luo, J., et al., Size-dependent brittle-to-ductile transition in silica glass nanofibers. *Nano letters*, 2016. **16**(1): p. 105-113. <https://doi.org/10.1021/acs.nanolett.5b03070>
2. Som, T. and B. Karmakar, Efficient green and red fluorescence upconversion in erbium doped new low phonon antimony glasses. *Optical Materials*, 2009. **31**(4): p. 609-618. <https://doi.org/10.1016/j.optmat.2008.06.018>
3. Soltani, M., et al., New alkali antimonate glasses. *Journal of Physics and Chemistry of Solids*, 2003. **64**(12): p. 2307-2312. [https://doi.org/10.1016/S0022-3697\(03\)00220-8](https://doi.org/10.1016/S0022-3697(03)00220-8)
4. Hamzaoui, M., et al., Optical properties of erbium doped antimony based glasses: Promising visible and infrared amplifiers materials. *physica status solidi (b)*, 2012. **249**(11): p. 2213-2221. <https://doi.org/10.1002/pssb.201248271>
5. Baazouzi, M., et al., Optical properties of alkali-antimonite glasses and purified processes for fiber drawing. *Optical Materials*, 2013. **36**(2): p. 500-504. <https://doi.org/10.1016/j.optmat.2013.10.017>
6. Dubois, B., et al., New oxyhalide glasses involving Sb_2O_3 . *Materials research bulletin*, 1984. **19**(10): p. 1317-1323. [https://doi.org/10.1016/0025-5408\(84\)90194-6](https://doi.org/10.1016/0025-5408(84)90194-6)
7. Grund, L. and B. Jonson, Compositional effect on fining and oxygen activity in mixed alkali silicate glass. *Glass Technology-European Journal of Glass Science and Technology Part A*, 2009. **50**(1): p. 62-64.
8. Falcão Filho, E., et al., Ultrafast nonlinearity of antimony polyphosphate glasses. *Applied physics letters*, 2003. **83**(7): p. 1292-1294. <https://doi.org/10.1063/1.1828216>
9. Terashima, K., et al., Structure and nonlinear optical properties of Sb_2O_3 - B_2O_3 binary glasses. *Journal of the Ceramic Society of Japan*, 1996. **104**(1215): p. 1008-1014. <https://doi.org/10.2109/jcersj.104.1008>
10. Nalin, M., et al., Characterization of the reversible photoinduced optical changes in Sb-based glasses. *Journal of non-crystalline solids*, 2006. **352**(32-35): p. 3535-3539. <https://doi.org/10.1016/j.jnoncrysol.2006.03.087>
11. Sincerbox, G.T., Holographic storage—the quest for the ideal material continues. *Optical Materials*, 1995. **4**(2-3): p. 370-375. [https://doi.org/10.1016/0925-3467\(94\)00089-1](https://doi.org/10.1016/0925-3467(94)00089-1)
12. Guesmia, N., et al., Glass formation, physical and structural investigation studies of the $(90-x)\text{Sb}_2\text{O}_3$ - 10WO_3 - $x\text{NaPO}_3$ glasses. *Materials Today Communications*, 2022. **30**: p. 103226. <https://doi.org/10.1016/j.mtcomm.2022.103226>

13. Krishna, G.M., et al., Induced crystallization and physical properties of $\text{Li}_2\text{O}-\text{CaF}_2-\text{P}_2\text{O}_5: \text{TiO}_2$ glass system: Part II. Electrical, magnetic and optical properties. *Journal of Alloys and Compounds*, 2008. **450**(1-2): p. 486-493. <https://doi.org/10.1016/j.jallcom.2006.10.148>
14. Abid, M., A. Shaim, and M. Et-Tabirou, Glass-forming region and electrical properties of $\text{Li}_2\text{O}-\text{PbO}-\text{P}_2\text{O}_5$ glasses. *Materials research bulletin*, 2001. **36**(13-14): p. 2453-2461. [https://doi.org/10.1016/S0025-5408\(01\)00716-4](https://doi.org/10.1016/S0025-5408(01)00716-4)
15. Ataalla, M., et al., Tungsten-based glasses for photochromic, electrochromic, gas sensors, and related applications: A review. *Journal of non-crystalline solids*, 2018. **491**: p. 43-54. <https://doi.org/10.1016/j.jnoncrysol.2018.03.050>
16. De Vicente, F. S., et al. "EPR, optical absorption and luminescence studies of Cr^{3+} -doped antimony phosphate glasses." *Optical Materials* 38 (2014): p. 119-125. <https://doi.org/10.1016/j.optmat.2014.10.012>
17. Franco, D.F., et al., Glass formation and the structural study of the $\text{Sb}_2\text{O}_3-\text{SbPO}_4-\text{WO}_3$ system. *Eclética Química*, 2017. **42**: p. 51-59. <https://doi.10.26850/1678-4618eqj.v42.1.2017.p51-59>
18. Poirier, E. and A. Dailly, Investigation of the hydrogen state in IRMOF-1 from measurements and modeling of adsorption isotherms at high gas densities. *The Journal of Physical Chemistry C*, 2008. **112**(33): p. 13047-13052. <https://doi.10.1021/jp711709r>
19. Knowles, J.C., Phosphate based glasses for biomedical applications. *Journal of Materials Chemistry*, 2003. **13**(10): p. 2395-2401. <https://doi.org/10.1039/B307119G>
20. Faughnan, B.W., R.S. Crandall, and M.A. Lampert, Model for the bleaching of WO_3 electrochromic films by an electric field. *Applied physics letters*, 1975. **27**(5): p. 275-277. <https://doi.org/10.1063/1.88464>
21. Faughnan, B., et al., IVB-1 the dynamics of coloring and bleaching of WO_3 amorphous electrochromic films. *IEEE Transactions on Electron Devices*, 1975. **22**(11): p. 1063-1064. <https://doi.org/10.1109/T-ED.1975.18305>
22. Granqvist, C., Electrochromism and smart window design. *Solid State Ionics*, 1992. **53**: p. 479-489. [https://doi.org/10.1016/0167-2738\(92\)90418-O](https://doi.org/10.1016/0167-2738(92)90418-O)
23. Çelikkbilek, M., et al., Crystallization kinetics of the tungsten-tellurite glasses. *Journal of non-crystalline solids*, 2011. **357**(1): p. 88-95. <https://doi.org/10.1016/j.jnoncrysol.2010.09.012>
24. Sudhakar, K., et al., Influence of modifier oxide on spectroscopic and thermoluminescence characteristics of Sm^{3+} ion in antimony borate glass system.

Journal of luminescence, 2008. **128**(11): p. 1791-1798.
<https://doi.org/10.1016/j.jlumin.2008.04.010>

25. Mohan, S., et al., Structural and luminescence properties of samarium doped lead alumino borate glasses. Optical Materials, 2017. **73**: p. 223-233.
<https://doi.org/10.1016/j.optmat.2017.08.015>

Chapter I

Generals on the glass

I.1 Introduction

In recent years, heavy metal oxide glasses, or HMOGs, have been the subject of much research compared to conventional glasses. The development of these materials is linked to their interesting physical and optical properties. These glasses can be said to be characterized by low phonon energy, a higher refractive index, and a wider infrared transmission spectrum. They also possess nonlinear optical properties to be used as materials for active optics.

Glass is an amorphous material that exhibits a glass transition phenomena and is also known as disordered materials or non-crystallized. The arrangement of atoms, observed by X-ray diffraction, is as disordered as in a liquid; the long-range order found in crystals no longer exists; there is only an order on the scale of the interatomic distance (it presents a short-range order). Glass on crystalline materials is characterized by a viscous state, a property that crystalline solids do not possess.

Among the desirable uses of glass found in windows, household utensils, glasses, bottles, or light bulbs, photonic applications have drawn the attention of many scientists for their uses in fields such as optical fibers, laser emission, optical amplifiers, and LEDs. Glass fibers have enabled humans to make major improvements in communications, medicine, and pollution detection. The exploration of new glass materials has always attracted the attention of scientists to improve the performance of glass and open new avenues of photonic applications. Lanthanide-doped glasses, in the form of bulk components, planar waveguides or fibers, have become promising options for optical amplification and Laser and LED emission [1-6].

The new research has turned to research glass competing with silica glass. Glass made from heavy elements, such as antimonite glass, is a promising line of research for applications in infrared and NLO applications, etc., due to its high refractive index [6, 7].

I.2 Glass definition

To the knowledge of most people, glass is a fragile and transparent material. From the scientific side, we can say that glass is a non-crystalline solid, presenting a glass transition phenomenon (figure I.1). "Amorphous solid to X-rays, that is to say, like that of a solidified liquid and illustrates the phenomenon of vitreous transition". For vitreous materials, this phenomenon is caused by a sudden change in the thermodynamic properties (heat capacity, expansion coefficient) derived from crystals to those of liquids [8].

From a physico-chemical point of view, glass is a frozen supercooled liquid. It has a disorganized structure devoid of long-range order, and there is no periodicity in the arrangement of atoms, but it exhibits short-range order. This definition is confirmed experimentally, whether by X-ray diffraction or by transmission electron microscopy (TEM), but it bears an arbitrary aspect since it depends on the size of the base pattern [8-10].

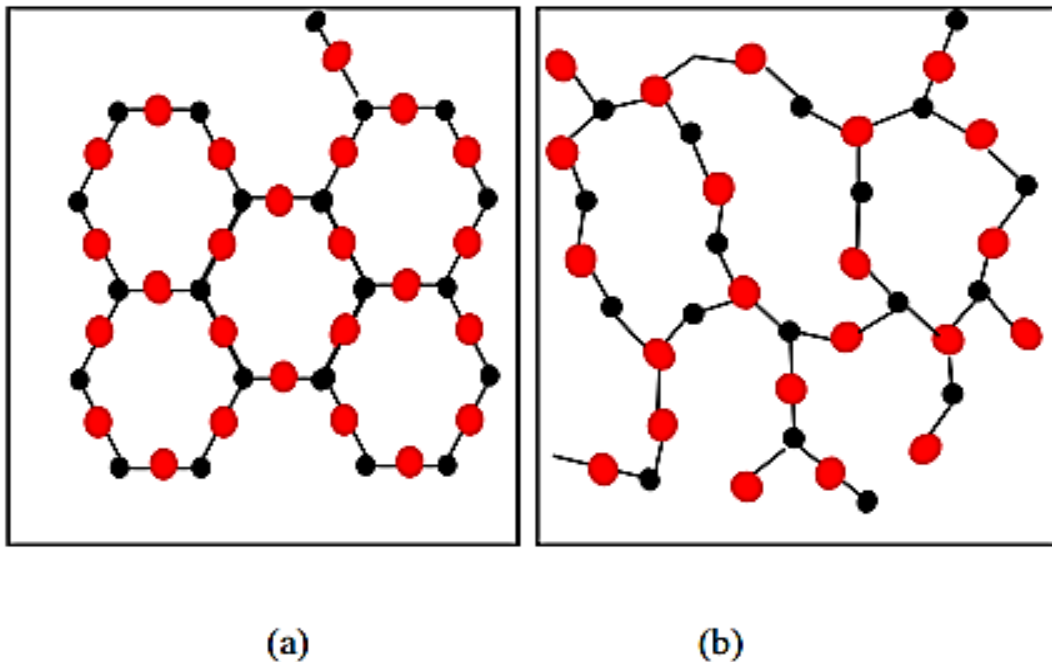


Figure I.1: Schematic representation in 2D of the ordered structure of a silica crystal (a), and of the disordered structure of a silica glass (b) [10].

I.3 Glass production

A non-crystalline solid is a glass that can be obtained essentially three different ways: by preserving the structural disorder of a liquid phase, by taking advantage of the disordered character of a gaseous phase, or by disorganizing a crystalline phase (fig I.2).

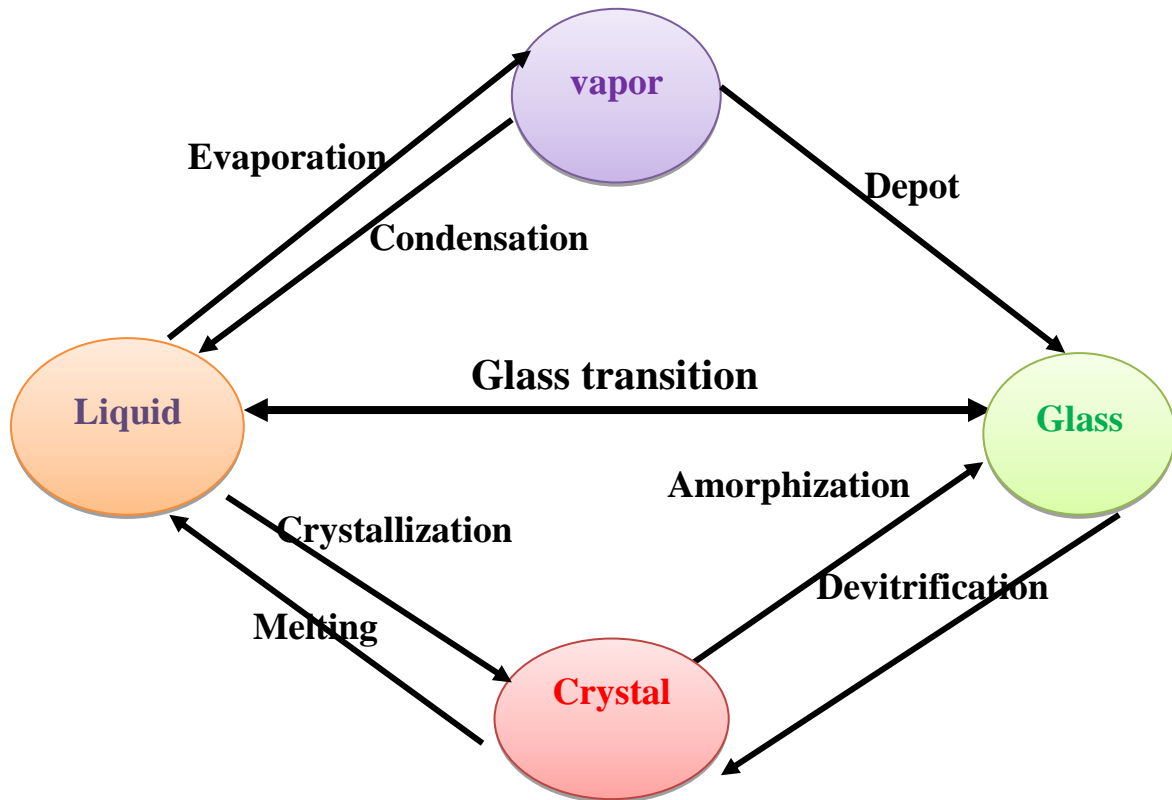


Figure I.2 : The interaction of physical states.

1. Starting from a **gaseous phase** by the condensation of the gas (vapor), which gives glass in the form of thin layers, this method is applicable to metals, semi-conductors, from Si to Ge and metal alloys.
2. From a **solid phase**, by the deformation of the crystalline structure under the effect of radiation or mechanical actions.
3. From a **liquid phase**, this technique is the most commonly used in the synthesis of glass; it is based on melting the main materials until a homogeneous liquid is obtained, which is followed by very rapid cooling (fast enough cooling speed) to avoid recrystallization [11].

I.4 Glass transition

The classic way to produce glass is to cool a liquid fast enough that crystallization does not have time to occur. The thermal behavior of glass can be described by the evolution of thermodynamic variables such as specific volume or enthalpy as a function of temperature [12].

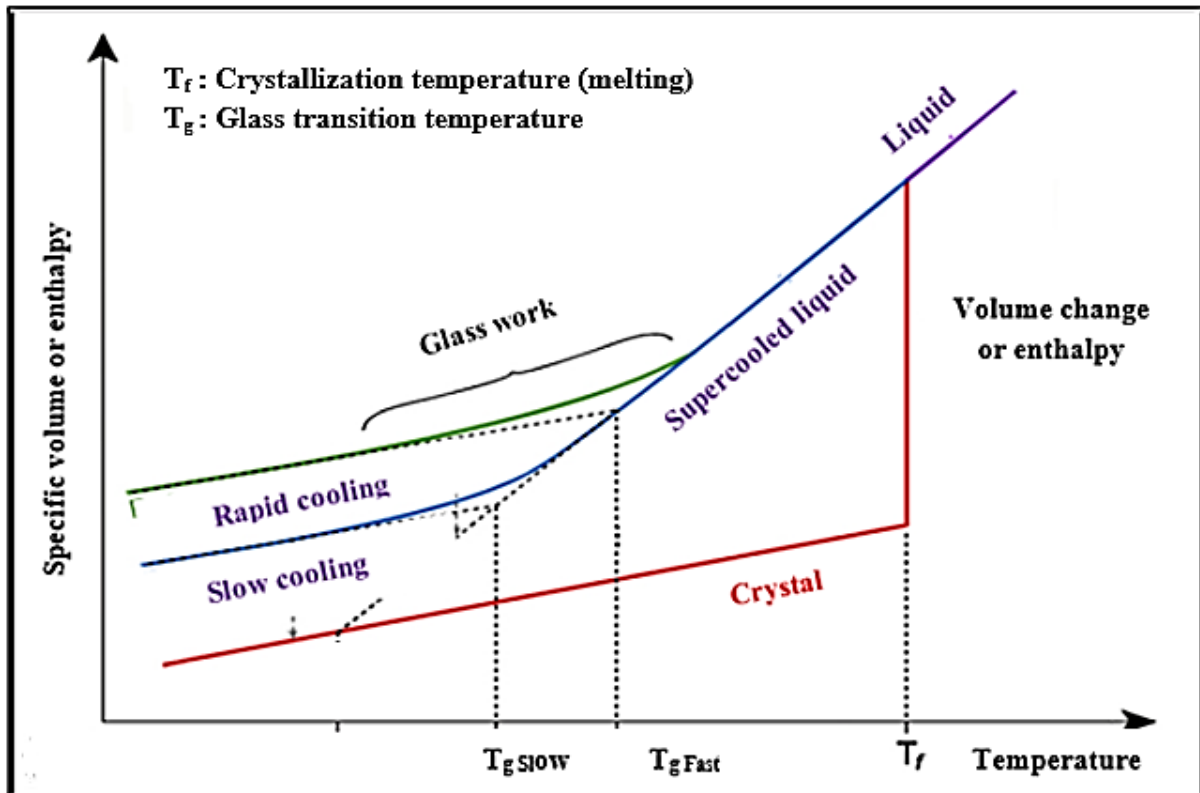


Figure I.3: Thermodynamic variation of the specific volume V (H) as a function of temperature T ; characterization temperatures [13].

Starting from the high temperature liquid phase, the molar volume V_M (or the enthalpy H) decreases with the temperature. At a temperature lower than the fusion temperature, for a treatment of infinite duration, the liquid will be transformed into a crystal whose molar volume (or enthalpy) is much lower than that of the corresponding super-cooled liquid (see figure I.3).

However, if the cooling is continuous and rapid from the stable liquid state to a very low temperature, the liquid passes into a temperature range where it is in a super-cooled state. It is this meta-stable state which will gradually freeze to give rise to glass at room temperature.

As the temperature decreases, the super-cooled liquid becomes more and more viscous and the atomic rearrangements take place with longer and longer relaxation times. Unlike the crystal, the variation of the molar volume between the two states is continuous over this temperature interval.

The glass transition temperature T_g is one of the fundamental characteristics of glass. This is a “reference” temperature. It is defined by Scholze as being the temperature at which the viscosity of the material reaches 10^{13} [Poise] is defined as the intersection of the curves

extrapolated from the liquid and the glass. This domain extends over a temperature range depending on the nature of the glass and the cooling rate. The higher the cooling rate, the higher the transformation takes place at a high temperature. The reverse is true for slow cooling (figure I.3).

The glass is in a meta-stable or non-equilibrium state. It is distinguished from the crystal by two essential aspects: a thermodynamic aspect characterized by an excess of energy and a geometric aspect characterized by an absence of order at a long distance, even if it appears to have a conservation of order at a short range.

By continuing the cooling, the viscosity of the liquid increases exponentially and the super-cooled liquid becomes almost solid. When it reaches 10^{13} [poises], the rigidity prevents local microscopic movements and a change in the slope of the enthalpy is observed (the slope becomes almost the same as that of the crystallized compound). The temperature at which this change occurs is called the glass transition temperature, T_g . For a temperature lower than T_g , the material is a solid with a structural disorder close to that of a liquid: it is a glass. The disorder, and therefore the entropy, is higher in a glass than in a crystal. From a thermodynamic point of view, the glass is in a meta-stable state, the minimum energy state being the crystallized state. The glass transition temperature T_g is an intrinsic property of glass. It depends on the one hand on the nature of the material and, on the other hand, on its history of formation (temperature and pressure conditions). In particular, it depends on the cooling rate used during quenching: the faster the liquid is cooled, the higher the temperature T_g .

I.5 Glass formation

To explain the formation of glasses, several very empirical approaches have been proposed. They are based on crystallographic and thermodynamic criteria or on considerations concerning the nature of the bond (Goldschmidt, Poulain and Zachariasen models, etc.).

In 1932, Zachariasen [14] put forward the hypothesis of a disordered lattice of oxide glasses. According to the structural role they play during vitrification, the cations involved in the composition of oxide glass are classified into three categories: network formers, network modifiers and intermediaries.

I.5.1 Formative elements

Lattice formers (SiO_2 , B_2O_3 , GeO_2 , As_2O_3 , P_2O_5) are elements that can form a glass on their own by constructing to each other by “bridging” oxygen with purely covalent bonds (see figure I.4) [15].

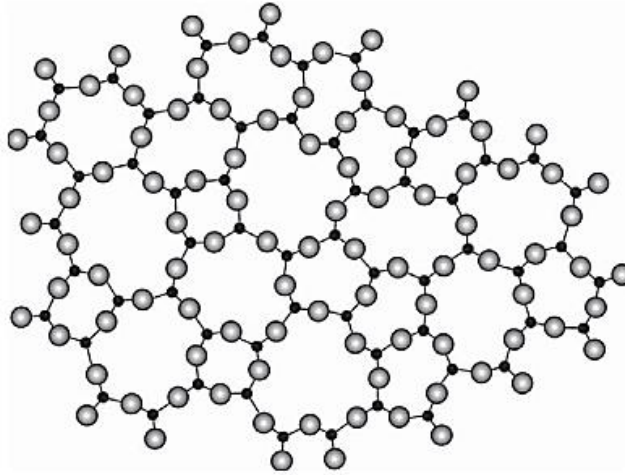


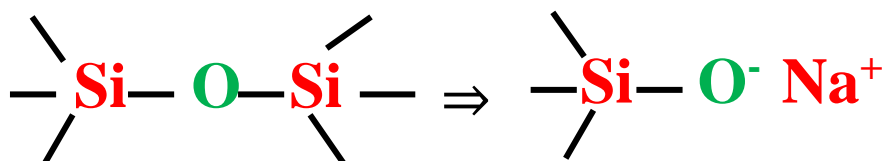
Figure I.4: A two-dimensional glass network of composition A_2O_3 (after Zachariasen 1932).

Dark circles are A atoms and light circles are O atoms. Note that the network is fully connected with all O atoms being shared between 2 A atoms. In addition, different sized rings can be observed [14].

I.5.2 Modifiers elements

Lattice modifiers (or non-formers) are elements that cannot form glass on their own. These are mainly the alkalis (Li_2O , Na_2O and K_2O), the alkaline earths (CaO , BaO) and certain transition elements or rare earths.

Their introduction into the glass network has the effect of depolymerizing the vitreous network by breaking bridges to form entities.



Oxygen, carrying an excess electronic charge, no longer establishes the connection between neighboring tetrahedrons. It is "non-bridging" oxygen.

The lattice-modifying oxide cation lodges in a cavity close to the filled bonds to compensate for the excess charge (figure I.5).

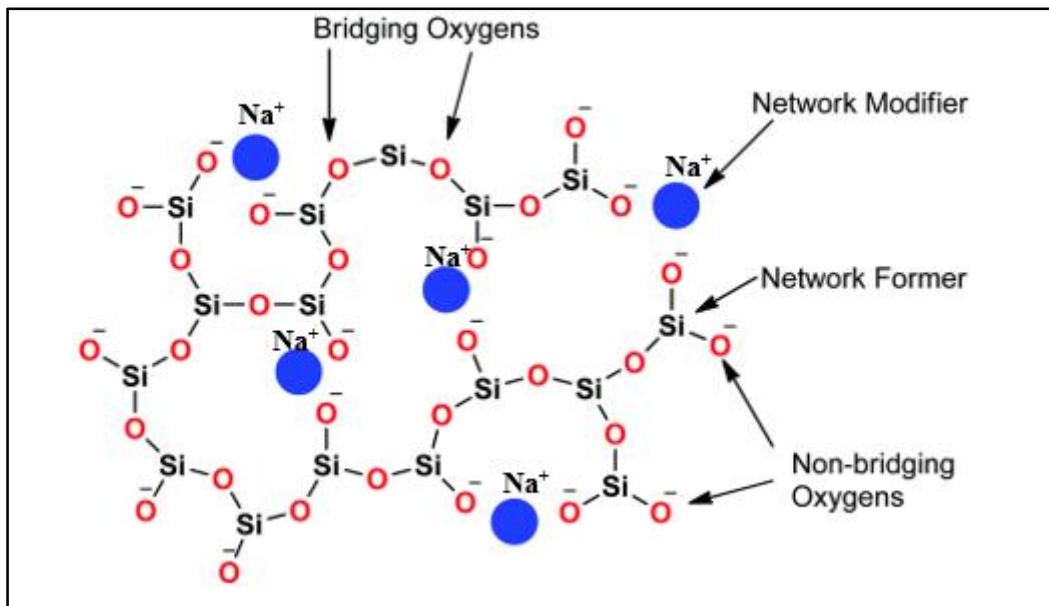


Figure I.5: Two-dimensional schematic representation of the structure of a $(\text{Si}_2\text{O}-\text{Na}_2\text{O})$ glass [16].

They are generally bulkier (larger ionic radius) than lattice formers, weakly charged, and their bonds to oxygen atoms are more ionic than those established by formers. They can have two very different structural roles: either as true network modifiers or load compensators.

- True lattice modifiers break the bonds between the polyhedrons of the vitreous lattice, causing depolymerization of the latter. They then transform bridging oxygens, which link two network-forming elements, into non-bridging oxygens, linked to a single network-forming element.
- Charge compensators, on the other hand, compensate for a negative charge on a lattice-forming polyhedron, allowing it to be stable in this configuration.

I.5.3 Intermediate elements

The best known intermediate oxides are: Al_2O_3 , Fe_2O_3 , PbO , TiO_2 , ZnO , MoO_3 , WO_3 . Depending on the composition of the glass, they behave either as network formers in the presence of charge compensators, or as modifiers in the absence of charge compensators (they will break the bridging bonds to form their polyhedrons), or neither of these functions but have an intermediate role such as coloring substances which are generally oxides of cobalt, chromium, iron, rare earths, sulphides, and metals (Cu, Ag, Au...) (fig I.6) [10].

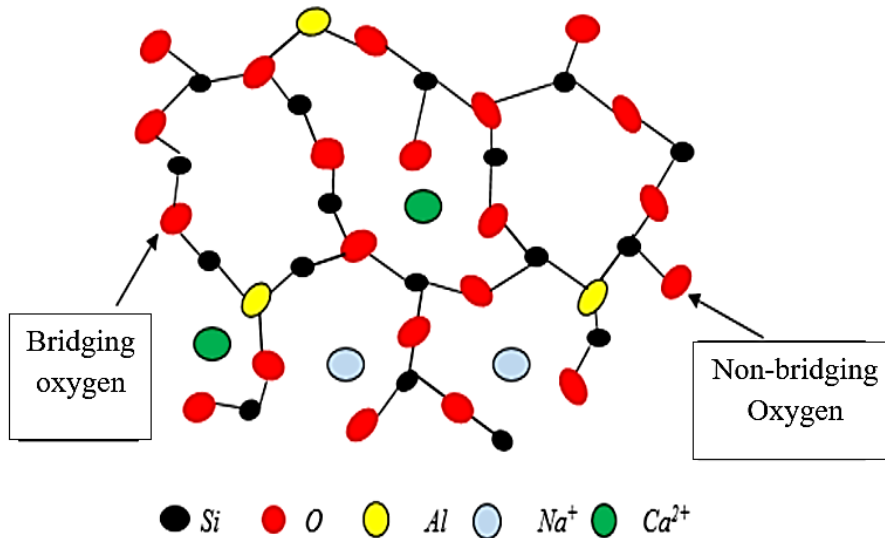


Figure I.6: The role played by the different constituents of glass (soda-lime): Si, former, true modifier Na, Ca, charge compensator, Al, intermediate [10].

I.6 General characteristics of glass chemical compositions

I.6.1 Antimony oxide Sb_2O_3

According to Zachariasen [14], antimony oxide (Sb_2O_3) was predicted to be a glass former. It is found naturally as an ore, stibine Sb_2S_3 , and as an oxide, Sb_2O_3 [17], and can exist as Sb_2O_3 or Sb_2O_5 . Table I.1 brings together some characteristics of antimony oxide ores [18, 19].

Table I.1: Physical constants of inorganic constituents [19].

Formula	Molar mass	Color incrystalline form	Density (g/cm^3)	T_f ($^{\circ}C$)	T_c ($^{\circ}C$)	Refractive index	solubility
Cervantitis Sb_2O_4	307.5	White powder	5.82	-	-	2	water, nitric and
Senarmontit e α - Sb_2O_3	291.5	White powder	5.2	656	1550	2.087	sulfuric acids
Valentinite β - Sb_2O_3	291.5	Color	5.67	656	1550	2.18, 2.35	

Antimony oxide glasses are attractive because of their wide use [19, 20], this importance of (Sb_2O_3) is due to:

- ✓ Wide forbidden band (indirect) $E_g = 3.3 \text{ eV}$ [21].
- ✓ Solubilize RE oxides in glass [18].
- ✓ Low synthesis temperature is $700\text{-}900^\circ\text{C}$ compared to silica oxide glasses at 1700°C .
- ✓ The synthesis of air glasses is compared to fluoride glasses, which go through several stages.
- ✓ Chemical durability.
- ✓ Transmissible up to $8 \mu\text{m}$ in the infrared spectrum [22], which leaves room for several applications as active or passive materials: laser, amplifier.
- ✓ Low phonon energy (about 600 cm^{-1} due to low Sb-O-Sb band stretching vibrations and high refractive indices [19, 23]), and also have extensive IR transmission, which makes Sb_2O_3 glasses suitable for studying them in the IR region [24].
- ✓ They have potential applications in nonlinear optical devices such as ultra-fast optical switches, power limiters, and broadband optical amplifiers [23].

Antimony oxide exists in several forms depending on the oxygen content. Sb_2O_3 oxide has two allotropic forms (fig I.7):

- $\alpha\text{-Sb}_2\text{O}_3$: senarmontite is cubic in shape (stable at low temperatures).
- $\beta\text{-Sb}_2\text{O}_3$: valentinite (stable at high temperatures) [12, 19, 20, 25].

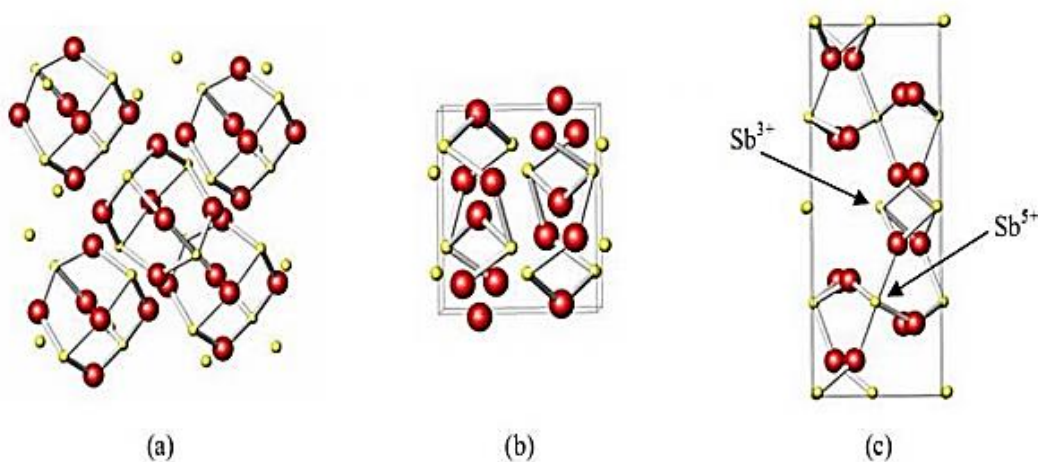


Figure I.7: The structures of: (a) $\alpha\text{-Sb}_2\text{O}_3$, senarmontite, (b) $\beta\text{-Sb}_2\text{O}_3$, valentinite, and (c) $\alpha\text{-Sb}_2\text{O}_4$, cervantite [12].

Sb_2O_3 participates in the glassy lattice with the structural unit SbO_3 and can be considered as tetrahedra with three corner oxygens and a single pair of antimony electrons (Sb^{3+}) in the fourth corner, located in the third equatorial direction of the Sb atom. The deformation of this pair is responsible for the high order 3 nonlinear optical susceptibility of antimony oxide glasses [19].

I.6.2 Tungsten trioxide WO_3

Tungsten trioxide (WO_3) has gained importance in the industrial sector because of its electrical, catalytic and photochromic properties [26]. The principle of this effect is based on the possibility of the element to change its degree of oxidation under excitation and therefore change color. This phenomenon may be reversible. Therefore, many studies have been performed on the characterization of amorphous WO_3 films deposited on glass substrates [19, 27]. All these benefits are because of WO_3 :

- ❖ Sensitive to visible light [28].
- ❖ Corrosion resistivity [29].
- ❖ Forbidden band of 2.7 eV [19].
- ❖ Insulation at room temperature [30].

Its crystallographic structure is cubic ReO_3 type [31-33], slightly deformed. The W^{6+} cations are in an octahedral WO_6 environment [34]. Tungsten trioxide WO_3 exists in several crystal forms. In all cases, the structure is composed of a three-dimensional assembly of WO_6 octahedra linked together by the vertices. Each oxygen atom therefore belongs to two octahedra, hence the chemical formula $\text{WO}_{6/2}$ or WO_3 of this oxide. This three-dimensional assembly of octahedra is shown in figure I.8 [26].

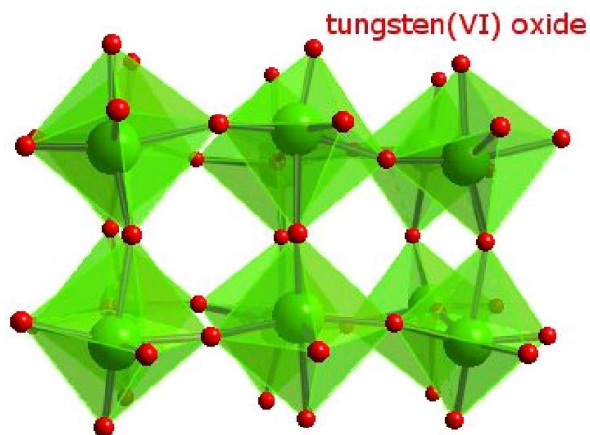
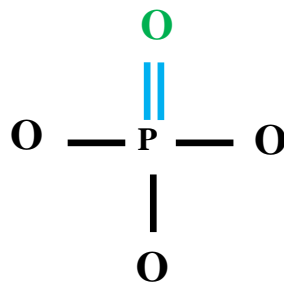


Figure I.8: Crystal structure of tungsten oxide WO_3 [19, 26].

I.6.3 Phosphate

Phosphate glasses have numerous benefits over traditional silicate and borate glasses due to their better physical characteristics, such as high thermal expansion coefficients, low melting and softening temperatures, and strong ultra-violet and far infrared transmission. They're also the preferred materials for high-power laser applications [6].

Phosphate compounds have several structures and can form three-dimensional or linear networks. These networks are based on the arrangement of PO_4 tetrahedra. The PO_4 tetrahedron forms five covalent bonds with four oxygens (three single bonds and one double bond).



Oxygen having a single bond with phosphorus can then be terminal (P-O^-) or bonded to another phosphorus atom (P-O-P). It is the number of terminal and bridging oxygens that will determine the nature of the phosphorus site. There is a nomenclature to describe the PO_4 tetrahedron [26, 35]. This tetrahedron is called Q^n , where n is the number of bridging oxygen atoms. There are therefore four possible types of Q^n tetrahedra (fig I.9):

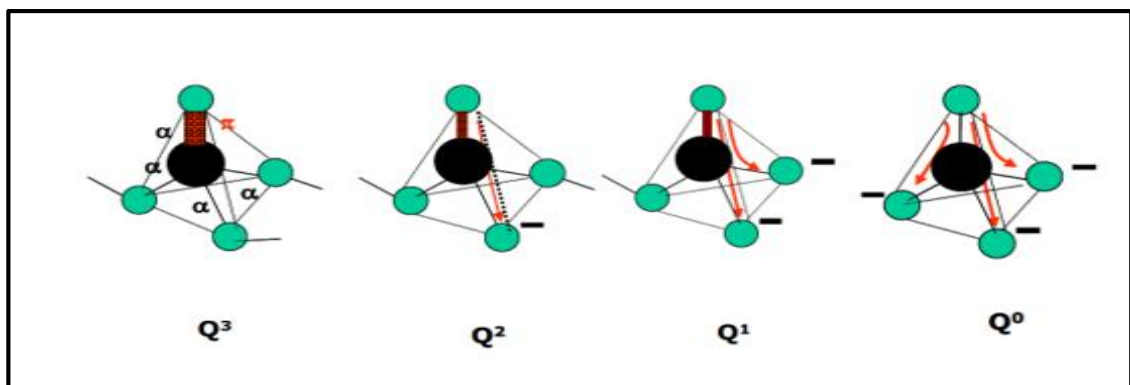


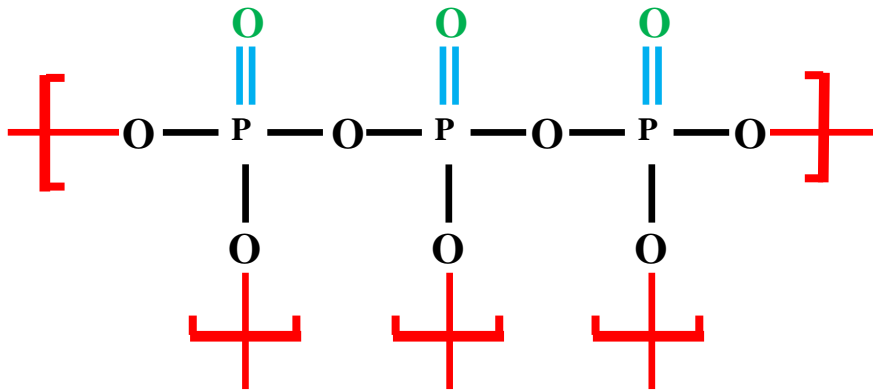
Figure I.9: Schematic representation of phosphate groups and their denomination in terms of Q^n [36].

The bridging oxygen atoms are bound to PO_4 groups and the non-bridging oxygen atoms have their negative charge neutralized by a cation.

I.6.3.1 Tetrahedra Q^3

The three oxygen atoms forming a single bond with phosphorus are bridging, i.e. bonded to another phosphorus. In this case, the arrangement of PO_4 tetrahedra forms a three-dimensional network and the compound formed is called ultraphosphate. Only phosphorus pentoxide (P_2O_5) forms this type of network. This ultraphosphate compound contains two distinct types of phosphorus-oxygen bonds:

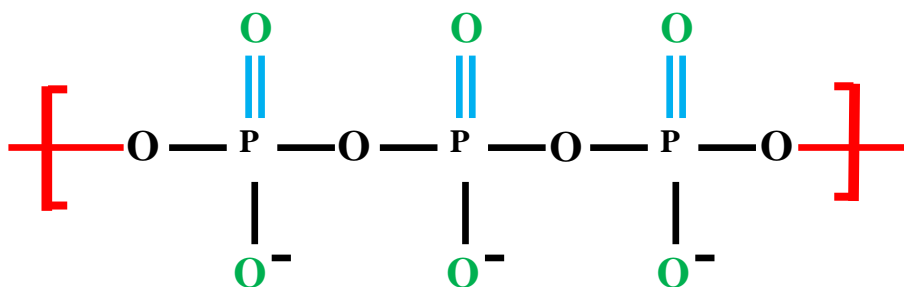
- terminal $P=O$ double bonds.
- The single bridging P-O bonds connect the PO_4 tetrahedra (P-O-P bonds).



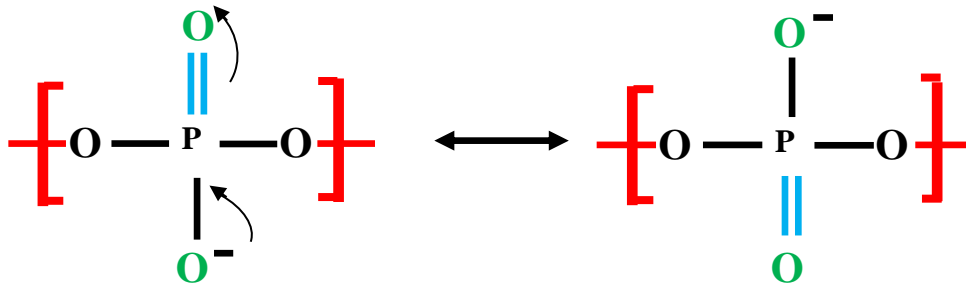
I.6.3.2 Tetrahedra Q^2

In this case, among the three oxygens forming a single bond with phosphorus, two oxygens are bridging and one oxygen is terminal. The arrangement of PO_4 tetrahedra then forms a one-dimensional chain and the compound is called metaphosphate. In this case, the cations stabilize the negatively charged terminal oxygen. This is the case, for example, of sodium metaphosphate ($NaPO_3$). These chains can have very variable dimensions, and it is generally customary to give the average length of the chains. The compound is then described by $(NaPO_3)_n$, n being the average number of tetrahedrons included in these linear chains. This compound also has two types of phosphor oxygen bonds:

- bridging P-O links.
- Terminal P-O bonds.



Indeed, we consider the double bond P=O and the terminal single bond P-O identical because there is resonance between the two bonds.

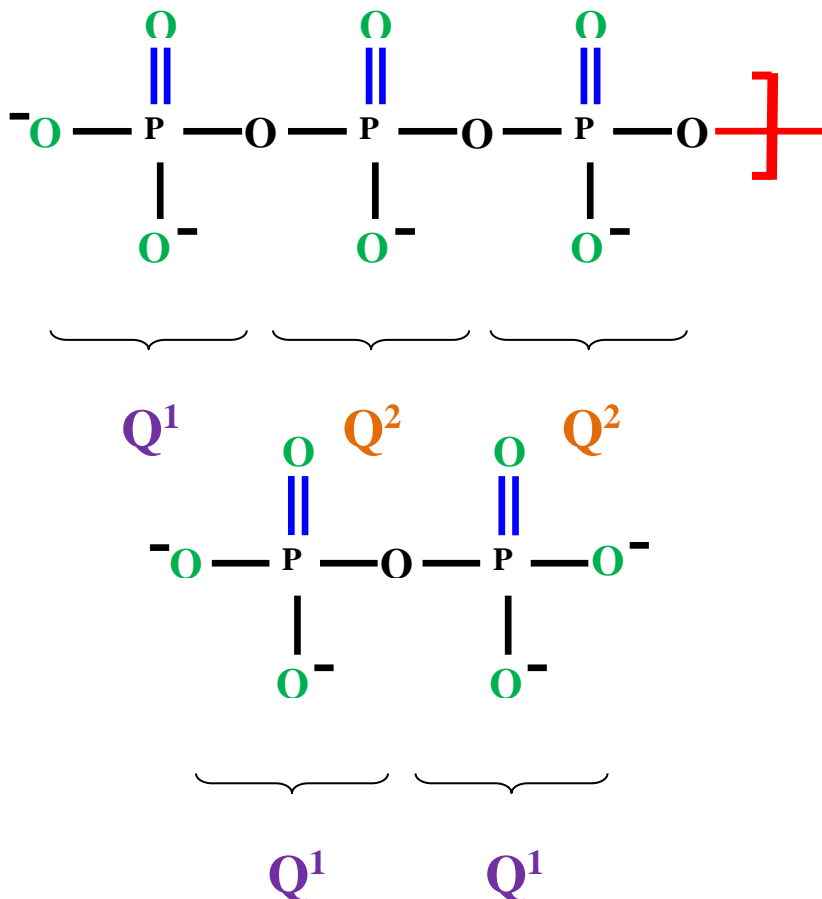


I.6.3.3 Tetrahedra Q¹

Of the three oxygens forming a single bond with phosphorus, one oxygen is bridging and the other two are terminal, negatively charged and stabilized by cations.

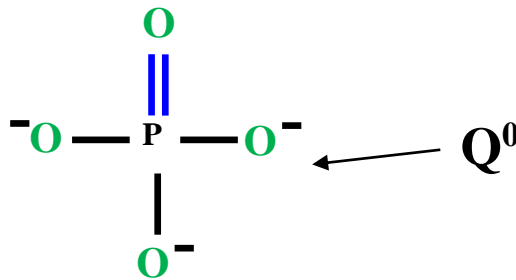
These tetrahedrons are then called pyrophosphates and are sometimes denoted PO₃²⁻. There are then two possibilities: the Q¹ tetrahedron is placed at the end of the metaphosphate chain and therefore linked to a Q², or it is linked to another Q¹, then forming a P₂O₇⁴⁻ dimer. It is therefore present, for example, in the sodium metaphosphate NaPO₃ at the end of the chain or only in the form of dimers, for example in the sodium pyrophosphate Na₄P₂O₇.

Pyrophosphate tetrahedra also have two types of phosphorus-oxygen bonds: terminal P-O bonds and bridging P-O bonds.



I.6.3.4 Tetrahedra Q^0

In this case, all the oxygens bound to the phosphorus atom are terminals, so the PO_4 tetrahedron is isolated. These compounds are called orthophosphates and the tetrahedra are sometimes denoted PO_4^{3-} . This is the case, for example, of sodium orthophosphate (Na_3PO_4). Orthophosphate tetrahedra have only one type of phosphorus-oxygen bond because the double bond is resonant with all oxygens [26, 34-36].



I.7 Rare earth ions

The lanthanide group of fifteen elements, together with scandium (Sc) and yttrium (Y), are collectively referred to as rare earth elements. When placed into a host material, rare earth ions in particular act as luminescence centers. For use in fiber lasers, optical amplifiers and telecommunication, as well as high density optical memory, glasses are renowned as good host materials for rare-earth ions.

The primary source of these ions' characteristics is the shielding provided by the $5S^2$ and $5P^6$ orbitals, which mostly cover the $4f$ orbitals fully. The valence electrons are thus only slightly perturbed by the surroundings, and their electronic transitions result in thin and intense lines [37, 38].

I.7.1 Samarium ions

In glasses, samarium ions can be found in a divalent or trivalent form. The glasses that have been made using traditional glass melting processes are the ones where these ions are most stable in their trivalent condition. Sm ions' electrical structures are displayed in [Table I.2 \[37\]](#):

Table I.2: Electronic configuration of samarium ions [37].

Trivalent rare earth ion	Electronic configurations
Sm	[Xe] 4f ⁶ 6s ² 1s ² 2s ² 2p ⁶ 3s ² 3p ⁶ 4s ² 3d ¹⁰ 4p ⁶ 5s ² 4d ¹⁰ 5p ⁶ 6s ² 4f ⁶
Sm³⁺	[Xe] 4f ⁵ 1s ² 2s ² 2p ⁶ 3s ² 3p ⁶ 4s ² 3d ¹⁰ 4p ⁶ 5s ² 4d ¹⁰ 5p ⁶ 4f ⁵
Sm²⁺	[Xe] 4f ⁶ 1s ² 2s ² 2p ⁶ 3s ² 3p ⁶ 4s ² 3d ¹⁰ 4p ⁶ 5s ² 4d ¹⁰ 5p ⁶ 4f ⁶

The Sm³⁺ ion's electronic structure is [Xe] 4f⁵, and its free ion ground state is ⁶H_{5/2}. As a Kramer's ion, Sm³⁺ is thought to contain an odd number of electrons in the 4f shell, which results in double degeneracy in this ion's energy levels due to the ligand-field. The lowest excited state for the Sm²⁺ ion's [Xe] 4f⁶ electron configuration is ⁷F₀. These ions are not Kramer ions since they contain an even number of electrons in their 4f shell. As a result, there are several doublet and singlet energy levels.

Sm³⁺ ions exhibit four emissions corresponding to ⁴G_{5/2} → ⁶H_{5/2, 7/2, 9/2, and 11/2} transitions that correspond to luminescence bands at about 563, 598, 644, and 705 nm, respectively [37, 39, 40]. Also, Sm²⁺ ion's photoluminescence has the emission corresponding to the transitions (⁵D₀ → ⁷F_J; J = 0, 1, 2, 3, 4), which have luminescence maxima at wavelengths of 683, 700, 724, 760, and 810 nm, respectively [37].

N. Deopa and A.S. Rao.,[41] studied the excitation and emission spectrum of Sm³⁺ in LiPbAl glasses. Samarium ions are excited from the ground state of ⁶H_{5/2} to different levels of transition and swiftly relax through a non-radiative transition to the energy level of ⁴G_{5/2}. The excitation spectrum of LiPbAlB glasses exhibits nine prominent bands at 344, 361, 374, 388, 401, 416, 439, 463 and 477 nm corresponding to the transitions ⁶H_{5/2} → ⁴H_{9/2} + ⁴D_{7/2}, ⁴D_{3/2}, ⁶P_{7/2}, ⁴L_{15/2}, ⁴F_{7/2}, (⁶P, ⁴P)_{5/2}, ⁴G_{9/2}, ⁴I_{13/2} and ⁴I_{11/2} respectively (see fig I.10). It has a prominent excitation peak at 401nm, which corresponds to the ⁶H_{5/2} → ⁴F_{7/2} transition. Fig I.10 shows the excitation spectrum (at λ_{em}=597 nm), emission (at λ_{ex}= 401 nm) and energy level diagram of Sm³⁺ ions in LiPbAlB glass [41]. Additionally, the substantial energy difference between the upper ⁴G_{5/2} level and the lower ⁶F_{11/2} level is a major factor in the multiphoton relaxation. In fig I.10, the potential cross-relaxation channels for LiPbAlB

glasses doped with Sm^{3+} ions are depicted. When the absorption and emission transitions coincide with each other, a process known as cross-relaxation takes place.

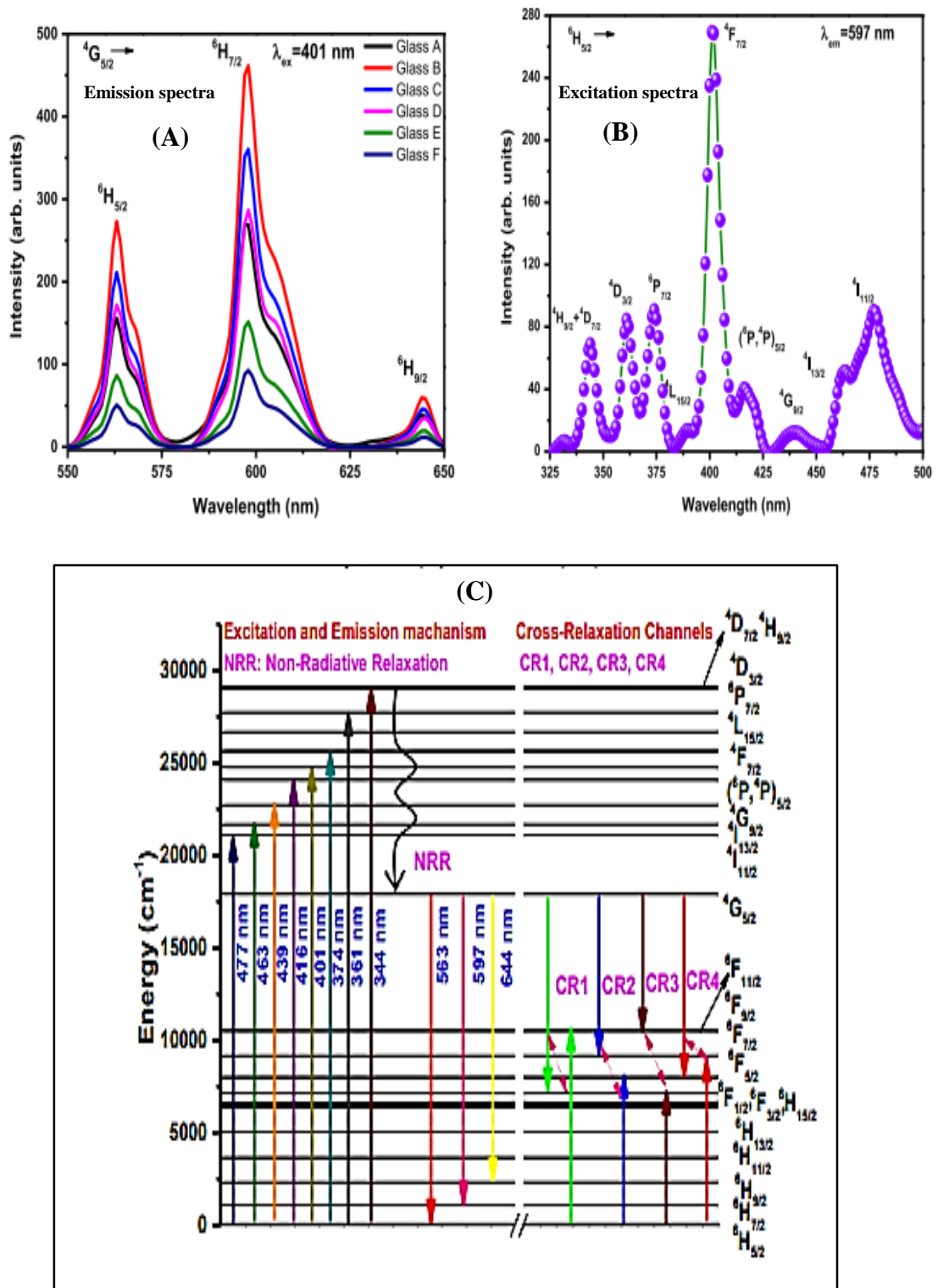


Figure I.10: (A) Emission spectra, (B) excitation spectrum, and (C) energy level diagram of Sm^{3+} ions in LiPbAl glass with cross-relaxation channels [41].

I.7.2 Effect of RE doping on the glass structure

The incorporation of RE ions is more practical in glasses with a large concentration of non-bridging oxygen, such as phosphate glasses. In the glass matrix, RE^{3+} ions (such as Sm^{3+}) replace a network modifier (such as Na^+ and Sr^{2+}), and are surrounded by structurally bridging oxygen and non-bridging oxygen (figure I.11) [42]. When non-bridging oxygen is decreased in glasses like borate, phosphate or pure silica, RE ions cluster, which lowers the radiative transitions.

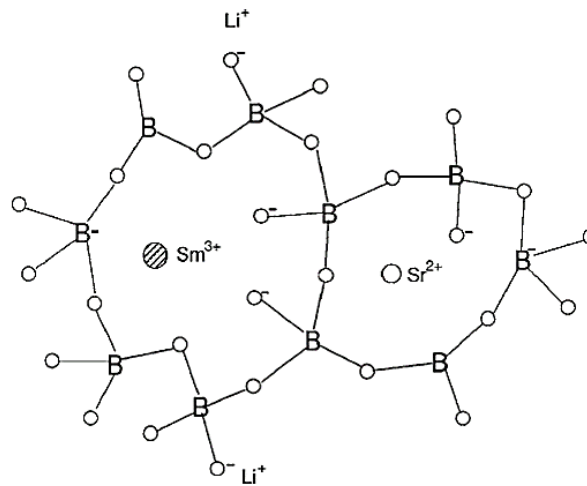


Figure I.11: The proposed model for the structure of Sm^{3+} doped $Li_2O-SrO-B_2O_3$ glass [42].

I.8 Photonic applications

Glasses are a potential material for the photonics applications, which includes LEDs, lasers, optical fibers for telecommunication, ultrafast optical switches, power limiters, etc., (fig I.12) [43]. Because our glass array included samarium ion doping, which is well-known for its uses in red-orange light, we'll mention some of LED applications [41].

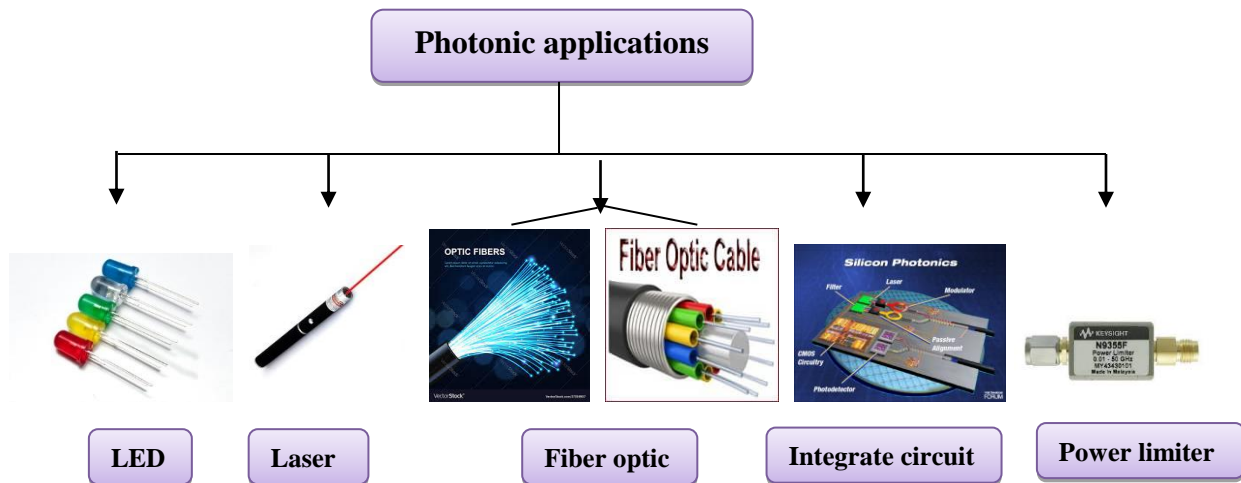


Figure I.12: Some application in photonics.

✚ Lighting technologies were born out of the need to supplement sunlight. From prehistory to the present day, three types of technology have been successively developed: combustion lamps; incandescent lamps; and discharge lamps. Among the criteria for classifying these different light sources is the energy efficiency of light/electricity conversion, which remains low. A considerable global effort is devoted to this field of research with the aim of reducing electricity consumption. The latest advance is the discovery of white light-emitting diodes (LEDs) to replace traditional lighting (incandescent lamps and fluorescent tubes) thanks to their better performance and longer life.

✚ LEDs are increasingly present in our daily lives, for viewing and transmitting information, lighting in televisions and mobile phones, etc. As we will see, for each of these applications, the use of LEDs is based on well-considered choices (economic, aesthetic, etc.) [44].

References

1. Nandi, P. and G. Jose, Superfluorescence from Yb-and Yb–Er-doped phosphotellurite glass fibres. *Optical Fiber Technology*, 2008. **14**(4): p. 275-280. <https://doi.org/10.1016/j.yofte.2008.01.004>
2. Moore, P.J., Z.J. Chaboyer, and G. Das, Tunable dual-wavelength fiber laser. *Optical Fiber Technology*, 2009. **15**(4): p. 377-379. <https://doi.org/10.1016/j.yofte.2009.04.001>
3. Oh, K., et al., Spectral control of optical gain in a rare earth-doped optical fiber using novel triple layered structures. *Optical Fiber Technology*, 2006. **12**(4): p. 297-304. <https://doi.org/10.1016/j.yofte.2006.03.005>
4. Xiong, Z. and T. Chen, Multi-wavelength Raman fiber laser with 2-and 3-stage cavities in a phosphosilicate fiber. *Optical Fiber Technology*, 2007. **13**(1): p. 81-84. <https://doi.org/10.1016/j.yofte.2006.09.003>
5. Chillce, E., et al., Er³⁺–Tm³⁺ co-doped tellurite fibers for broadband optical fiber amplifier around 1550 nm band. *Optical Fiber Technology*, 2006. **12**(2): p. 185-195. <https://doi.org/10.1016/j.yofte.2005.07.007>
6. Guesmia, N., et al., Glass formation, physical and structural investigation studies of the (90-x) Sb₂O₃-10WO₃-xNaPO₃ glasses. *Materials Today Communications*, 2022. **30**: p. 103226. <https://doi.org/10.1016/j.mtcomm.2022.103226>
7. Ersundu, A., et al., Characterization of new Sb₂O₃-based multicomponent heavy metal oxide glasses. *Journal of alloys and compounds*, 2014. **615**: p. 712-718. <http://dx.doi.org/10.1016/j.jallcom.2014.07.024>
8. Veron, O., Etude des mécanismes de coloration de verres obtenue par échange ionique Ag⁺/Na⁺ et précipitation de nano agrégats métalliques, 2010, Université d'Orléans.
9. Haase, R., Mischkristalle, in *Thermodynamik der Mischphasen* 1956, Springer. p. 547-560.
10. Ben Slimen, F., Caractérisation des verres luminescents préparés par la méthode sol-gel, 2016, Angers.
11. BENSAAIDA, S. and M. BOUZIANE, Lamellar precipitation of the influence of the plastic deformation In the Ni-1, 4 at.% In alloy. *Revue Science des Matériaux*, 2017(09): p. 29-35.
12. BAAZOUZI, M., Elaboration et caractérisation des verres d'oxydes à indice de réfraction complexe pour application dans l'optique non linéaire, 2014, Université Mohamed Khider Biskra.

13. GUEZZOUNE, H., Etude physico-chimique et spectroscopique de l'ion de cobalt dans les verres $\text{Sb}_2\text{O}_3\text{-Li}_2\text{O-WO}_3$, 2012, Université de Ouargla-Kasdi Merbah.
14. Zachariasen, W., The atomic arrangements in glass. *Journal of American Chemical Society*, 1932. **54**: p. 3841-2851. <https://doi.org/10.1021/ja01349a006>
15. Henderson, G.S., The structure of silicate melts: a glass perspective. *The Canadian Mineralogist*, 2005. **43**(6): p. 1921-1958.
16. Deshmukh, K., et al., Recent advances and future perspectives of sol-gel derived porous bioactive glasses: a review. *RSC advances*, 2020. **10**(56): p. 33782-33835. DOI: [10.1039/d0ra04287k](https://doi.org/10.1039/d0ra04287k)
17. Roy, E., Elaboration électrochimique et caractérisations de nanofils d'antimoine et d'or, 2002, Université de Marne la Vallée.
18. Nouadji, M., Effet des oxydes alcalino-terreux et les métaux de transitions sur les propriétés physiques des verres d'oxydes basés sur Sb_2O_3 , 2012, Université Mohamed Khider-Biskra.
19. Mihi, S., Etude et fabrication de nouveaux amplificateurs optiques opérant dans le proche infrarouge basé sur les verres Sb_2O_3 , 2019, Université Mohamed Kheider-Biskra.
20. Fan, G., et al., Synthesis of micro-sized Sb_2O_3 hierarchical structures by carbothermal reduction method. *Materials Letters*, 2011. **65**(8): p. 1141-1144. <https://doi.org/10.1016/j.matlet.2010.09.084>
21. Bouhdjer, A., Study of Thin Layers of Indium Oxide (In_2O_3) Elaborated by Chemical Means, 2016, Université Mohamed Khider-Biskra.
22. Ouannes, K., Etude structurale et spectroscopique des verres d'antimoine dopés par les terres rares trivalents Er^{3+} , 2015, Université Mohamed Khider Biskra.
23. Petkova, P., et al. Infrared spectroscopy of undoped and Cu-doped (80-x) $\text{Sb}_2\text{O}_3\text{-}20\text{Li}_2\text{O-xMoO}_3$ glasses. in *AIP Conference Proceedings*. 2016. AIP Publishing LLC. <https://doi.org/10.1063/1.4945972>
24. Petkova, P., et al., Urbach's Rule in Undoped and Co Doped (80-x) $\text{Sb}_2\text{O}_3\text{-}20\text{Na}_2\text{O-xWO}_i$ Glasses. *Acta Physica Polonica-Series A General Physics*, 2012. **121**(1): p. 152.
25. Panasenko, A., et al., Phase composition of antimony (III) oxide samples of different origin. *Inorganic Materials*, 2009. **45**(4): p. 402-408. <https://doi.org/10.1134/S002016850904013>
26. Poirier, G., Nouveaux verres à base d'oxyde de tungstène, 2003, Rennes 1.

27. Granqvist, C.G., Electrochromic tungsten oxide films: review of progress 1993–1998. *Solar Energy Materials and Solar Cells*, 2000. **60**(3): p. 201-262. [https://doi.org/10.1016/S0927-0248\(99\)00088-4](https://doi.org/10.1016/S0927-0248(99)00088-4)
28. Bondarenko, N., O. Eriksson, and N.V. Skorodumova, Polaron mobility in oxygen-deficient and lithium-doped tungsten trioxide. *Physical Review B*, 2015. **92**(16): p. 165119. <https://doi.org/10.1103/PhysRevB.92.165119>
29. Waller, M.R., et al., Single-crystal tungsten oxide nanosheets: photochemical water oxidation in the quantum confinement regime. *Chemistry of Materials*, 2012. **24**(4): p. 698-704. <https://doi.org/10.1021/cm203293j>
30. Pinter, Z., Caractérisation de couches épaisses de semi-conducteur WO₃ et WO₃/TiO₂ pour la réalisation de capteurs à NO₂, 2002, Lyon, INSA.
31. Ma, S., Reactions of alcohols and organophosphonates on tungsten trioxide epitaxial films 2003: The University of Maine.
32. Reeswinkel, T., Self-lubricious tool coatings for ecological metal cutting, 2012, Fachgruppe für Metallurgie und Werkstofftechnik.
33. BELATEL, H., L'Université Louis Pasteur de Strasbourg. 2005.
34. Koutiri, I., Étude Ab Initio du trioxyde de Tungstène WO₃ en Volume et en Surface, 2012, Université de Bourgogne.
35. Manzani, D., Vidros óxidos contendo átomos pesados para aplicações em óptica não linear e fotônica na região do infravermelho. 2011.
36. MAKHLOUFI, R., Synthèse et caractérisation de nouveaux verres à base d'oxysulfure d'antimoine, 2017, UNIVERSITE DE MOHAMED KHIDER BISKRA.
37. Al Sabea, H., Optical and redox switching of lanthanide (III) luminescence and synthesis of new organometallic molecular wires, 2020, Rennes 1.
38. Jackson, S.D., Towards high-power mid-infrared emission from a fibre laser. *Nature photonics*, 2012. **6**(7): p. 423-431. <https://doi.org/10.1038/nphoton.2012.149>
39. Venkatramu, V., et al., Optical spectroscopy of Sm³⁺ ions in phosphate and fluorophosphate glasses. *Optical Materials*, 2007. **29**(11): p. 1429-1439. <https://doi.org/10.1016/j.optmat.2006.06.011>
40. Qin, C., et al., Luminescence spectroscopy and crystallographic sites of Sm²⁺ doped in Sr₅BP₅O₂₀. *Materials chemistry and physics*, 2010. **121**(1-2): p. 286-290. <https://doi.org/10.1016/j.matchemphys.2010.01.037>

41. Deopa, N. and A. Rao, Spectroscopic studies of Sm³⁺ ions activated lithium lead alumino borate glasses for visible luminescent device applications. *Optical Materials*, 2017. **72**: p. 31-39. <http://dx.doi.org/10.1016/j.optmat.2017.04.067>
42. Huang, Y., et al., Luminescence and microstructure of Sm²⁺ ions reduced by x-ray irradiation in Li₂O–SrO–B₂O₃ glass. *Journal of Applied Physics*, 2008. **103**(11): p. 113519. <https://doi.org/10.1063/1.2942404>
43. Abdel-Baki, M. and F. El-Diasty, Glasses for photonic technologies. *Int. J. Opt. Appl*, 2013. **3**(6): p. 125-137.
44. Bouchouicha, H., Élaboration, caractérisation structurale et étude des propriétés de luminescence des verres et des vitrocéramiques alumino-silicatés de calcium dopés à l'euporium, 2016, Université de Lyon; Faculté des sciences de Bizerte (Tunisie).

Chapter II
Experimental
technique of
characterization of
glasses

II.1 Introduction

This chapter outlines the many characterization procedures used on glasses in our investigation:

- ⊕ Differential scanning calorimetry (DSC) is used to identify the typical temperatures of glasses.
- ⊕ Physical properties.
- ⊕ Mechanical and elastic properties.
- ⊕ Optical properties: calculates several optical parameters using absorption in the UV-Vis and NIR spectrometers and studies luminescence with the spectrofluorometer.
- ⊕ Infrared spectroscopy (IR) and FTIR as well as Raman spectroscopy provide information on the local internal structure of the material, in particular impurities.

II.2 Characterization techniques

We will examine the thermal, mechanical, optical, and structural characteristics of our manufactured glasses through experimental instruments matched to each feature after creating the ternary $\text{Sb}_2\text{O}_3\text{-WO}_3\text{-NaPO}_3$ glasses (see Figure II. 1).

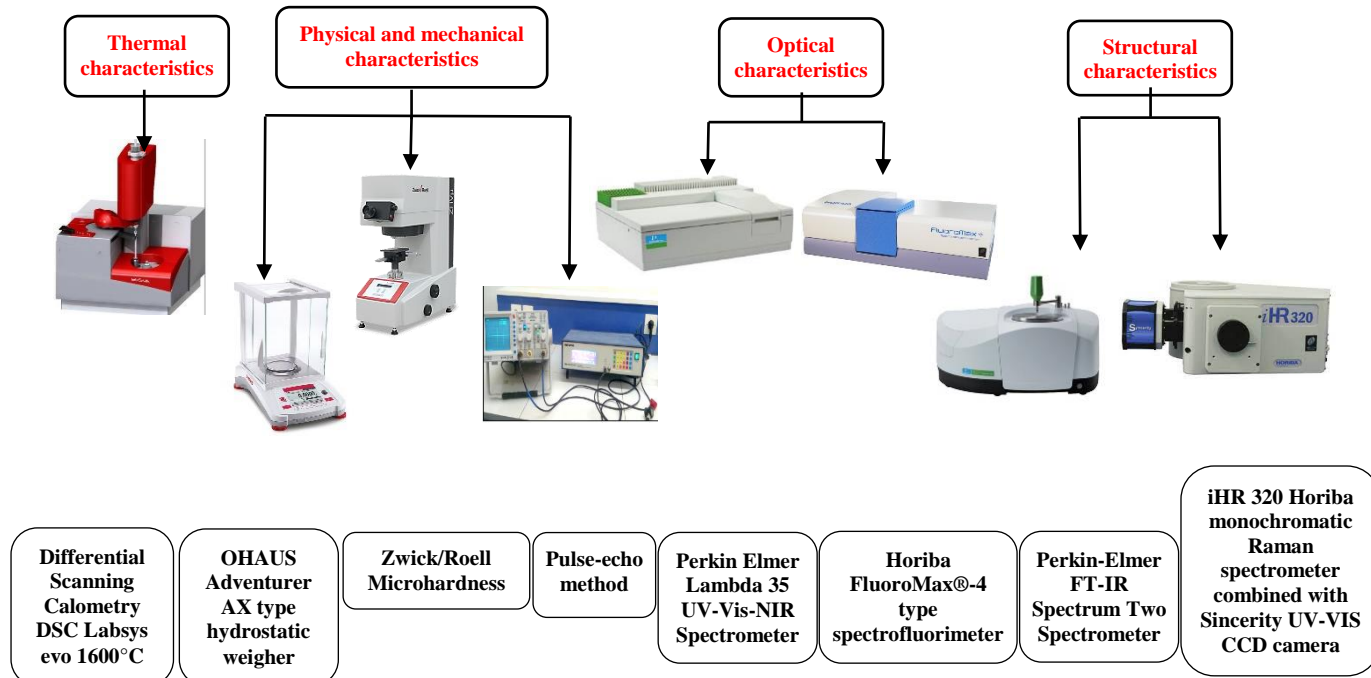


Figure II.1: Difference characterization techniques used in our work.

II.3 Thermal characteristics

To perform the thermal analysis of a material, there are two experimental techniques: differential thermal analysis (DTA) and differential scanning calorimetry (DSC) [1, 2]. The typical temperature of our glasses was determined by employing Differential Scanning Calorimetry (DSC). Figure II. 2 shows the Labsys evo Tg/ DSC 1600 °C device.



Figure II.2: Differential Scanning Calorimeter (DSC) device labsys evo 1600°C.

Differential Scanning Calorimeters come in two types (DSC). The heat flux DSC is the 1st kind (on the left in [figure II.3](#)), where sample and reference are in the same chamber powered by the same heat source. The 2nd type of DSC (on the right in [figure II.3](#)) is the power-compensated DSC, for which sample and reference are in separate chambers equipped with an autonomous heating system.

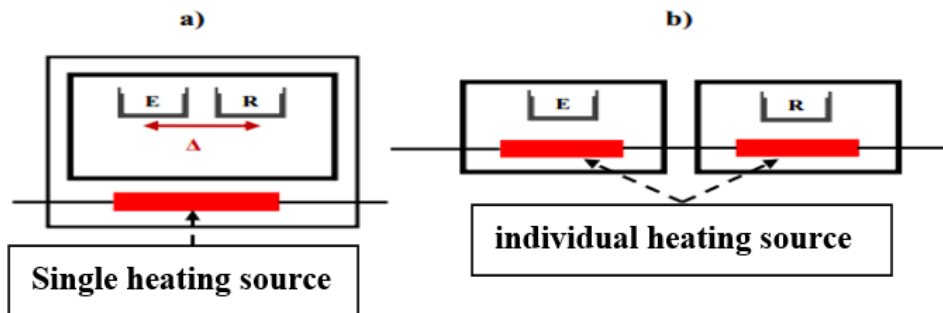


Figure II.3: Schematic diagram of the DSC [2].

a) Heat flux and b) Power compensation.

In this case, the temperature of the sample is maintained equal to that of the reference by varying the power of the ovens. The experimental principle is as follows: the vitreous samples are placed in a sealed capsule, introduced into the DSC cell and heated with a regular temperature rise rate. The heat flux released or absorbed by the sample is then recorded. Changes in heat capacity or enthalpy of the sample (E) cause a relative temperature difference between the reference and the sample to be recorded. It is possible to trace enthalpy variations through calibration experiments. Finally, it gave DSC curves (see [fig II.4](#)). The DSC curve of a glass makes it possible to determine the characteristic temperatures of the material (T_g , T_x (or T_c), T_p and T_f) [3, 4].

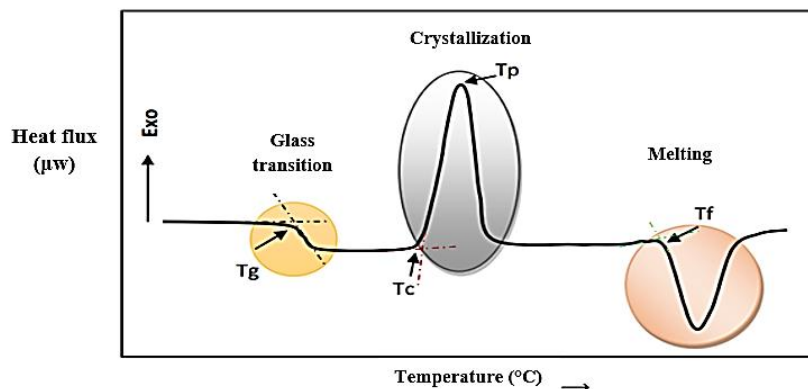


Figure II.4: Spectra of DSC [2].

The SC curve gives information about the studied material. For example, in the glass, it is distinguished from the rest of materials by the presence of the glassy transition phase.

The characteristic temperatures are therefore used to define stability criteria:

$$\text{- Thermal stability [4]:} \quad \Delta T = T_x - T_g \quad (\text{II.1})$$

$$\text{- Factor of Saad and Poulain [5] defined us :} \quad S = \frac{[(T_p - T_x)(T_x - T_g)]}{T_g} \quad (\text{II.2})$$

$$\text{- Factor of Hruby [6] defined us :} \quad H_f = \frac{(T_x - T_g)}{(T_f - T_x)} \quad (\text{II.3})$$

T_g : Glass transition temperature.

T_x : Crystallization start temperature (or T_c).

T_p : Maximum crystallization peak temperature.

T_f : melting temperature.

II.3.1 Experimentation equipment

The vitreous samples were ground into a powder, then weighed and introduced into an aluminum crucible (75 μ l). The analyses are carried out with an Ar gas sweeping to avoid any reaction of the material to be studied with the furnace's. The characteristic temperatures were measured by DSC (Labsys evo1600°C). With these characteristic temperatures, we can calculate the stability factor (ΔT), etc. The measurements were carried out between 20°C and 500°C with a temperature heating rate of 10°K/min. The measurement error is estimated to be within $\pm 2^\circ\text{C}$ for T_g and T_x and $\pm 1^\circ\text{C}$ for T_p (see [fig II.5](#)).

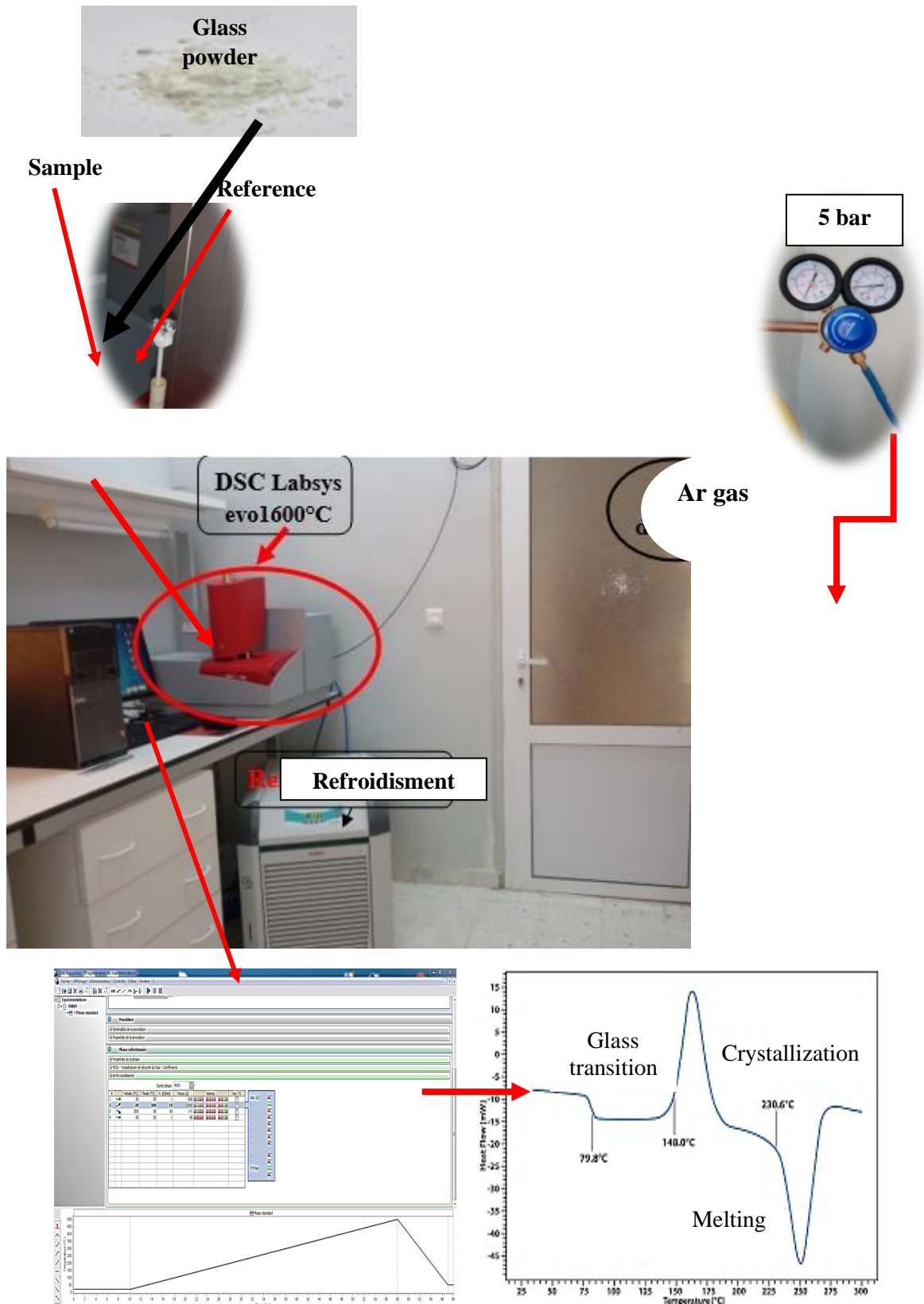


Figure II.5: DSC devise operation principal used in our work.

II.4 Physical and mechanical properties

II.4.1 Density

The density of glass is an essential physical property that may be used to compute a variety of material qualities. The Archimedes technique was used to determine densities in a solvent (water), in this case, distilled water. The measurement principle is relatively simple: the sample is weighed in air and then in the solvent (water). Its density is then determined by the following relationship [7]:

$$\rho = \frac{m_{air}}{m_{air} - m_{water}} \times \rho_{water} \quad (\text{II.4})$$

With: m_{air} = mass of the sample in air (g).

m_{water} = mass of the sample in water (g).

ρ_{water} = the density of water at T°C (known between 25-30°C equals (1 g/cm³)).

II.4.1.1 Experimental equipment

The density measurements were carried out according to the Archimedes method (OHAUS adventurer AX type). Each density resulted from an average calculated over 5 consecutive measurements carried out on the same sample, with an error equal to ± 0.0005 g/cm³. The density assessment process is depicted in figure II.6.

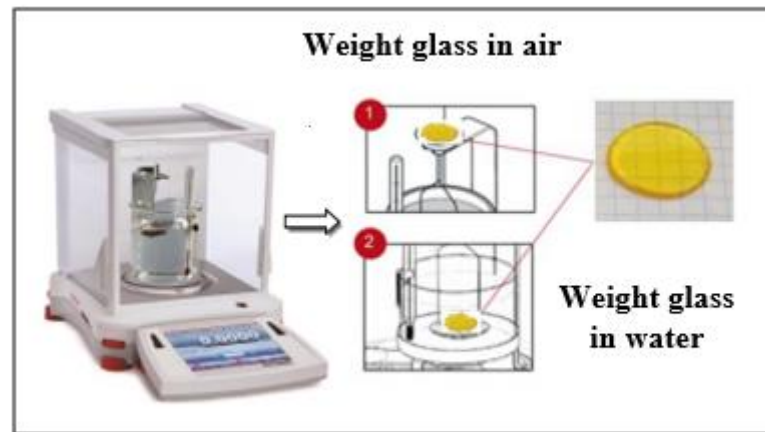


Figure II.6: Scale equipped with a hydrostatic weighing device (OHAUS Adventurer AX type) [7].

II.4.2 Elastic properties

There is a non-destructive and simpler method based on the measurement of the longitudinal V_L and transverse V_T propagation velocities of an ultrasonic wave in the material studied. Ultrasonic waves are mechanical vibrations with a frequency between 10 KHz and a few hundred Mhz. In our measurements, the transducers used have a frequency of 10 MHz.

Any material can be schematized by a network of elementary masses (atoms) connected to each other by springs (interatomic forces). If the bonds are rigid, the movement of the wave will be transmitted instantaneously, and all the atoms will move in phase. The presence of elastic bonds leads to a time lag which increases with distance and reveals a wave propagation speed directly related to the rigidity of the interatomic bonds.

The measurements of the elastic moduli were carried out by reflection using piezoelectric transducers (transmitters and receivers). This method is called Pulse-Echo. Through a gel, the transducer submits a mechanical excitation pulse to the material. The response of the latter is visualized on an oscilloscope by a series of echoes of decreasing amplitude corresponding to the successive reflections of the sound wave on the face of the sample opposite to that in contact with the transducer.

There are two types of waves which can propagate with different speeds in an infinite and isotropic homogeneous (figure II.7):

- ⊕ Longitudinal waves (traction-compression waves) correspond to a displacement of the particles parallel to the direction of propagation of the wave (figure II.7a).
- ⊕ Transversal waves (shear waves) correspond to a displacement of particles perpendicular to the propagation of the wave (figure II.7b).

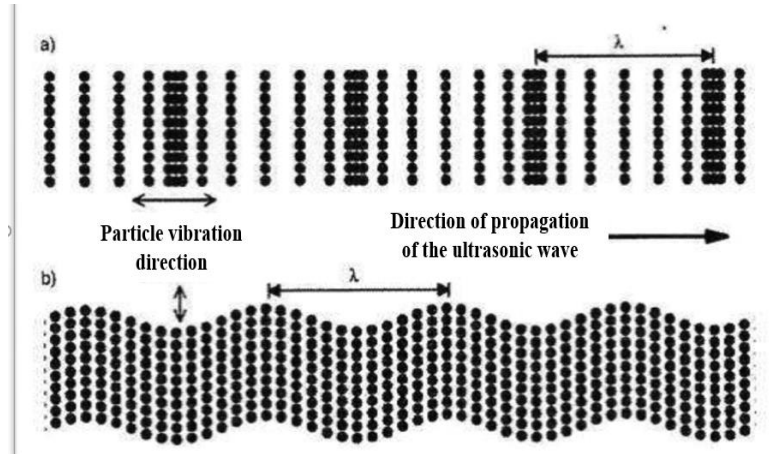


Figure II.7: The different types of propagation wave in a homogeneous and infinite medium [8].

We can calculate the propagation speed of the wave using the following relationship:

$$V = \frac{2 \cdot l}{\tau} \quad (\text{II.5})$$

V: propagation speed of the wave.

l: the thickness of the sample.

τ: The time taken by the wave.

The measurement of the elastic moduli E , G , K , L and ν is deduced from the longitudinal V_L and transverse V_T velocities of propagation according to the following expressions [8, 9]:

- Young's modulus

$$E = \rho V_T^2 \frac{3V_L^2 - 4V_T^2}{V_L^2 - V_T^2} \quad (\text{II.6})$$

- Shear modulus

$$G = \rho \cdot V_T^2 \quad (\text{II.7})$$

- Longitudinal module

$$L = \rho \cdot V_L^2 \quad (\text{II.8})$$

- Volume modulus

$$K = \frac{\rho}{3} (3V_L^2 - 4V_T^2) \quad (\text{II.9})$$

- Poisson coefficient

$$\nu = \frac{V_L^2 - 2V_T^2}{2(V_L^2 - V_T^2)} \quad (\text{II.10})$$

With: the elastic moduli E , G , L and K in [GPa]

V_L : longitudinal propagation velocity [m/s].

V_T : transverse propagation velocity [m/s].

ρ : density [g/cm³].

II.4.2.1 Experimental apparatus

The device used is ultrasonic echography to measure the elastic moduli. It is a non-destructive method, based on the determination of the speeds V_L and V_T of an ultrasonic wave propagating through of the material. Ultrasonic measurements were performed using a high-power ultrasonic pulse receiver (Olympus NDT, 5900 PR) using X-cut and Y-cut quartz transducers each with a frequency of 10 MHz and a digital storage oscilloscope (figure II.8). On the oscilloscope screen, we see a signal consisting of a series of echoes with diminishing amplitudes, which correspond to consecutive reflections of the sound wave on the face of the sample opposite the transducer. The measurement of the delay τ (time taken by the wave to go back and forth between two successive echoes) makes it possible to calculate the propagation

speed of the wave from relation (II.5) and deduce the elastic moduli E, G, K, L in [GPa] and ν .



Figure II.8: Pulse-Echo device equipment: Immersion transducer with an Olympus Model 5800RP generator, coupled to a 20GHz oscilloscope (HAMEG type).

II.4.3 Micro-hardness

The hardness of a material when exposed to a localized plastic deformation (for example, a tiny indentation or scratch) is used to determine the behavior of a material when subjected to a force (brittle or ductile behavior). Among the many methods proposed, we have opted to determine the hardness of our glasses by diamond impression with the Vickers pyramid (micro-hardness).

The micro Vickers hardness (Hv) of a material is defined as the pressure exerted by a load (with a square-based pyramid-shaped diamond with an apex angle of 136°) on the surface of the material and is measured by the ratio of this load on the contact area formed between the indenter and the indented surface of the material [10-13].



Figure II.9: Zwisch/Roell (Indentec) micro-hardness tester.

II.4.3.1 Experimentation equipment

The measurements were taken using a direct-reading Zwich/Roell (Indentec) micro-hardness tester (figure II.9). A very small load of 50 g is applied for a time of 10 seconds. For the same sample, the hardness values always show some dispersion. This device allows the study of a localized area of the surface. To access the Vickers hardness, the length d of the diagonal of the square base of the indentation must be measured. Each length d is the result of an average calculated from 5 consecutive measurements taken on the same sample. The measurement uncertainty ΔH_V is equal to 1%. In practice, the average value of the lengths d_1 and d_2 of the two diagonals (see figure II.10) is measured and allows the device to directly calculate the hardness according to the equation (II.11) [12, 13].

$$H_V = \frac{F}{9,81 S} = \frac{2F \sin\left(\frac{\theta}{2}\right)}{9,81 d^2} = \frac{0,1891F}{d^2} \quad (\text{II.11})$$

With: F : Applied load (N).

S : surface of the indentation (mm^2).

d : Average value of the diagonal $((d_1+d_2)/2)$.

θ : Angle at the top of the indenter ($\theta = 136^\circ$).

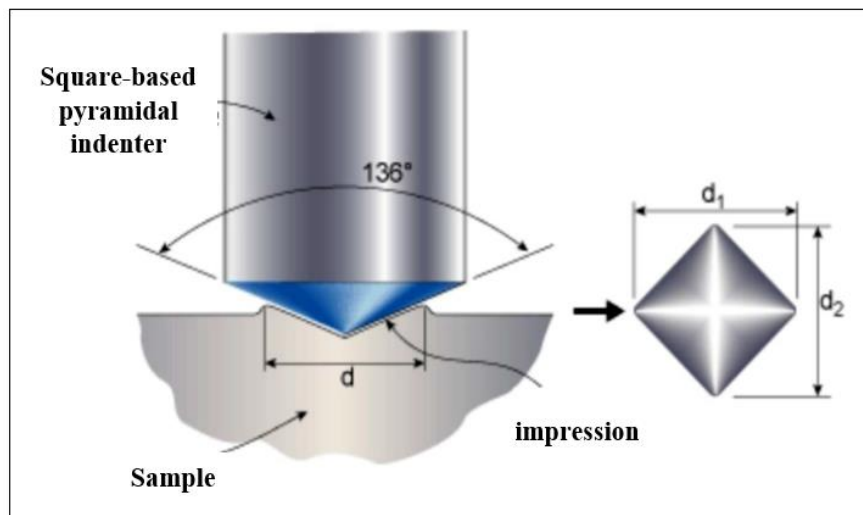


Figure II.10: The Vickers test principle [13].

II.5 Optical and structural characteristics

II.5.1 UV-Vis and IR spectroscopy

We can say that the most fundamental property of glass is its field of transparency, which depends on the chemical composition and the elements present in the glass, and

through which we will determine the field of application of this glass. The transmission window or transparency of a glass is delimited by two boundaries in the electromagnetic spectrum.

- ✚ **The band gap boundary (at short wavelengths (UV-Vis)):** corresponds to the absorption of light by electronic transitions from the BV to the BC of the material.
- ✚ **The multi-phonon boundary (at long wavelengths (IR)):** is due to the vibrations of chemical bonds and their harmonics.

These two types of absorption are said to be intrinsic to the material, they depend directly on the chemical elements that make it up. Figure II.11 presents the schematic transmission spectra of the three main families of glass, namely oxide glasses, such as silica, halides, mainly consisting of fluoride glasses, and chalcogenide glasses [7, 8].

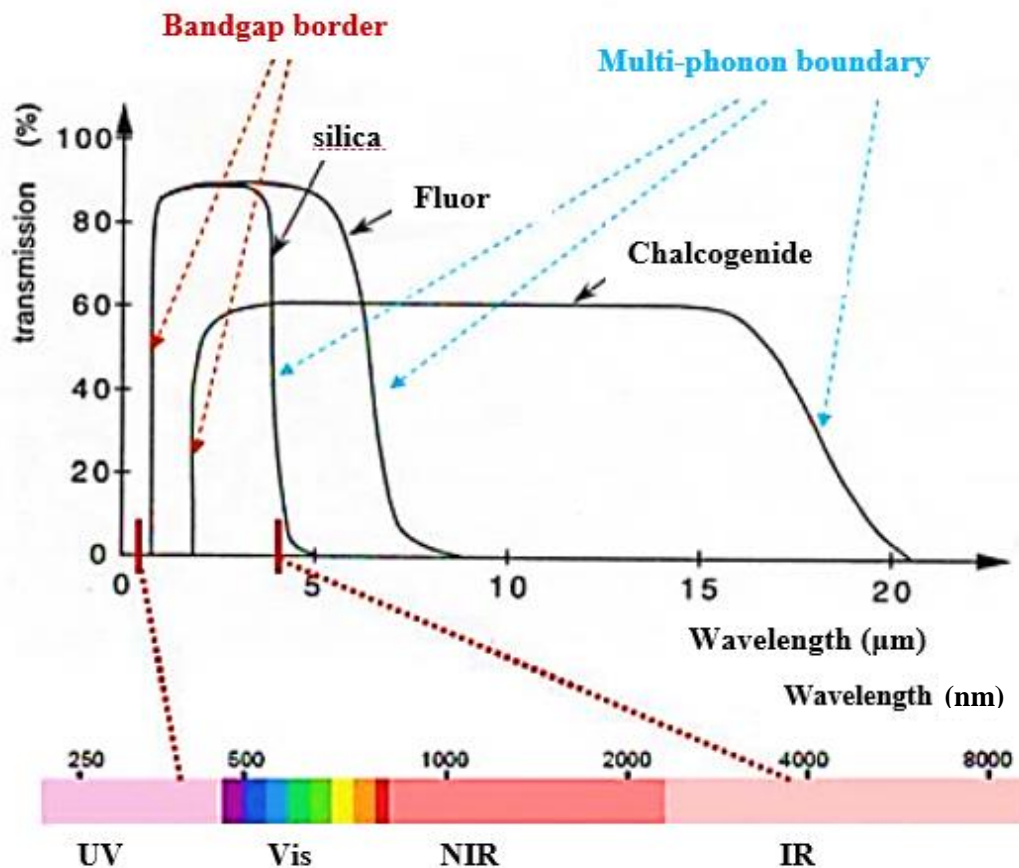


Figure II.11: Transparency domains of the three main families of oxide, halide, and chalcogenide glasses [7, 8].

II.5.2 Optical characteristics

Optical methods make it possible to characterize a large number of parameters. Optical absorption is based on the interaction of electromagnetic radiation with matter in the UV-visible and near-infrared spectral range. The absorbance of molecules depends on electronic transitions [8, 14, 15]. This transition corresponds to the passage of electrons from one electronic level to another electronic level of higher energy under the effect of radiation. However, the absorbance of matter in the UV and visible domains is intensively exploited in quantitative analysis by the application of the B er-Lambert law. Figure II.12 illustrates the typical operating principle of a transmission spectrophotometer.

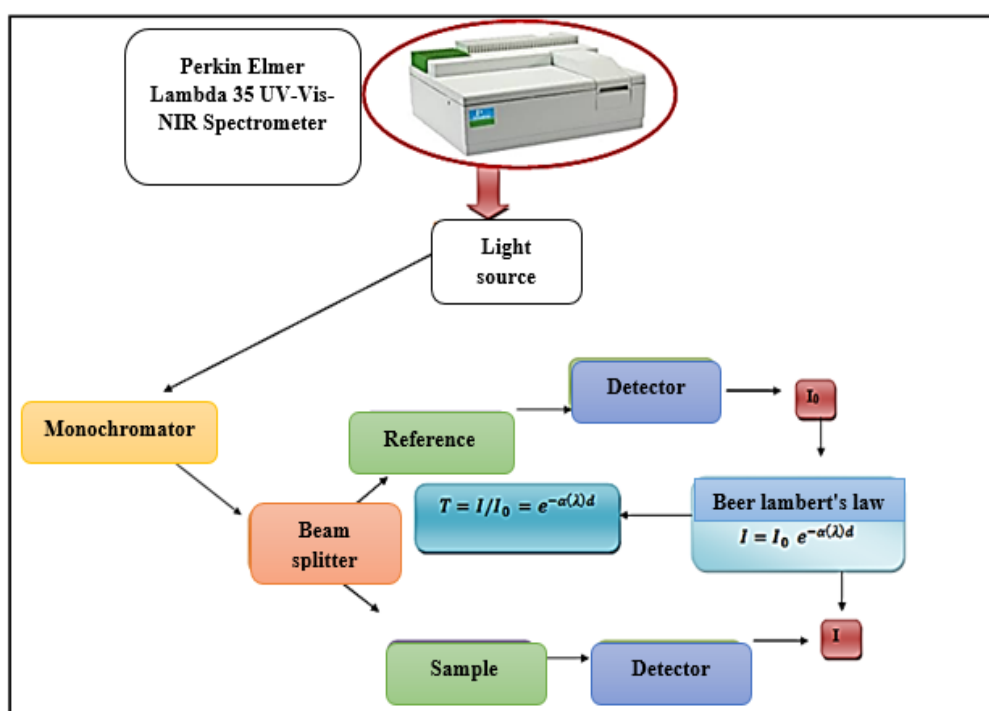


Figure II.12: Typical UV-Visible spectrophotometer operating.

First, polychromatic light from a light source (UV-Vis-NIR) passes through a monochromator. The monochromatic beam is then split into two arms. The first corresponds to the reference line and ends with a detector which makes it possible to automatically correct the measurement signal by the intensity fluctuations of the light source I_0 . The second arm crosses the glass sample to be characterized and ends with a detector I . therefore, it measures the intensity of the light (I) passing through a sample and compares it to the intensity of the light before this passage (I_0).

The ratio I / I_0 is called transmittance, and is usually expressed as a percentage (T%). From the transmission spectrum T, the optical density (OD) can be calculated by the following equation [16]:

$$DO= A = - \log \frac{I}{I_0} \quad (\text{II.12})$$

Where A is the absorbance or optical density, which has a wavelength. From the absorbance spectrum, we can determine: the absorption coefficient, the optical band, the refractive index, etc.

II.5.2.1 Experimentation equipment

Transmittance is measured using a Perkin Elmer Lambda 35 UV-Vis-NIR spectrometer. The sample is in the form of polished glass and a few millimeters thick. This device, controlled by a computer using Winlab UV software, makes it possible to study absorption over a wide spectral range extending from 200 nm (ultraviolet) to 1100 nm (near infrared) (figure II.13).

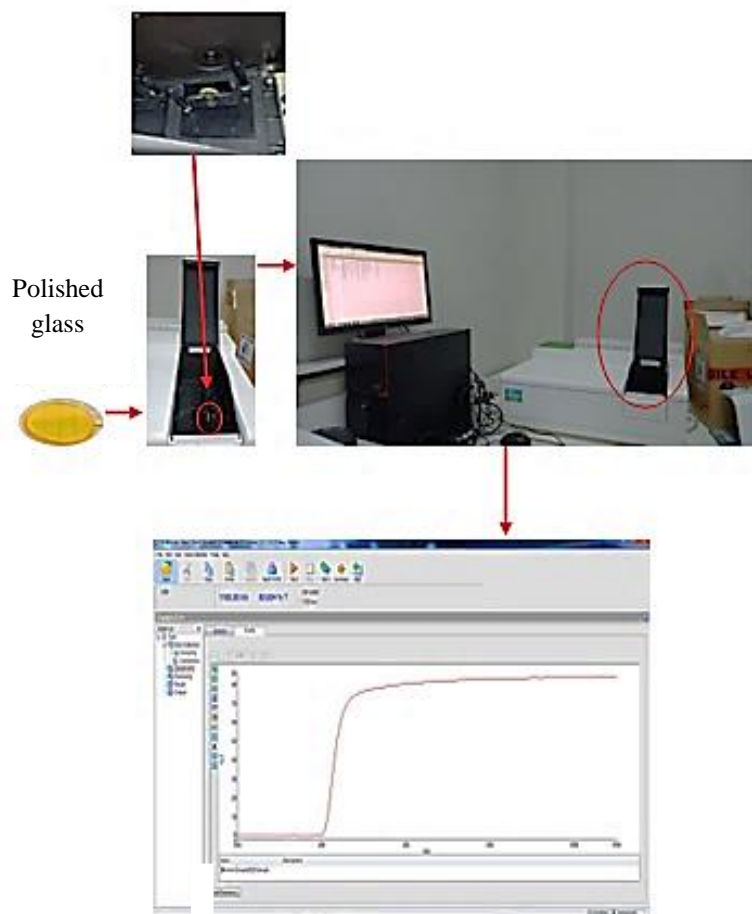


Figure II.13: Typical operating principle of a transmittance spectrophotometer in the UV-Vis and NIR range.

II.5.2.2 Determination of the forbidden band width (E_g) and the Urbach energy (E_u)

From the transmittance spectra, we deduced two important parameters: the optical band gap E_g and the parameter E_u (Urbach energy), which gives an evaluation of the width of the band tails of the states located in the gap.

✚ Determination of the forbidden band width

Firstly, we must to determine the absorption coefficient (α), we used the Beer-Lambert relationship (relation II.14). If we express the transmittance, T , as (%)

$$T = \exp(-\alpha d) \quad (\text{II.13})$$

The optical absorption coefficient (α) is given by the following (approximate) formula:

$$\alpha = \frac{1}{d} \ln \frac{100}{T} \quad (\text{II.14})$$

This approximate relationship is established, neglecting the reflection at all the interfaces; air/glass. Knowing the thickness of the glass, d , one can calculate the absorption coefficient for each value of the transmittance that corresponds to an energy. By sweeping the entire energy domain on (see figure II.14) [16-18], we have plotted the typical variation of the absorption coefficient (α^2) as a function of the energy of the incident photons ($h\nu$).

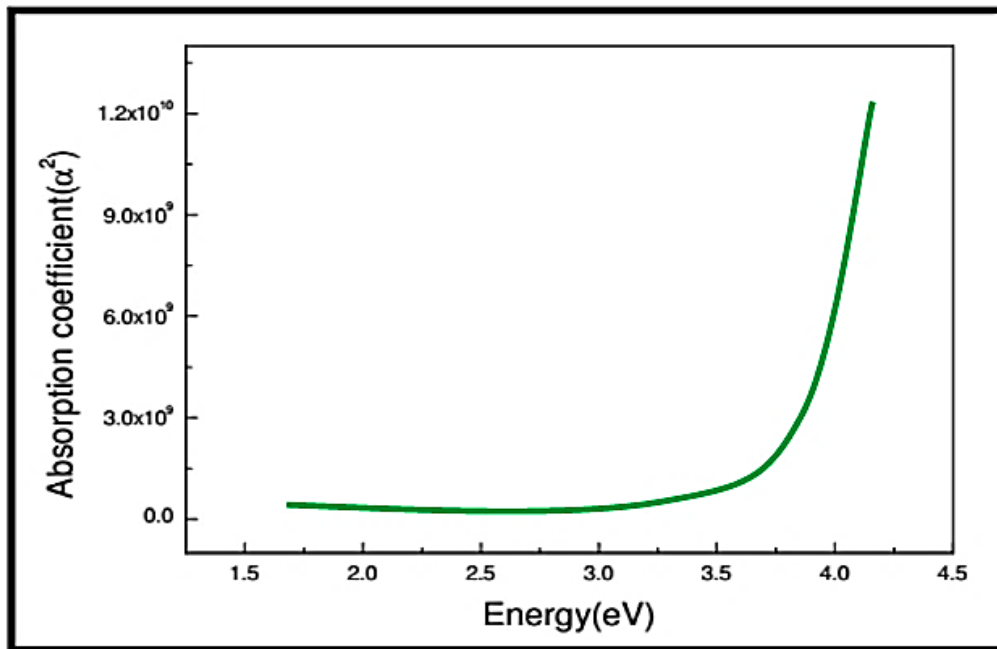


Figure II.14: Variation of the absorption coefficient (α^2) as a function of $h\nu$ [18].

In the high absorption range ($\alpha > 10^4 \text{ cm}^{-1}$), α is expressed as a function of the gap (E_g) according to the following equation [16-18][16-18]:

$$(\alpha h\nu)^n = A(h\nu - E_g) \quad (\text{II.15})$$

It is then possible to determine the nature of the gap:

- ✓ for $n = 1/2$ the transition will be indirect.
- ✓ for $n = 2$ the transition will be direct.

Where: A: constant, E_g : optical gap in eV, h: the energy of a photon.

$$E = h\nu = \frac{hc}{\lambda} = \frac{12400}{\lambda} \quad (\text{II.16})$$

Then we plot $(\alpha h\nu)^n$ as a function of the photon energy ($h\nu$). We extend the linear part of $(\alpha h\nu)^n$ to the abscissa axis, we obtain the value of E_g as shown in figure II.15.

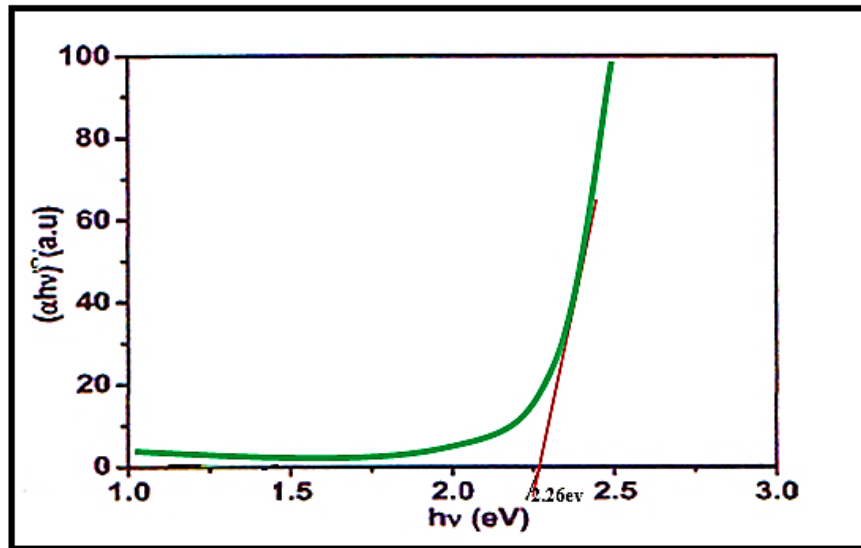


Figure II.15: Determination of the energy gap [18].

The optical gap for the different glasses is obtained by plotting $(\alpha h\nu)^{n=1/2}$: indirect transition as a function of $h\nu$ as shown in figure II.15. By extrapolation of the linear part of the curves, the value of the optical gap is obtained.

✚ Determination of the Urbach energy

The parameter that characterizes the disorder of the material is the Urbach tail energy (E_u). According to Urbach's law, the expression of the absorption coefficient is of the form [18, 19]:

$$\alpha = \alpha_0 \exp \frac{h\nu}{E_u} \quad (\text{II.17})$$

α : is constant.

E_u : Urbach energy (or simply E_{00}).

The energy values of Urbach E_u were calculated from the extrapolation of the linear portion of the curves $\ln(\alpha)$ with respect to $h\nu$. they were obtained from equation II.18 and represented in figure II.16. By plotting $(\ln \alpha)$ as a function of $(h\nu)$, we can determine the value of (E_u) by using the following formula.

$$\ln \alpha = \ln(\alpha_0) + \left(\frac{h\nu}{E_u}\right) \quad (\text{II.18})$$

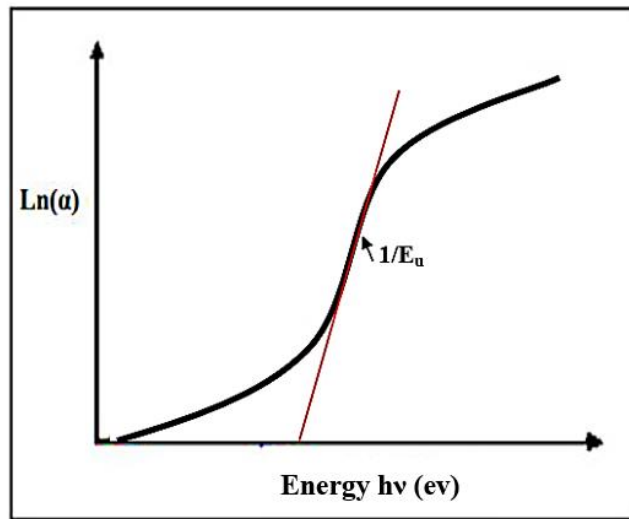


Figure II.16: Variation of $\ln(\alpha)$ as a function of $h\nu$ [18].

II.5.3 Infrared spectroscopy (FTIR)

Because it is a generally non-destructive and sensitive characterization approach, IR spectroscopy is one of the most extensively utilized ways to analyze a material's molecular bonds. Indeed, the position of the absorption bands is directly related to the bond strength constant between the atomic nuclei [20]. It will therefore be possible to return to the structural groups present in the vitreous matrix and to obtain precise information on the structural organization of the materials.

Infrared transmission is generally limited by multi-phonon cutoff, which is mainly due to fundamental vibrations of chemical bonds or harmonics of vibrations. The absorption wavelength λ of these energies is expressed by the following relationship [7, 21]:

$$\lambda = 2\pi c \sqrt{\frac{\mu}{\kappa}} \quad (\text{II.19})$$

With : c : The speed of light in vacuum.

μ : The reduced mass of vibrators or atomic groups concerned two atoms.

K : The strength constant of interatomic bonds.

$$\mu = \frac{m_1 m_2}{m_1 + m_2} \quad (\text{II.20})$$

So as with other types of energy absorption, molecules are excited to a higher energy state when they absorb infrared radiation. The absorption of infrared radiation is, like any other absorption process, a quantitative process. A molecule only absorbs a selected frequency of incident radiation. The position of the absorption bands in the infrared absorption spectrum of a sample therefore makes it possible to determine the chemical bonds present in the material. It is important to remember that a bond can vibrate in different ways. It is said to have different modes of vibration. One can distinguish the modes of elongation and the modes of deformation of the chemical bonds. Each of them also has a symmetrical vibration mode and an anti-symmetrical vibration mode (see figure II.17) [7, 21].

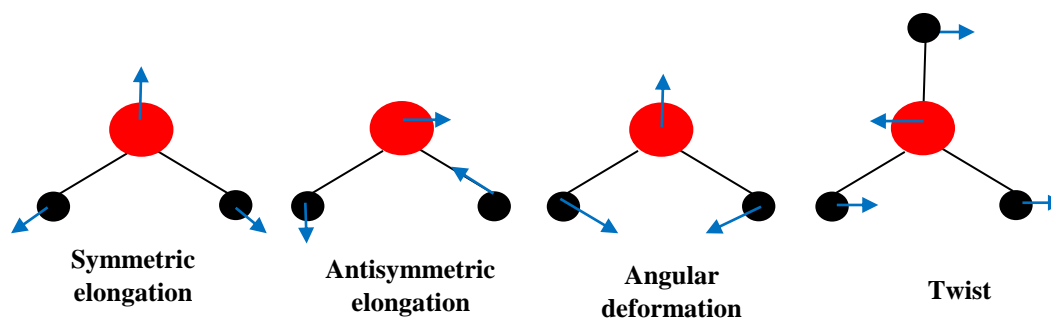


Figure II.17: Same vibrations mode [7].

In an infrared spectrometer, the infrared beam coming from the IR source is directed towards the interferometer. The generation of the latter occurs upon recombination of the beams from the fixed mirror, and the rest passes through the splitter and is directed onto the moving mirror, which moves at a fixed frequency. The beam then arrives at the detector to be transformed into an electrical signal. The detector appears as an interferogram, i.e., a signature of the intensity as a function of the position of the mirror, and it is possible to convert the interferogram by the Fourier transform [7, 22].

There are two main types of devices. Their differences lie mainly in the system of wavelength selectors:

- Dispersive spectrometers (by UATR techniques of the Perkin Elmer spectrophotometer).

- Fourier transform spectrometers (FT-IR) (non-dispersive): This device ((FT-IR) (non-dispersive)) is the interferometer for measuring all frequencies simultaneously. It includes a light source, the device, the sample compartment, the detector, and the analog-digital converter (fig II.18(a)).

While the UATR consists of an optical base on which the crystal plate is fixed, the latter is a solid diamond that is set in a stainless steel plate to ensure the best mechanical and chemical resistance. The glasses are placed on the stainless steel plate and start the analysis (fig II.18(b)). The detector measures the amount of energy for each frequency that passes through the sample. The diamond stage is fully recognized by the software, which identifies the number of reflections, the number series, and the nature of the crystal. As a function of wavenumber, this information is collected with each intensity spectrum. Finally, the stainless steel plate can be cleaned with a dry cloth or cloth soaked in distilled water or ethanol after analysis [23].

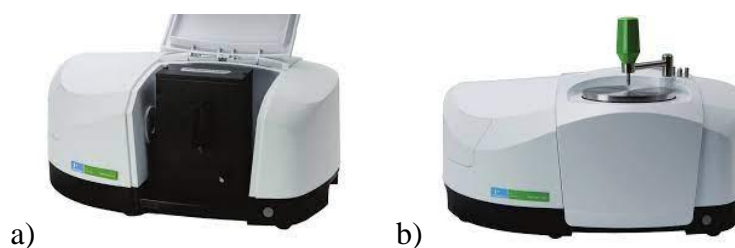


Figure II.18: a) FT-IR spectrometer Spectrum Two. b) Perkin Elmer spectrophotometer UATR techniques.

II.5.3.1 Experimental equipment

The transmission spectra of the glasses are recorded using a Perkin-Elmer FT-IR Spectrum Two spectrometer. This gadget, which is operated by a computer and runs on Winlab UV software, allows researchers to investigate absorption across a broad spectral range, ranging from 4000cm^{-1} to 400 cm^{-1} (for UATR technology) and $1,5\text{-}8\mu\text{m}$ (for FTIR technology) (see fig II.19).

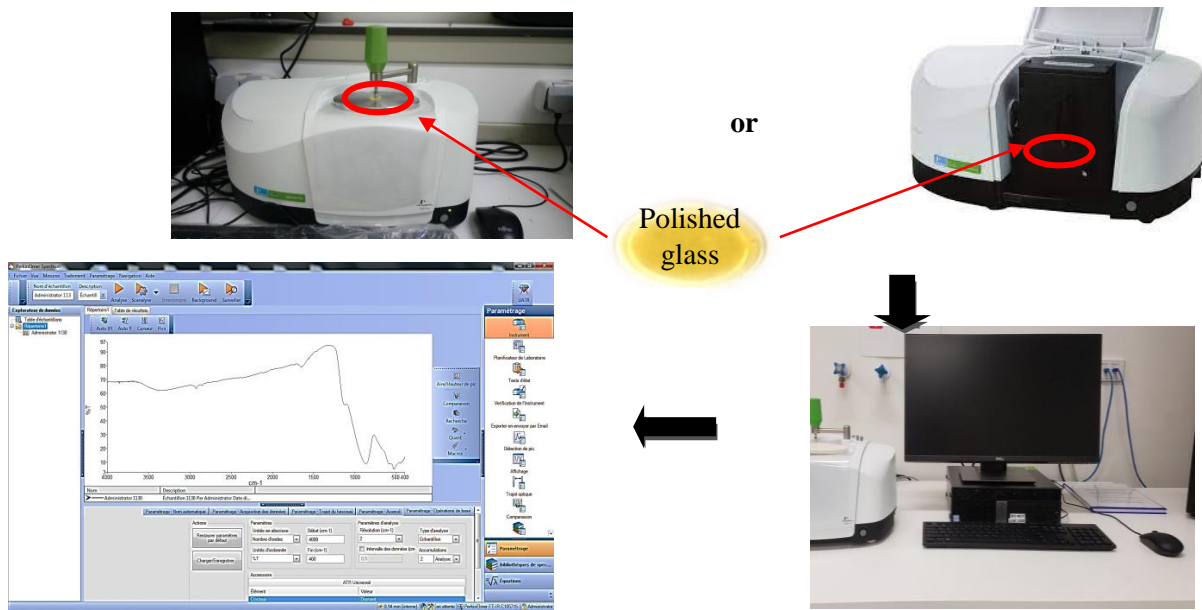


Figure II.19: Device operation principle Spectrometer: Perkin Elmer Spectrum Two.

II.6 Fluorescence spectroscopy

Fluorescence spectroscopy is a type of electromagnetic spectroscopy that analyzes the fluorescence of a sample. It involves the use of a ray of light which will excite the electrons of the molecules of certain compounds and cause them to emit light.

Luminescence constitutes “the emission of light, ultraviolet, visible, or infrared, by certain substances under the effect of various excitations”. These substances can be solids, liquids, or gases. The advantages of PL analysis lie in the simplicity of optical measurement and the power to provide information about the electronic properties of the material [7, 21].

Figure II.20 presents the principle of the photoluminescence phenomenon with three levels: 0, 1 and 2.

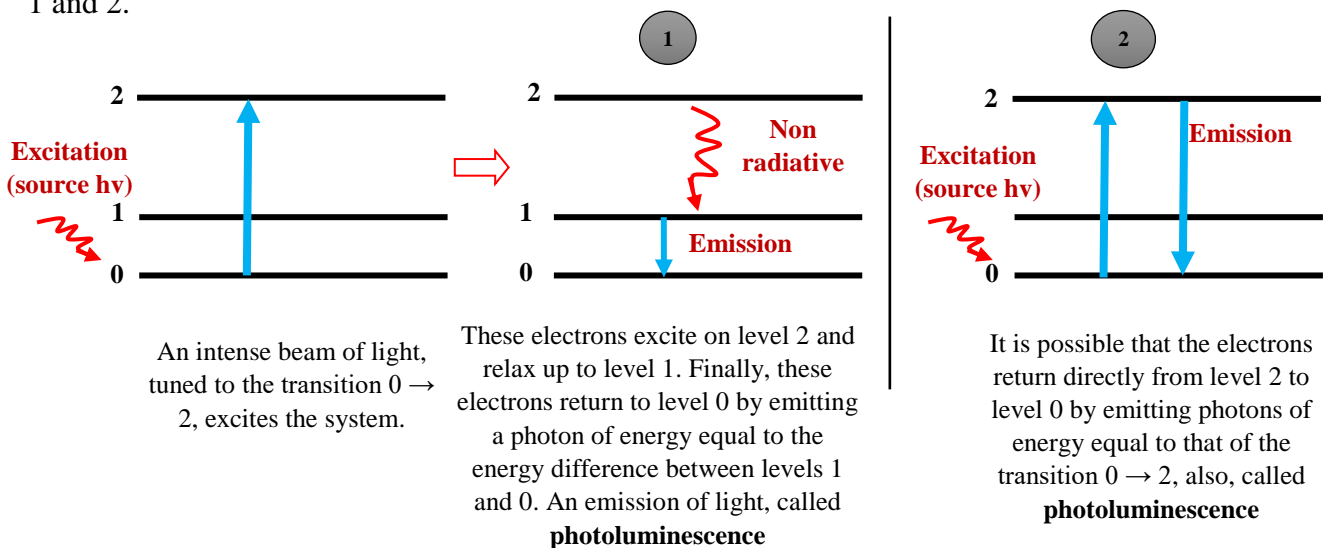


Figure II.20: Diagram of the principle of photoluminescence phenomenon [21, 24].

II.6.1 Experimental equipment

The emission, excitation and lifetime spectra were recorded on a Horiba FluoroMax®-4 type spectrofluorimeter (see [fig II.21](#)) controlled by means of the origin® program. The excitation source is a 450 W Xenon lamp (laser excitation source), which allows continuous excitations from 200 nm to 800 nm. The lamp is mounted vertically to increase stability and reduce lamp life. The source lamp focuses on the use of an elliptical mirror. The reflective surface effectively collects all wavelengths and focuses them onto the entrance slit of the excitation monochromator. Before the excitation light reaches the sample, a photodiode reference detector measures the intensity as a function of time and wavelength. It provides information on the electronic properties of the material, it explores the long-term average fluorescence of a glass subjected to UV and visible radiation. Emission spectra are recorded from the optical converter at wavelengths above 300-850 nm and excitation spectra between 200 nm and 750 nm.

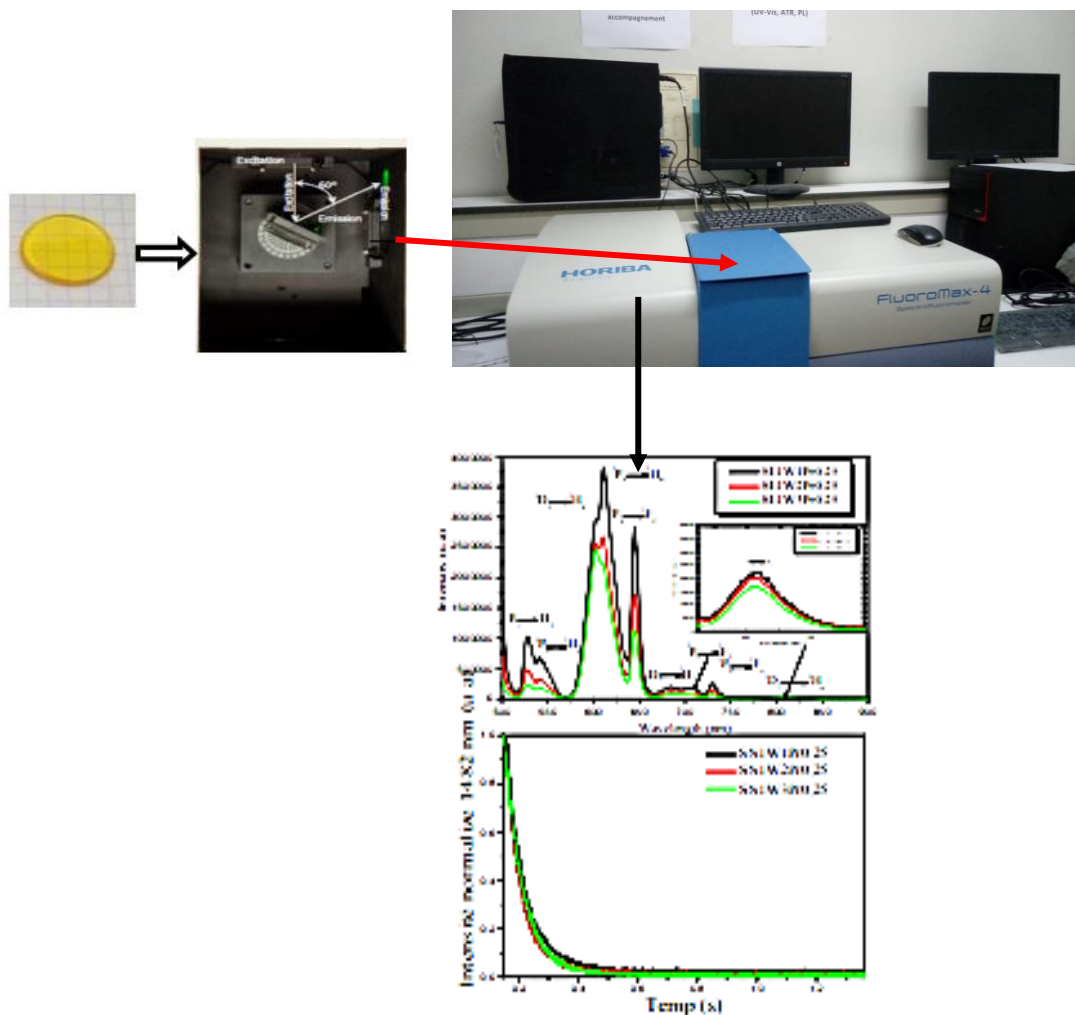


Figure II.21: Schematic of the spectrofluorimeter equipment used for recording excitation, emission, and lifetime spectra.

II.7 Raman spectroscopy

Raman spectroscopy [21] is a non-destructive technique for determining a material's molecular composition and structure, as well as chemical bonding. It's been designed specifically for studying vitreous materials. The light-matter interaction causes Raman scattering, which allows access to molecular and crystalline vibrations (phonons) [25, 26]. This technique is complementary to infrared spectroscopy, which also makes it possible to study the vibrational modes of a material.

The principle of the technique follows the interaction between a sample and a laser beam: The Raman spectrum is due to the elastic or inelastic scattering of a monochromatic beam of laser light of frequency ν_0 acting on a molecule. The frequency differences between incident and scattered radiation constitute the Raman spectrum. The diffusion mechanisms can be represented by the diagrams in [figure II.22](#).

- ✚ In Raman **Stokes scattering**: a photon with energy $h\nu_0$ interacts with a molecule in the fundamental vibrational state E_0 , leading in an intermediate state E_i (which is not necessarily an energy level of the molecule) and being scattered with energy $h(\nu_0 - \nu_v)$ where ν_v is the vibrational frequency corresponding to the transition $E_1 - E_2 = h\nu_v$.
- ✚ In **anti-Stokes Raman** scattering, in the case where the photon interacts with the molecule at the excited vibrational level E_2 , the scattered photon can, by falling from the intermediate level E_i to the fundamental level E_0 , have an energy $h(\nu_0 + \nu_v)$ larger than the incident photon, giving rise to anti-Stokes Raman scattering.
- ✚ In **Raman Rayleigh** scattering, if the incident photon undergoes a purely elastic collision, it will be scattered with the same frequency ν_0 , giving rise to the Rayleigh radiation.

Thus, a Raman spectrum unambiguously represents a signature containing both the chemical composition and the crystalline organization of the material. A Raman spectrum represents bands whose position is linked to the frequency of the mode of vibration considered and whose intensity is linked to the number of photons corresponding to this mode of vibration. The spectrum represents the intensity of the scattering (in a.u.) in relation to the wave number of the vibrations (in cm^{-1}). The Raman spectrum is essentially dominated at low

frequencies by the presence of the “boson peak”, resulting from the presence of acoustic vibrations [2, 21].

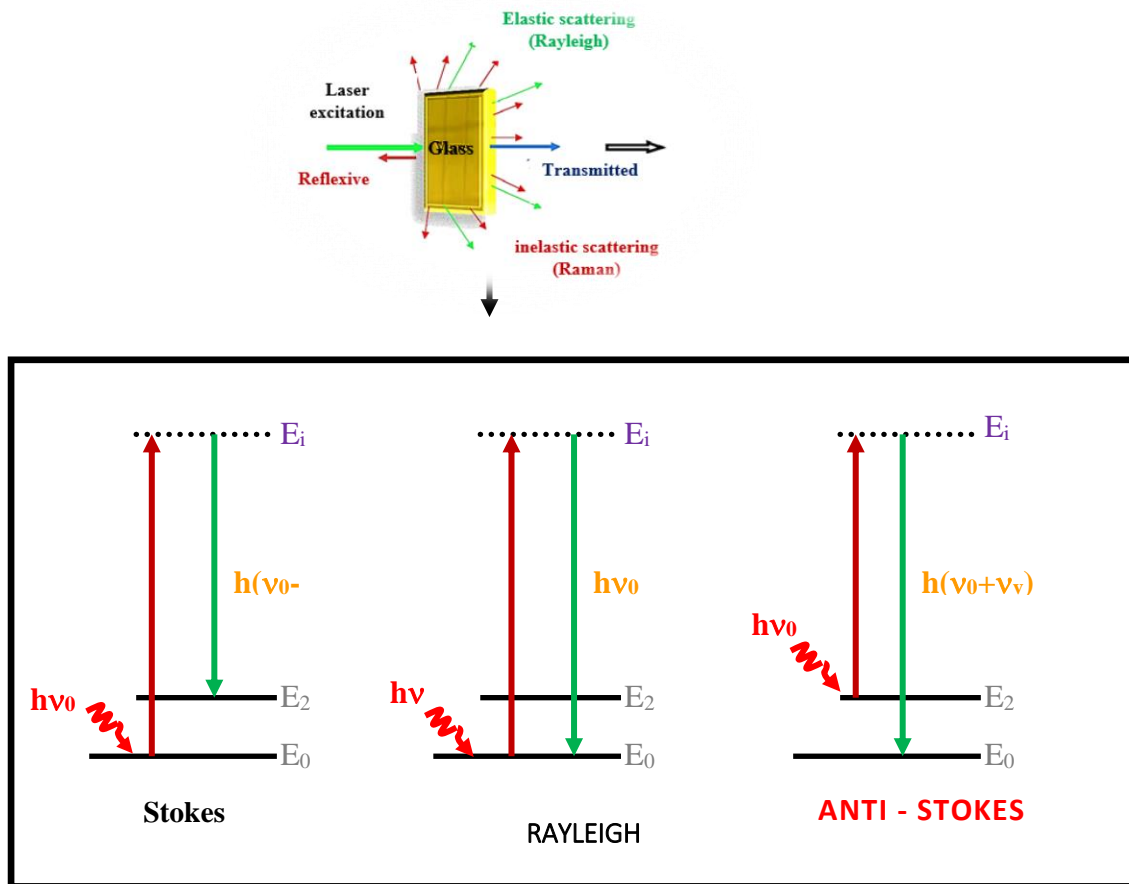


Figure II.22: Dispersion mechanisms of Stokes, Rayleigh and Anti-Stokes [21].

To produce the Raman spectrum, the Stokes lines are used. The Raman spectrum contains various information; each line or band can be characterized by:

- Its position in the spectrum can be linked to the frequency of a vibration mode.
- Its intensity is linked to the number of diffusing molecules as well as to the mode of vibration considered.
- Its state of polarization, which provides information on the symmetry of the corresponding mode.
- Its profile, which allows the study of movements or interactions in condensed phases or certain determinations of temperatures in the gas phase.

A schematic of potential Raman microscopy setup is shown in figure II.23. An objective lens for a microscope is used to focus laser light onto the sample surface and gather backscattered light. After passing through notch or edge filters, which filter out Raman-shifted

photons, they are then fed into a grating spectrometer where a charge-coupled device (CCD) camera detector may simultaneously detect wavenumbers in a chosen spectral range [27, 28].

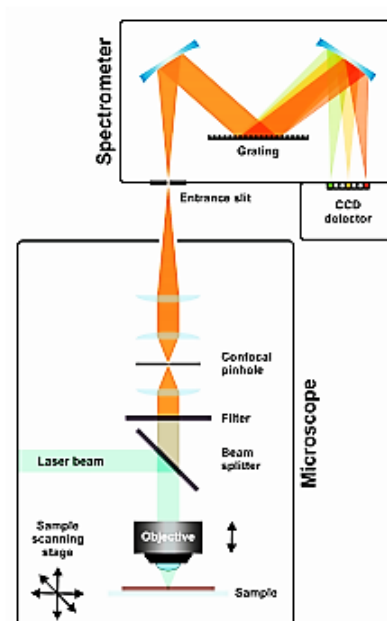


Figure II.23: Schematic of an upright Raman microscope [27].

II.7.1 Experimental equipment

Analysis of our samples was performed using an IHR 320 Horiba monochromator spectrometer with a UV-VIS CCD camera ($2048 \times 70,14 \mu\text{m}$) and a laser excitation source equal to 532 nm (laser beam) was used for excitation in the range of $10\text{-}1400 \text{ cm}^{-1}$ (see figure II.24). The experiments were carried out thanks to the collaboration with **M. Toufik. Soltani** and **D. de Ligny** from the institute of Glass and Ceramics, department of Materials Science and Engineering, University of Erlangen-Nuremberg, Germany.



Figure II.24: Microscope connected to an IHR 320 Horiba monochromator with a UV-VIS CCD camera.

References

1. Weiss, L., Contribution au développement d'un procédé de découpe laser haute-énergie/jet d'eau haute-pressure couplés. Application à la découpe d'alliages métalliques, 2013, Université de Lorraine (Metz).
2. MAKHLOUFI, R., Synthèse et caractérisation de nouveaux verres à base d'oxysulfure d'antimoine, 2017, UNIVERSITE DE MOHAMED KHIDER BISKRA.
3. Ghribi, N., Synthèse, caractérisations structurale et mécanique de nouveaux matériaux tellurites pour des applications en optique non linéaire, 2015, Université de Limoges.
4. Ersundu, M.Ç. and A. Ersundu, Structure and crystallization kinetics of lithium tellurite glasses. *Journal of non-crystalline solids*, 2016. **453**: p. 150-157. <https://doi.org/10.1016/j.jnoncrysol.2016.10.007>
5. Saad, M. and M. Poulain. Glass forming ability criterion. in *Materials Science Forum*. 1987. Trans Tech Publ. <https://doi.org/10.4028/www.scientific.net/MSF.19-20.11>
6. Hrubý, A., Evaluation of glass formation tendency by DTA. *Czechoslovak J. Phys*, 1972. **22**(11): p. 1187-1193. <https://doi.org/10.1007/BF01690134>
7. Mihi, S., Etude et fabrication de nouveaux amplificateurs optiques opérant dans le proche infrarouge basé sur les verres Sb_2O_3 , 2019, Université Mohamed Kheider-Biskra.
8. HAMZAOUI, M., Verres d'oxydes lourds a base de Sb_2O_3 , exploration, caractérisation physico-chimiques et application al'amplification optique, 2013, Université Mohamed Khider-Biskra.
9. Damodaran, K. and K. Rao, Elastic properties of alkali phosphomolybdate glasses. *Journal of the American Ceramic Society*, 1989. **72**(4): p. 533-539. <https://doi.org/10.1111/j.1151-2916.1989.tb06172.x>
10. Scholze, H., *Le verre*, Institut du Verre, Paris, English version:(1991) *Glass: Nature, Structure, and Properties*, 1974, Springer-Verlag, New York.
11. Tiegel, M., et al., Young' s modulus, Vickers hardness and indentation fracture toughness of alumino silicate glasses. *Ceramics International*, 2015. **41**(6): p. 7267-7275. DOI :[10.1016/j.ceramint.2015.01.144](https://doi.org/10.1016/j.ceramint.2015.01.144)
12. Taabouche, A., Etude structurale et optique de films minces ZnO élaborés par voie physique et/ou chimique, 2015, Université de Constantine 1.
13. Blétry, M., *Méthodes de caractérisation mécanique des matériaux*. École Nationale Supérieure des Mines de Paris, 2006.

14. Morton, M., Basic infrared spectroscopy. JH van der Maas, Heyden, London, 1972, pp. 109, price£ 1.25. Journal of Molecular Structure, 1972. **14**(3): p. 480-480. DOI: [10.1016/0022-2860\(72\)85213-X](https://doi.org/10.1016/0022-2860(72)85213-X)
15. Silver Stein, R., G. Basler, and T. Morill, Identification Spectrométrique de composés organiques, traduction de la cinquième édition américaine, 1991, University of Michigan, USA: De Boeck.
16. Mort, N. and E. Davis, Electronic processes in non-crystalline materials. Clarendon, Oxford, 1979.
17. Scholze, H., Nature and structure of glass, in Glass1991, Springer. p. 3-155.
18. Kouidri, N., Contribution à l'étude de couches minces d'oxydes transparents conducteurs à base de zinc et cobalt par spray pneumatique, 2019, University of Mohamed Khider, BISKRA.
19. Urbach, F., The long-wavelength edge of photographic sensitivity and of the electronic absorption of solids. Physical Review, 1953. **92**(5): p. 1324. DOI: <https://doi.org/10.1103/PhysRev.92.1324>
20. DES PHASES, E.D.L.S., Présentée pour l'obtention du diplôme de DOCTORAT EN SCIENCES ET GENIE DES MATERIAUX Option: Physico-chimie des Matériaux, 2010, Université de Mostaganem.
21. Poirier, G., Nouveaux verres à base d'oxyde de tungstène, 2003, Rennes 1.
22. Achour, Z.B., et al., Effect of doping level and spray time on zinc oxide thin films produced by spray pyrolysis for transparent electrodes applications. Sensors and Actuators A: Physical, 2007. **134**(2): p. 447-451. <https://doi.org/10.1016/j.sna.2006.05.001>
23. Agti, F.Z., ELABORATION ET ETUDES DES VERRES ANTIMOINO-PHOSPHATE POUR APPLICATION DANS L'AMPLIFICATION OPTIQUE, 2022, Université de mohamed kheider biskra.
24. Harhira, A., Photoluminescence polaron dans le niobate de lithium: approche expérimentale et modélisation, 2007, Université Paul Verlaine-Metz.
25. Hammoum, R., Etude par spectroscopie Raman de la structure des domaines périodiquement polarisés dans le niobate de lithium (PPLN), 2008, Université de Metz.
26. Maurel, C., Verres pour la Photostructuration, 2009, Université Sciences et Technologies-Bordeaux I.

27. Schmid, T. and P. Dariz, Raman microspectroscopic imaging of binder remnants in historical mortars reveals processing conditions. *Heritage*, 2019. **2**(2): p. 1662-1683. DOI:[10.3390/heritage2020102](https://doi.org/10.3390/heritage2020102)
28. Veber, A., et al., Combined Differential scanning calorimetry, Raman and Brillouin spectroscopies: A multiscale approach for materials investigation. *Analytica chimica acta*, 2018. **998**: p. 37-44. <https://doi.org/10.1016/j.aca.2017.09.045>

Chapter III

Physical properties of glasses on the ternary system

Sb_2O_3 - WO_3 - NaPO_3

III.1 Introduction

The objective of this work is to synthesize and characterize glasses based on antimony oxide (Sb_2O_3) with large vitreous domains and better characterization for photonic applications. For this reason, we have chosen the following new glass system: $\text{Sb}_2\text{O}_3\text{-NaPO}_3\text{-WO}_3$.

In the **first part**, we will present the description of the synthesis glass in the vitreous system $\text{Sb}_2\text{O}_3\text{-NaPO}_3\text{-WO}_3$.

The physical, thermal, mechanical and elastic properties of these glasses in the vitreous system $(90-x) \text{Sb}_2\text{O}_3\text{-}10\text{WO}_3\text{-}x\text{NaPO}_3$, x varies from 10 to 80 and $(80-x) \text{Sb}_2\text{O}_3\text{-}20\text{WO}_3\text{-}x\text{NaPO}_3$, x varies from 10 to 70, were studied in the **second part** of this chapter. Also, we compared the experimental and theoretical elastic modulus with Makishima and Mackenzie's theory. The physical properties of the studied glasses turn out to depend directly on their structure and composition.

III.2 Production of glass

The synthesis of vitreous samples depends on many important parameters that must be taken into consideration by: the type of glass we want to obtain; the choice of starting materials and their purity; and the appropriate crucible. Subject to conditions necessary for manufacture, etc.

III.2.1 Choosing a crucible

The choice of crucible was dependent on the chemical nature of the starting materials and the melting temperature of the reaction mixture. Soda-calcic crucibles (tubes) were used during the first stage of exploration of the vitreous state (determination of the vitreous zone) for each system studied. Then we used a silica-crucible for massif study glasses. Silica crucibles resist high temperatures well and are more expensive than soda-calcic.

III.2.2 Starting materials

These glasses were synthesized by the conventional melt-quenching-annealing method and were prepared by using the following starting materials:

Table III.1: starting materials of the Sb₂O₃-WO₃-NaPO₃ ternary system.

	Sb₂O₃	WO₃	H₂NaPO₄
Properties	Antimony oxide	Tungsten oxide	sodium hydrogenophosphate
Provider	Aldaich	Alfa Aesar	Aldaich
Purity (%)	~ 99	~ 99.998	P ₂ O ₅ > 60
Molecular weight (g/mol)	291,52	231,837	137,99

III.2.3 Synthesis

The synthesis of our glasses is carried out in the air, in a soda-calcic or silica tube. We are calculated the weight of the initial components by the following relationship:

$$\mathbf{m_x} = \mathbf{x_x} \times \frac{\mathbf{m_{glass}}}{\mathbf{M_{glass}}} \times \mathbf{M_x} \quad \text{(III.1)}$$

Where x_x : The stoichiometric coefficient, M_x : The mole mass of a raw material, m_{glass} : the mass of the glass, M_{glass} : The molecular weight of the glass and the molecular weight of the raw materials.

Example: for the ternary system 50 **Sb₂O₃**-10 **WO₃**-40 **NaPO₃**

With the molar weight: $M_{\text{Sb}_2\text{O}_3} = 291.52$ g/mol, $M_{\text{WO}_3} = 231.84$ g/mol and $M_{\text{H}_2\text{NaPO}_3} = 137.99$ g/mol.

-We can calculate the weight of each raw material (as Sb₂O₃) by using:

$$m_{\text{Sb}_2\text{O}_3} = x_{\text{Sb}_2\text{O}_3} \times \frac{m_{\text{glass}}}{M_{\text{glass}}} \times M_{\text{Sb}_2\text{O}_3} \quad (\text{III.2})$$

-The weight of glass: $m_{\text{glass}} = 5$ g

$$M_{\text{glass}} = (x_{\text{Sb}_2\text{O}_3} \times M_{\text{Sb}_2\text{O}_3}) + (x_{\text{WO}_3} \times M_{\text{WO}_3}) + (x_{\text{H}_2\text{NaPO}_3} \times M_{\text{H}_2\text{NaPO}_3})$$

$$M_{\text{glass}} = (0.5 \times 291.52) + (0.1 \times 231.84) + (0.4 \times 137.99)$$

$$M_{\text{glass}} = 224,14 \text{ g/mol}$$

$$m_{\text{Sb}_2\text{O}_3} = 0,5 \times \frac{5}{224,14} \times 291,52$$

$$m_{\text{Sb}_2\text{O}_3} = 3,2515 \text{ g}$$

So, by the same way we calculate m_{WO_3} and $m_{\text{H}_2\text{NaPO}_3}$: $m_{\text{WO}_3} = 0,5172$ g and $m_{\text{H}_2\text{NaPO}_3} = 1,2313$ g.

We mixed these powders in appropriate proportions to give about 5g and put them in soda-calcic or silica tubes. Then, the batch was melted at 900 °C to 1100 °C for 10 min to 20 min on a burner flame to obtain a homogeneous and clear liquid. The melted glass was cast in a brass mold that had been preheated below the glass transition temperature ($T = T_g - 20^\circ\text{C}$) and was left at this temperature for 6 hours (this is the annealing of the glass), followed by a slow cooling to room temperature to eliminate mechanical stresses.

The glasses were polished using abrasive paper (240-800-1200-4000) after they had been annealed and cooled. These samples were submitted to a variety of physical tests, including thermal, elastic and mechanical properties, in this study (see [fig III.1](#)).

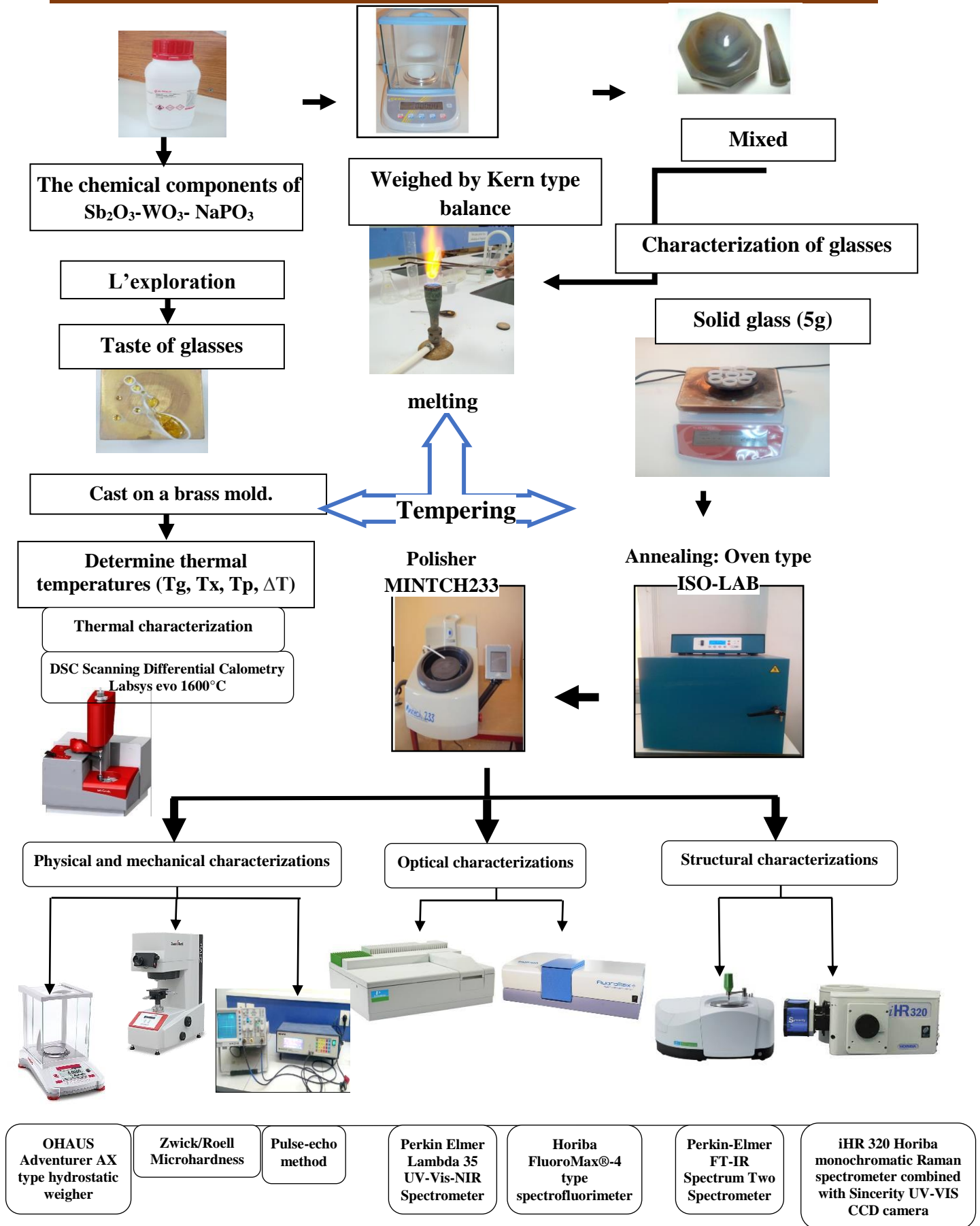


Figure III.1: Elaboration assembly from our glass.

III.3 Vitreous domains

In this chapter, we will study the glass field of the binary and ternary systems of glass produced from antimony. We studied the binary systems ($\text{Sb}_2\text{O}_3\text{-WO}_3$), ($\text{Sb}_2\text{O}_3\text{-NaPO}_3$), ($\text{NaPO}_3\text{-WO}_3$), and ternary systems of $\text{Sb}_2\text{O}_3\text{-WO}_3\text{-NaPO}_3$. The two lines with a constant proportion of 10% and 20% of tungsten oxide were chosen to evaluate the effect of NaPO_3 inclusion on the characteristics of SWN glasses.

III.3.1 Binary systems

Fig III. 2 shows the glassy areas observed in the binary systems ($\text{Sb}_2\text{O}_3\text{-WO}_3$), ($\text{Sb}_2\text{O}_3\text{-NaPO}_3$) and ($\text{NaPO}_3\text{-WO}_3$).

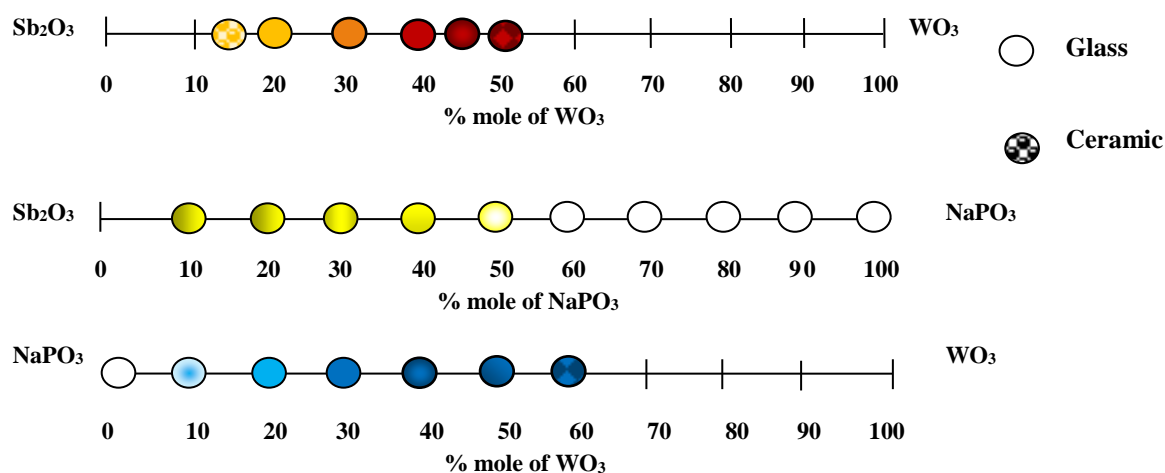


Figure III. 2: The vitreous domain of the studied binary systems.

III.3.1.1 (100-x) Sb₂O₃-xWO₃ and (100-x) NaPO₃- xWO₃ binary systems

The inclusion of WO_3 in NaPO_3 is easier than that of antimony oxide since the maximum concentration of WO_3 is ($60\text{NaPO}_3 - 40\text{WO}_3$). Gael et al. [1], prepared glasses containing up to 80 mole% of WO_3 by quenching on steel plates. This glass is difficult to synthesize because the melting temperature and the required glass transition temperature are too high and the liquid mixture remains difficult to homogenize. The authors suggest that this increase in T_g is due to the formation of tungsten oxide groups (WO_4 and/or WO_3), which form a linear chain with the tetrahedral phosphate, leading to the reinforcement of the glass network, and that this is linked to the presence of P-O-W connections.

On the other hand, the binary system (100-x) $\text{Sb}_2\text{O}_3\text{-x WO}_3$ synthesis forms glasses with a maximum concentration of ($55 \text{Sb}_2\text{O}_3\text{-}45 \text{WO}_3$). However, even if in this case, the melting temperature is very high and the glass unstable (it must quench very quickly). There are literature reports from M. Nalin et al. [2] on the preparation of glasses containing up to 60% moles of WO_3 by quenching between two pieces of brass heated to 20 °C.

III.3.1.2 In the binary system $(100-x) \text{Sb}_2\text{O}_3 - x \text{NaPO}_3$

Unlike the previous binary, the $\text{Sb}_2\text{O}_3\text{-NaPO}_3$ binary system shows a very large vitreous domain since virtually all compositions can vitrify because both components are formers (forming glass). Another advantage of this binary system is that the necessary melting temperatures are lower because the melting temperature of NaPO_3 ($T_m=610^\circ\text{C}$) is approximately low compared to Sb_2O_3 .

III.3.2 The ternary system

Our research consisted of exploring new glasses. We chose the ternary system (Sb_2O_3 - NaPO_3 - WO_3) as the vitreous matrix. It can be seen in figure III. 3 that the selected of our ternary system $\text{Sb}_2\text{O}_3\text{-WO}_3\text{-NaPO}_3$ shows a wide range of the glass-forming region. We know that NaPO_3 poly-phosphate glasses have the disadvantage that they absorb water from the air (material hygroscopic), but by including it in the $\text{Sb}_2\text{O}_3\text{-WO}_3$ binary system, a stable glass is obtained and it can be stored in atmospheric conditions for weeks and months without noticing the appearance of corrosion.

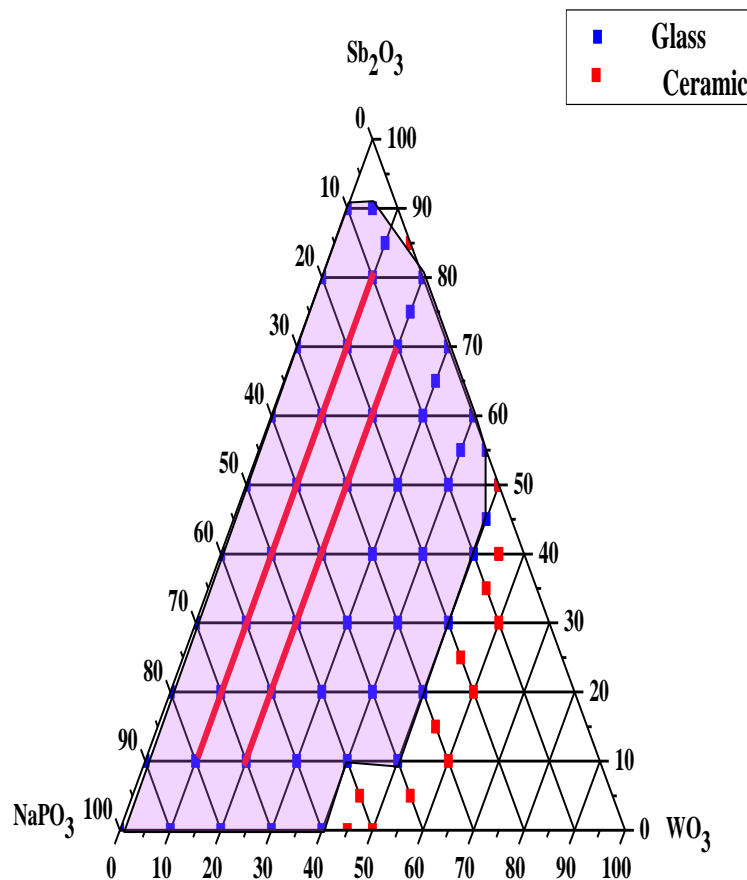






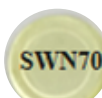


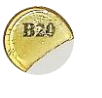














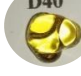



Figure III.3: Glass forming domain of our ternary system $\text{Sb}_2\text{O}_3\text{-NaPO}_3\text{-WO}_3$.

Table III.2: Composition, density ρ , characteristic temperature, thermal stability ΔT and the color of samples of glasses from the Sb₂O₃-WO₃-NaPO₃ ternary system.

Line	Composition			Characteristic temperatures (°C)				ρ (g/cm ³)	Photos of samples
	Sb ₂ O ₃	WO ₃	NaPO ₃	T _g	T _x	T _p	ΔT		
				$\pm 2^\circ\text{C}$	$\pm 2^\circ\text{C}$	$\pm 1^\circ\text{C}$	$\pm 4^\circ\text{C}$		
10WO ₃	80	10	10	290	377	390	87	5.256	
	70	10	20	300	401	418	101	4.975	
	60	10	30	312	417	437	105	4.827	
	50	10	40	315	-	-	-	4.580	
	40	10	50	327	-	-	-	4.325	
	30	10	60	333	-	-	-	4.078	
	20	10	70	336	-	-	-	3.725	
	10	10	80	338	-	-	-	3.328	
20 WO ₃	70	20	10	300	403	432	103	5.1932	
	60	20	20	303	434	466	131	4.9055	
	50	20	30	336	438	476	102	4.8844	

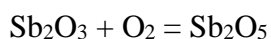
	40	20	40	337	-	-	-	4.6106	
	30	20	50	340	-	-	-	4.4029	
	20	20	60	356	-	-	-	4.1012	
	10	20	70	371	-	-	-	3.654	
30 WO₃	60	30	10	334	450	483	116	5.3740	
	50	30	20	342	462	490	120	5.2099	
	40	30	30	351	-	-	-	5.0311	
	30	30	40	360	-	-	-	4.7388	
	20	30	50	377	-	-	-	4.5248	
	10	30	60	380	-	-	-	4.0235	
40 WO₃	50	40	10	352	458	474	106	5.4491	
	40	40	20	361	468	488	107	5.3002	
	30	40	30	366	-	-	-	5.1224	
	20	40	40	370	-	-	-	4.8570	
	10	40	50	385	-	-	-	4.4084	

The incorporation of NaPO₃ into the Sb₂O₃-WO₃ binary system leads to an increase in the viscosity of the glass, which means that the lattice shrinks, and this is what we observed during the casting process of the melt in the brass mold, which increases the hardness and durability of our manufactured glass.

From [table III.2](#), thermal analysis for the same tungsten oxide line revealed a significant increase in glass transition temperature (T_g), crystallization onset (T_x), maximum crystallization peak (T_p), and crystallization parameter. The thermal stability parameter (T_x – T_g) is increased by the incorporation of NaPO₃ in the vitreous matrix, which causes an increase in the vitreous chain and an increase in the thermal stability parameter (T_x–T_g). We record the absence of the crystallization curve for some sample glasses with the increase of (WO₃ or / NaPO₃), which means high resistance against devitrification. The decrease in the density of these glasses is due to the lower molecular weight of NaPO₃ compared to the other oxides, NaPO₃ and Sb₂O₃ (for the same line of WO₃).

Our glasses showed considerable variation in their color, which is highlighted in [table III.2](#). These color changes (yellow-colorless-blue) may be related to metal-glass interface effects and the oxy-reduction process.

Due to its multivalent properties, antimony oxide oxidizes by taking up oxygen from the air, as seen below:



The change from colorless to yellowish tint of SWN glasses as antimony oxide content increases is due to host uptake caused by the transition between HOMO (Sb 5s + O 2p π) and LUMO (Sb 5p) [3].

For higher values of tungsten oxide, the color of this glass becomes blue. The blue coloration observed in certain compounds is in fact attributed to the simultaneous presence of W⁵⁺ and W⁴⁺. In particular, it is due to the transition of the poles between two non-equivalent sites [1].

In all our investigations, we have studied the two red lines in [fig III. 3](#), which contain (10% and 20% molar of WO₃). The formula of the ternary system study is (90-x) Sb₂O₃ - x NaPO₃ -10WO₃ with x varying from 10 to 80 and (80-x) Sb₂O₃ - x NaPO₃ -20WO₃ with x varying from 10 to 70.

III.4 Physical characteristics

III.4.1 Density, molar volume, oxygen molar volume and oxygen packing density

The density(ρ) is an important physical parameter and was measured by the Archimedes method at room temperature using distilled water as the immersion liquid. The principle of the measurements is simple. We weighed the samples in air rather than in water. Its values are calculated using the following relationship [4, 5]:

$$\rho = \frac{W_a}{W_a - W_b} \rho_b \quad (\text{III.3})$$

where W_a and W_b are the weights of glass in air and distilled water respectively, and ρ_b the distilled water's density ($\rho_b=0.998 \text{ g/cm}^3$)

-Theoretical values of the density were estimated using the following relation [4]:

$$\rho_{theo} = \sum \rho_{theoi} x_i = \rho_{theo(Sb_2O_3)} x_{Sb_2O_3} + \rho_{theo(WO_3)} x_{WO_3} + \rho_{theo(NaPO_3)} x_{NaPO_3} \quad (\text{III.4})$$

-The molar volume (V_m) of the glasses is calculated using the following relation [4-6]:

$$V_m = \frac{\sum x_i M_i}{\rho} = \frac{M_{glass}}{\rho} \quad (\text{III.5})$$

-The oxygen molar volume (V_o) for all glasses can be calculated by means of these formula [4-6]:

$$V_o = \frac{M_{glass}}{\rho} \left(\frac{1}{\sum x_i n_i} \right) = \frac{M_{glass}}{\rho(3 \times x_{Sb_2O_3} + 3 \times x_{WO_3} + 3 \times x_{NaPO_3})} \quad (\text{III.6})$$


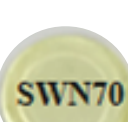
-Oxygen packing density (OPD) is given by the equation [6]:

$$OPD = 1000C \left(\frac{\rho}{M_{glass}} \right) \quad (\text{III.7})$$

Where ρ_{theoi} , M_i and x_i are the theoretical density, the molecular weight and the mole fraction of each component, respectively, ρ is the density of the glass, n_i is the number of oxygen atoms in each constituent oxide, and C is the number of oxygen atoms per formula unit.








- In the series (90-x) Sb₂O₃ - x NaPO₃ -10WO₃

Table III.3: The theoretical density (ρ_{theo}), experimental density (ρ_{exp}), molar volume (V_m), molar volume of oxygen (V_o) and oxygen packing density (OPD).

Code. N°	Photo	ρ_{theo} (g/cm ³)	ρ_{exp} (g/cm ³)	V_m (cm ³ /mol)	V_o (cm ³ /mol)	OPD (mol/l)
AN10		5,006	5,256	50,722	16,907	59,145
AN20		4,751	4,975	49,777	16,592	60,269
AN30		4,496	4,827	47,376	15,792	63,323
AN40		4,241	4,580	45,792	15,264	65,513
AN50		3,986	4,325	44,109	14,703	68,013
AN60		3,731	4,078	42,236	14,079	71,029
AN70		3,476	3,725	41,037	13,679	73,106
AN80		3,221	3,328	40,236	13,412	74,560

- In the series (80-x) Sb₂O₃ - x NaPO₃ -20WO₃

Table III.4: The theoretical density (ρ_{theo}), experimental density (ρ_{exp}), molar volume (V_m), molar volume of oxygen (V_o) and oxygen packing density (OPD).

Code. N°	Photos	ρ_{theo} (g/cm ³)	ρ_{exp} (g/cm ³)	V_m (cm ³ /mol)	V_o (cm ³ /mol)	OPD (mol/l)
BN10		5,217	5,462	47,717	15,906	62,871
BN20		4,962	5,212	46,369	15,456	64,699
BN30		4,707	4,954	44,954	14,985	66,736
BN40		4,452	4,693	43,422	14,474	69,089
BN50		4,197	4,403	41,974	13,991	71,473
BN60		3,942	4,181	39,666	13,222	75,632
BN70		3,687	3,927	37,406	12,469	80,201

Several physical properties of the synthesized samples were collected using suitable formulas and are listed in tables III.3 and III.4. The density and molar volume of **AN samples** (10% WO₃) gradually drop with the addition of NaPO₃, from 5.256 to 3.328 (g/cm³) and 50.722 to 40.236 (cm³/mol), respectively (see fig III.4). The same observation for **BN samples** (20% mole of WO₃) shows that density and molar volume gradually decrease with the addition of NaPO₃ from 5.462 to 3.927 (g/cm³) and from 47.717 to 37.406 (cm³/mol), respectively (shown in fig III.5). The V_o results of the **AN** and **BN** glass samples decreased

from 16.907 to 13.412 (cm³/mol) and 15.906 to 12.469 (cm³/mol), respectively, with the increase of NaPO₃ content. On the other hand, the OPD values of the AN and BN glasses increased from 59.145 to 74.560 (mol/l) and from 62.871 to 80.201 (mol/l), respectively (see fig III.6 and fig III.7).

The experimental density values were consistent compared to their theoretical values. The decrease in density value of our SWN glasses (AN and BN glasses) with the addition of NaPO₃ could be explained by the low density values of NaPO₃, and also by the variation in molecular weights and atomic radii of constituent components [6, 7]. The decrease in order ($M_{NaPO_3}=101.96$ (g/mol) < $M_{WO_3}=231.85$ (g/mol) < $M_{Sb_2O_3}=291.52$ (g/mol)) and ($r_{P^{5+}} = 0.017nm < r_{W^{6+}} = 0.065nm < r_{Sb^{3+}} = 0.076nm < r_{O^{2-}} = 0.14nm$) was caused by decline in oxygen atom levels, which have the highest ionic radius in the glass structure[8, 9].

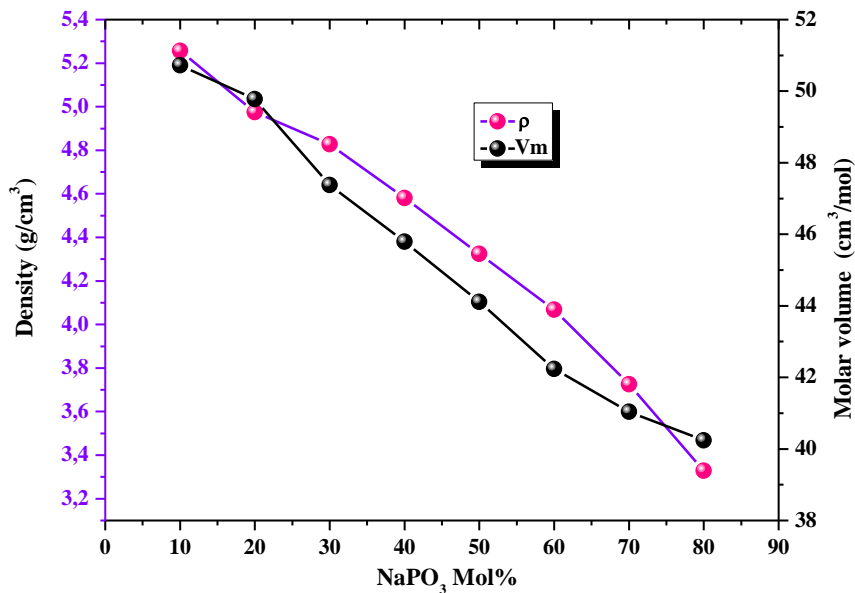


Figure III.4: The variation of ρ and V_m with the content of NaPO₃ in (90-x) Sb₂O₃-10WO₃-xNaPO₃ glasses.

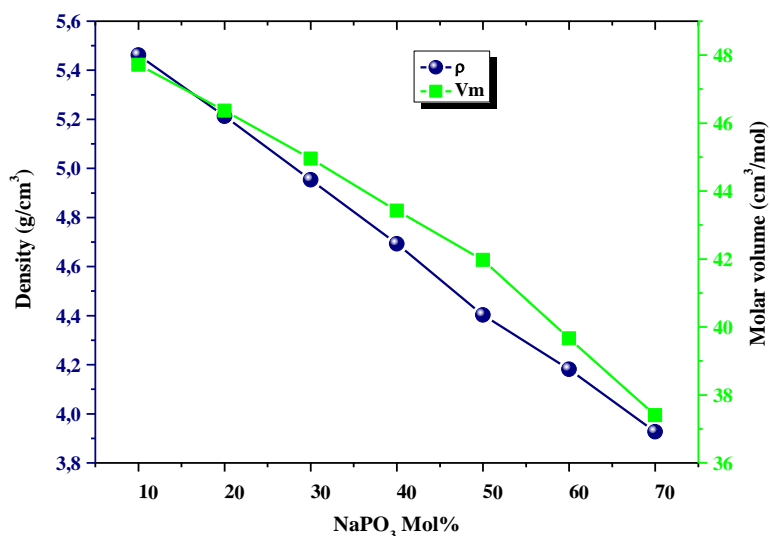


Figure III.5: The variation of ρ and V_m with NaPO_3 content in glasses $(80-x)\text{Sb}_2\text{O}_3\text{-}20\text{WO}_3\text{-}x\text{NaPO}_3$.

As a consequence, it can be concluded that decreasing the oxygen content in the glass composition resulted in a decrease in molar volume (V_m) with the addition of NaPO_3 to the glass matrix, implying a possible contraction in the existing glass network. The fact that the molar volume of these glasses has decreased shows that their structure is less chaotic. This produces a decrease in bond length or interatomic space between the atoms due to an increase in the stretching force constant of the bonds inside SWN (AN and BN) glasses [6].

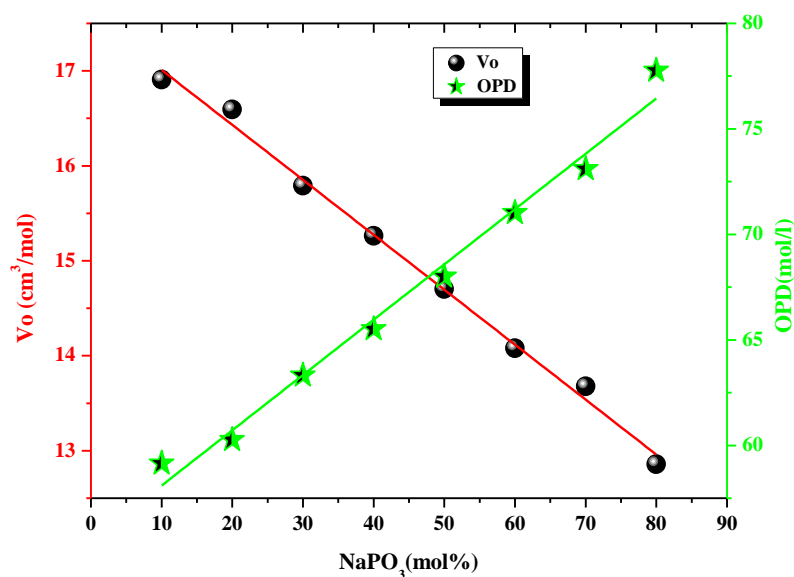


Figure III.6: The variation of V_0 and OPD with the content of NaPO_3 in AN glasses.

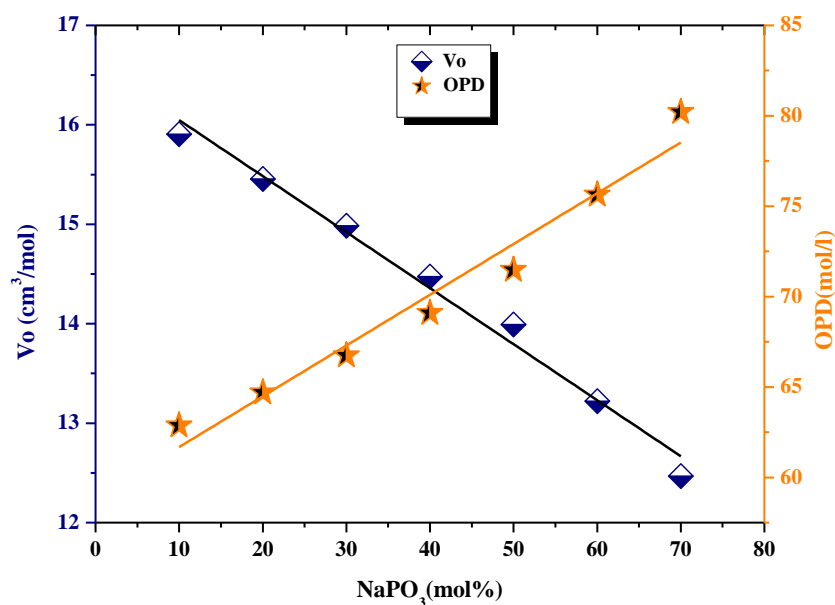


Figure III.7: The variation of V_o and OPD with NaPO_3 content in BN glasses.

In tables III.3 and 4, the oxygen molar volume (V_o) increases in the opposite way to the oxygen packing density (OPD), whereas the V_o decreases with rising OPD values of the SWN glasses with rising NaPO_3 concentration. It might be attributed to a decrease in NBOs while maintaining strong connections in the glass network, implying that the glass structure has become more compact and rigid, necessitating a considerable amount of energy to break the network link [10, 11].

III.5 Thermal properties by DSC

The glass compositions, typical glass temperatures, and the stability parameters are summarized in table III.2 (T_x - T_g). The stability parameter is a commonly used metric for determining the thermal stability of glasses in the face of devitrification. The glass transition temperature and thermal stability ΔT of AN glasses (10% mole of WO_3) vary between 290°C – 338°C and 87°C – 105°C, respectively. Also, the glass transition temperature and thermal stability ΔT of BN glasses (20% mole of WO_3) vary between 300°C – 371°C and 102°C – 131°C, respectively.

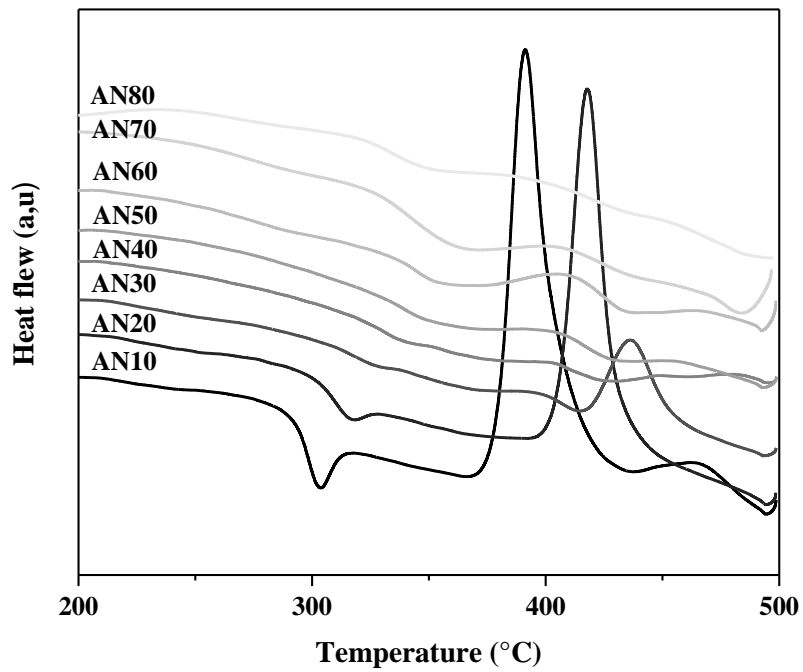


Figure III.8: DSC curves of glass samples in the $(90-x) \text{Sb}_2\text{O}_3-x \text{NaPO}_3-10\text{WO}_3$ ternary system (AN series).

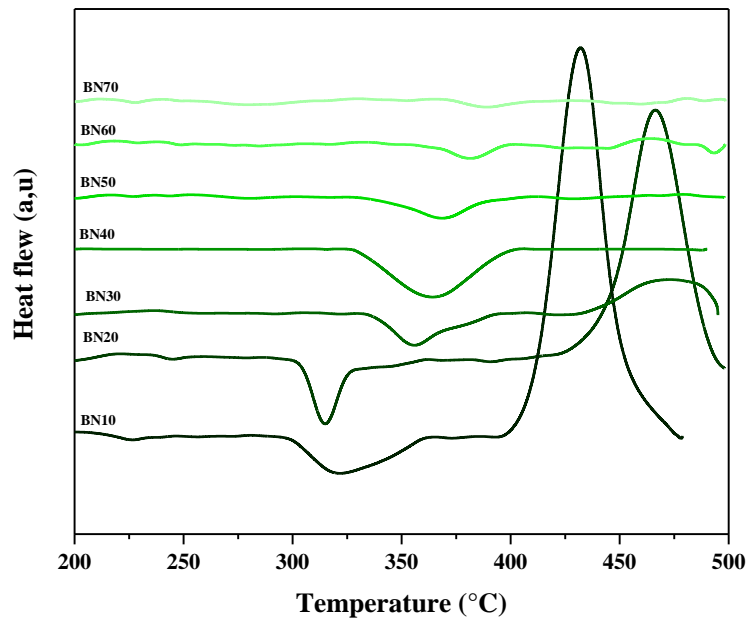


Figure III.9: DSC curves of glass samples in the ternary system $(80-x) \text{Sb}_2\text{O}_3-x\text{NaPO}_3-20\text{WO}_3$ (BN series).

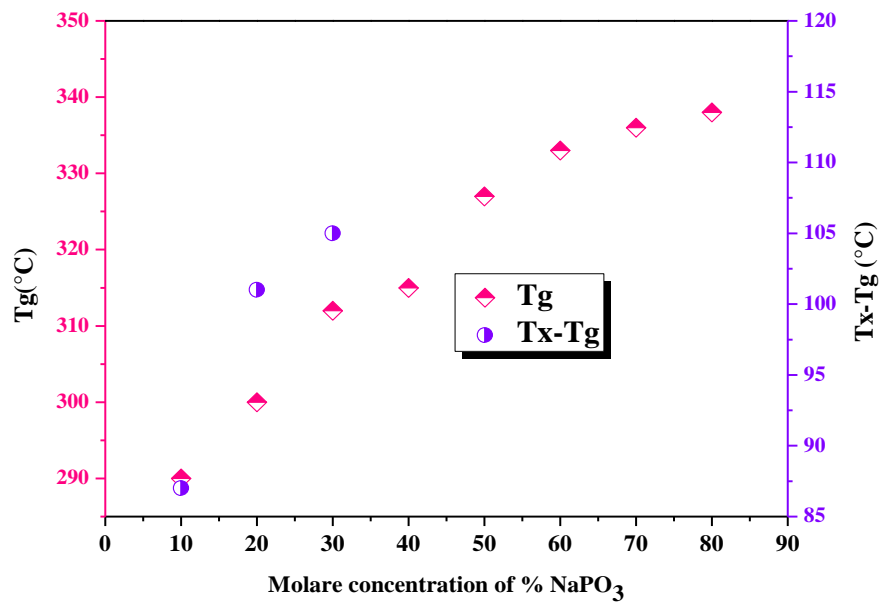


Figure III.10: Evolution of T_g and ΔT for $(90-x)\text{Sb}_2\text{O}_3\text{-}10\text{WO}_3\text{-}x\text{NaPO}_3$ glass samples.

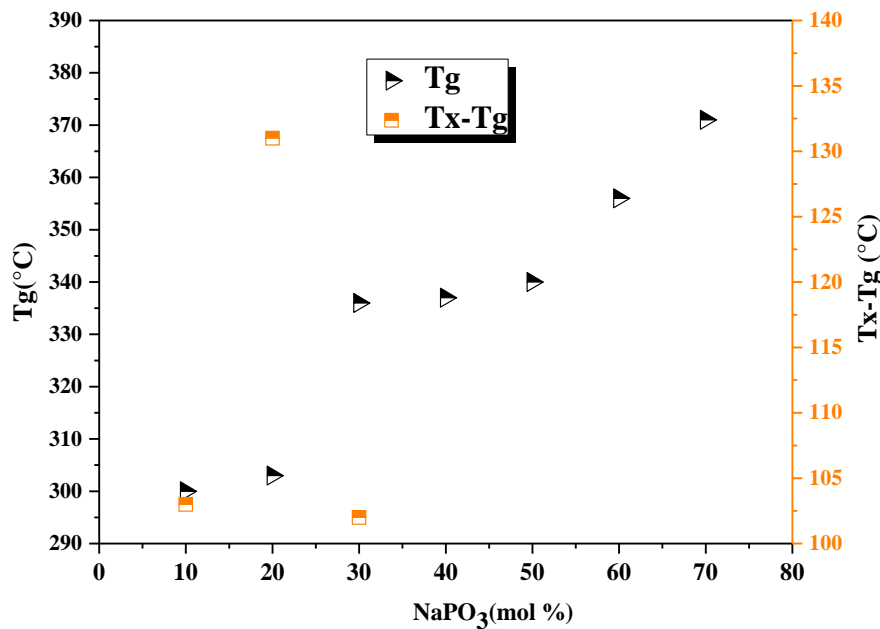
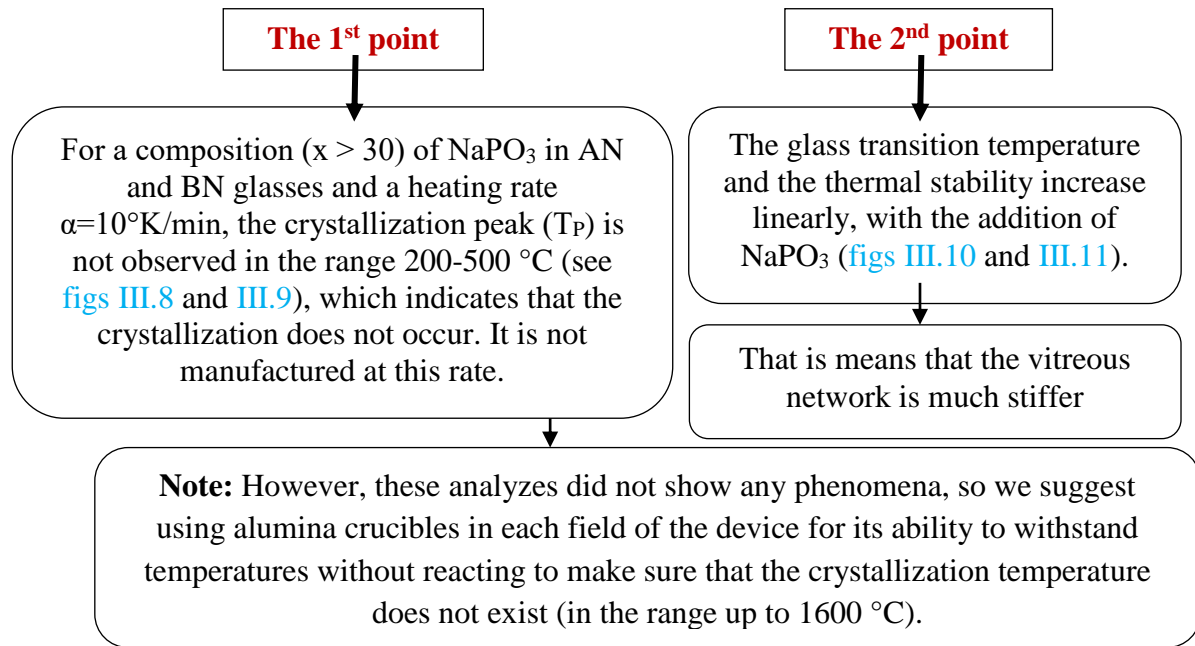


Figure III.11: Evolution of T_g and ΔT for $(80-x)\text{Sb}_2\text{O}_3\text{-}20\text{WO}_3\text{-}x\text{NaPO}_3$ glass samples

According to the DSC curves (fig III.8 and fig III.9), we can see two spots of interest on the produced SWN sample (AN and BN glasses).



These results suggest that the incorporation of NaPO₃ into the matrix makes the vitreous network much stiffer. In other words, this incorporation would have the effect of increasing the viscosity of the glasses. This can be confirmed by a simple visual observation: during the synthesis of glasses and more precisely during the casting of the molten mixture, it was observed that the viscosity at the same temperature of the liquid increased with the NaPO₃ content. Some authors have suggested that this increase in the glass transition temperature is due to the fact that the tungsten oxide groups (WO₄ and WO₆) or antimony oxides Sb₂O₃ form a single network with the phosphate tetrahedral. These groups would enter the phosphate network. This means that the reinforcement of the vitreous network would be linked to the presence of P-O-W or/and P-O-Sb bonds [12, 13]. This possibility needs to be verified by structural investigations. Moreover, the presence of MO_n polyhedra with a high coordination number such as WO₆ could also be at the origin of the increase in T_g due to the increase in the average connection of the network. However, we must remain cautious about the possible causes of the increase in T_g because this magnitude depends on many factors.

We can generally say that the matrix (90-x) Sb₂O₃ -x NaPO₃-10 WO₃ gives glasses stable against devitrification (for 10<x≤80), since the stability factor ΔT>100 °C and the crystallization peak is not observed for (30<x) in AN glass samples. Well, for the matrix (80-x) Sb₂O₃ -x NaPO₃-20 WO₃, we can observe the peak of crystallization just of **BN10**, **BN20** and **BN30**, which means a high thermal stability against crystallization with the rise of NaPO₃ and tungsten oxide. It would be very easy to produce fiber optics from these samples because crystallization is not occurring and they have high thermal stability.

-The Debye temperature (θ_D) is an important parameter for solids. We can calculate (θ_D) a correlation with the relations [6, 14]:

$$\theta_D = \frac{h}{K} \left(\frac{3\rho N_a n}{4\pi M} \right)^{1/3} \left[\frac{1}{3} \left(\frac{1}{v_L^3} + \frac{1}{v_T^3} \right) \right]^{-1/3} \quad (\text{III.8})$$

where h is Planck's constant, K is Boltzman's constant, N_a is Avogadro's number and n is the number of atoms in the unit formula.

Another's important parameters are the thermal expansion coefficient (α_p) and acoustic impedance (Z) determined by [15] :

-The thermal expansion coefficient

$$\alpha_p = 23.2(V_L - C) \quad (\text{III.9})$$

With C is a constant and equal to 0.57457.

- Acoustic impedance

$$Z = (V_L \rho) \quad (\text{III.10})$$

The Debye temperature, acoustic impedance and the thermal expansion coefficient are illustrated in table III.5. It can be observed that the Debye temperatures, acoustic impedance, and the thermal expansion coefficient increased in AN and BN glasses with the augmentation of NaPO₃. The increase in Debye temperature is ascribed to an increase in the number of atoms in the glass' chemical formula due to the production of BO atoms as a direct result of the addition of NaPO₃ [16]. The rise in thermal coefficient (α_p) in the SWN (AN and BN) glasses demonstrates an increase in the number of bonds per unit volume and the stiffness of the glass structure.

Table III.5: Acoustic impedance (Z), Thermal expansion coefficient (α_p) and Debay temperature (θ_D).

S. n°	Z*10 ⁷	α_p (10 ⁻⁶ K ⁻¹)	θ_D (K)	S. n°	Z*10 ⁷	α_p (10 ⁻⁶ K ⁻¹)	θ_D (K)
AN10	1,467	5,141	127,87	BN10	1,468	5,284	133,42
AN20	1,506	5,688	133,43	BN20	1,721	6,537	134,40
AN30	1,437	5,575	139,25	BN30	1,635	5,490	142,04
AN40	1,508	6,304	151,43	BN40	1,652	6,921	152,73
AN50	1,546	6,960	152,48	BN50	1,501	6,589	168,25
AN60	1,518	7,327	168,22	BN60	1,489	7,115	180,61
AN70	1,466	7,795	180,50	BN70	1,544	7,789	187,31
AN80	1,493	8,643	191,09				

III.6 Elastic properties

III.6.1 Elastic modulus experiment

The following formulas were used to compute elastic constants, Young's modulus E, shear modulus G, longitudinal modulus L, bulk modulus K, the Poisson ratio ν and fractal bond connectivity d [17]:

- Young's modulus:

$$E_{\text{exp}} = \rho V_T^2 \frac{3V_L^2 - 4V_T^2}{V_L^2 - V_T^2} \quad \text{(III.11)}$$

- Shear modulus:

$$G_{\text{exp}} = \rho \cdot V_T^2 \quad \text{(III.12)}$$

- Longitudinal modulus:

$$L_{\text{exp}} = \rho \cdot V_L^2 \quad \text{(III.13)}$$

- Bulk modulus:

$$K_{\text{exp}} = \frac{\rho}{3} (3V_L^2 - 4V_T^2) \quad \text{(III.14)}$$

- Poisson coefficient :

$$\nu_{\text{exp}} = \frac{V_L^2 - 2V_T^2}{2(V_L^2 - V_T^2)} \quad \text{(III.15)}$$

-Fractal bond connectivity [18] $d = \frac{4G_{exp}}{K_{exp}}$ **(III.16)**

With: the elastic moduli E, G and K in (GPa), V_L: longitudinal propagation speed (m/s), V_T: transverse propagation speed (m/s) and ρ the density (g/cm³).

In general, the behavior of elastic moduli (E_{exp}, G_{exp}, K_{exp}, and L_{exp}) and Poisson ratio (ν_{exp}) is expected to increase by the rise of sodium metaphosphate in SWN glasses (AN and BN glasses) (see tables III.6 and III.7). We can say that the value of Young's modulus of this glass is similar to phosphate glasses [19].

Table III.6: Physical and experimental elastic properties of the ternary system (90-x) Sb₂O₃-xNaPO₃-10WO₃.

S.N°	ρ _{exp} (g/cm ³)	E _{exp} (GPa)	K _{exp} (GPa)	G _{exp} (GPa)	L _{exp} (GPa)	d	ν _{exp}
AN10	5,256	36,754	20,554	15,289	40,930	2,98	0,156
AN20	4,975	38,362	25,012	15,414	45,564	2,47	0,195
AN30	4,827	38,303	21,591	15,902	42,794	2,95	0,158
AN40	4,580	42,708	26,503	17,340	49,624	1,62	0,182
AN50	4,325	44,494	34,014	15,939	55,267	1,87	0,247
AN60	4,078	45,446	32,966	17,888	56,818	2,17	0,220
AN70	3,725	46,730	33,023	18,482	57,666	2,24	0,214
AN80	3,471	47,730	39,700	18,362	64,180	1,85	0,250

Table III.7: Physical and experimental elastic properties of the ternary system (80-x) Sb₂O₃-xNaPO₃-20WO₃.

S.N°	$\rho_{\text{exp}}(\text{g/cm}^3)$	$E_{\text{exp}}(\text{GPa})$	$K_{\text{exp}}(\text{GPa})$	$G_{\text{exp}}(\text{GPa})$	$L_{\text{exp}}(\text{GPa})$	d	ν_{exp}
BN10	5,148	38,590	20,067	16,359	41,878	3,26	0,136
BN20	5,073	40,212	38,130	15,183	58,374	1,59	0,276
BN30	4,850	41,325	33,905	15,933	55,149	1,88	0,247
BN40	4,642	44,324	35,935	17,121	58,763	1,91	0,244
BN50	4,396	46,634	25,144	19,579	51,250	3,11	0,146
BN60	4,088	48,984	26,925	20,465	54,211	3,04	0,151
BN70	3,927	49,655	34,434	19,710	60,713	2,29	0,209

III.6.2 Elastic moduli and Poisson's ratio by Makishima-Mackenzie's theory

Makishima and Mackenzie's model proposed a theoretical approach to calculating the elastic moduli of oxide glasses with consideration of the chemical composition (x_i) of the constituting oxide, packing factor (V_i), and their corresponding dissociation energies per unit volume (G_i) [20, 21].

For Ith component oxide in the form of A_xO_y , the values of V_i and G_i can be determined by:

-Packing factor:

$$V_i = \frac{4\pi Na}{3} (xR_A^3 + yR_O^3) \quad \text{(III.17)}$$

-Dissociation energy per unit volume :

$$G_i = \frac{\rho_i}{M_i} U_i \quad \text{(III.18)}$$

Table III.8: Molecular weight, Density, packing factor of oxide and dissociation energy per unit volume of Sb₂O₃, WO₃ and NaPO₃.

Oxide	M _i (g/mol)	ρ _i (g/cm ³)	V _i [22] (cm ³ /mol)	G _i [22] (kcal/cm ³)
Sb ₂ O ₃	291,52	5,05	22,97	8,43
WO ₃	231,85	7.16	21,45	16,22
NaPO ₃	101,96	2,50	20,77	8,79

The packing density (V_t), and the dissociation energy (G_t) were calculated by the next equation[22-24]:

$$\text{-Packing density : } V_t = \frac{\rho_i}{M_i} \sum V_i x_i \quad \text{(III.19)}$$

$$\text{-The dissociation energy per unit volume : } G_t = \sum G_i x_i \quad \text{(III.20)}$$

Where R_A and R_O are the respective ionic radius of metal and oxygen atoms, respectively [8, 9], N_a is Avogadro's number and U_i is the dissociation energy per mole (molar dissociation energy) of the ith component, M_i is glass molecular weight, ρ is glass density, x_i is the ith component's molar fraction, G_i and V_i are the respective dissociation energy per unit volume and packing factor of the ith component (table III.8).

In the theory of Makishima and Mackenzie [20, 21], Young's modulus (E_t), bulk modulus (K_t), shear modulus (G_t), longitudinal modulus (L_t) and Poisson ratio (ν_t) for oxide glasses are calculated as follows [24]:

-Young's modulus:

$$E_t = 8.36V_t \sum G_i x_i \quad \text{(III.21)}$$

-Bulk modulus:

$$K_t = 10V_t^2 G_t \quad \text{(III.22)}$$

-Shear modulus:

$$G_t = \frac{3K_t}{(10.2V_t - 1)} \quad \text{(III.23)}$$

-Longitudinal modulus :

$$L_t = K_t + \left(\frac{4S_t}{3}\right) \quad \text{(III.24)}$$

-Poisson's ratio :

$$\nu_t = 0.5 - \left(\frac{1}{7.2 \nu_t} \right) \quad \text{(III.25)}$$

On the other hand, all the theoretical values of the moduli of compression, shear, Young and longitudinal are very close to the experimental values. This shows a good agreement between these values (for AN and BN glasses).

Figure III.12 shows an increase in experimental elastic moduli in AN glasses with the addition of NaPO₃; Young's modulus ranged from 36.754 to 47.730 (GPa), shear modulus from 15.289 to 18.362 (GPa), compression modulus from 20.554 to 39.700 (GPa) and longitudinal modulus from 40.930 to 64.180 (GPa).

Similarly, for the theoretical moduli of elasticity of AN samples (fig III.13), the Young's modulus varied from 34.47 to 43.39 (GPa), the shear modulus from 15.55 to 18.60 (GPa), the compression modulus from 18.39 to 28.37 (GPa) and the longitudinal modulus from 39.12 to 53.17 (GPa).

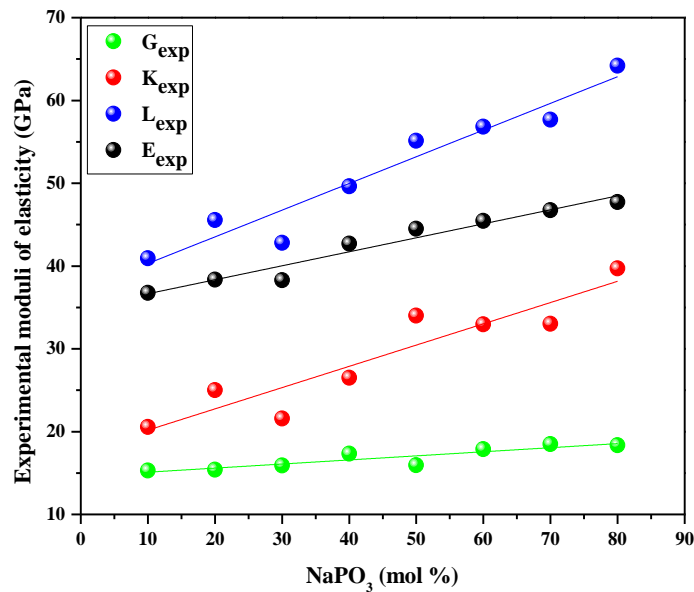


Figure III.12: Experimental moduli of elasticity of AN glasses containing NaPO₃.

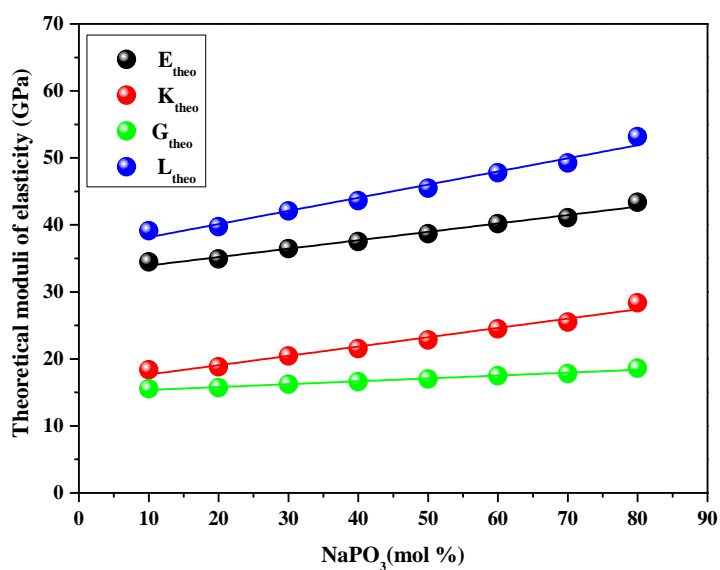


Figure III.13: Theoretical moduli of elasticity of AN glasses containing NaPO₃.

Table III.9: Theoretically calculated compositional and elastic properties of AN glasses based on the Makishima-Mackenzie theory.

S.N°	V _t	G _t (kcal/cm ³)	E _{theo} (GPa)	K _{theo} (GPa)	G _{theo} (GPa)	L _{theo} (GPa)	v _{theo}
AN10	0,45	9,25	34,47	18,39	15,55	39,12	0,189
AN20	0,45	9,28	34,92	18,80	15,71	39,75	0,191
AN30	0,47	9,32	36,47	20,43	16,23	42,07	0,203
AN40	0,48	9,35	37,51	21,52	16,58	43,63	0,210
AN50	0,49	9,39	38,69	22,82	16,99	45,48	0,218
AN60	0,51	9,43	40,16	24,48	17,49	47,80	0,227
AN70	0,52	9,46	41,06	25,50	17,81	49,25	0,232
AN80	0,45	9,25	43,39	28,37	18,60	53,17	0,246

Table III.10: Theoretically calculated compositional and elastic properties of BN glasses based on the Makishima-Mackenzie theory.

S.N°	V _t	G _t (kcal/cm ³)	E _{theo} (GPa)	K _{theo} (GPa)	G _{theo} (GPa)	L _{theo} (GPa)	v _{theo}
BN10	0,45	10,02	37,97	20,58	17,05	43,31	0,193
BN20	0,46	10,06	38,51	21,10	17,24	44,09	0,197
BN30	0,48	10,10	40,29	23,00	17,84	46,79	0,209
BN40	0,49	10,13	41,51	24,33	18,26	48,67	0,217
BN50	0,51	10,17	42,93	25,93	18,74	50,92	0,225
BN60	0,52	10,20	44,69	28,00	19,34	53,79	0,235
BN70	0,54	10,24	45,88	29,42	19,76	55,76	0,241

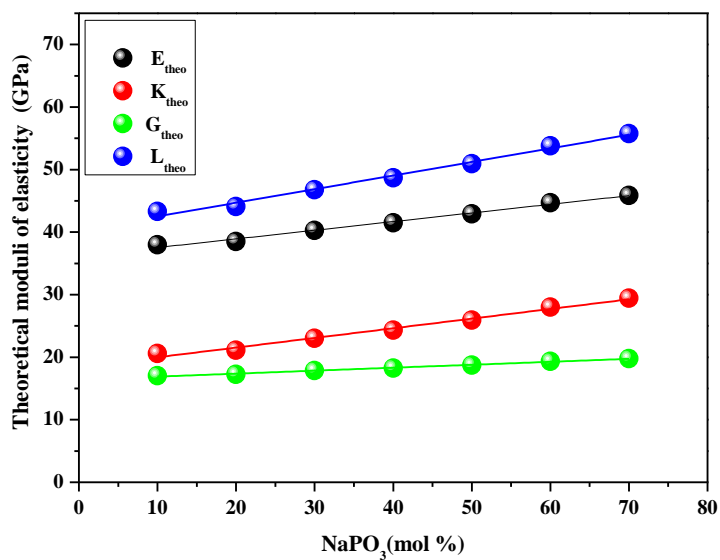


Figure III.14: The theoretical moduli of elasticity of BN glasses containing NaPO₃.

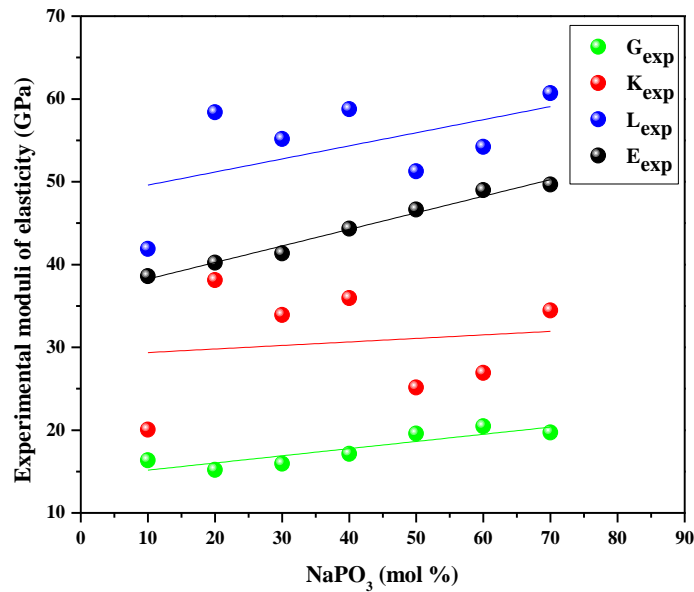


Figure III.15: Experimental moduli of elasticity of BN glasses containing NaPO₃.

Also, for the theoretical moduli of elasticity of **BN** samples (fig III.14), the Young's modulus varied from 37.97 to 45.88 (GPa), the shear modulus from 17.05 to 19.76 (GPa), the compression modulus from 20.58 to 29.42 (GPa) and the longitudinal modulus from 43.31 to 55.76 (GPa).

Figure III.15 shows an increase in experimental elastic moduli in **BN** glasses with the addition of NaPO₃; Young's modulus ranged from 38.590 to 49.655 (GPa), shear modulus from 16.359 to 19.710 (GPa), compression modulus from 20.067 to 34.434 (GPa) and longitudinal modulus from 41.878 to 60.713 (GPa).

Frequently, structural changes in the glass network are related to changes in its physical and elastic properties. With the addition of NaPO₃ in the AN and BN glass samples, the elastic moduli demonstrate a tightening of the structure and an increase in the stiffness of the glass.

An increase in NaPO₃ concentration leads to more bridging oxygen atoms (BO), which reduces the atoms (NBO) and improves network connectivity. The addition of NaPO₃ caused the depolymerization of PO₄ units and created BO bonds such as P-O-Sb, and P-O-W, which helped to increase the connectivity of the glassy matrix, which is confirmed by the high values of T_g. It will increase the chemical durability and thermal stability of SWN glasses. This strong bond makes the glass network strong in its resistance to mechanical deformation.

This agrees with the different physical properties (ρ , V_m , V_o , OPD) of these glass samples, which support this discussion [6].

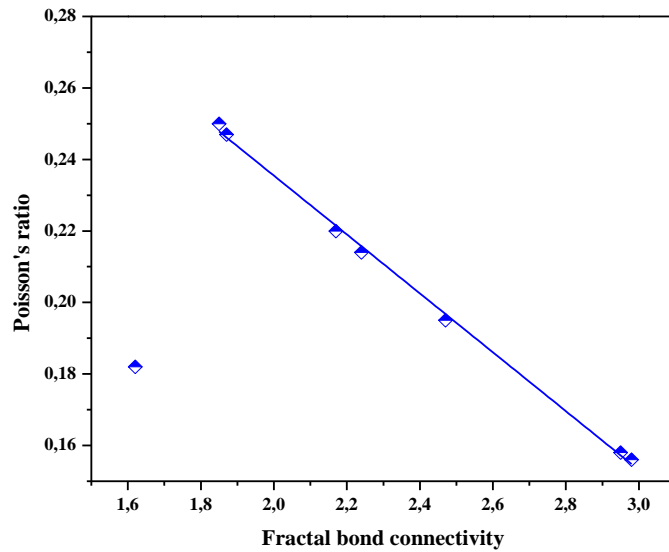


Figure III.16: Poisson's ratio of AN glasses as a function of fractal bond connectivity.

The connectivity of fractal bonds (d) is an extensive parameter used to indicate changes in the dimensionality of the network and the elastic properties of the material [18]. Figs III.16 and III.17 display the variation of the Poisson ratio with the connectivity of fractal bonds ($d = 4G_{exp} / K_{exp}$).

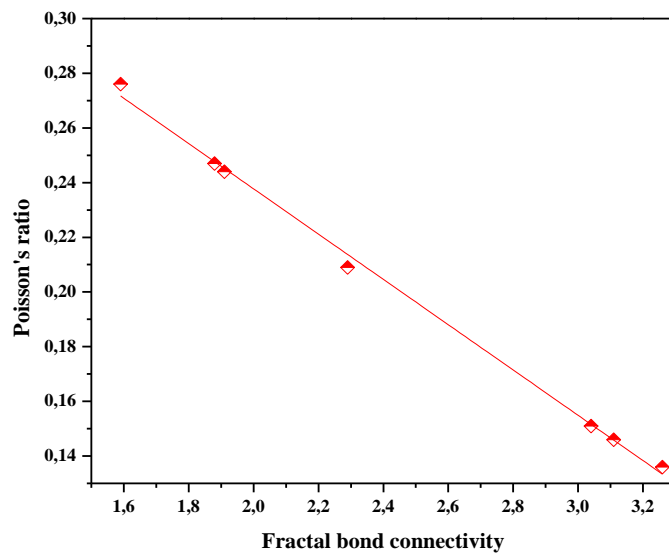


Figure III.17: Poisson's ratio of BN glasses as a function of fractal bond connectivity.

It has been proposed that the value of d ($d=3$: three-dimensional networks, $d=2$: two-dimensional layer structures, and $d=1$: the one-dimensional chain) [6, 18]. The decrease in d from 2.97 to 2.23 in AN glasses and from 3.26 to 2.29 from 10 in BN glasses with increasing NaPO₃ content means that the lattice of these glasses gradually changes from a 3D structure to a 2D layer.

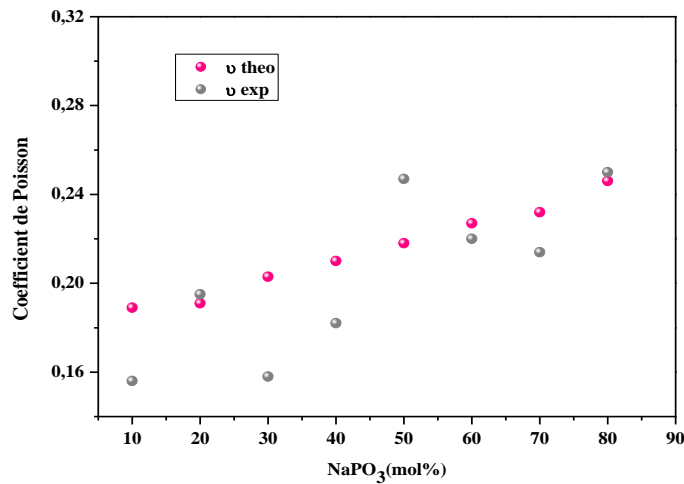


Figure III.18: Theoretical and experimental Poisson's ratio of AN glasses as a function of NaPO₃ (mol%).

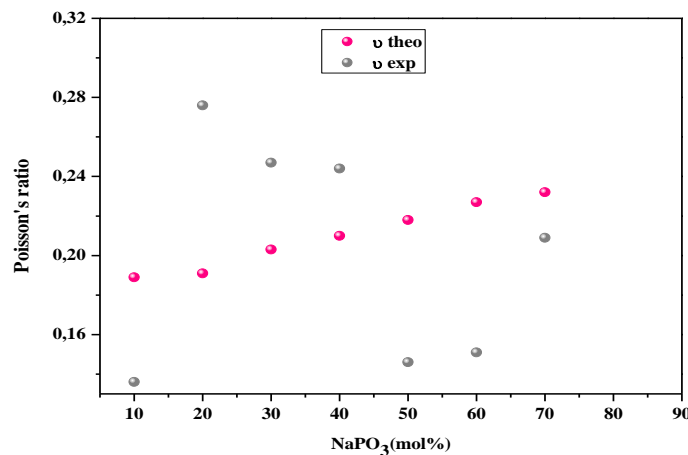


Figure III.19: Theoretical and experimental Poisson's ratio of BN glasses as a function of NaPO₃ (mol%).

The value of d ($d=3$: 3D, $d=2$: 2D, and $d=1$: 1D chain) has been considered. The (ν) increased from 0.202 to 0.297 and 0.136 to 0.209 for AN and BN glasses, respectively (see fig

III.18 and fig III.19), denoting an increase in the crosslink density of the glass network and an increase in connectivity in the glass structure, as well as an increase in rigidity [25].

There is a link between the Poisson's ratio and the structure of glasses. When the value of (ν) approaches 0.25, the glass has been deformed due to structural unit elongation, stretching, or compression. If (ν) is smaller than 0,25, the outcome part of the energy results in a tetrahedral deformation (SiO₄, for example). When the Poisson's ratio (ν) is larger than 0.25, when combined with the lattice distortion, there is a deformation of the ions [26].

III.7 Micro- Hardness

The micro-hardness Vickers H_v is expressed by the measurement of the dimension or the depth of the indentation made by indentation tests on a pyramidal shaped diamond. The resultant values of AN glasses are illustrated in fig III.20. We can include H_v from the length of the projected indentation diagonals (d) from the following relationship [27]:

$$H_v = 1.8544 \frac{P}{d^2} \tag{III.26}$$

with P is the peak load equal to 4.905N (= 50g) and d is the length of the projected indentation diagonals

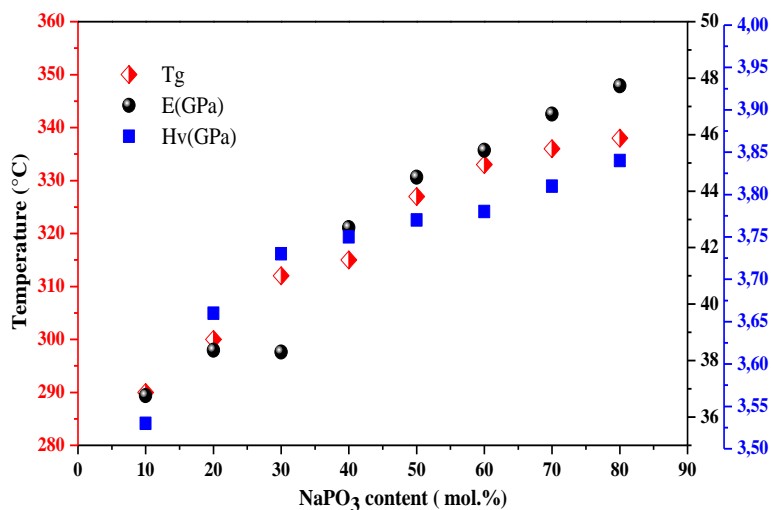


Figure III.20: Values of temperature of glass transition, Young modulus and micro-hardness of AN glasses.

Fig III.20 exhibits the micro-hardness, T_g, and Young modulus E of the ternary glasses (90-x) Sb₂O₃-xNaPO₃-10WO₃ against NaPO₃ concentration. They demonstrate increases in these parameters with NaPO₃ content. Micro-hardness is proportional to the dilatometric softening point T_d, which is proportional to the glassy transition temperature (T_g). As a result, the micro-hardness and Young module change in a manner similar to the T_g.

Micro-hardness expresses the required stress to eliminate the free volume (deformation of the network) of the glass. The increase in micro-hardness indicates an increase in the rigidity of these glasses, which demonstrates that these sample glasses can be used in the fiber optic process [6, 26].

III.8 Conclusion

Makishima and Mackenzie's theoretical evaluation of the elastic moduli of the SWN (AN and BN glasses) samples revealed an increase in the elastic moduli, as evidenced by the data presented. The physical results indicate that increasing NaPO₃ concentration in a glass structure leads to an increase in OPD, T_g, H_v and elastic modulus values, while decreasing the density, molar volume and molar volume of oxygen values. The trend increases the oxygen packing density, and glass transition of SWN glasses, and it is related to the compaction and strengthening of cross-links between phosphate chains, as measured by density and DSC. All this demonstrates that these sample glasses can be used in the fiber optic processes.

References

1. Poirier, E. and A. Dailly, Investigation of the hydrogen state in IRMOF-1 from measurements and modeling of adsorption isotherms at high gas densities. *The Journal of Physical Chemistry C*, 2008. **112**(33): p. 13047-13052. <https://doi.org/10.1021/jp711709r>
2. Nalin, M., et al., Antimony oxide based glasses. *Journal of non-crystalline solids*, 2001. **284**(1-3): p. 110-116. [https://doi.org/10.1016/S0022-3093\(01\)00388-X](https://doi.org/10.1016/S0022-3093(01)00388-X)
3. Som, T. and B. Karmakar, Efficient green and red fluorescence upconversion in erbium doped new low phonon antimony glasses. *Optical Materials*, 2009. **31**(4): p. 609-618. <https://doi.org/10.1016/j.optmat.2008.06.018>
4. Kavaklıoğlu, K.B., et al., The TeO₂-Na₂O System: Thermal Behavior, Structural Properties, and Phase Equilibria. *International Journal of Applied Glass Science*, 2015. **6**(4): p. 406-418. <https://doi.org/10.1111/ijag.12103>
5. Kumar, A., et al., Physical, structural, optical and gamma ray shielding behavior of (20+ x) PbO–10 BaO–10 Na₂O–10 MgO–(50-x) B₂O₃ glasses. *Physica B: Condensed Matter*, 2019. **552**: p. 110-118. <https://doi.org/10.1016/j.physb.2018.10.001>
6. Guesmia, N., et al., Glass formation, physical and structural investigation studies of the (90-x) Sb₂O₃-10WO₃-xNaPO₃ glasses. *Materials Today Communications*, 2022. **30**: p. 103226. <https://doi.org/10.1016/j.mtcomm.2022.103226>
7. Upender, G., et al., Optical band gap, glass transition temperature and structural studies of (100– 2x) TeO₂–xAg₂O–xWO₃ glass system. *Journal of Alloys and Compounds*, 2010. **504**(2): p. 468-474. <https://doi.org/10.1016/j.jallcom.2010.06.006>
8. Çelikkilek, M., A. Ersundu, and S. Aydin, Preparation and characterization of TeO₂–WO₃–Li₂O glasses. *Journal of non-crystalline solids*, 2013. **378**: p. 247-253. <https://doi.org/10.1016/j.jnoncrysol.2013.07.020>
9. Shannon, R.T. and C.T. Prewitt, Effective ionic radii in oxides and fluorides. *Acta Crystallographica Section B: Structural Crystallography and Crystal Chemistry*, 1969. **25**(5): p. 925-946. <https://doi.org/10.1107/S0567740869003220>
10. Sidek, H., et al., Synthesis and optical properties of ZnO-TeO₂ glass system. *American Journal of Applied Sciences*, 2009. **6**(8): p. 1489. <https://doi.org/10.3844/ajassp.2009.1489.1494>

11. Upender, G. and M. Prasad, Raman, FTIR, thermal and optical properties of TeO₂-Nb₂O₅-B₂O₃-V₂O₅ quaternary glass system. *Journal of Taibah University for Science*, 2017. **11**(4): p. 583-592. <https://doi.org/10.1016/j.jtusci.2016.02.008>
12. Cherbib, M.A., et al., Structure properties relationship in calcium sodium metaphosphate and polyphosphate glasses. *Journal of non-crystalline solids*, 2018. **485**: p. 1-13. <https://doi.org/10.1016/j.jnoncrysol.2018.01.043>
13. Omrani, R.O., et al., Structural and thermochemical properties of sodium magnesium phosphate glasses. *Journal of Alloys and Compounds*, 2015. **632**: p. 766-771. <https://doi.org/10.1016/j.jallcom.2015.01.297>
14. Saddeek, Y.B., Ultrasonic study and physical properties of some borate glasses. *Materials Chemistry and Physics*, 2004. **83**(2-3): p. 222-228. <https://doi.org/10.1016/j.matchemphys.2003.09.051>
15. Sathish, K. and S. Thirumaran, Spectroscopic and ultrasonic investigations on structural characterization of borate glass specimen doped with transition metal ions. *Spectrochimica Acta Part A: Molecular and Biomolecular Spectroscopy*, 2015. **147**: p. 163-172. <https://doi.org/10.1016/j.saa.2015.02.031>
16. Halimah, M., et al., Ultrasonic study and physical properties of borotellurite glasses. *Am. J. Appl. Sci*, 2005. **2**(11): p. 1541-6. <https://doi.org/10.3844/ajassp.2005.1541.1546>
17. Hamzaoui, M., et al., Thermal and elastic characterization of Sb₂O₃-Na₂O-ZnO glasses. *Physica Scripta*, 2013. **2013**(T157): p. 014029. <https://doi.org/10.1088/0031-8949/2013/T157/014029>
18. Bogue, R. and R. Sladek, Elasticity and thermal expansivity of (AgI) x (AgPO₃) 1- x glasses. *Physical Review B*, 1990. **42**(8): p. 5280. <https://doi.org/10.1103/PhysRevB.42.5280>
19. Sampaio, J., et al., Rare earth doping effect on the elastic moduli of low silica calcium aluminosilicate glasses. *Journal of non-crystalline solids*, 2002. **304**(1-3): p. 293-298. [https://doi.org/10.1016/S0022-3093\(02\)01037-2](https://doi.org/10.1016/S0022-3093(02)01037-2)
20. Makishima, A. and J.D. Mackenzie, Direct calculation of Young's modulus of glass. *Journal of non-crystalline solids*, 1973. **12**(1): p. 35-45. [https://doi.org/10.1016/0022-3093\(73\)90053-7](https://doi.org/10.1016/0022-3093(73)90053-7)
21. Makishima, A. and J.D. Mackenzie, Calculation of bulk modulus, shear modulus and Poisson's ratio of glass. *Journal of non-crystalline solids*, 1975. **17**(2): p. 147-157. [https://doi.org/10.1016/0022-3093\(75\)90047-2](https://doi.org/10.1016/0022-3093(75)90047-2)

22. Inaba, S., S. Oda, and K. Morinaga, Heat capacity of oxide glasses at high temperature region. *Journal of non-crystalline solids*, 2003. **325**(1-3): p. 258-266. [https://doi.org/10.1016/S0022-3093\(03\)00315-6](https://doi.org/10.1016/S0022-3093(03)00315-6)
23. Shelby, J.E., *Introduction to glass science and technology*2020: Royal society of chemistry. <https://doi.org/10.1002/ange.19971092243>
24. Abd El-Moneim, A. and R. El-Mallawany, Analysis and prediction for elastic properties of quaternary tellurite Ag₂O–V₂O₅–MoO₃–TeO₂ and WO₃–B₂O₃–MgO–TeO₂ glasses. *Journal of non-crystalline solids*, 2019. **522**: p. 119580. <https://doi.org/10.1016/j.jnoncrysol.2019.119580>
25. Rouxel, T., Elastic properties and short-to medium-range order in glasses. *Journal of the American Ceramic Society*, 2007. **90**(10): p. 3019-3039. <https://doi.org/10.1111/j.1551-2916.2007.01945.x>
26. Chang, K., T. Lee, and L. Hwa, Structure and elastic properties of iron phosphate glasses. *Chinese Journal of Physics*, 2003. **41**(4): p. 414-421.
27. Limbach, R., et al., Elasticity, deformation and fracture of mixed fluoride–phosphate glasses. *Journal of non-crystalline solids*, 2015. **430**: p. 99-107. <https://doi.org/10.1016/j.jnoncrysol.2015.09.025>

Chapter IV
Optical and
structural studies of
SWN glasses

IV.1 Introduction

In this present work, we show the optical and structural properties of the ternary systems (90-x) Sb₂O₃-10WO₃-xNaPO₃ and (80-x) Sb₂O₃-20WO₃-xNaPO₃ as potential optical materials for NLO application. Linear optical properties are studied via transmittance spectra, indirect and direct optical band gaps, and Urbach energy. We calculated their optical coefficients to reinforce the application of these materials as photonic materials. The behavior of the structural changes such as cross-link density, number of bonds per unit volume, IR, FTIR and Raman investigations has been discussed with regard to the amount of phosphate concentration. The chemical bonds that are present in our glasses may be identified by measurements of FTIR absorption and Raman scattering. Only well-known structural references will be used to compare these conclusions. In particular, vibrational spectroscopy enables the detection of M-O-M bridging or M-O⁻ terminating bonds (with M = P, W, Sb, etc.), providing information on the vitreous network's degree of connectivity.

IV.2 Optical characteristics

IV.2.1 Band gap energy and Urbach energy

UV-Vis spectra can also be used to determine the optical bandgap of our glasses, which is an intrinsic property of each solid. The bandgap (or energy gap) of a material can be defined as the amount of energy you need to transfer an electron from the valence band to the conduction band. The relationship between absorption coefficient α and E_g is provided according to the Davis and Mott theory by [1, 2]:

$$(\alpha h\nu)^n = A(h\nu - E_g) \quad (\text{IV.1})$$

Where $\alpha = (1/d) \ln (100/T\%)$. Here α is the absorption coefficient, d is the thickness of the sample (in cm), ($\%T$) is the quantity percent of transmittance, A is constant depending on the type of material, $h\nu$ is incident photon energy and E_g is the optical band gap. The values of n are 2 and 1/2 for direct and indirect transitions, respectively. We can obtain indirect optical band gap energies by extrapolating the linear section of the curve to cross the photon energy axis at zero absorption. The slope of the linear component of the plot $(\alpha h\nu)^{1/2}$ and $(\alpha h\nu)^2$ vs $h\nu$ is intersected to obtain the E_g values (in eV).

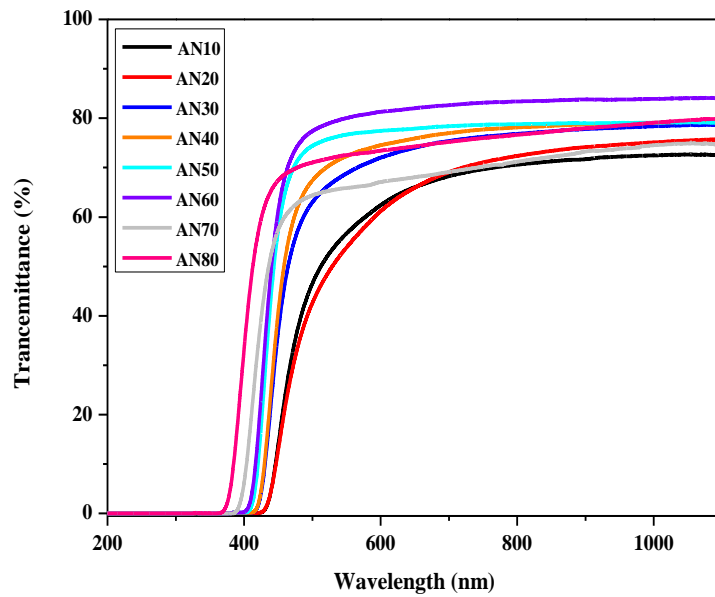


Figure IV.1: Transmittance spectra in the UV-visible, and NIR ranges of the $(90-x) \text{Sb}_2\text{O}_3\text{-}10\text{WO}_3\text{-}x \text{NaPO}_3$ ternary system.

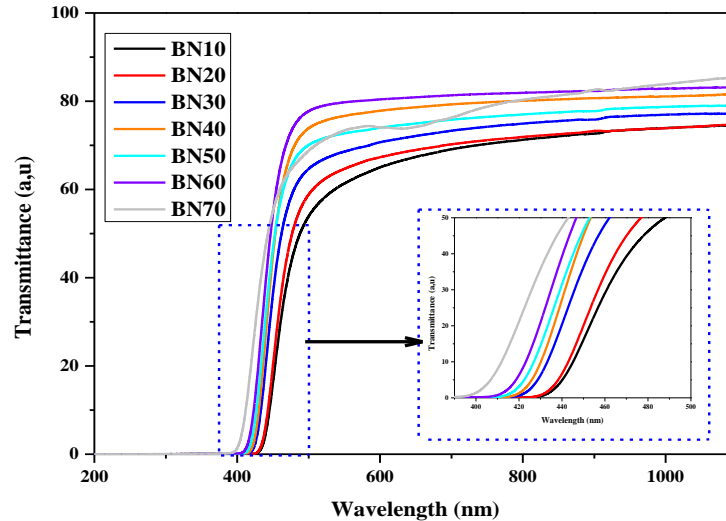


Figure IV.2: Transmittance spectra in the UV-visible, and NIR ranges of the $(80-x) \text{Sb}_2\text{O}_3\text{-}20\text{WO}_3\text{-}x \text{NaPO}_3$ ternary system.

Figs IV.1 and IV.2 show the transmission limits of SWN (AN and BN) glasses in the UV-Visible and NIR region range of 200 to 1100 nm. The addition of NaPO_3 shifted the transmission limit of the material towards the lower wavelengths from the visible to ultraviolet spectrum. That is why our samples with the highest concentration of NaPO_3 have

turned transparent. In the BN70 sample, we observed a large absorption band between 600 nm and 700 nm. This absorption is attributed to the partial reduction of W^{6+} to W^{5+} .

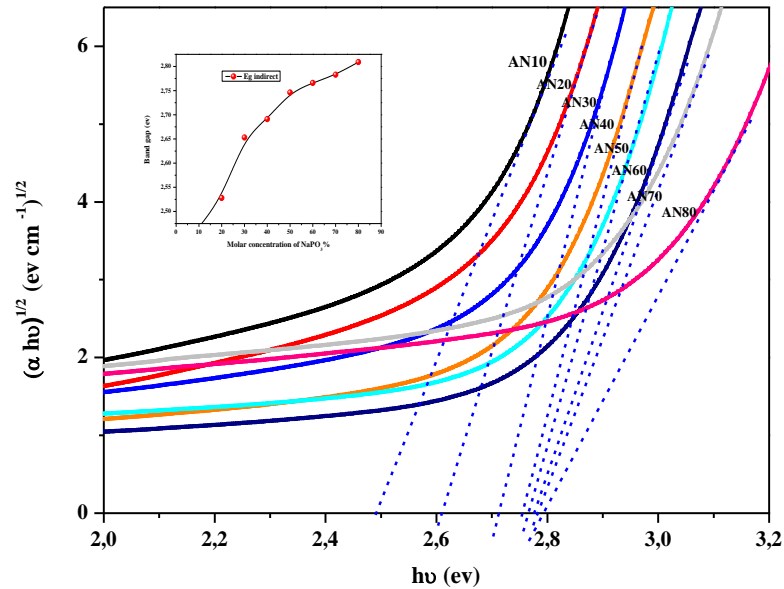


Figure IV.3: Plot of $(\alpha hv)^{1/2}$ versus $h\nu$ curve to estimate the band gap ($E_{g \text{ indirect}}$) of AN glasses.

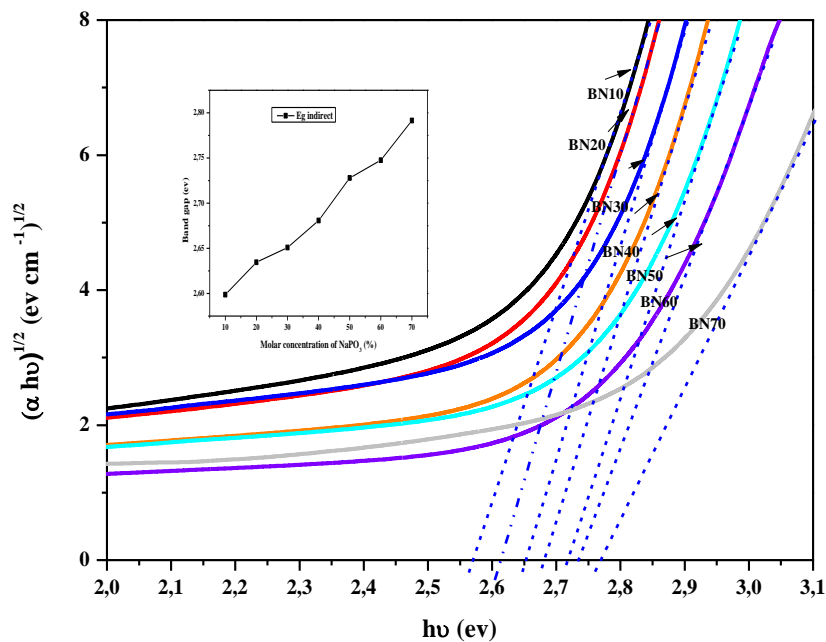


Figure IV.4: Plot of $(\alpha hv)^{1/2}$ versus $h\nu$ curve to estimate the band gap ($E_{g \text{ indirect}}$) of BN glasses.

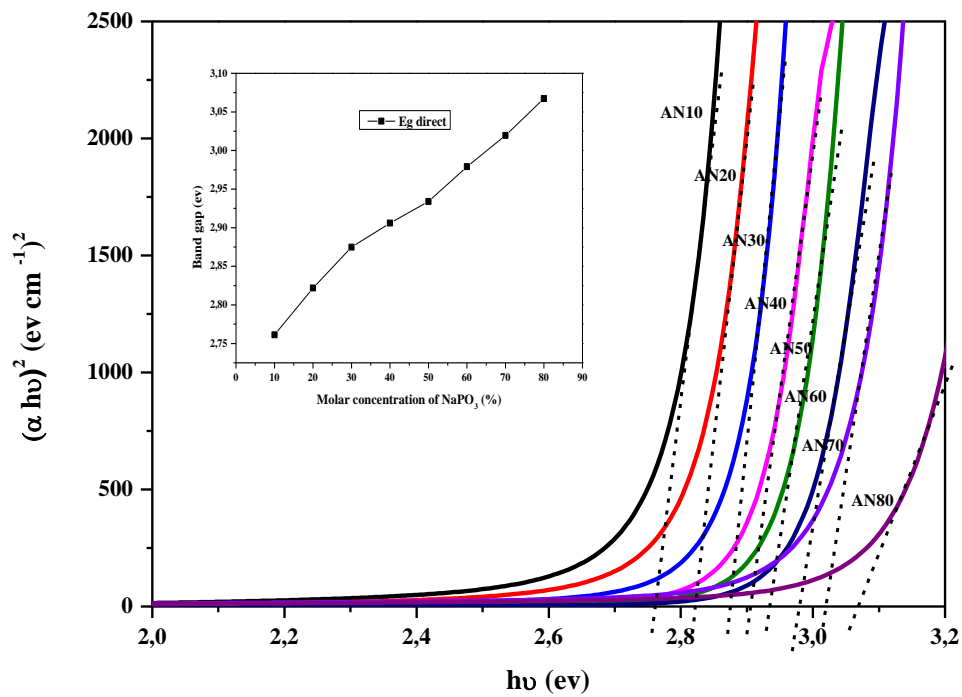


Figure IV.5: Plot of $(\alpha hv)^2$ versus $h\nu$ curve to estimate the band gap ($E_{g \text{ direct}}$) of AN glasses.

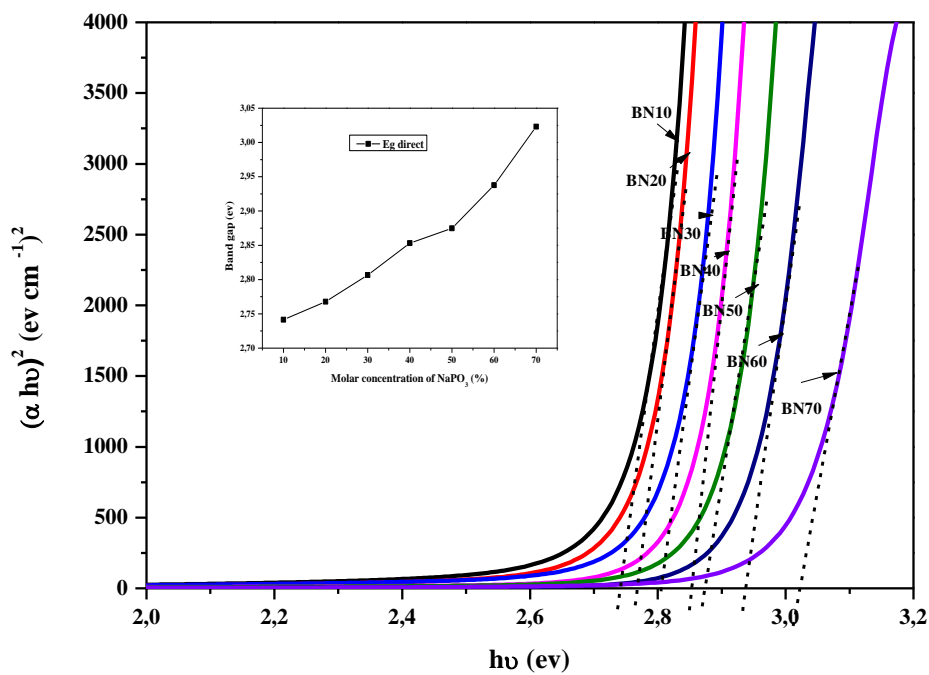


Figure IV.6: Plot of $(\alpha hv)^2$ versus $h\nu$ curve to estimate the band gap ($E_{g \text{ direct}}$) of BN glasses.

The E_g direct and indirect values in the AN glasses both rise from 2.76 to 3.07 eV and from 2.47 to 2.81 eV, respectively (see [figs IV.5 and IV.3](#)). When the concentration of NaPO_3 grows, the E_g direct and indirect increase from 2.74 to 3.02 eV and from 2.60 to 2.79 eV, respectively, in the BN glasses (see [figs IV.6 and IV.4](#)).

The structural changes in SWN glasses are caused by the replacement of Sb_2O_3 with NaPO_3 , and also the presence of W^{5+} or W^{6+} ions is predicted to aid in the de-polymerization of bonds such as W-O-W, Sb-O-Sb etc [3]. Phosphate creates stronger linear chains like P-O-Sb and P-O-W linking, which means the glass matrix has fewer bonding defects and NBO atoms (the glass structure becomes more ordered). As a result of the reduction in NBO atoms, the number of donor centers in the glass matrix decreases, causing the optical band gap to grow.

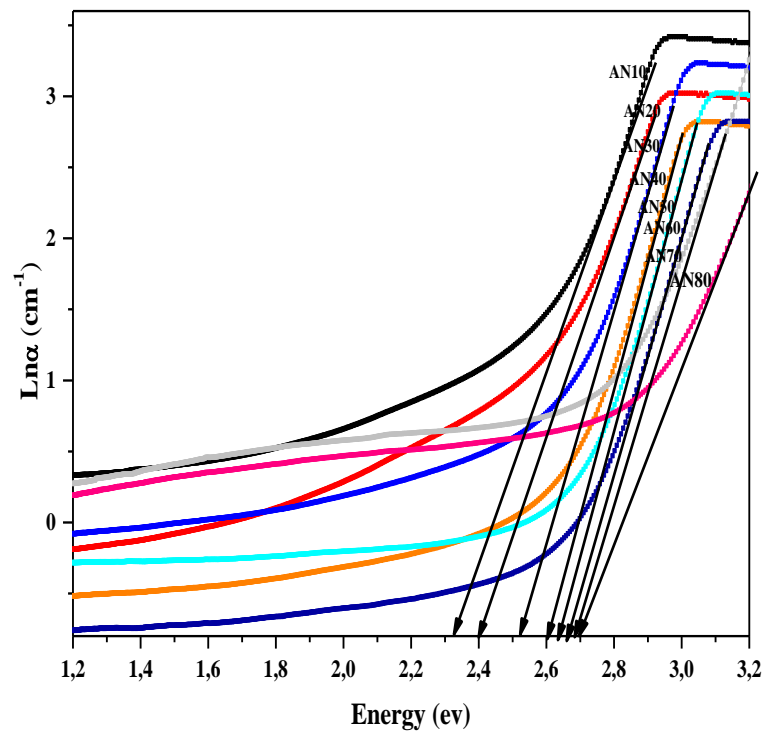


Figure IV.7: $\ln(\alpha)$ as a function of $h\nu$ for AN glasses to estimated E_u values.

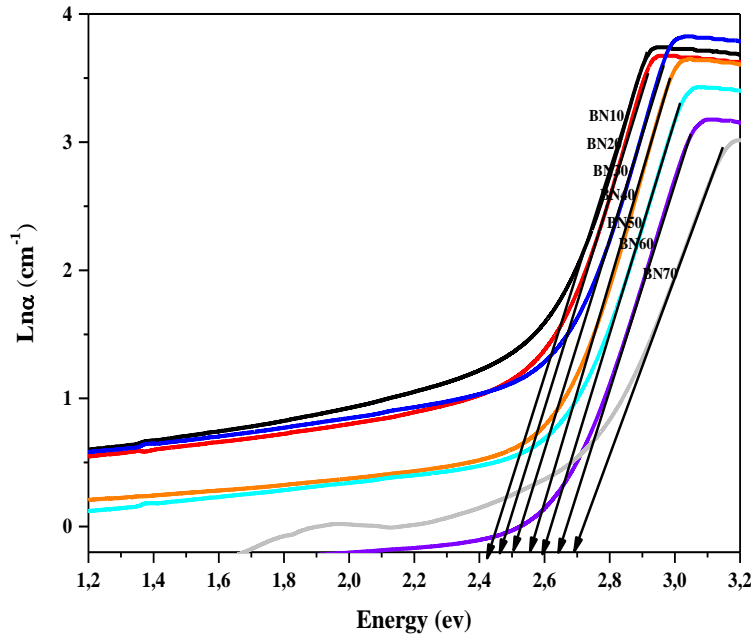


Figure IV.8: $\ln(\alpha)$ as a function of $h\nu$ for BN glasses to estimated E_u values.

The parameter which characterizes the disorder of the material is the tail energy of (Urbach). The band tail can be estimated by using the Urbach rule [4]:

$$\alpha = \alpha_0 \exp\left(\frac{h\nu}{E_u}\right) \quad (\text{IV.2})$$

where α_0 is a constant and E_u is the width of the band tails of the electron states in the forbidden band gap; it is also known as the Urbach energy.

The Urbach energy (E_u) [5-9] is used to calculate variations in imperfections in the glass complex, and it can also be defined as the width of localized states that corresponds to the optical transition between localized tail states in the adjacent valence band and the extended state in the conduction band lying above the mobility edge [10].

It is measured by using the logarithmic equation (IV.2) and by taking the reciprocal of the slope in the linear part of a plot between $\ln(\alpha)$ versus $h\nu$.

$$\ln\alpha = \ln\alpha_0 + \frac{h\nu}{E_u} \quad (\text{IV.3})$$

The E_u values predicted by the reciprocal slope of $\ln\alpha$ versus $h\nu$ are shown in Figs IV.7 and IV.8. The E_u is inversely proportional to the E_g . The Urbach energies (E_u) of AN samples decrease up to 60% of NaPO_3 content from 0.144 to 0.121 eV then increases from

0.153 to 0.168 eV for AN70 and AN80 glasses, respectively. While, the E_u values of BN samples decreased up to 50% of NaPO_3 content and from 0.124 to 0.121 eV than increases from 0.126 to 0.147 eV for BN60 and BN70 glasses, respectively.

This drop in E_u values indicates a decrease in the bonding defects and NBOs in the glass network, which causes a reduction in the degree of localization of electrons and the donor centers of the glass matrix. On the other hand, random internal electric fields caused by short-range arrangement or defects in amorphous materials may cause energy levels to expand in the tail region and vice versa [11].

IV.2.2 Calculation of optical properties

A theoretical equation can be proposed to calculate the refractive index (n_0) of the studied glasses by using the expression [12]:

$$n_0 = \sum_i x_i n_i \quad (\text{IV.4})$$

Where x_i is the amount of the component i of the glass sample and n_i is the refractive index of its component, which is given by

$$n_i = -\ln(0.102\Delta\chi) \quad (\text{IV.5})$$

where $\Delta\chi$ is the difference in the electronegativity between the anion and the cation of the glass sample component i ($\Delta\chi = \chi_a - \chi_c$). $\Delta\chi$ was calculated and equal to 1.6, 1.8 and 2 for Sb_2O_3 , WO_3 and NaPO_3 , respectively. From Eq. (IV.5), the values of n_i for Sb_2O_3 , WO_3 and NaPO_3 are presented in Table IV.1. Therefore, the estimated refractive index of the present glasses can be obtained from eq. (IV.4).

Table IV.1: Electronegativity, Refractive index, Optical basicity and ionic polarizability of oxides (α_{0-2}) values of Sb_2O_3 , WO_3 and NaPO_3 oxide.

Oxides	electronegativity	Refractive index	Optical basicity	α_{0-2}
Sb_2O_3	1.6	1.8128	1.18	3.429
WO_3	1.8	1.6950	1.045	2.670
NaPO_3	2.1	1.5408	0.47	1.35

Table IV.2: Some calculated physical properties of the AN samples.

Property	Sample n° /property value							
	AN10	AN20	AN30	AN40	AN50	AN60	AN70	AN80
E_g indirect (eV)	2,47	2,53	2,65	2,69	2,75	2,77	2,78	2,81
E_u (eV)	0,144	0,142	0,122	0,123	0,123	0,121	0,153	0,168
Refractive index, n	1,779	1,756	1,734	1,711	1,689	1,667	1,644	1,622
Molar refraction, R_m (cm³/mol)	21,253	20,407	18,986	17,922	16,843	15,717	14,865	13,586
Total molar polarizability, α_m(Å³)	8,428	8,093	7,529	7,107	6,679	6,233	5,895	5,388
Total molar polarizability of cation, Σα_m(Å³)	1,794	1,574	1,354	1,134	0,914	0,694	0,474	0,254
Polarizability of oxide ions, α_{o2-}(Å³)	2,211	2,173	2,058	1,991	1,922	1,846	1,807	1,711
Optical basicity from refractive index, Λ(n)	0,915	0,901	0,859	0,831	0,801	0,766	0,746	0,694
Optical basicity from optical band gap, Λ(E_g)	1,225	1,221	1,197	1,187	1,174	1,160	1,155	1,155
Theoretical optical basicity, Λ_{th}	1,096	1,025	0,954	0,883	0,812	0,741	0,670	0,599
Metallization criterion(M)	0,581	0,590	0,599	0,609	0,618	0,628	0,638	0,648
Dielectric constant, ε	3,164	3,084	3,006	2,929	2,853	2,778	2,704	2,631
Transmittance T	0,854	0,860	0,866	0,871	0,877	0,882	0,888	0,893
Reflectivity R_L	0,079	0,075	0,072	0,069	0,066	0,063	0,059	0,056
Optical electronegativity (χ)	1,470	1,452	1,395	1,358	1,318	1,271	1,244	1,176
Electronic susceptibility (χ_e)	0,172	0,166	0,160	0,154	0,148	0,142	0,136	0,130
Third order nonlinear susceptibility χ⁽³⁾×10⁻¹²	13,091	10,775	7,510	6,795	5,913	5,638	5,415	5,093

Table IV.3: Some calculated physical properties of the BN samples.

Property	Sample n° /property value						
	BN10	BN20	BN30	BN40	BN50	BN60	BN70
$E_{g \text{ indirect}} \text{ (eV)}$	2,60	2,63	2,65	2,68	2,73	2,75	2,79
$E_u \text{ (eV)}$	0,124	0,120	0,118	0,115	0,121	0,126	0,147
Refractive index, n	1,767	1,744	1,722	1,700	1,677	1,655	1,633
Molar refraction, $R_m \text{ (cm}^3\text{/mol)}$	19,767	18,786	17,795	16,777	15,813	14,555	13,352
Total molar polarizability, $\alpha_m \text{ (Å}^3\text{)}$	7,839	7,450	7,057	6,653	6,271	5,772	5,295
Total molar polarizability of cation, $\sum \alpha_m \text{ (Å}^3\text{)}$	1,587	1,367	1,147	0,927	0,707	0,486	0,266
Polarizability of oxide ions, $\alpha_{O_2-} \text{ (Å}^3\text{)}$	2,084	2,028	1,970	1,909	1,855	1,762	1,676
Optical basicity from refractive index, $\Lambda(n)$	0,869	0,846	0,822	0,795	0,770	0,722	0,674
Optical basicity from optical band gap, $\Lambda(E_g)$	1,194	1,186	1,178	1,169	1,158	1,138	1,115
Theoretical optical basicity, Λ_{th}	1,082	1,011	0,940	0,869	0,798	0,727	0,656
Metallization criterion(M)	0,586	0,595	0,604	0,614	0,623	0,633	0,643
Dielectric constant, ϵ	3,122	3,043	2,966	2,889	2,813	2,739	2,665
Transmittance T	0,857	0,863	0,869	0,874	0,880	0,885	0,891
Reflectivity R_L	0,077	0,074	0,070	0,067	0,064	0,061	0,058
Optical electronegativity (χ)	1,408	1,379	1,346	1,310	1,276	1,213	1,148
Electronic susceptibility (χ_e)	0,169	0,163	0,156	0,150	0,144	0,138	0,133
Third order nonlinear susceptibility $\chi^{(3)} \times 10^{-12}$	8,728	7,894	7,555	6,977	6,188	5,895	5,307

The molar refraction (R_m) is calculated using the Lorentz-Lorentz Equation [13] as follows:

$$R_m = \left(\frac{n_0^2 - 1}{n_0^2 + 2} \right) V_m \quad (\text{IV.6})$$

The molar polarizability (α_m) of a compound is related to molar refraction [13, 14] and by using the Lorentz-Lorentz relation given by:

$$\alpha_m = \frac{3}{4\pi N_A} R_m \quad (\text{IV.7})$$

where n_0 is the linear refractive index and V_m is the molar volume, where N_A is the Avogadro's number with α_m in (\AA^3), Eq. (IV.7) can be transformed into:

$$\alpha_m = \frac{R_m}{2.52} \quad (\text{IV.8})$$

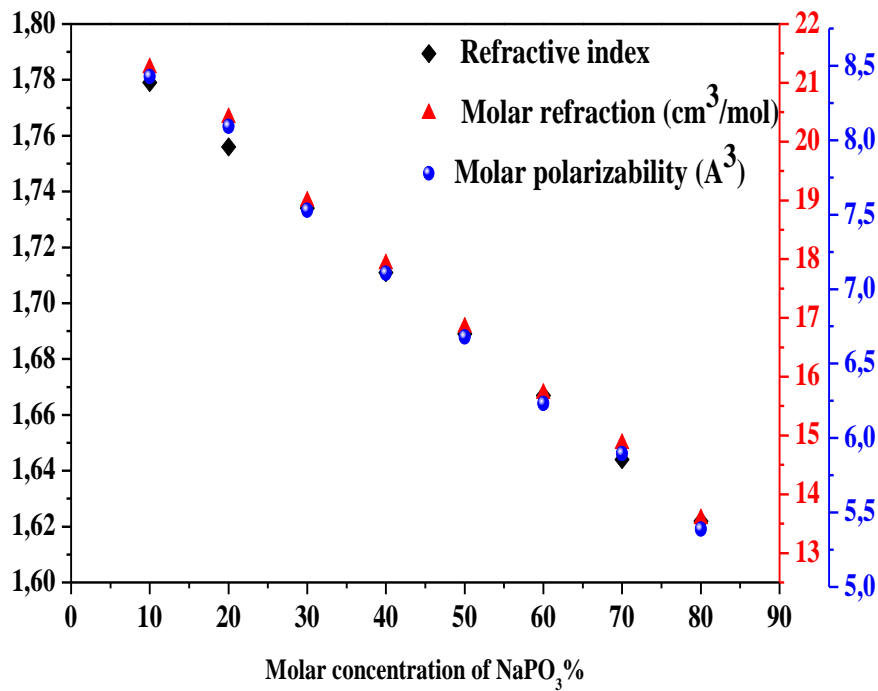


Figure IV.9: Variation of n , R_m and α_m against NaPO_3 % content of AN glasses.

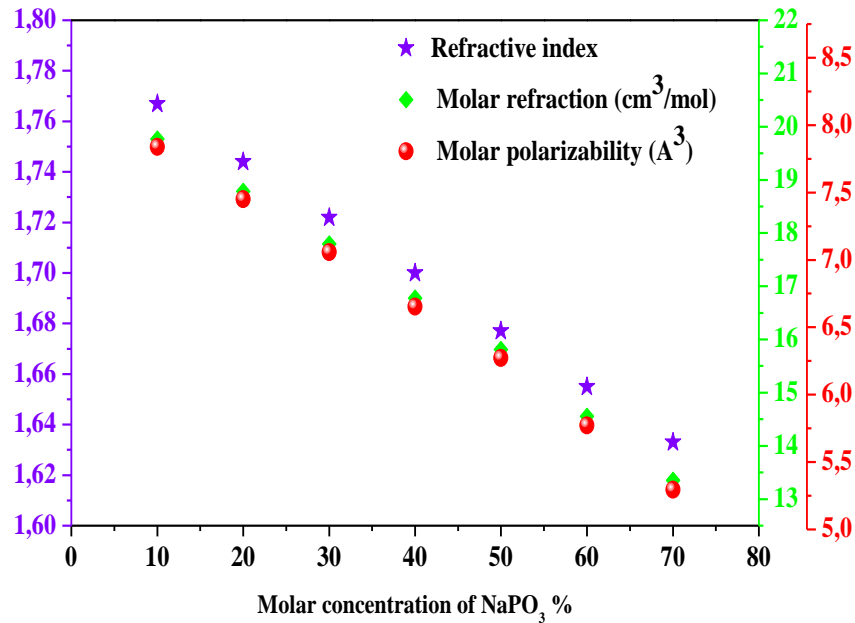


Figure IV.10: Variation of n , R_m and α_m against NaPO_3 % content of BN glasses.

The refractive index (n_0) of the $(90-x)\text{Sb}_2\text{O}_3-10\text{WO}_3-x\text{NaPO}_3$ and $(80-x)\text{Sb}_2\text{O}_3-20\text{WO}_3-x\text{NaPO}_3$ glass systems ranges from 1.779 to 1.622 and 1.767 to 1.633, respectively. Molar refraction's (R_m) and the molar polarizability (α_m) for AN glasses range from 21.253-13.586 cm^3/mol and from 8.428×10^{-24} - 5.388×10^{-24} cm^3 , respectively. Well, in BN glasses, molar refraction (R_m) and the molar polarizability (α_m) range from 19.767-13.352 cm^3/mol and from 7.839×10^{-24} - 5.295×10^{-24} cm^3 , respectively. All of these parameters decrease when the concentration of NaPO_3 rises, as seen in [figs IV.9](#) and [IV.10](#). This is due to the fact that P^{5+} ions have lower polarizability than Sb^{3+} ions.

Another significant application of the Lorentz-Lorentz equation and refractive index is in the prediction of metallic or non-metallic behavior of solids, based on the ratio of $R_m: V_m$ explained by Dimitrov and Komatsu [15]. According to the Herzfeld theory of metallization, if $(R_m/V_m) < 1$, the material is transformed into non-metal and if $(R_m/V_m) > 1$, the material is changed into metal.

As a result, the metallization criterion (M) is given by the following equation [15]:

$$M = 1 - \frac{R_m}{V_m} \quad (\text{IV.9})$$

The metallization criterion (M) of AN and BN glasses is in the range of 0.581-0.648 and 0.586-0.643, respectively (as shown in [table IV.2](#) and [table IV.3](#)). The positive values of M suggest that these glasses exhibit non-metallic behavior. From these results, we can say that our obtained glasses are useful in non-linear optical applications. Because the metallization criterion of oxide glasses with excellent optical non-linearity ranges from 0.30 to 0.45 [16]. In other words, larger metallization criterion values indicate a large band gap between the band of valence and the band of conduction [17].

The optical transmission coefficient (T) and the reflection loss (R_L) from the glass surface are obtained using Fresnel's formula according to the refractive index (n_0) as reported in [18]:

$$R_L = \left(\frac{n_0 - 1}{n_0 + 1} \right)^2 \quad (\text{IV.10})$$

$$T = \frac{2n}{n^2 + 1} \quad (\text{IV.11})$$

When the quantity of NaPO_3 rises, T increases and R_L drops ([tables IV.2](#) and [IV.3](#)) in SWN glasses. That is, due to the addition of more P^{+5} ions to the glass series, the increment of T makes the glasses more transparent in the UV-Vis region [19, 20].

Electronic oxide polarizability ($\alpha_{O^{2-}}$) of examined glass samples is measured by using n_0 and given by [9]:

$$\alpha_{O^{2-}} = (\alpha_m - \sum \alpha_{cat}) / N_{O^{2-}} \quad (\text{IV.12})$$

where α_m is the molar polarizability of the sample, $\sum \alpha_{cat}$ indicates molar cation polarizability and $N_{O^{2-}}$ represents the number of oxide ions. For the ternary glass system $x\text{A}_l\text{O}_m - y\text{B}_n\text{O}_o - z\text{C}_p\text{O}_q$, the ($\sum \alpha_{cat}$) and ($N_{O^{2-}}$) can be found as

$$\sum \alpha_{cat} = x\alpha_A + y\alpha_B + z\alpha_C \quad (\text{IV.13})$$

and

$$N_{O^{2-}} = xm + yo + zq \quad (\text{IV.14})$$

Here $\alpha_A = \alpha_{Sb^{+3}} = 1.111$, $\alpha_B = \alpha_{W^{+6}} = 0.147$ and $\alpha_C = \alpha_{P^{+5}} = 0.021 \text{ \AA}^3$ values [21, 22].

Duffy and Ingram [23] established optical basicity as a criterion for determining the acid-base characteristics of glass in terms of the electron density transported by oxygen. It measures the average electron donation capacity of oxide (II) species in the medium after

component cations have polarized their electron charge clouds. The optical basicity (Λ) [24, 25] of glass can be obtained by using $\alpha_{O^{2-}}$ with the following relation:

$$\Lambda = 1.67 \left(1 - \frac{1}{\alpha_{O^{2-}}} \right) \quad (\text{IV.15})$$

The strength with which an ion attracts electrons in oxide glasses is known as electronegativity (χ). If the ions' electronegativity is stronger, it will attract the linked oxide ions more strongly, resulting in tight ion network bonding. As a result, the material acquires covalent properties. Electronegativity (χ) and electronic susceptibility (χ_e) [24, 26] are calculated using the following relations:

$$\chi = \left(\frac{\Lambda}{0.75} + 0.25 \right) \quad (\text{IV.16})$$

$$\chi_e = \left(\frac{n_0^2 - 1}{4\pi} \right) \quad (\text{IV.17})$$

The theoretical (ideal) optical basicity (Λ_{th}) is calculated according to the expression [9, 15]

$$\Lambda_{th} = \sum x_i \Lambda_i \quad (\text{IV.18})$$

For SWN glasses, Eq. (IV.18) can be transformed into:

$$\Lambda_{th} = x_{Sb_2O_3} \Lambda_{Sb_2O_3} + x_{WO_3} \Lambda_{WO_3} + x_{NaPO_3} \Lambda_{NaPO_3} \quad (\text{IV.19})$$

where $x_{(Sb_2O_3)}$, $x_{(WO_3)}$ and $x_{(NaPO_3)}$ are the equivalent fractions based on the proportion of oxygen, and $\Lambda_{(Sb_2O_3)} = 1.18$, $\Lambda_{(WO_3)} = 1.045$ and $\Lambda_{(NaPO_3)} = 0.47$ are the basicity of each oxide [27].

The electronic oxide polarizability (χ_e) and the electronegativity (χ) of glasses have been found to change as the quantity of $NaPO_3$ rises, and the theoretical optical basicity (Λ_{th}) of glasses has also been examined (in table IV.2 and table IV.3). Due to the decreasing quantity of (NBO) in the glass system, low values of n_0 , Λ_{th} and polarizability are anticipated [28]. This means that the oxide ions' ability to transfer electrons to nearby cations is reduced. The result is consistent with our samples' metallization criterion (M) values.

The third order nonlinear susceptibility $\chi^{(3)}$ can be calculated from the E_g values as follows [29]:

$$\chi^{(3)} = \frac{(1.4 \times 10^{-11})}{((E_g - 1.96)(E_g - 1.31)(E_g - 0.65))} \quad (\text{IV.20})$$

Tables IV.2 and IV.3 illustrate that the values of $\chi^{(3)}$ are greater than those of pure SiO₂ glass (2.8×10^{-12} e.s.u), indicating that all of the SWN samples tested are suitable materials for nonlinear optical devices with rises in antimony oxide. In addition, it is established that raising NaPO₃ concentration increases the optical energy gap (E_g), leading to a decrease in the $\chi^{(3)}$, and vice versa with the addition of Sb₂O₃ [29].

IV.3 Structural properties

IV.3.1 Number of network bonds (n_b) and average cross-link density (\bar{n}_c)

We calculated the \bar{n}_c and n_b of our AN and BN glasses by using the formula in refs [30-32]. The mean cross-link density, \bar{n}_c , of AN and BN glasses rose from 1.37 to 2.84 and 1.56 to 2.89, respectively, while the number of links per unit volume, n_b , of AN and BN glasses increased from 41,65 to $73.35 \times 10^{21} \text{cm}^{-3}$ and 47,96 to $80.51 \times 10^{21} \text{cm}^{-3}$, respectively. Since antimony oxide is substituted by glass former NaPO₃, which has a higher cationic coordination number than Sb₂O₃ ($n_{f(\text{NaPO}_3)} = 4$) and therefore creates a BO site, the network has become stiffer and more linked in SWN glasses. With the increase in NaPO₃ concentration, both \bar{n}_c and n_b values improve enhancement (see table IV.4).

Table IV.4: Values of average cross-link density (\bar{n}_c) and number of bonds per unit volume (n_b) of glasses in the AN and BN glass samples.

S.n°	\bar{n}_c	$n_b(\times 10^{21} \text{cm}^{-3})$	S.n°	\bar{n}_c	$n_b(\times 10^{21} \text{cm}^{-3})$
AN10	1,37	41,56	BN10	1,56	47,96
AN20	1,58	44,77	BN20	1,78	51,96
AN30	1,79	49,58	BN30	2,00	56,27
AN40	2,00	53,93	BN40	2,22	61,03
AN50	2,21	58,72	BN50	2,44	66,01
AN60	2,42	64,17	BN60	2,67	72,89
AN70	2,63	68,98	BN70	2,89	80,51
AN80	2,84	73,35			

IV.3.2 Average interionic separations(d_{P-P}), the single bond strength (B_{M-O})

The average ($\langle d_{P-P} \rangle$) interionic separations can be calculated as follows [33]:

$$d_{P-P} = \left(\frac{V_m}{N_A \times X_P} \right)^{1/3} \quad (\text{IV.21})$$

where N_A , V_m and X are the Avogadro's number, molar volume and molar fraction of phosphate, respectively.

Table IV.6 illustrate that with an increment in NaPO_3 , the average phosphate-phosphate separations of AN and BN glasses decreased from 0,186 to 0,112 nm and from 0,194 to 0,119 nm, respectively. This led to the lower ionic radius and molar volume of phosphate, which resulted in an applied decrease in the density. As a result, the glass network exhibits an increasing tendency to contract, implying that the addition of NaPO_3 causes the lattice to compress significantly.

Based on their dissociation energy E_d , which may be defined (E_d) as the energy necessary to break the oxide into its component gaseous atoms, Sun et al. [34] presented extensive data on the strength of the B_{M-O} single bond for a variety of simple oxides.

Table IV.5: The value of coordination number, CN, single bond strength, B_{M-O} of Sb_2O_3 , WO_3 and P_2O_5 oxide [34-36].

Oxides	CN	B_{M-O} (KJ/mol)
Sb_2O_3	3	228.9
WO_3	6	672
P_2O_5	4	464

A method for determining the single bond strength B_{M-O} has been put out by Dimitrov and Komatsu [22]. For example, the equation for the $(90-x)\text{Sb}_2\text{O}_3-10\text{WO}_3-x\text{NaPO}_3$ ternary system might be proposed

$$B_{M-O} = (90 - x)B_{Sb-O} + 10B_{W-O} + xB_{P-O} \quad (\text{IV.22})$$

where x is the molar fraction of sample glasses and B_{Sb-O} , B_{W-O} and B_{P-O} are the single bond strengths of Sb-O, W-O and P-O bonds in SbO_3 , WO_6 and PO_4 units, respectively.

SWN glasses (B_{M-O}) exhibit a tendency toward increasing single-bond strength with increasing P^{5+} concentration. In reality, the development of linear chains of PO_4 units makes it possible for the substitution of Sb by P in the glass network to produce a significant quantity of BO oxygen. The development of P-O-W units, which have greater ionicity, may be the cause of this stiffness.

According to Gael and al [37], the solid state in the binary system $NaPO_3-WO_3$ and at low concentration of WO_3 , NMR and Raman structural investigations have shown that the sole tungsten oxide entities are octahedral and serve as covalent chain intermediates (WO_6). Low WO_3 concentrations allow isolated WO_6 to be incorporated into phosphate chains, generating strong P-O-W connections and improving the host matrix's cross-linking.

The calculated values of average phosphore-phosphore separation and single bond B_{M-O} of AN and BN glasses with augmentation of $NaPO_3$ are provided in table IV.6.

Table IV.6: Average phosphore-phosphore separation, single bond B_{M-O} , $\alpha(OH)$ and OH content (ppm) of AN and BN glasses.

S.n°	d_{P-P} (nm)	B_{M-O} (KJ/mol)	$\alpha(OH)$ (cm^{-1})	OH Content (ppm)	S.n°	d_{P-P} (nm)	B_{M-O} (KJ/mol)	$\alpha(OH)$ (cm^{-1})	OH content (ppm)
AN10	0,186	296,72	2,108	63,241	BN10	0,194	341,03	1,691	50,725
AN20	0,150	320,23	1,961	58,844	BN20	0,157	364,54	1,445	43,345
AN30	0,135	343,74	2,625	78,752	BN30	0,140	388,05	1,572	47,174
AN40	0,126	367,25	2,701	81,022	BN40	0,130	411,56	1,296	38,870
AN50	0,120	390,76	2,420	72,587	BN50	0,124	435,07	1,276	38,276
AN60	0,116	414,27	1,902	57,059	BN60	0,121	458,58	1,773	53,181
AN70	0,112	437,78	2,895	86,850	BN70	0,119	482,09	2,392	71,773
AN80	0,112	461,29	4,803	144,076					

IV.3.3 IR and ATR spectroscopy

The ATR spectra of the raw powder used in glass preparation is shown in [fig IV.11](#). From looking at [fig IV.11\(a\)](#), we see that there are many bands of senarmonite and valentinite combined together in the raw powder of Sb_2O_3 used to make our glasses. [Fig IV.11\(a\)](#) displays several small bands at 525, and 466 cm^{-1} due to symmetric and asymmetric bending modes of valentinite form of SbO_3 trigonal pyramids, respectively. The two band at 689, 624 cm^{-1} are led to symmetric and asymmetric stretching vibration modes of valentinite form of SbO_3 unit. It exhibits a small peak at 872 cm^{-1} corresponding to Sb-O stretching vibrations of the senarmonite form of SbO_3 . The small peak at 748 cm^{-1} corresponds to the symmetric stretching vibration mode of the senarmonite form of SbO_3 . This affirms once more that the starting material of Sb_2O_3 contains both forms of the senarmonite and valentinite form of SbO_3 unit [38, 39].

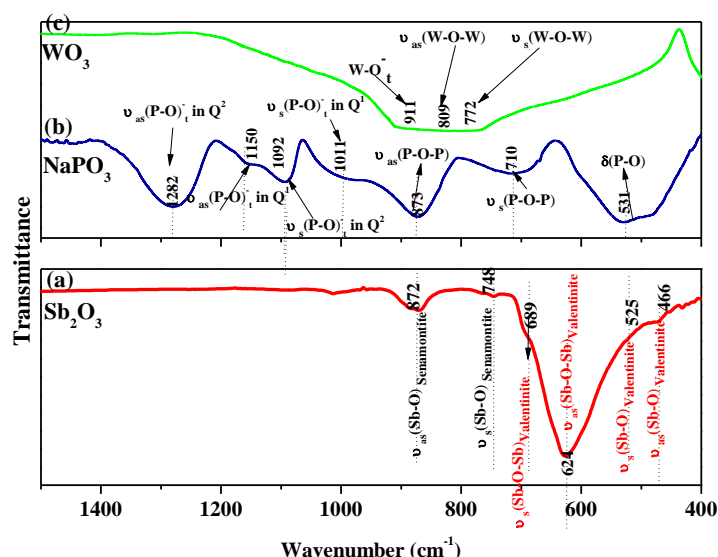


Figure IV.11: ATR transmittance spectrum of the raw materials ((a) Sb_2O_3 , (b) NaPO_3 and (c) WO_3) in the region 1500-400 cm^{-1} .

IV.3.3.1 IR spectra (1,5-8 μm)

The techniques used to characterize the glass structure of our glasses in the (90-x) Sb_2O_3 -10 WO_3 -x NaPO_3 and (80-x) Sb_2O_3 -20 WO_3 -x NaPO_3 ternary systems have proven to be very complementary and have made it possible to obtain precise information on the structural changes according to the compositions. The infrared spectra of AN and BN glasses is illustrated in the region of 1.5-8 μm and shown in [figs IV.12](#) and [IV.13](#). These glasses are

transparent at limit 7 μm , which is characteristic of antimony glasses. The IR transmission spectra illustrates three major regions. The first wide band is around 3000cm^{-1} ($3.33\mu\text{m}$), and is due to the hydroxyl (OH) groups. These broad and strong absorption bands indicate the presence of the amount of water in the SWN (AN and BN) glasses. The second band around 2500cm^{-1} ($4\mu\text{m}$) is due to a harmonic of the fundamental vibration of the P-O bonds in the PO_4 tetrahedra. The third group of bands, which occurs at 1900cm^{-1} ($5.2\mu\text{m}$) is due to the fundamental vibration of Si-O bands, which stems from the silica crucible used during the melting processes. The fourth group of bands at 1492cm^{-1} ($6.7\mu\text{m}$) is attributed to the contributions from Sb-O bond vibration. We observed the same samples small transmission disturbance at $4.2\mu\text{m}$, which is due to the CO_2 present in the measuring cell [39, 40].

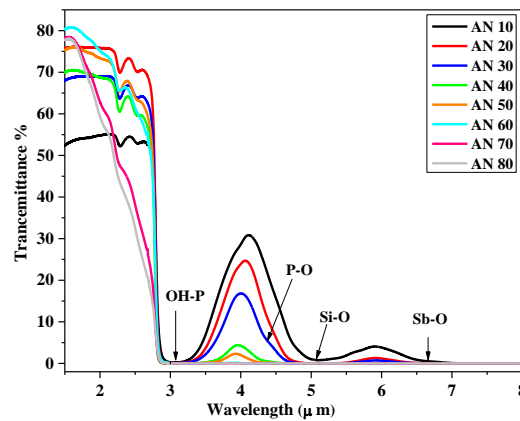


Figure IV.12: IR transmittance spectra of AN glasses in the region 1,5-8 μm .

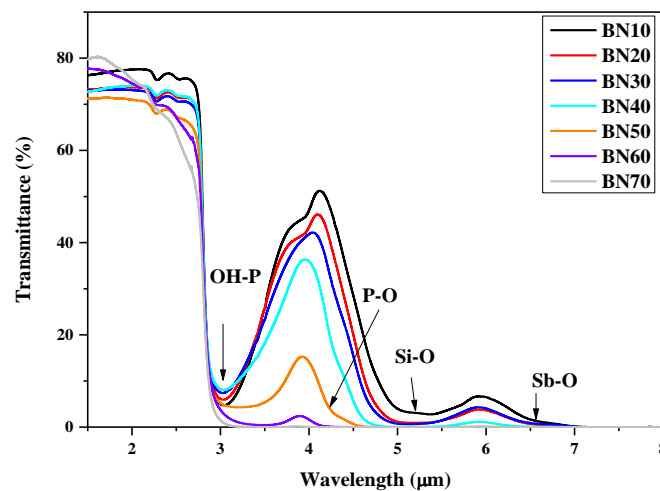


Figure IV.13: IR transmittance spectra of BN glasses in the region 1,5-8 μm .

The hydroxyl group (OH) concentration of glasses may be determined using the IR spectra. The approach provided by Ebendroff-Heidepriem et al. [41] can be used to determine the OH content of the glasses. Using the following relationship, the absorption coefficient α at 3259cm^{-1} ($3,068\mu\text{m}$) in SWN glasses can be used to determine the OH concentration in our glass.

$$\alpha_{OH} = \frac{1}{d} \text{Ln} \left(\frac{T_0}{T} \right) \quad (\text{IV.23})$$

where T_0 is the highest transmission at $\sim 1.5 \mu\text{m}$, T is the transmission of the glass at 3259cm^{-1} ($3,068\mu\text{m}$) and d is the thickness of the glass samples (cm). The OH content can be calculated using the above relation and according to the following α_{OH} [41].

$$\text{OH content(ppm)} = 30 \times \alpha_{OH}(\text{cm}^{-1}) \quad (\text{IV.24})$$

It is widely known that the presence of a significant quantity of OH content in the glasses increases non-radiative losses, lowering the quantum efficiency of the glass materials. The presence of higher OH content is indicated by the high intensity of the OH band found on SWN glasses. The OH content is calculated using the coefficient of OH vibration $\alpha_{(\text{OH})}$ at 3000cm^{-1} ($3,33\mu\text{m}$). Table IV.6 enlisted the corresponding OH content of several of the samples investigated. The concentration of OH in SWN glasses rises as the concentration of NaPO_3 increases. These results are similar to those of fluorophosphate [42] and calcium metaphosphate [43]. Consequently, these OH groups might have come from both the raw material H_2NaPO_4 or/and the environment (phosphor materiaux hygroscopic). Because these glasses have a relatively high OH content, they are unsuitable for efficient lasers with high non-radiative losses.

IV.3.3.2 ATR spectra ($1600\text{-}400\text{cm}^{-1}$)

ATR spectra from $400\text{-}1600 \text{ cm}^{-1}$ are presented in figs IV.14 and IV.15 (the assignment wavenumber bands illustrated in table IV.7). The first weak absorption bands at $508\text{-}544 \text{ cm}^{-1}$ and $550\text{-}583 \text{ cm}^{-1}$ correspond to deformation vibration modes of O–P–O in Q^2 tetrahedra and asymmetric stretching of Sb–O from Sb_2O_3 , respectively [44-46]. The second absorption band around $605\text{-}635\text{cm}^{-1}$ is due to the symmetric and asymmetric stretching vibration mode of the Sb–O–Sb bond of Sb_2O_3 , or assigned to the asymmetrical stretching P–O–Sb bridge of SbPO_4 [45-48]. The third band at $714\text{-}730 \text{ cm}^{-1}$ is assigned to symmetrical

stretching vibrations of P–O–P bridges or P–O–M linkages (M=Sb or W), which increase with increasing NaPO₃ content and also may be due to symmetric stretching vibrations of the W–O–W linkages [45, 47]. The fourth peak around 830-871 cm⁻¹ is attributed to the asymmetric stretching vibrations of the W–O–W linkages mode of WO₄ units, and asymmetric stretching of the P–O–P bridge [48]. The intense band at 900-967 cm⁻¹ is due to stretching vibration of W-O and W=O in structural units WO₄ and WO₆. The maximum phono energy of these glasses is defined by the highest intensity peak at 915 cm⁻¹, which is a significant finding that reveals the predominance of W–O bonds and therefore the glass structure [45, 48]. The last band at 1058-1083 cm⁻¹ is assigned to symmetrical stretching vibrations of the PO₂⁻ terminal group in Q² tetrahedra. The band at 1107-1194 cm⁻¹ is assigned to asymmetrical stretching vibrations of the PO₃²⁻ terminal group (tetrahedral mode Q¹). The band at 1240-1360 cm⁻¹ is assigned to asymmetrical stretching vibrations of the PO₂⁻ terminal group (tetrahedral mode Q²) [45].

The existence of the strong P–O–W bonds in SWN glasses probably leads to the interaction between highly polarizing ions: PO₃²⁻ tetrahedral anions and W⁶⁺ or W⁵⁺ cations, which increases the connectivity of the glass network [40].

Table IV.7: Assignment of the ATR transmittance bands of AN and BN glasses.

Wavenumber (cm ⁻¹)	Vibrational mode
508-544	δ (O–P–O) in Q ² tetrahedra
550-583	ν _{as} (Sb–O) valentinite from Sb ₂ O ₃
605-635	ν _s (Sb–O–Sb) valentinite and ν _{as} (Sb–O–Sb) valentinite bonds of Sb ₂ O ₃ or Sb–O–P bridge of SbPO ₄
714-730	ν _s (P–O–P) in Q ² mode or P–O–M linkage or ν _s (W–O–W) linkage
830-871	ν _{as} (W–O–W) and ν _{as} (P–O–P)
900-967	stretching vibration of W–O ⁻ and W=O in structural units WO ₄ and WO ₆
1058-1083	ν _s (PO ₂ ⁻) in Q ² tetrahedra ((P–O) ⁻ or (P=O))
1107-1194	ν _{as} (PO ₃ ²⁻) in Q ¹ (tetrahedral) ((P–O) ⁻ or (P=O))
1240-1360	ν _{as} (PO ₂ ⁻) in Q ² tetrahedral ((P–O) ⁻ or (P=O))

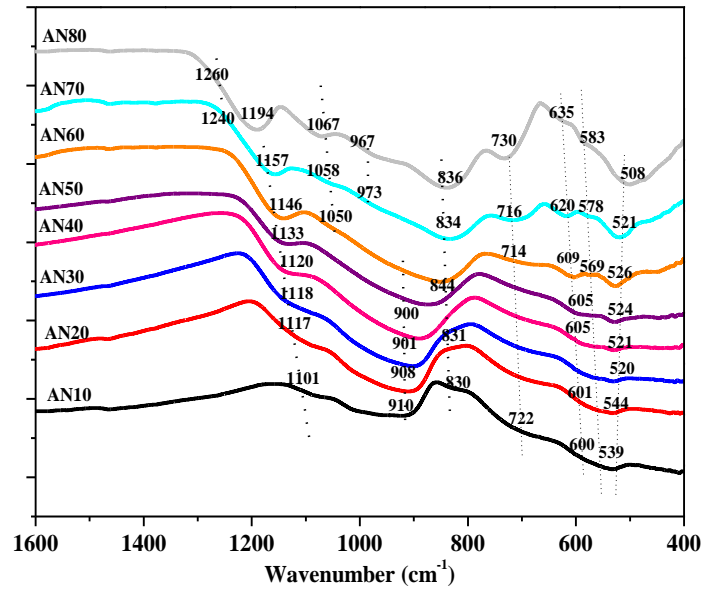


Figure IV.14: ATR absorption spectra of AN glasses in the region (1600-400cm⁻¹).

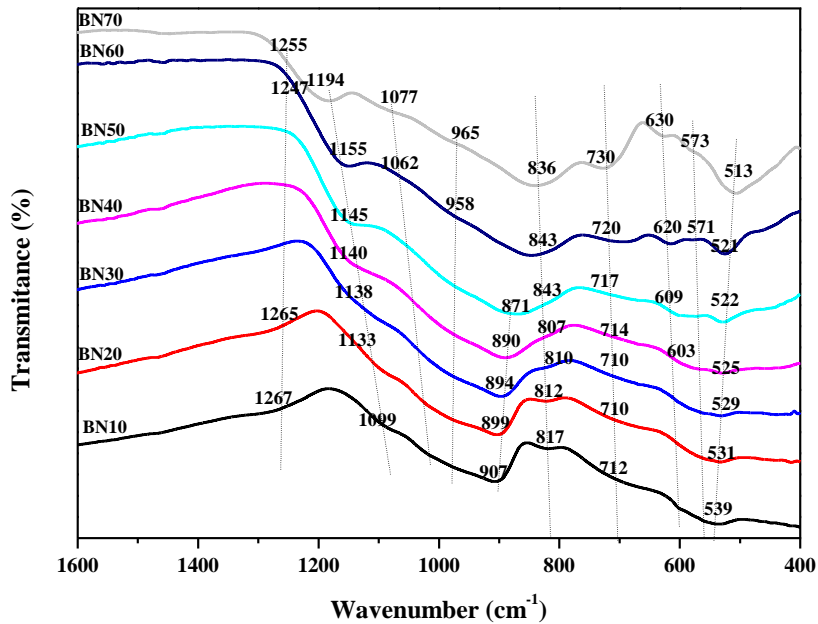


Figure IV.15: ATR absorption spectra of BN glasses in the region (1600-400cm⁻¹).

IV.3.4 Raman spectroscopy

The Raman spectra of the vitreous samples of system $(90-x) \text{Sb}_2\text{O}_3\text{-}10\text{WO}_3\text{-}x\text{NaPO}_3$ with x varying from 10 to 80, is shown in [fig IV.16](#).

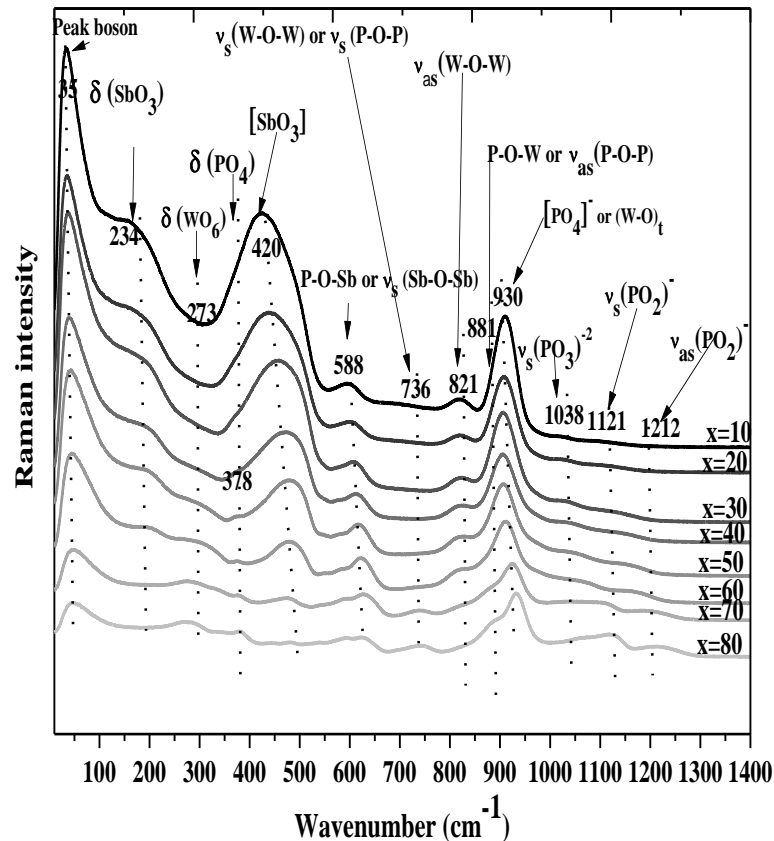


Figure IV.16: Raman absorption spectra of system $(90-x) \text{Sb}_2\text{O}_3\text{-}10\text{WO}_3\text{-}x\text{NaPO}_3$ with x varying from 10 to 80 glasses.

The attributions of the bands of the observed Raman absorption spectra are illustrated in [table IV.8](#). It is clear that it comprises a significant number of elemental absorption bands that are difficult to distinguish. As a result, we can only make de-convoluted peak Raman spectra of our samples (see [fig IV.17](#)).

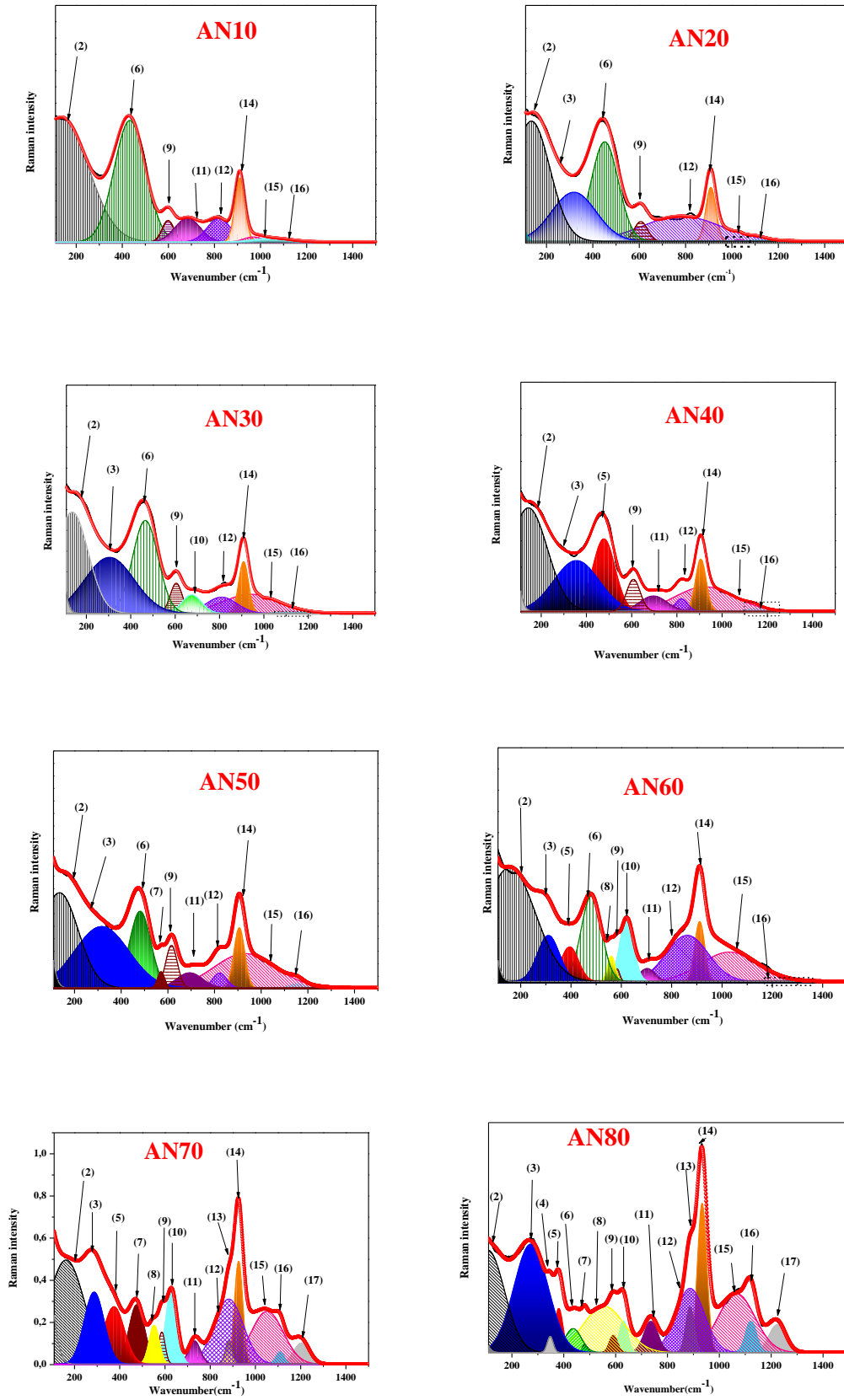


Figure IV.17: Deconvolution analysis of the Raman spectra of AN glasses.

- i. The very strong peak at around 45-57 cm^{-1} is identified as the Boson peak, a feature characteristic of the vitreous state. In general, we can accept that the origin of the Boson peak can be related to long-range spatial correlations in the structure. This peak shifts to a higher wavenumber when we add NaPO_3 to the glass network (the atom of Sb with the highest molecular weight is replaced by the lowest atom of P).
- ii. The two-weak band near 230 and 330 cm^{-1} leads to the deformation of WO_6 octahedra, Sb_2O_3 or PO_4 tetrahedra. It is increased with the increase of NaPO_3 [37, 45, 46].
- iii. The large band near 440 cm^{-1} is caused by the $\nu_{\text{sym}}(\text{Sb}_2\text{O}_3)$ of the SbO_3 pyramidal unit [46] or by the bending vibration of the PO_4 structural unit, and it decreases as the NaPO_3 concentration increases [49].
- iv. The symmetric and asymmetric stretching vibration modes of the Sb-O-Sb bond of Sb_2O_3 or P-O-Sb linkage are responsible for the two weak broads at 600 and 680 cm^{-1} . It rises when the concentration of NaPO_3 rises [47, 50, 51].
- v. With increasing NaPO_3 (mole%), the intensity of two weak shoulders closed at 330 and 280 cm^{-1} rises, with the first band attributable to the bending vibration of WO_6 and the second band to the bending vibration of the $(\text{W-O})_t$ band in WO_6 [52, 53].
- vi. The asymmetric and symmetric stretching vibrations of the W-O-W linkage are responsible for the characteristics near 820 and 720 cm^{-1} , respectively. The bands near 820 cm^{-1} decrease in intensity with increasing NaPO_3 content, while the strong band at 930 cm^{-1} is caused by $(\text{W-O})_t$ or (W=O) terminal bonds in WO_6 octahedra [37, 45, 52, 53].
- vii. Two shoulders near 880 and 730 cm^{-1} , on the other hand, are caused by stretching vibration of the $(\text{P-O})_t$ terminal bond in (PO_4) tetrahedra linked with WO_6 and symmetric stretching vibration of P-O-P bridges or P-O-W stretching, respectively. It is exclusively seen in AN70 and AN80 samples, and gets stronger with NaPO_3 .
- viii. It has three weak bands centered at about 1240, 1160, and 1010 cm^{-1} , which correspond to the asymmetric and symmetric stretching vibration of the terminal $(\text{P-O})_t$ bond in Q^2 and the symmetric stretching vibrations of the terminal $(\text{P-O})_t$ bond in Q^1 tetrahedra, respectively [37, 45, 49].

A progressive reduction in the degree of disorder in the glass network is indicated by a rise in the concentration of the Q^2 tetrahedra (owing to the symmetric vibrations of PO_2) and P-O-P modes with a simultaneous slight reduction in the Q^1 bands. The structure of the lattice can be estimated since Q^1 is focused on the extremities of the linear chains, whereas Q^2

produces numerous linear chains in the interior of the glass network and the number of Q^2 increases with the addition of NaPO_3 (mole percent).

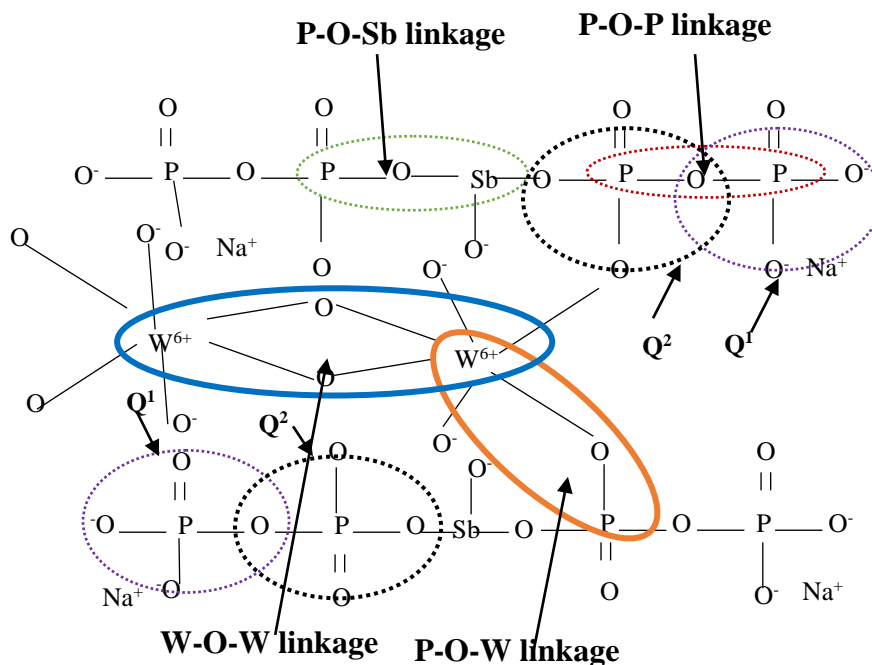


Figure IV.18: Suggested of structural of SWN glasses with high concentration of NaPO_3 .

The bond about 700 cm^{-1} did not appear for a NaPO_3 concentration of less than 50% mol, but then it noted a growth in this band for AN50, AN60, AN70 and AN80 samples. This band lead to the connection of the ν_s (W-O-W) and ν_s (P-O-P) in Q^2 mode or P-O-W bridging. The P-O-W bridging links are formed, which strengthens the glass network and makes the glass structure more compact. The formation of the P-O-W linkage is expected because both W and P atoms have comparable electronegativity and can therefore substitute for each other. This strengthens in the glass network, implying a link between the network and results in the growth of T_g values of SWN glasses, which is supported by the rise in viscosity of the viscous mixture during cooling. As a result, the amount of NBO in our glasses is extremely low, and this is the reason why the glass is stiff and connected.

With the addition of NaPO_3 , we include a rise in the bridging P-O-M bond while the number of $(\text{W-O})_t$ bonds is reduced.

In conclusion, the stiff vitreous of the SWN samples is responsible for the formation of P-O-P, W-O-W, P-O-W, and P-O-Sb bonds, etc. As a result of the increased of NaPO₃ rising the glass transition temperature and the NBO atoms are reduced (see [fig IV.18](#)).

Table IV.8: Assignment of the Raman absorption bands (10-1400 cm⁻¹) of AN glass.

Bands n°	Wavenumber (cm ⁻¹)	Vibrational mode
1	35-50	Peak Boson
2	190-234	δ (SbO ₃) _(Tr)
3	270-283	δ (WO ₆) _(Oh) or bending vibration of phosphate polyhedra
4	310-330	O—P—O bending.
5	335-380	δ (PO ₄) _(Td)
6	420-440	Vib [SbO ₃] unit
7	440-480	Vib [SbO ₃] unit
8	500-530	ν_s (Sb-O-Sb) and δ_{as} (PO ₄)
9	530-590	δ (P-O-P)
10	623-680	ν_{as} (Sb-O-Sb)or Sb-O-P bond
11	710-730	ν_s (W-O-W) and ν_s (P-O-P)in Q ² mode or P-O-W
12	820-870	ν_{as} (W-O-W)
13	888-890	ν_{as} (P-O-P) in Q ¹ mode or P-O-W linkage
14	901-937	ν (P-O) _t in PO ₄ ⁻ withWO ₆ or ν (W-O) _t in WO ₆ units
15	1058-1083	ν_s (PO) _t in Q ¹ ((P-O) ⁻ or (P=O))
16	1160	ν_s (P-O) _t in Q ² ((P-O) ⁻ or (P=O))
17	1270	ν_{as} (P-O) _t in Q ² ((P-O) ⁻ or (P=O))

IV.4 Conclusion

The investigation revealed that the density, molar volume, energy of Urbach, refractive index, molar refractive, molar polarizability, oxide ion polarizability, and optical basicity decreases with the amount of P^{5+} ions concentration. While the energy of band gap, metallization criterion, cross-link density, the number of links per unit volume and the third non-linear susceptibility ($\chi^{(3)}$) increases with the increasing concentration of P^{5+} ions in the glass network. The high amount of Sb_2O_3 , the high refractive index, high polarizability, and good optical transparency of the SWN glass system present the glass potential in non-linear optical applications. The investigation revealed that the concentration of P^{5+} ions decreases the density, molar volume, energy of Urbach, refractive index, molar refractive, molar polarizability, oxide ion polarizability, and optical basicity. While the energy of the band gap, metallization criterion, crosslink density, number of links per unit volume, and third non-linear susceptibility ($\chi^{(3)}$) increases as the concentration of P^{5+} ions in the glass network increases, the high amount of Sb_2O_3 , the high refractive index, high polarizability, and good optical transparency of the SWN glass system, present the glass potential in non-linear optical applications.

The rise of \bar{n}_c and n_b values as $NaPO_3$ increases indicates the formation of the bridging oxygen linkage, which might have come from the P-O-W and P-O-P linkages, and therefore enhances the rigidity and viscosity of the glass network, making these materials good candidates for fiber optical devices.

In other words, the introduction of $NaPO_3$ into the SWN glass leads to the formation of more linear chains, which reduces the number of NBOs and leads to an increase in the structural compactness of these glasses. The structural studies of SWN glass supported this hypothesis by the formation of phosphate obeyed Q^2 with the modes of Q^1 and P-O-W linkage with the addition of $NaPO_3$.

By comparing the previous two series of AN and BN samples, we can say that they exhibit the same behavior in all the studied properties, but there are some differences that can be summarized as follows:

For non-linear optical applications, we suggest the sample AN10, which has the highest value of the $\chi^{(3)}$ (13,09 e.s.u), which is more than four times the $\chi^{(3)}$ value of pure SiO_2 and has the largest value of the refractive index, etc.

On the other hand, if we want to use this new series of antimony glasses in optical fiber applications, it is preferable to choose a BN series that has the highest value of viscosity, rigidity and high resistance against devitrification.

In general, these new glasses showed good behavior for producing optical fibers and nonlinear optical applications.

References

1. Mott, N.F. and E.A. Davis, *Electronic processes in non-crystalline materials* 2012: Oxford university press.
2. Scholze, H., *Nature and structure of glass*, in *Glass* 1991, Springer. p. 3-155. DOI: [10.1007/978-1-4613-9069-5_2](https://doi.org/10.1007/978-1-4613-9069-5_2)
3. Poirier, E. and A. Dailly, Investigation of the hydrogen state in IRMOF-1 from measurements and modeling of adsorption isotherms at high gas densities. *The Journal of Physical Chemistry C*, 2008. 112(33): p. 13047-13052. <https://doi.org/10.1021/jp711709r>
4. Urbach, F., The long-wavelength edge of photographic sensitivity and of the electronic absorption of solids. *Physical Review*, 1953. 92(5): p. 1324. DOI: [10.1103/PhysRev.92.1324](https://doi.org/10.1103/PhysRev.92.1324)
5. Azlan, M., et al., Polarizability and optical basicity of Er³⁺ ions doped tellurite based glasses. *Chalcogenide Lett*, 2014. 11(7): p. 319.
6. Hammad, A.H., et al., Investigation of some structural and optical properties of lithium sodium fluoroborate glasses containing cuprous oxide. *Measurement*, 2018. 116: p. 170-177. <https://doi.org/10.1016/j.measurement.2017.11.012>
7. Elkhoshkhany, N., et al., Properties of tellurite glass doped with ytterbium oxide for optical applications. *Journal of Materials Science: Materials in Electronics*, 2019. 30(7): p. 6963-6976. DOI :[10.1007/s10854-019-01013-9](https://doi.org/10.1007/s10854-019-01013-9)
8. Tasheva, T. and V. Dimitrov, Electronic polarizability, optical basicity and chemical bonding of zinc oxide-barium oxide-vanadium oxide glasses. *Bulg. Chem. Commun.*, 2017. 49(F): p. 76-83.
9. Vesselin, D. and T. Komatsu, Classification of simple oxides: a polarizability approach. *Journal of Solid State Chemistry*, 2002. 163: p. 100-112. <https://doi.org/10.1006/jssc.2001.9378>
10. Umar, S., et al., Physical, structural and optical properties of erbium doped rice husk silicate borotellurite (Er-doped RHSBT) glasses. *Journal of Non-Crystalline Solids*, 2017. 472: p. 31-38. <https://doi.org/10.1016/j.jnoncrysol.2017.07.013>
11. Siripuram, R., P.S.G. Rao, and S. Sripada, Influence of nano crystalline behavior of Nb₂O₅-Sb₂O₃-TeO₂ glass ceramics on structural and thermal studies. *Materials Today: Proceedings*, 2021. 46: p. 6344-6357. <https://doi.org/10.1016/j.matpr.2020.05.818>

12. Hager, I., Optical properties of lithium barium haloborate glasses. *Journal of Physics and Chemistry of Solids*, 2009. 70(1): p. 210-217. DOI : [10.1016/j.jpics.2008.10.007](https://doi.org/10.1016/j.jpics.2008.10.007)
13. Bhatia, O., basicity and polarizability of Nd³⁺-doped bismuth borate glasses, *New J. Glass Ceram*, (5): p. 44. DOI :[10.4236/njgc.2015.53006](https://doi.org/10.4236/njgc.2015.53006)
14. Berwal, N., et al., Physical, structural and optical characterization of silicate modified bismuth-borate-tellurite glasses. *Journal of Molecular Structure*, 2017. 1127: p. 636-644. DOI : [10.1016/j.molstruc.2016.08.033](https://doi.org/10.1016/j.molstruc.2016.08.033)
15. Dimitrov, V. and T. Komatsu, Classification of oxide glasses: a polarizability approach. *Journal of Solid State Chemistry*, 2005. 178(3): p. 831-846. <http://dx.doi.org/10.1016/j.jssc.2004.12.013>
16. Zaid, M.H.M., et al., Effect of ZnO on the physical properties and optical band gap of soda lime silicate glass. *International journal of molecular sciences*, 2012. 13(6): p. 7550-7558. <https://doi.org/10.3390/ijms13067550>
17. Upender, G. and M. Prasad, Raman, FTIR, thermal and optical properties of TeO₂-Nb₂O₅-B₂O₃-V₂O₅ quaternary glass system. *Journal of Taibah University for Science*, 2017. 11(4): p. 583-592. <https://doi.org/10.1016/j.jtusci.2016.02.008>
18. Escobar-Alarcón, L., et al., An alternative procedure for the determination of the optical band gap and thickness of amorphous carbon nitride thin films. *Applied surface science*, 2007. 254(1): p. 412-415. DOI :[10.1016/j.apsusc.2007.07.052](https://doi.org/10.1016/j.apsusc.2007.07.052)
19. Tanner, D.B., *Optical effects in solids* 2019: Cambridge University Press.
20. Bounakhla, M. and M. Tahri, X-ray fluorescence analytical techniques. National Center for Energy Sciences and Nuclear Techniques (CNESTEN), Rabat, Morocco, 2014. 1: p. 1-73.
21. Dimitrov, V. and S. Sakka, Electronic oxide polarizability and optical basicity of simple oxides. I. *Journal of Applied Physics*, 1996. 79(3): p. 1736-1740. <https://doi.org/10.1063/1.360962>
22. Dimitrov, V. and T. Komatsu, An interpretation of optical properties of oxides and oxide glasses in terms of the electronic ion polarizability and average single bond strength. *J. Univ. Chem. Technol. Metall*, 2010. 45(3): p. 219-250.
23. Duffy, J. and M. Ingram, *Optical properties of glass*. The American Ceramic Society, Westerville, 1991. 184.
24. Zhao, X., et al., Electronic polarizability and optical basicity of lanthanide oxides. *Physica B: Condensed Matter*, 2007. 392(1-2): p. 132-136. DOI : [10.1016/j.physb.2006.11.015](https://doi.org/10.1016/j.physb.2006.11.015)

25. Zhao, X., et al., Average electronegativity, electronic polarizability and optical basicity of lanthanide oxides for different coordination numbers. *Physica B: Condensed Matter*, 2008. 403(10-11): p. 1787-1792. DOI : [10.1016/j.physb.2007.10.005](https://doi.org/10.1016/j.physb.2007.10.005)
26. Dimitrov, V. and T. Komatsu, Electronic polarizability, optical basicity and non-linear optical properties of oxide glasses. *Journal of Non-Crystalline Solids*, 1999. 249(2-3): p. 160-179. [https://doi.org/10.1016/S0022-3093\(99\)00317-8](https://doi.org/10.1016/S0022-3093(99)00317-8)
27. Duffy, J., Optical basicity: A practical acid-base theory for oxides and oxyanions. *Journal of chemical education*, 1996. 73(12): p. 1138. <https://doi.org/10.1021/ed073p1138>
28. Elkhoshkhany, N., et al., Optical properties of quaternary $\text{TeO}_2\text{-ZnO-Nb}_2\text{O}_5\text{-Gd}_2\text{O}_3$ glasses. *Ceramics International*, 2014. 40(9): p. 14477-14481. <https://doi.org/10.1016/j.ceramint.2014.07.006>
29. Tasheva, T. and V. Dimitrov, SYNTHESIS, OPTICAL PROPERTIES AND STRUCTURE OF $\text{NiO-BaO-V}_2\text{O}_5$ GLASSES. *Journal of Chemical Technology & Metallurgy*, 2017. 52(2).
30. Çelikbilek, M., A. Ersundu, and S. Aydin, Preparation and characterization of $\text{TeO}_2\text{-WO}_3\text{-Li}_2\text{O}$ glasses. *Journal of Non-Crystalline Solids*, 2013. 378: p. 247-253. <https://doi.org/10.1016/j.jnoncrysol.2013.07.020>
31. Hager, I. and R. El-Mallawany, Preparation and structural studies in the $(70-x)\text{TeO}_2\text{-}20\text{WO}_3\text{-}10\text{Li}_2\text{O-xLn}_2\text{O}_3$ glasses. *Journal of materials science*, 2010. 45(4): p. 897-905. <https://doi.org/10.1007/s10853-009-4017-3>
32. Raghavaiah, B., C. Laxmikanth, and N. Veeraiah, Spectroscopic studies of titanium ions in $\text{PbO-Sb}_2\text{O}_3\text{-As}_2\text{O}_3$ glass system. *Optics Communications*, 2004. 235(4-6): p. 341-349. <https://doi.org/10.1016/j.optcom.2004.02.082>
33. Devaraja, C., et al., Optical properties of bismuth tellurite glasses doped with holmium oxide. *Ceramics International*, 2021. 47(6): p. 7602-7607. <https://doi.org/10.1016/j.ceramint.2020.11.099>
34. Sun, K.H., Fundamental condition of glass formation. *Journal of the American Ceramic Society*, 1947. 30(9): p. 277-281. <https://doi.org/10.1111/j.1151-2916.1947.tb19654.x>
35. Pietrucci, F., S. Caravati, and M. Bernasconi, TeO_2 glass properties from first principles. *Physical Review B*, 2008. 78(6): p. 064203. <https://doi.org/10.1103/PhysRevB.78.064203>

36. Guesmia, N., et al., Glass formation, physical and structural investigation studies of the (90-x) Sb_2O_3 -10 WO_3 -x NaPO_3 glasses. *Materials Today Communications*, 2022. 30: p. 103226. <https://doi.org/10.1016/j.mtcomm.2022.103226>
37. Poirier, G., et al., Structural study of tungstate fluorophosphate glasses by Raman and X-ray absorption spectroscopy. *Journal of Solid State Chemistry*, 2005. 178(5): p. 1533-1538. <https://doi.org/10.1016/j.jssc.2004.10.032>
38. Terashima, K., et al., Structure and nonlinear optical properties of Sb_2O_3 - B_2O_3 binary glasses. *Journal of the Ceramic Society of Japan*, 1996. 104(1215): p. 1008-1014.
39. Som, T. and B. Karmakar, Structure and properties of low-phonon antimony glasses and nano glass-ceramics in K_2O - B_2O_3 - Sb_2O_3 system. *Journal of Non-Crystalline Solids*, 2010. 356(20-22): p. 987-999. DOI : [10.1016/j.jnoncrysol.2010.01.026](https://doi.org/10.1016/j.jnoncrysol.2010.01.026)
40. Poirier, G., *Nouveaux verres à base d'oxyde de tungstène*, 2003, Rennes 1.
41. Ebendorff-Heidepriem, H., W. Seeber, and D. Ehrhart, Dehydration of phosphate glasses. *Journal of Non-Crystalline Solids*, 1993. 163(1): p. 74-80. [https://doi.org/10.1016/0022-3093\(93\)90647-G](https://doi.org/10.1016/0022-3093(93)90647-G)
42. Karmakar, B., P. Kundu, and R.N. Dwivedi, IR spectra and their application for evaluating physical properties of fluorophosphate glasses. *Journal of Non-Crystalline Solids*, 2001. 289(1-3): p. 155-162. [https://doi.org/10.1016/S0022-3093\(01\)00721-9](https://doi.org/10.1016/S0022-3093(01)00721-9)
43. Karmakar, B., et al., Effect of hydroxyl content on the physical properties of calcium metaphosphate glasses. *Bulletin of Materials Science*, 1999. 22(2): p. 115-119. <https://doi.org/10.1007/BF02745563>
44. Shaaban, K.S., et al., Electronic polarizability, optical basicity and mechanical properties of aluminum lead phosphate glasses. *Optical and Quantum Electronics*, 2020. 52(2): p. 1-16. <https://doi.org/10.1007/s11082-020-2191-3>
45. Boudlich, D., et al., Infrared, Raman, and electron spin resonance studies of vitreous alkaline tungsten phosphates and related glasses. *Journal of the American Ceramic Society*, 2002. 85(3): p. 623-630. <https://doi.org/10.1111/j.1151-2916.2002.tb00141.x>
46. Franco, D.F., et al., Glass formation and the structural study of the Sb_2O_3 - SbPO_4 - WO_3 system. *Eclética Química*, 2017. 42: p. 51-59. <https://doi.org/10.26850/1678-4618eqj.v42.1.2017.p51-59>
47. Leow, T.Q., et al., Study of structural and luminescence properties of lead lithium borophosphate glass system doped with Ti ions. *Sains Malaysiana*, 2014. 43(6): p. 929-934.

48. Roy, J.S., Y. Messaddeq, and S.J. Ribeiro, Formation and optical properties of new glasses within $\text{Sb}_2\text{O}_3\text{-WO}_3\text{-ZnO}$ ternary system. *Journal of Materials Science: Materials in Electronics*, 2019. 30(18): p. 16798-16805. <https://doi.org/10.1007/s10854-019-01340-x>
49. Hammad, A.H. and E.B. Moustafa, Study some of the structural, optical, and damping properties of phosphate glasses containing borate. *Journal of Non-Crystalline Solids*, 2020. 544: p. 120209. <https://doi.org/10.1016/j.jnoncrysol.2020.120209>
50. Nalin, M., et al., Glasses in the $\text{SbPO}_4\text{-WO}_3$ system. *Journal of Non-Crystalline Solids*, 2007. 353(16-17): p. 1592-1597. <https://doi.org/10.1016/j.jnoncrysol.2007.01.031>
51. Sudarsan, V. and S. Kulshreshtha, Study of structural aspects of $\text{PbO-P}_2\text{O}_5\text{-Sb}_2\text{O}_3$ glasses. *Journal of Non-Crystalline Solids*, 2001. 286(1-2): p. 99-107. [https://doi.org/10.1016/S0022-3093\(01\)00502-6](https://doi.org/10.1016/S0022-3093(01)00502-6)
52. Efimov, A.M., IR fundamental spectra and structure of pyrophosphate glasses along the $2\text{ZnO} \cdot \text{P}_2\text{O}_5\text{-}2\text{Me}_2\text{O} \cdot \text{P}_2\text{O}_5$ join (Me being Na and Li). *Journal of Non-Crystalline Solids*, 1997. 209(3): p. 209-226. [https://doi.org/10.1016/S0022-3093\(96\)00562-5](https://doi.org/10.1016/S0022-3093(96)00562-5)
53. Ouannes, K., et al., Antimony oxide based glasses, novel laser materials. *Optical Materials*, 2017. 65: p. 8-14. <https://doi.org/10.1016/j.optmat.2016.11.017>

Chapter V
Physical and
spectroscopy studies
of Sm³⁺ ions doped
SWN glasses

V.1 Introduction

In this chapter we investigated the physical, thermal, structural, optical and spectroscopy aspects of SWN glasses matrix after introducing Samarium (Sm³⁺) at various concentrations.

Other reported have been studied the luminescence behavior of the Sm³⁺ ions in the various host matrices such as fluoro-phosphate [1], borate [2], lead fluoroborate [3], borosulphate [4], cholcohalide [5], borotellurite [6], fluoroborate [7], niobate tellurite [8]. Generally, the emission spectra of Sm₂O₃ doped glasses show four emission peaks at 565, 602, 648 and 709 nm corresponds to the ⁴G_{5/2}→⁶H_{5/2}, ⁶H_{7/2}, ⁶H_{9/2} and ⁶H_{11/2} transitions, respectively. “The highest emission intensity at the transition ⁴G_{5/2}→⁶H_{7/2} is allowed magnetic dipole (MD) and electric dipole (ED), the ⁴G_{5/2}→⁶H_{5/2} transition is allowed magnetic dipole (MD) whereas; the ⁴G_{5/2}→⁶H_{9/2} transition is allowed electric dipole (ED) transition”. The emission intensities strongly depend on the Sm³⁺ ion concentration and glass composition. The Sm³⁺ ion exhibit strong orange–red emission in the visible region which is useful in high density optical storage, under sea communication, color displays and visible solid-state lasers, etc. Since, samarium doped glasses emit light in the orange-red region so they are used in orange-red LED applications [2, 9].

V.2 Experimental synthesis

The synthesis of glass with molar compositions of the (40-x) Sb₂O₃-10WO₃-50NaPO₃-xSm₂O₃ (x = 0.15, 0.30, 0.45, 0.60, and 0.75mol%) glass system is prepared via the melt-quenching-annealing method. These compositions are taken from the following raw materials: antimony oxide (Sb₂O₃), tungsten oxide (WO₃), sodium hydrogeno-phosphate (H₂NaPO₄) and samarium oxide (Sm₂O₃) powders with the appropriate mole % to yield around 5g, then mixed well and placed in silica tubes. The batch is then melted for 20 min in a burner flame set at 900 °C to 1100 °C. The molten samples are placed on a warmed brass plate that is kept at 300 °C, then placed immediately into the annealing furnace, where they are heated for roughly 6 hours at 300 °C to remove surface imperfections and thermal stress, then slowly cooled to room temperature. The resulting glasses (Fig V.1) are investigated for various physical, thermal, mechanical, optical, and structural properties, as described below.

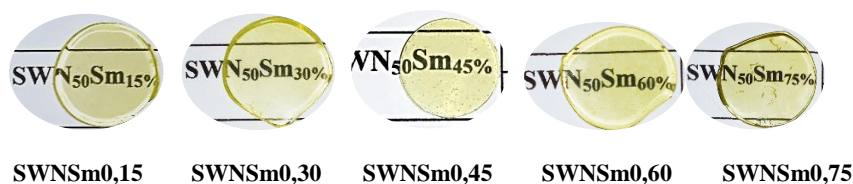


Figure V.1: The photos of SWNSm glasses with Sm³⁺ ions vary from 0,15 to 0,75 mole %.

Finally, the obtained glasses are polished into desired sizes to obtain a smooth surface for optical, structural, PL spectroscopy, and decay curves (life time) measurements. Also, don't forget that a portion of each sample is ground for differential calorimetry (DSC) measurement.

V.3 Physical properties

The augmentation in density is due to the higher molecular weight and atomic radii of Sm₂O₃ ($M_{Sm_2O_3}=348.70$ g/mol and $r_{Sm^{3+}}=0.109$ nm) as compared to other oxides present in the (40-x) Sb₂O₃-10WO₃-50NaPO₃-xSm₂O₃ glass matrix (see Fig V.2 and Table V.1). The addition of Sm₂O₃ causes an increase in ρ and a decrease in V_m , which results in an increase in compactness owing to the strong connectivity in the SWNSm glass structure (which suggests there is contraction in the glass matrix). Also, a reduction in V_m indicates that the structure of SWNSm glasses is less disordered. The oxygen molar volume (V_o) is dropping while the oxygen packing density (OPD) is growing (Table V.1). This leads to a drop in NBOs,

indicating that the strong connections in the SWNSm glass network and the glass structure has grown more compact and tighter [10].

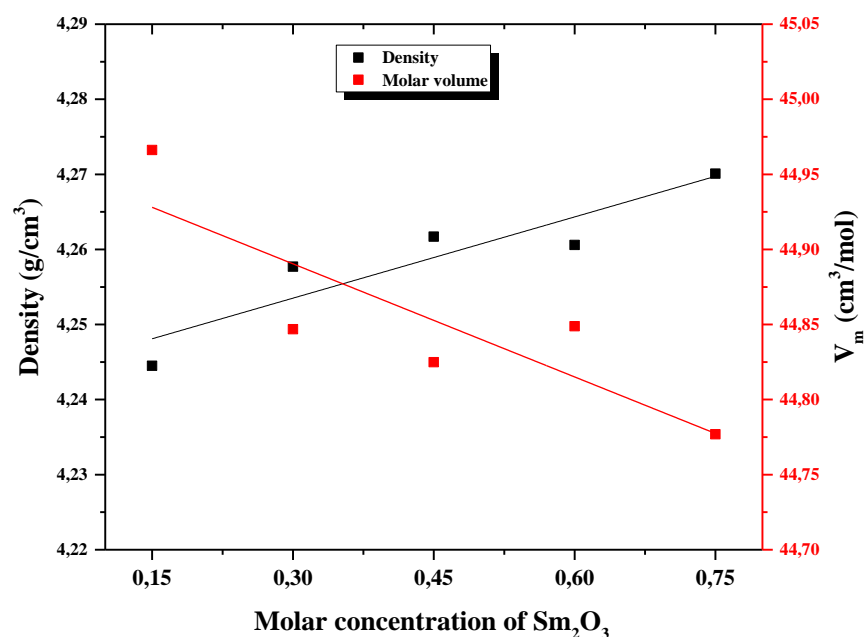


Figure V.2: Density and molar volume of (40-x) Sb₂O₃-10 WO₃-50NaPO₃-xSm₂O₃ glasses.

Table V.1: Glass composition in mole %, density (ρ), Molar volume (V_m), oxygen packing density (OPD), oxygen molar volume (V_o), Young modulus (E_t) and Poisson's ratio (ν_t).

S. n°	Sb ₂ O ₃	WO ₃	NaPO ₃	Sm ₂ O ₃	ρ (g/cm ³)	V_m (cm ³ /mol)	OPD (mol/L)	V_o (cm ³ /mol)	E_t (GPa)	ν_t
SWNSm0,15	39,85	10	50	0,15	4,2445	44,966	66,717	14,989	37,88	0,212
SWNSm0,30	39,70	10	50	0,30	4,2577	44,847	66,894	14,949	37,91	0,213
SWNSm0,45	39,55	10	50	0,45	4,2617	44,825	66,927	14,942	37,85	0,212
SWNSm0,60	39,40	10	50	0,60	4,2566	44,899	66,817	14,966	37,75	0,212
SWNSm0,75	39,25	10	50	0,75	4,2701	44,777	66,999	14,926	37,74	0,212

Table V.2: The number density of Sm³⁺ ions (N), the inter-nuclear distance (r_i), polaron radius (r_p), field strength (F), number of bonds per unit volume (n_b) and cross-link density (\bar{n}_c) and the average antimony–antimony separation (d_(Sb-Sb)).

S. n°	N(10 ²⁰ ions/cm ³)	r _i (10 ⁻⁷ cm)	r _p (10 ⁻⁷ cm)	F(10 ¹⁴ cm ²)	n _b (10 ²¹ cm ³)	\bar{n}_c	d _(Sb-Sb) (10 ⁻⁸ cm)
SWNSm0,15	0,201	3,679	1,482	28,220	16,010	1,689	3,099
SWNSm0,30	0,403	2,917	1,175	44,877	15,993	1,694	3,092
SWNSm0,45	0,605	2,548	1,027	58,824	15,940	1,698	3,088
SWNSm0,60	0,805	2,316	0,933	71,182	15,868	1,703	3,085
SWNSm0,75	1,009	2,148	0,866	82,749	15,836	1,708	3,079

The various parameters such as ρ , V_m, V_O, OPD, \bar{n}_c and n_b are calculated using a formula from previous work [10]. In table V.2, both \bar{n}_c and n_b show a positive trend with the augmentation of Sm³⁺ concentration. Antimony oxide (Sb₂O₃) is replaced with another oxide (Sm₂O₃), which has a cationic coordination number greater than Sb₂O₃ (n_f(Sm₂O₃) = 6) and leads to an increase the compactness inside the glass network.

Table V.2 includes a number of measured physical parameters. From the following formulas [11, 12], the following polaron radius (r_p), internuclear distance (r_i), and field strength (F) were calculated using the Sm³⁺ concentration (N) (ions/cm³).

$$N = \frac{X_{Sm^{3+}} \times N_a \times \rho_{glass}}{M_{glass}} \quad (\text{V.1})$$

$$r_i = \left(\frac{1}{N}\right)^{1/3} \quad (\text{V.2})$$

$$r_p = \frac{1}{2} \left(\frac{\pi}{6N}\right)^{1/3} \quad (\text{V.3})$$

$$F = \frac{Z}{r_p^2} \quad (\text{V.4})$$

Where X_{Sm³⁺} is the molar concentration of Sm₂O₃, ρ_{glass} is the density of glasses M_{glass} is average molecular weight of glasses and Z is atomic number of the dopant (Z_{Sm}=62).

As shown in [table V.2](#), the concentration of samarium ions (N) increases with increasing Sm₂O₃ concentration while both polaron radius, r_p (°A) and inter-nuclear distance, r_i (°A) decrease in the glass matrix. The polaron radius r_p is shortened with the increase in the Sm³⁺ ion. This observation is attributed to the overfilling of Sm³⁺ ions inside the SWNSm glass matrix. The rise in Sm³⁺ ions (N) increases Sm-O bond strength and leads to the development of stronger field strength (F) around Sm³⁺ and increases the compactness of the SWNSm glass structure. In fact, the enhanced field strength (F), indicating a strong correlation in the host matrix with the amount of Sm³⁺, generates a large number of BO. This might be the outcome of the formation of P–O–W units that have stronger and higher ionicity.

However, incorporation of Sm₂O₃ at a higher level inside the disordered network structure shortens the antimony–antimony separation ($d_{(Sb-Sb)}$), implying that SWNSm glasses are more compact (there is contraction in the SWNSm glass matrix).

The refractive index (n_0), molar polarizability (α_m), molar refractivity (R_m) and reflection loss (R) drop with the addition of Sm₂O₃ in the SWN glasses as depicted in [table V.3](#). The refractive index of the glasses depends on the polarizability of the glasses. This decrease confirms decrease in the number of non-bridging oxygen's (NBO's) in the SWNSm glasses which in turn decreases the refractive index.

The decrease in oxide ion polarizability (α_{O-2}) values with the addition of Sm₂O₃ is due to the decrease in n_0 and supports the observed decrease in V_m of the prepared glasses. The theoretical optical basicity (Λ_{th}) is calculated and depicted in [table V.3](#). It is observed that the decrease in the (Λ_{th}) of SWN glasses with the addition of Sm₂O₃, leads to lower optical basicity value of Sm₂O₃ ($\Lambda=0,984$) at the cost of Sb₂O₃ ($\Lambda=1,18$) [[13-17](#)].

The positive values of (M) suggest that the SWNSm glasses exhibit non-metallic behavior and our prepared samples are useful in (NLO) applications because of the M values of SWNSm glasses with excellent (NLO) range between 0.30 and 0.45 (see [table V.3](#)) [[15](#)].

Table V.3: Various physical and optical properties of SWNSm glasses.

Property	Sample n° /property value				
	SWNSm0,15	SWNSm0,30	SWNSm0,45	SWNSm0,60	SWNSm0,75
Refractive index, n	1,867	1,867	1,866	1,866	1,865
E _g indirect (eV)	2,837	2,856	2,848	2,859	2,870
E _u (eV)	0,1408	0,1471	0,1500	0,1548	0,1409
Molar refraction, R _m (cm ³ /mol)	24,921	24,846	24,825	24,833	24,780
Total molar polarizability, α _m (10 ⁻²⁴ cm ³)	9,885	9,855	9,846	9,850	9,829
Total molar polarizability of cation, Σα _m (Å ³)	0,9246	0,9248	0,9249	0,9251	0,9252
Polarizability of oxide ions, α _{O2-} (Å ³)	2,240	2,232	2,230	2,231	2,226
Optical basicity from refractive index, Λ(n)	0,925	0,922	0,921	0,922	0,920
Theoretical optical basicity, Λ _{th}	0,8112	0,8109	0,8106	0,8103	0,8100
Metallization criterion M	0,4458	0,4460	0,4462	0,4464	0,4466
Dielectric constant, ε	3,487	3,485	3,483	3,480	3,478
Reflection loss R	0,4532	0,4530	0,4528	0,4526	0,4524
Temperature of transition T _g (°C)	324	326	324	330	339
OH content (ppm)	41,146	33,862	39,402	40,275	46,670

V.4 Mechanical properties

V.4.1 Theoretical elastic modulus

In the theory of Makishima and Mackenzie, and by using [table V.4](#), we can define the Young modulus (E_t) and the Poisson's ratio (ν_t) of the SWNSm glasses with consideration of the chemical composition (x_i) of the constituting oxide, the packing factor (V_i), and their corresponding dissociation energies per unit volume (G_i) [10, 18].

We realize that there is no noticeable change in the elasticity coefficients (E_t and ν_t), and this is what distinguishes our obtained glass. The more samarium ions inside the glass lattice, the more value of the stiffness remains high and constant. Also, the Poisson's ratio (ν)

of SWNSm systems indicates their stiffness (see Table V.1). The (ν) values in this study is less than 0.3, indicating that the density of cross-linking for the examined glass system is high [10].

Table V.4: Molecular weight, density, packing factor of oxide, dissociation energy per unit volume, optical basicity and of Sb_2O_3 , WO_3 , NaPO_3 and Sm_2O_3 .

Oxide	M_i (g/mol)	ρ_i (g/cm ³)	V_i [10, 18] (cm ³ /mol)	G_i [10, 18] (kcal/cm ³)	Λ [14, 17, 19, 20]	α (A ³) [14, 17, 19, 20]
Sb₂O₃	291,52	5,05	22,97	8,43	1,18	1,111
WO₃	231,85	7,16	21,45	16,22	1,045	0,147
NaPO₃	101,96	2,50	20,77	8,79	0,47	0,021
Sm₂O₃	348,70	8,35	24,32	5,89	0,984	1,16

V.4.2 Experiment elastic modulus of SWNSm glasses

In general, the theoretical values of the elastic moduli are very close to the experimental values in the SWNSm glasses. On the other hand, we can say that the value of Young's modulus of these glasses is similar to phosphate glasses ($E=40\text{-}50$ GPa) and in the same range of tellurium glasses ($E=38$ GPa). We realize that there is no noticeable change in the elasticity coefficients with the addition of samarium ions inside the glass lattice and this is what distinguishes our obtained glass, the value of the stiffness remains high and constant, which demonstrates the rigidity and non-deformable of SWNSm glasses. Also, the Poisson's ratio (ν) of SWNSm systems indicates their stiffness of these glasses (see table V.5).

Table V.5: The experimental elastic properties of the SWNSm glasses.

S.N ^o	E_{exp} (GPa)	K_{exp} (GPa)	G_{exp} (GPa)	L_{exp} (GPa)	ν_{exp}
SWNSm0,15	40,783	30,529	15,964	51,814	0,227
SWNSm0,30	37,898	25,348	15,149	45,547	0,201
SWNSm0,45	41,428	29,454	16,367	51,276	0,215
SWNSm0,60	39,318	28,265	15,502	48,935	0,218
SWNSm0,75	42,467	32,411	16,568	54,501	0,231

V.5 Thermal properties

Fig V.3 depicts the DSC curves of SWNSm samples measured between 200 and 500°C. This curve illustrates the absence of a crystallization peak, which indicates good thermal stability against devitrification with a high amount of Sm³⁺ ions in SWN glasses. Inserting Sm₂O₃ into SWN glasses raises the glass transition temperature (T_g) (see Fig V.4), implying increased stiffness in the host matrix (confirmed by FTIR spectra).

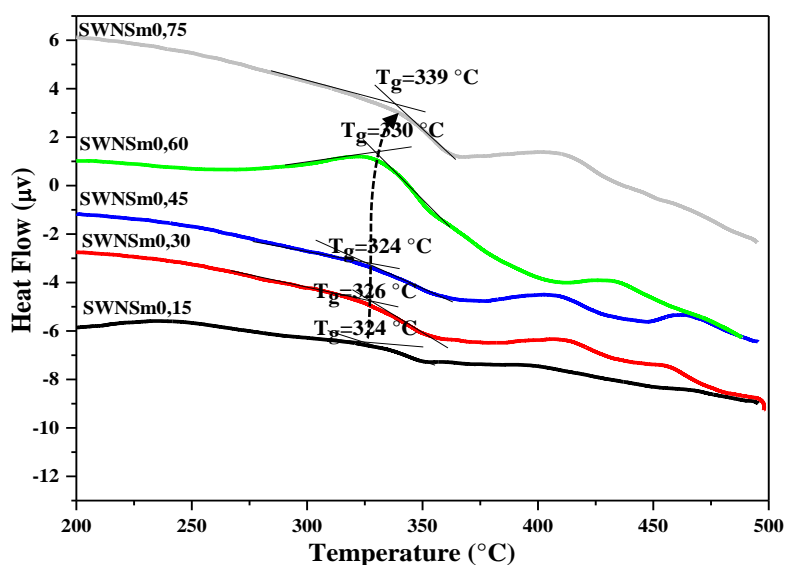


Figure V.3: DSC curves of (40-x) Sb₂O₃-10 WO₃-50NaPO₃-xSm₂O₃ glasses.

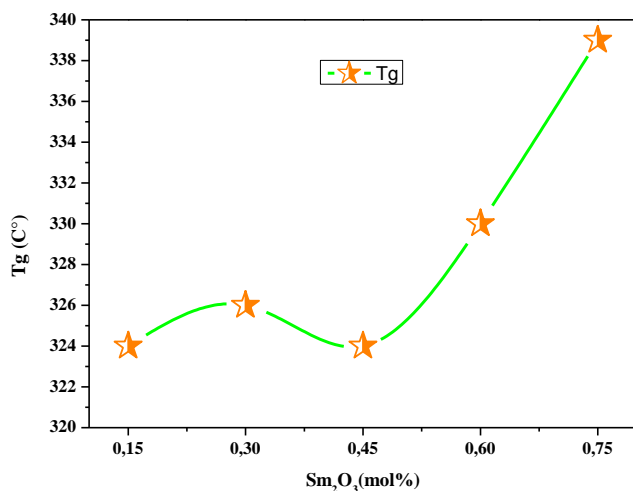


Figure V.4: The value of transition temperature of SWNSm glasses.

V.6 Structural properties

➤ IR spectra in the region of 1,5-8 μ m

The IR spectra of SWNSm glasses is illustrated in the region of 1,5-8 μ m and shown in Fig V.5. The IR transmission spectra illustrates four major regions. The first wide band is around 3000 cm^{-1} (3,33 μ m), and is due to the hydroxyl (OH) groups. The second group of bands, which occurs at 2500 cm^{-1} (4 μ m) is due to a harmonic of the fundamental vibration of the P-O bonds in the PO₄ tetrahedra. The third band, around 1900 cm^{-1} (5,2 μ m), is due to the fundamental vibration of Si-O bands, which comes from the silica crucible used during the melting processes. The fourth group of bands at 1492 cm^{-1} (6,7 μ m) is attributed to the contributions from Sb-O bond vibration [21, 22].

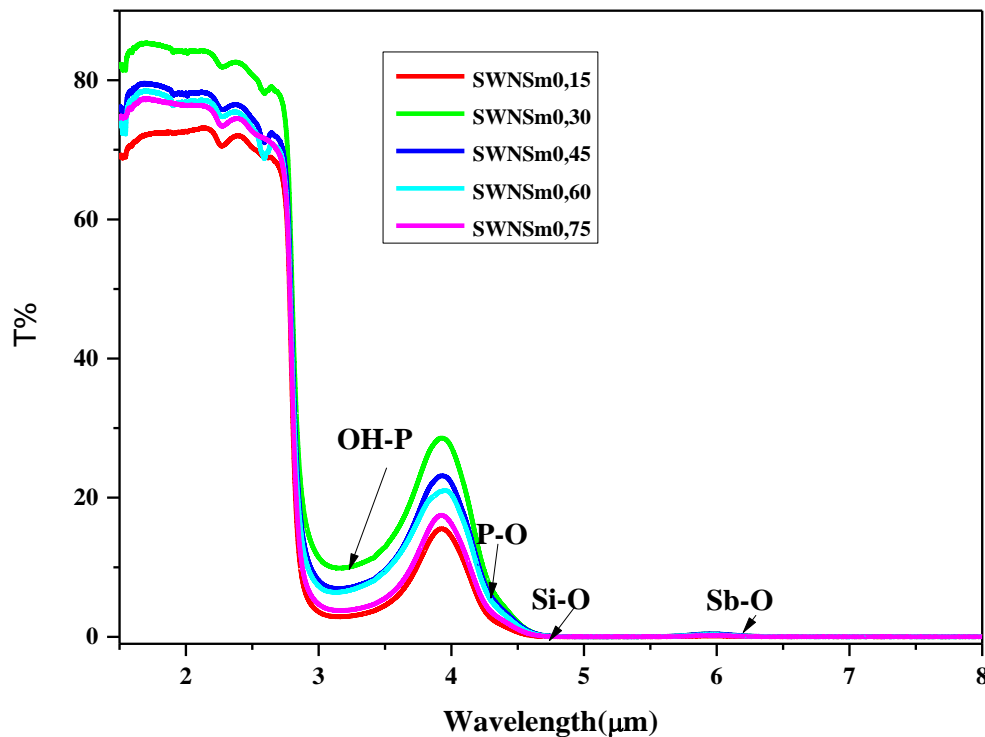


Figure V.5: IR transmittance spectra of SWNSm glasses in the region 1,5-8 μ m.

The presence of a large amount of hydroxide content in the glasses increases the non-radiative losses and reduces the quantitative efficiency of glass materials. In our glasses, we can observe the lower OH content compared to other glasses such as fluorophosphate [23] and calcium metaphosphate [24]. SWNSm0,30 sample have the lowest OH content, which makes them suitable for efficient lasers with low non-radiative losses. The intensity of the absorption OH group vibrations decreases (up to Sm0.30%) and then increases (up to Sm0.75%) with the

addition of Sm³⁺ ion content (see Table V.3), which is also a reason for the occurrence of luminescence quenching in the prepared glasses [25]. Baazouzi et al [26], study how to eliminate OH and Si-O absorption bands using an alumina crucible and perform vacuum glass synthesis to improve the optical properties of glass samples.

➤ **ATR spectra in the region of 4000-400 cm⁻¹**

The ATR absorption band (Fig V.6.a) at 3347 cm⁻¹ is due to the O–H stretching vibrations and confirms the presence of OH groups in the glass composition. The presence of hydrogen bonding is indicated by the bands located at 2927 cm⁻¹ and 2861 cm⁻¹. The bands located in the interval (2400-1600 cm⁻¹) are due to the H₂O molecules (with very low intensity) [21, 23]. Table V.6 illustrates the assignment of the ATR transmittance bands in the range of 4000-400 cm⁻¹ of SWNSm glasses. The UATR spectra of SWNSm samples are deconvoluted in the frequency range between 1400 and 400 cm⁻¹ (Fig V.6.b).

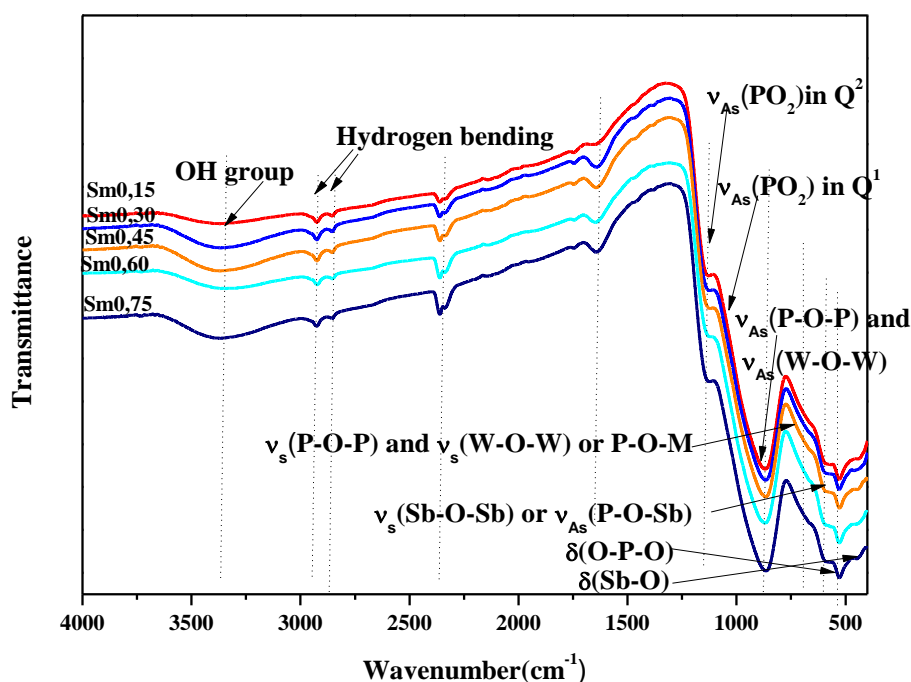


Figure V.6.a: The ATR spectra of SWNSm glasses in the range 4000-400cm⁻¹

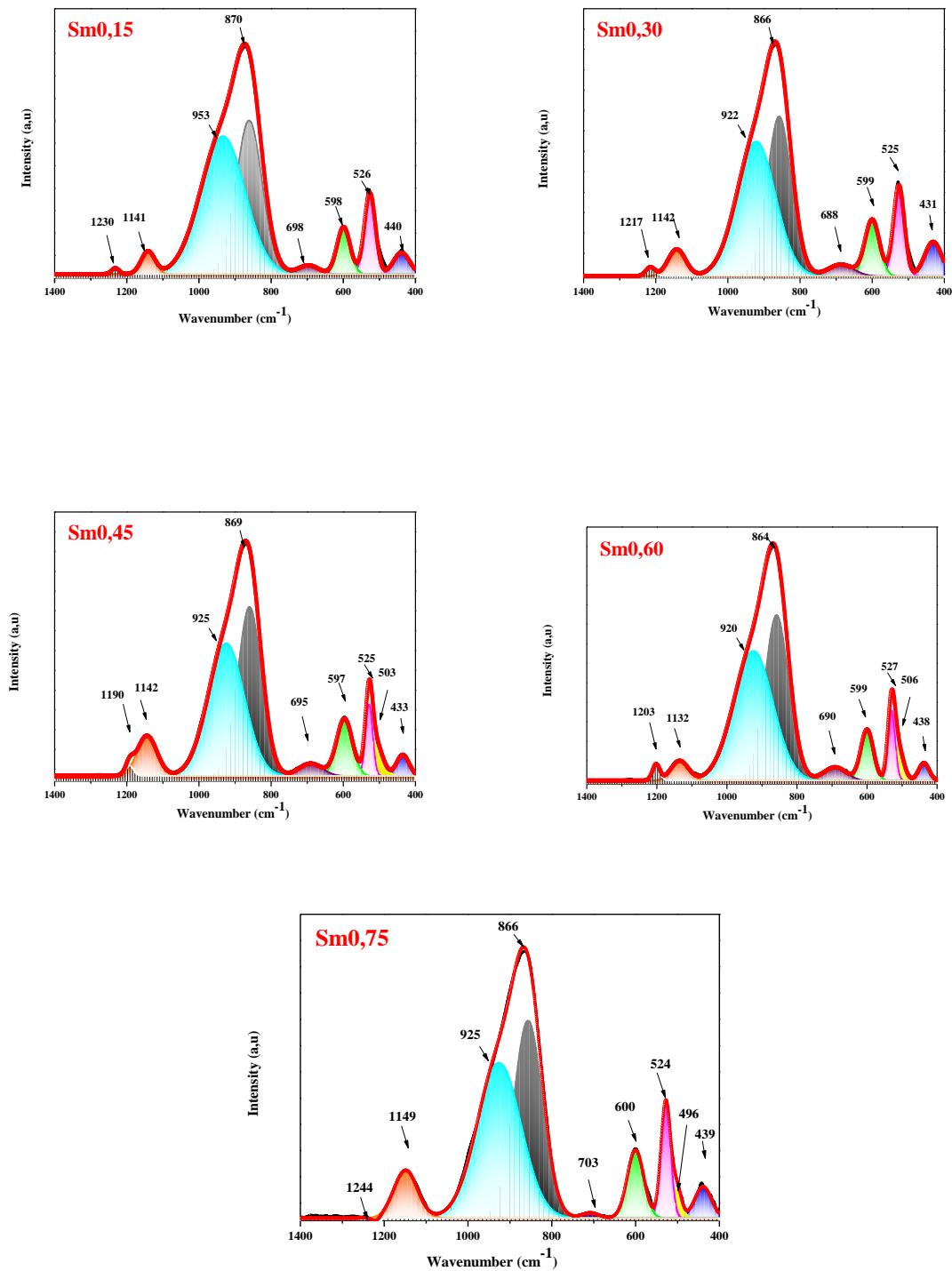


Figure V.6.b: Deconvolution analysis of the ATR spectra of SWNSm glasses.

A symmetric stretching mode of the two non-bridging oxygen atoms bonded to phosphorus atoms, the P–O_t ($\nu_{as}(\text{PO}_2)$) units in Q² [11, 27] and the stretching mode of P=O double bonds [28] are assigned to the band near 1190–1244 cm⁻¹. This band decreases with the addition of Sm³⁺ ions, which means more BO in the glass matrix. The band at around 1132–

1149 cm⁻¹ is assigned to the $\nu_{\text{as}}(\text{PO}_2)$ asymmetric stretching mode in Q¹, which shows an augmentation with the addition of Sm³⁺ ions. The strong absorption bands at 920-925 cm⁻¹ are attributed to the stretching vibrations of WO_t or W=O, the tungsten-non-bridging oxygen NBOs portion of WO₄ or WO₆ unit in a chain structure [29-32], with small lowering with the addition of Sm₂O₃ concentration. The highest absorption bands near 864-870 cm⁻¹ are assigned to the asymmetric stretching of the $\nu_{\text{as}}(\text{P-O-P})$ and $\nu_{\text{as}}(\text{W-O-W})$ linkages. This higher intensity increases with the amount of Sm₂O₃, which means an increase in linkage in the host matrix (formation P-O-P or W-O-W linkage) and this leads to the augmentation of the rigidity and transition temperature (T_g) of our obtained glasses. The band at 698-703 cm⁻¹ is assigned to symmetrical stretching vibrations of P-O-P bridges ($\nu_{\text{s}}(\text{P-O-P})$) or P-O-M linkages (with M=Sb or W) and may also be due to symmetric stretching vibrations of the $\nu_{\text{s}}(\text{W-O-W})$ linkages, which means more and more linear bridging atoms (and BOs) increase with increasing Sm₂O₃ content [29, 30, 33]. The absorption peak at around 597-600 cm⁻¹ is due to the symmetric and asymmetric stretching vibration modes of the Sb-O-Sb bond of Sb₂O₃, or assigned to the asymmetrical stretching P-O-Sb bridge of SbPO₄ [30, 34]. The two bands at around 524-527 and 503-506 cm⁻¹ are ascribed to the deformation vibration modes of O-P-O in Q² tetrahedra (bridging oxygen atoms, BOs) and asymmetric stretching of Sb-O from Sb₂O₃, respectively [11, 22, 27, 35]. The intensity of this band increases with the increase of Sm₂O₃, which confirm previous results. The band at around 431-440 cm⁻¹ is attributed to deformation modes of SbO₃ units. The introduction of Sm₂O₃ into the glass matrix increases the BOs, which causes an increase in the rigidity and compactness of our host matrix [28, 36].

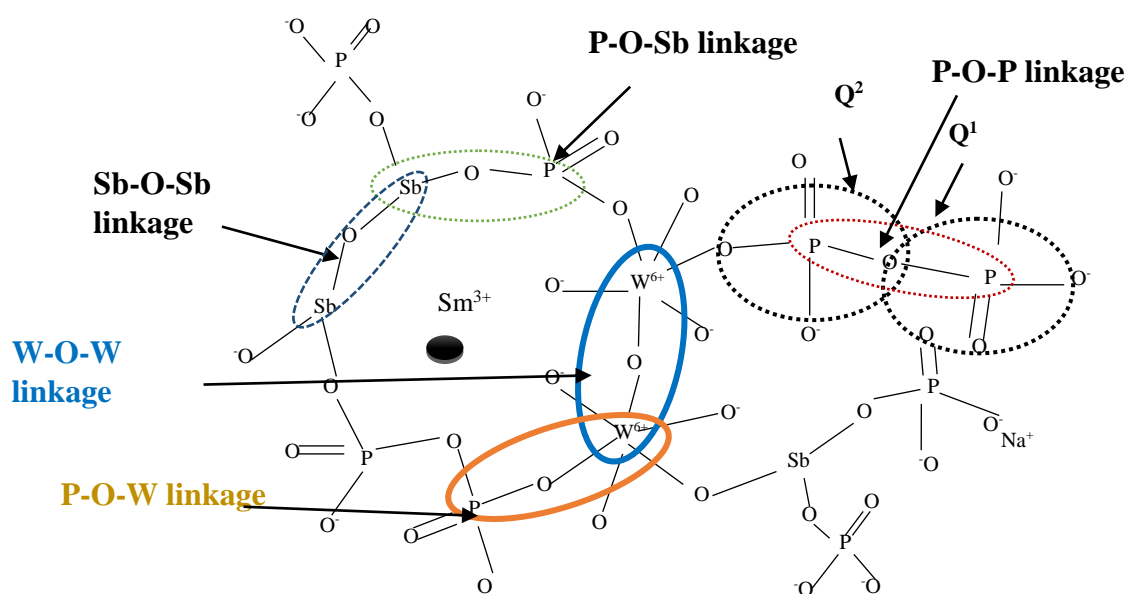


Figure V.7: The structural suggests of SWNSm glasses.

In conclusion, the small increase in bridging oxygen atoms (BO) is related to the formation of linear connections of phosphate chains as P-O-M (with M=W, P or Sb, etc.) linkages, which confirm the increase in the connectivity and rigidity of the SWNSm host matrix (see [fig V.7](#)).

Table V.6: Assignment of the ATR transmittance bands (4000-400 cm⁻¹) of SWNSm glasses.

Wavenumber (cm ⁻¹)	Vibrational mode
431-440	δ (Sb-O) in SbO ₃
503-506	asymmetric stretching of Sb-O from Sb ₂ O ₃
524-527	δ (O-P-O) in Q ² tetrahedral
597-600	ν_s (Sb-O-Sb) and ν_{as} (Sb-O-Sb) bond of Sb ₂ O ₃ or Sb-O-P bridge of SbPO ₄
698-703	ν_s (P-O-P) in Q ² mode or P-O-M linkage or ν_s (W-O-W) linkage
864-870	ν_{as} (W-O-W) and ν_{as} (P-O-P)
920-925	stretching vibration of W-O _t and W=O in units WO ₄ and WO ₆
1132-1149	ν_{as} (PO ₃ ²⁻) in Q ¹ tetrahedral ((P-O) ⁻ or (P=O))
1190-1244	ν_{as} (PO ₂ ⁻) in Q ² tetrahedral ((P-O) ⁻ or (P=O))
2400-1600	H ₂ O molecules
2855-2861	hydrogen bonding
2921-2927	hydrogen bonding
3323-3347	fundamental hydroxyl OH stretching vibrations

V.7 Optical properties

[Fig V.8a](#) and [Fig V.8b](#) depict the absorption spectra of SWNSm glasses. In addition to the spin orbit and electrostatic interactions of 4f-4f energy level transitions from the ground state ⁶H_{5/2} to various excited states, these spectra include multiple absorption bands with varied strengths in the UV-Vis and NIR ranges (shown in [table V.7](#)). The absorption spectra of the prepared glasses are similar to other reported Sm³⁺ doped glasses [\[20\]](#).

Table V.7: The transition of Sm³⁺ and assignment wavelength correspond to the excited states from the ground states ⁶H_{5/2} to various excited states.

Region	Transition	Wavelength (nm)
UV-Vis	⁶ P _{3/2}	401
	⁴ I _{13/2}	461
	⁴ I _{11/2}	472
	⁴ I _{9/2}	478
	⁴ G _{7/2}	480
	⁴ F _{3/2}	563
	⁴ G _{5/2}	570
NIR	⁶ F _{11/2}	942
	⁶ F _{9/2}	1076
	⁶ F _{7/2}	1232
	⁶ F _{5/2}	1377
	⁶ F _{3/2}	1415
	⁶ H _{15/2}	1476
	⁶ F _{1/2}	1549
	⁶ H _{13/2}	1916

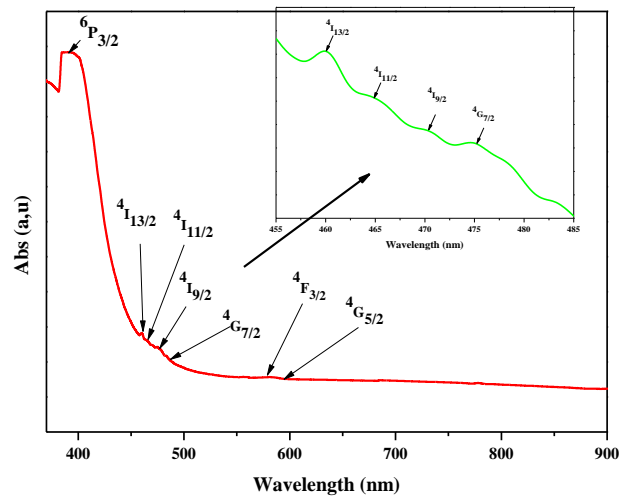


Figure V.8a: UV-Vis region absorption spectrum of SWNSm_{0,30} sample.

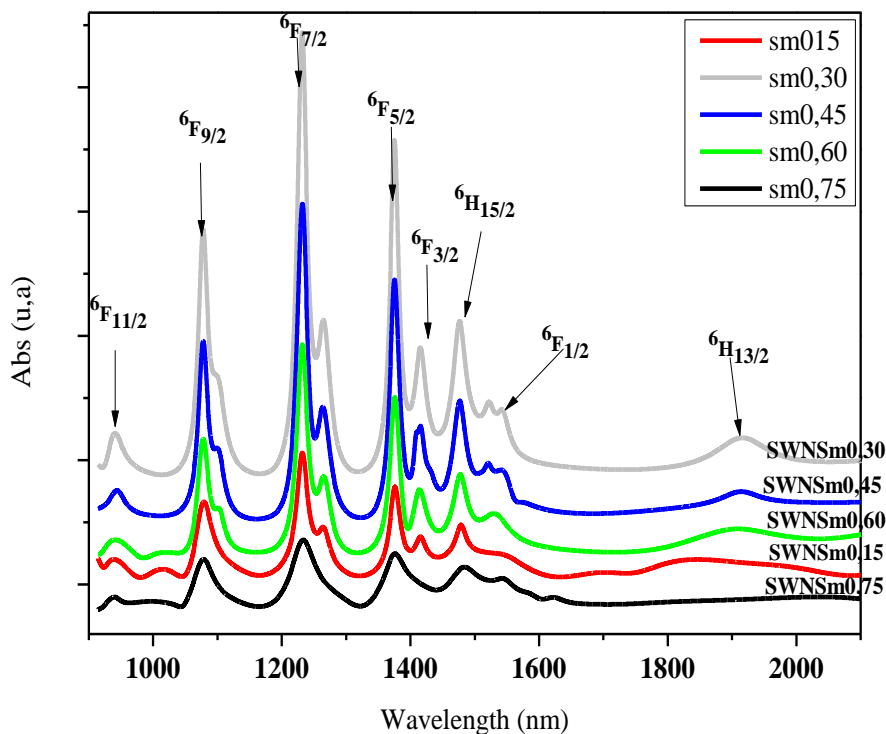


Figure V.8b: NIR region absorption spectrum of SWNSm glasses.

The intensity of all bands improves when the Sm₂O₃ content climbs to 0,30% mole, then drops to 0,75% mol. This rise in intensity causes the cutoff wavelength to increase (see Fig V.8b)[36].

The optical energy band gap (E_g) of the glasses is computed using the Davis and Mott theory's connection between absorption coefficient (α) and (E_g) [37, 38]. The indirect band gap is calculated by extrapolating the linear section of the curve to cross the photon energy axis at zero absorption ($(\alpha h\nu)^{1/2} = 0$). The slope of the linear component of the plot $(\alpha h\nu)^{1/2}$ vs $h\nu$ is intersected to obtain the $E_{g \text{ indirect}}$ values (in eV) of our glasses (see figure V.9).

The observed values of the $E_{g \text{ (indirect)}}$ are 2.837, 2.856, 2.848, 2.859 and 2.870 eV for SWNSm0,15, SWNSm0,30, SWNSm0,45, SWNSm0,60 and SWNSm0,75 samples, respectively. Also, the value of E_u of our obtained glasses decreases with the addition of Sm₂O₃ from 0,1408 to 0,1548 eV (see table V.3 and fig V.10).

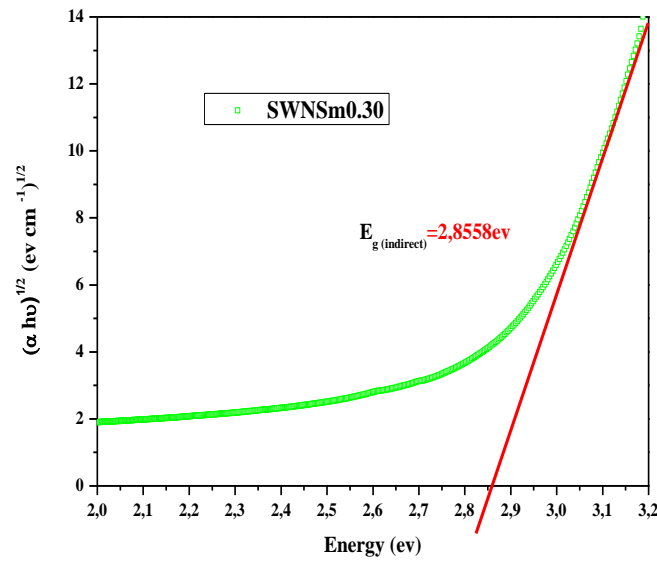


Figure V.9: Plot of $(\alpha hv)^{1/2}$ vs $h\nu$ curve to estimate the $E_{g \text{ indirect}}$ of SWNSm0,30 glass.

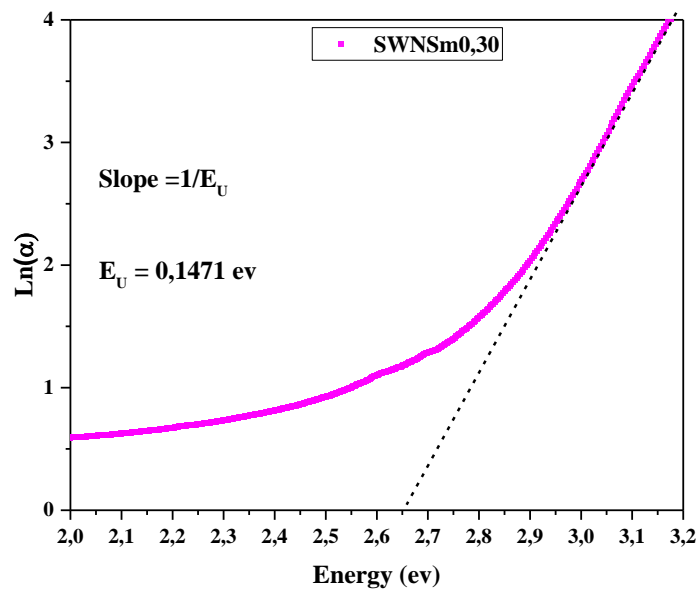


Figure V.10: Plot of $\text{Ln}(\alpha)$ vs $h\nu$ curve to estimate the E_u of SWNSm0,30 glass.

The increase in bandgap and decrease in Urbach (E_u) band indicate that our glass has an insulating nature in which the forbidden bandwidth increases with the gradual increase in the number of oxygen bridges (BO), implying decreased bonding defects in the SWNSm glass network [39]. As a result, the degree of electron localization is reduced, and the number of donor centers in the vitreous matrix is reduced.

V.8 Photoluminescence (PL) study

V.8.1 Excitation spectra

The overlaid excitation spectra of the SWNSm glasses were recorded from the emission at 596nm and are displayed in [fig V.11](#). Samarium ions are excited from the ground state of $^6H_{5/2}$ to different levels of transition and swiftly relaxed through a non-radiative transition to the energy level of $^4G_{5/2}$ [40]. The SWNSm glasses have a prominent excitation peak at 402nm, which corresponds to the $^6H_{5/2} \rightarrow ^4F_{7/2}$ transition. The emission spectra are measured at this wavelength.

The strong excitation peak at 402nm in the SWNSm glasses corresponds to the $^6H_{5/2} \rightarrow ^4F_{7/2}$ transition. This wavelength is used to measure the emission spectra. The transitions corresponding to the excitation of Sm³⁺ from the ground states $^6H_{5/2}$ to various excited states of SWNSm glasses are illustrated in [table V.8](#). [Fig V.12](#) illustrates the energy level diagram of Sm³⁺ stimulated at 402 nm.

Table V.8: The transition of Sm³⁺ and assignment wavelength corresponding to the excited states from the ground states $^6H_{5/2}$ to various excited states.

$^6H_{5/2} \rightarrow$	Wavelength (nm)
$^4D_{7/2} + ^4H_{9/2}$	343
$^4D_{3/2}$	362
$^6P_{7/2}$	375
$^4L_{15/2}$	388
$^4F_{7/2}$	402
$^6P_{5/2}$	416
$^4P_{5/2}$	420
$^4G_{9/2}$	439
$^4F_{5/2}$	449
$^4I_{13/2}$	463
$^4I_{11/2}$	474

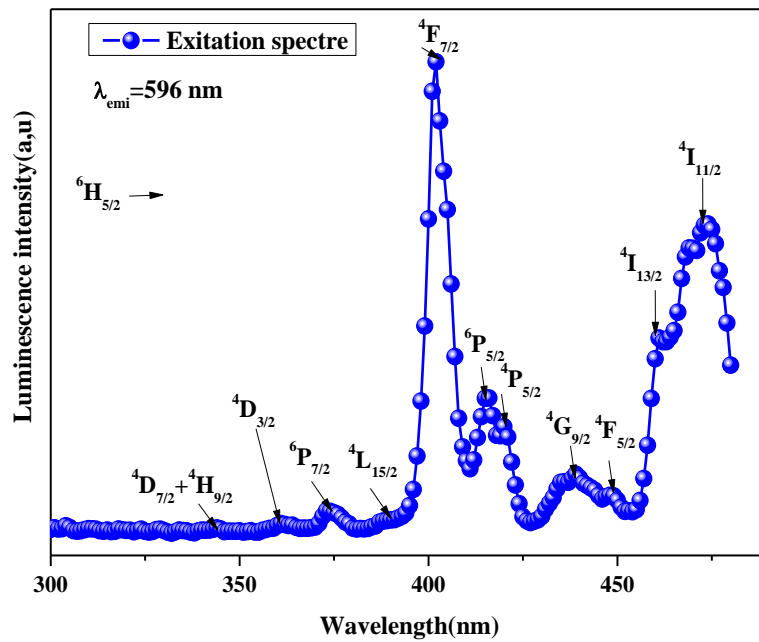


Figure V.11: Excitation spectra of Sm³⁺ ions doped SWN glasses.

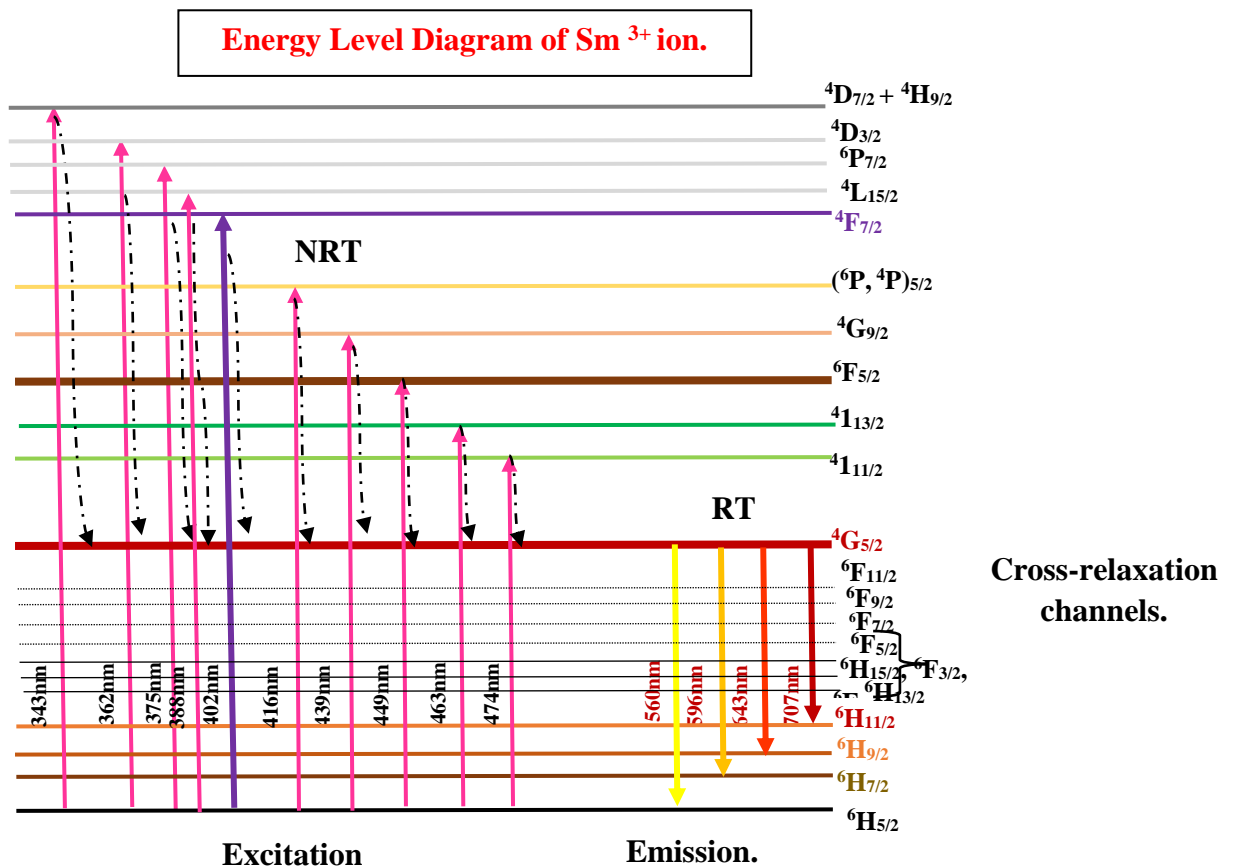


Figure V.12: Schematic energy level diagram for the Sm³⁺ ion: SWNSm glasses.

V.8.2 Emission spectral

The emission spectra of SWNSm glasses are displayed in fig V.13. The emission spectra of all SWNSm glasses demonstrate four transitions in the visible range from the initial state $^4G_{5/2}$ to levels $^6H_{(2n+1)/2}$ with $n=2, 3, 4$ and 5 , which correspond to the bands at 560nm, 596nm, 643nm and 707nm, respectively. The intense emission bands are observed at 596 nm, corresponding to the transitions $^4G_{5/2} \rightarrow ^6H_{7/2}$ (orange). This orange emission is used in LEDs and solid-state laser applications, etc [3, 40-42]. The energy level scheme of the emission mechanism of Sm³⁺ ions in the glass samples is shown in fig V.12. From fig V.13, we can say that the intensity of the luminescence of emission bands increases until Sm0,30, after which it drops. The concentration quenching phenomena is to blame for this outcome [3]. The OH band and energy transfer between the Sm³⁺ ions are linked to the quenching in emission intensity via a cross-relaxation process.

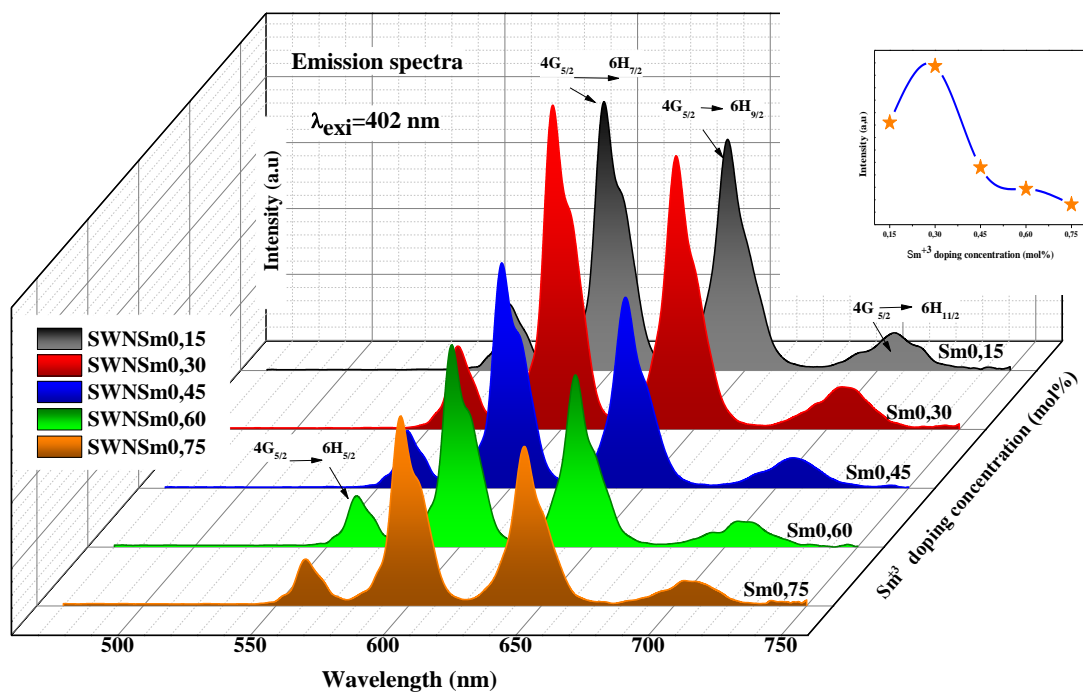


Figure V.13: Emission spectra of Sm³⁺ ions doped SWN glasses.

V.8.3 Cross-relaxations and energy transfer mechanism in Sm³⁺ ions

The emission intensity of our glasses increases up to 0,30 mole % of Sm³⁺ ions then decreases; this is due to the quenching phenomenon. The luminescence quenching may be due to the efficient energy transfer between the Sm³⁺-Sm³⁺ ion sites through a cross-relaxation mechanism, and the possible cross-relaxation channels are presented in fig V.14.

Emission channels	Absorption channels
I: E ₁ (⁴ G _{5/2} → ⁶ F _{5/2}) (10551cm ⁻¹)	A ₁ (⁶ H _{5/2} → ⁶ F _{11/2}) (10615cm ⁻¹)
II: E ₂ (⁴ G _{5/2} → ⁶ F _{7/2}) (9691cm ⁻¹)	A ₂ (⁶ H _{5/2} → ⁶ F _{9/2}) (9294cm ⁻¹)
III: E ₃ (⁴ G _{5/2} → ⁶ F _{9/2}) (8567cm ⁻¹)	A ₃ (⁶ H _{5/2} → ⁶ F _{7/2}) (8117cm ⁻¹)
IV: E ₄ (⁴ G _{5/2} → ⁶ F _{11/2}) (7301cm ⁻¹)	A ₄ (⁶ H _{5/2} → ⁶ F _{5/2}) (7262cm ⁻¹)

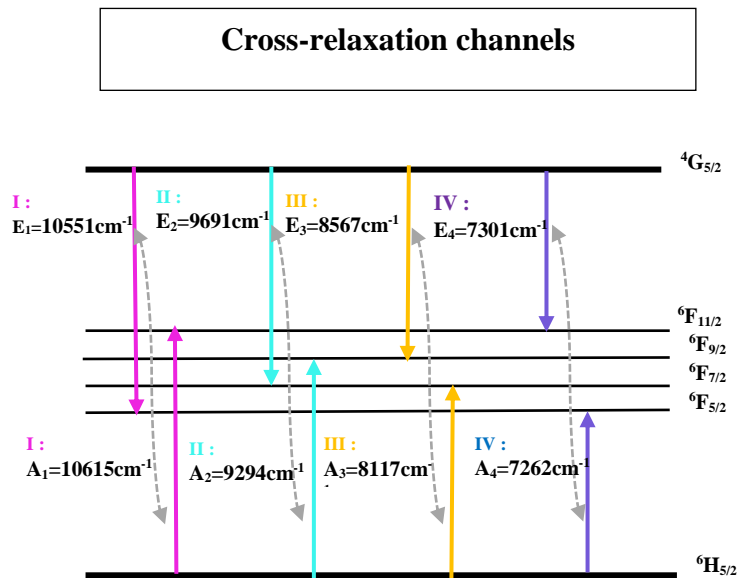


Figure V.14: The cross-relaxation channels involved in Sm³⁺ ions in SWNSm glasses.

For more details, we can say that with the increase in the concentration of the Sm³⁺ ion the distance between the RE ion centers reduces, and the contact between them increases [25].

When we excite the samarium (1) atom, it moves to a higher energy level to become an unstable atom then emits **a photon** to return to stability. During its return, this **photon** is absorbed by a neighboring samarium (2) atom because the distance between the samarium ions has become smaller. Thus, each excited atom (Sm) will transfer its energy to the atom

(Sm) next to it, and therefore some small amount photons, will be captured. Because that we show decreases in the luminescence intensity [25, 43].

In other words, this cross-relaxation is due to energy transfer from the excited ${}^4G_{5/2}$ energy state to the nearby Sm³⁺ ions in the ${}^6H_{5/2}$ ground state. The possible cross-relaxation channels in the prepared glasses are I: (${}^4G_{5/2}, {}^6H_{5/2}$) \rightarrow (${}^6F_{5/2}, {}^6F_{11/2}$), II: (${}^4G_{5/2}, {}^6H_{5/2}$) \rightarrow (${}^6F_{7/2}, {}^6F_{9/2}$), III: (${}^4G_{5/2}, {}^6H_{5/2}$) \rightarrow (${}^6F_{9/2}, {}^6F_{7/2}$), and IV: (${}^4G_{5/2}, {}^6H_{5/2}$) \rightarrow (${}^6F_{11/2}, {}^6F_{5/2}$).

This is possible when the energy of the emission transitions closely matches that of the absorption transitions. In each channel, two Sm³⁺ ions, one in the ground state and the other in the excited state, swap energies to reach intermediate states and then relax non-radiative [1, 44-47]. Also, we can say that the increase of OH content in our glass network can be the reason of decreases the luminescence intensity of emission spectra.

The intensity ratio (E/M) between ${}^4G_{5/2} \rightarrow {}^6H_{9/2}$ (ED) and ${}^4G_{5/2} \rightarrow {}^6H_{5/2}$ (MD) transitions suggests the symmetric nature of Sm³⁺ in the host glass [25, 43]. If the intensity ratio of the electric dipole transition to the magnetic dipole transition (Asymmetry Ratio = ${}^4G_{5/2} \rightarrow {}^6H_{9/2} / {}^4G_{5/2} \rightarrow {}^6H_{5/2}$) is high, it exhibits more asymmetry in the nature of Sm³⁺ ions in the network. The (E/M) ratio of the prepared glasses is found to be 3.48, 3.30, 3.35, 3.38 and 3.44 for the SWNSm0,15, SWNSm0,30, SWNSm0,45, SWNSm0,60 and SWNSm0,75, respectively. In the present work, the spectral intensity of the ${}^4G_{5/2} \rightarrow {}^6H_{9/2}$ (ED) transition of the Sm³⁺ ion is more than the ${}^4G_{5/2} \rightarrow {}^6H_{5/2}$ (MD) transition, which indicates that the asymmetric nature is predominant. This asymmetric ratio is high for SWNSm0,15 glass and low for SWNSm0,30 glass, indicating that SWNSm0,15 glass has more local disorder and SWNSm0,30 glass has less local disorder for the Sm³⁺ ions in the present glass network.

In the present study, “the magnetic dipole transition is more intense than the electric dipole transition, which suggests that there is deviation from the inversion center, and it is more asymmetric in nature” [20, 25].

V.8.4 Emission lifetime analysis

The luminescence decay analysis can be studied via the energy transfer process from Sm³⁺ to Sm³⁺ and luminescence quenching of RE ions [48]. In all SWNSm glasses, the Sm³⁺ ions are assumed to behave as isolated centers with low concentration of Sm³⁺ ions. with the high concentration of the Sm³⁺ ions, the interaction between Sm³⁺ - Sm³⁺ ions increases, which leads to decrease the luminescence intensity. Fig V.15 represents the decay curves

(lifetime) of our glasses and is obtained by a single exponential fit, given by the equation [49, 50]:

$$I = A \exp(-t/\tau) \quad (\text{V.5})$$

Where I is the luminescence intensity at time t, A is a constant, t is the time after excitation and τ is the decay time of the component (lifetime).

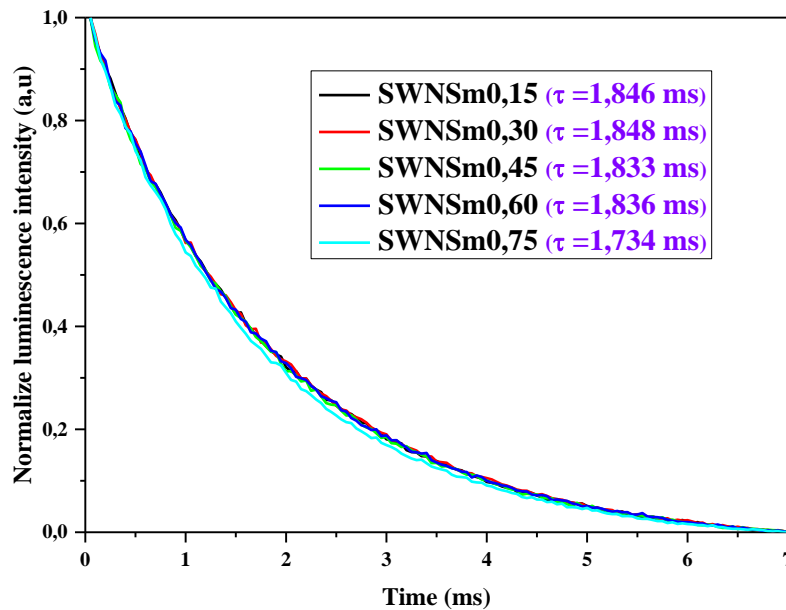


Figure V.15: Decay (lifetime) curves of SWNSm glasses.

The odd exponential nature of these decay curves is due either to the faster decay of the excited Sm³⁺ ions and a probably of interaction between the Sm³⁺ and Sm³⁺ ions. On the other hand, with a very large content of Sm³⁺ ions indicate a large interaction between samarium ions and thus a significant increase in the decay speed due to non-radiative energy transfer between Sm³⁺ ions through cross-relaxation channels [43, 48-51].

We can say that the cause of lifetime quenching (lifetime drop) is the increase of OH groups in the prepared glass, as evidenced by the presence of large OH stretching vibrations in the 3000-3500 cm⁻¹ region of the FTIR spectra [43], and this is also due to the probability of non-radiative relaxation (cross-relaxation channel).

For more details, the natural phonon energy of the antimony glass is around 600 cm⁻¹, but the OH groups produce high energy vibrational modes (~3259 cm⁻¹). Through

multiphonon relaxation, the OH group with high energy vibrations is predicted to quench the excited Sm³⁺ ions so fast.

Par ex: The $^4I_{11/2} \rightarrow ^4G_{5/2}$ transition is facilitated by the high energy OH vibration by multiphonon relaxation process. One phonon of OH groups is more effective than the intrinsic antimony phonons in the SWN glasses, which need at least five phonons of antimony or three phonons of phosphate to bridge the energy gap between the two energy levels [52].

V.9 CIE chromaticity coordinates

In order to understand the color emitted by the Sm³⁺ ion doped SWN glasses, the chromaticity coordinate values (x, y) are evaluated from the emission spectra by using the ColorCalculator-32 program. These coordinates are calculated from the emission spectra obtained after exciting the SWNSm samples at 402 nm. The chromaticity coordinates x and y are given in table V.9 and displayed in the CIE diagram in fig V.16.

Table V.9: The CIE –chromaticity diagram of Sm³⁺ ions doped SWN glasses.

S.n°	SWNSm0,15	SWNSm0,30	SWNSm0,45	SWNSm0,60	SWNSm0,75
x-co-ordinate	0,6078	0,6044	0,6060	0,6026	0,6015
y-co-ordinate	0,3913	0,3935	0,3920	0,3932	0,3931

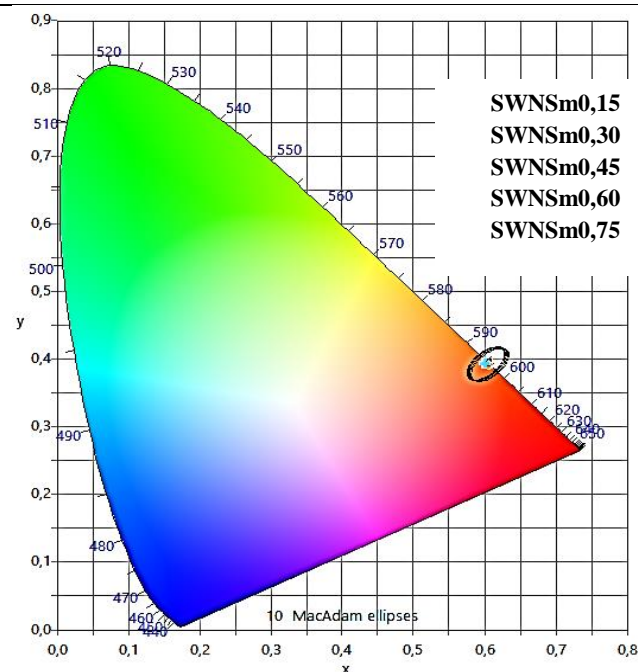


Figure V.16: The CIE coordinates of SWNSm glasses.

It is observed that the CIE coordinates for all SWNSm studied glasses are in the orange-red region. A little change in the (x, y) values is observed for the studied glasses from (0.6078, 0.3913) to (0.6015, 0.3931) and high emission intensity in the orange region of the chromaticity diagram, which could be useful in orange lighting applications (see [fig V.16](#) and [table V.9](#)) under $\lambda_{ex} = 402\text{nm}$.

V.10 Conclusion

The antimony- tungsten- sodium metaphosphate (SWN) glasses doped with Sm₂O₃ show the following conclusions:

1. The addition of larger quantities of Sm³⁺ ions causes an increase in density and a decrease in V_m demonstrating their ability to change their structure, contraction and high compactness within the host matrix.
2. The DSC curves and the elastic modulus values (E and ν) show good thermal stability and mechanical resistance inside these glasses (the glass is more rigid).
3. From the FTIR spectra and the structural parameters, we can say that the compactness inside SWNSm glasses increases.
4. The M values is range between 0.446 and 0.447, which suggests that the SWNSm glasses exhibit non-metallic behavior and are useful in NLO applications.
5. The decrease in E_u , and an increase in E_g are owing to the decline in NBOs and less disorder in the glass network.
6. The intensity of the emission spectra rises up to Sm³⁺ 0,30 mole % and then decreases. This is attributed to the quenching phenomenon.
7. The lifetime decreased by adding high concentrations of Sm³⁺ due to OH groups also a probability of non-radiative relaxations through cross-relaxation channels (quenching phenomenon).
8. The presence of significant OH groups in the produced glasses, which is validated through IR spectrum investigations, results in a lower experimental lifetime and relatively lower quantum efficiency.
9. According to the CIE diagram and (x, y) coordinates, all SWNSm glasses emit orange light under $\lambda_{ex} = 402\text{nm}$, which makes them useful for the orange LED applications.

References

1. Kesavulu, C. and C. Jayasankar, Spectroscopic properties of Sm³⁺ ions in lead fluorophosphate glasses. *Journal of luminescence*, 2012. **132**(10): p. 2802-2809. <https://doi.org/10.1016/j.jlumin.2012.05.031>
2. Sundari, S.S., et al., Composition dependent structural and optical properties of Sm³⁺-doped sodium borate and sodium fluoroborate glasses. *Journal of luminescence*, 2010. **130**(7): p. 1313-1319.
3. Souza Filho, A., et al., Optical properties of Sm³⁺ doped lead fluoroborate glasses. *Journal of Physics and Chemistry of Solids*, 2000. **61**(9): p. 1535-1542. [https://doi.org/10.1016/S0022-3697\(00\)00032-9](https://doi.org/10.1016/S0022-3697(00)00032-9)
4. Jayasankar, C. and E. Rukmini, Optical properties of Sm³⁺ ions in zinc and alkali zinc borosulphate glasses. *Optical Materials*, 1997. **8**(3): p. 193-205. [https://doi.org/10.1016/S0925-3467\(97\)00021-9](https://doi.org/10.1016/S0925-3467(97)00021-9)
5. Tang, G., et al., The study of Sm³⁺-doped low-phonon-energy chalcogenide glasses. *Journal of non-crystalline solids*, 2011. **357**(11-13): p. 2463-2467. <https://doi.org/10.1016/j.jnoncrysol.2010.11.060>
6. Maheshvaran, K., K. Linganna, and K. Marimuthu, Composition dependent structural and optical properties of Sm³⁺ doped boro-tellurite glasses. *Journal of luminescence*, 2011. **131**(12): p. 2746-2753. <https://doi.org/10.1016/j.jlumin.2011.06.047>
7. Jayasankar, C., et al., High-pressure fluorescence study of Sm³⁺-doped borate and fluoroborate glasses. *Journal of applied physics*, 2005. **97**(9): p. 093523. <https://doi.org/10.1063/1.1890448>
8. Jayasankar, C., et al., Effect of pressure on luminescence properties of Sm³⁺ ions in potassium niobate tellurite glass. *Journal of luminescence*, 2008. **128**(5-6): p. 718-720. <https://doi.org/10.1016/j.jlumin.2007.10.014>
9. Mohan, S., et al., Structural and luminescence properties of samarium doped lead alumino borate glasses. *Optical Materials*, 2017. **73**: p. 223-233. <https://doi.org/10.1016/j.optmat.2017.08.015>
10. Guesmia, N., et al., Glass formation, physical and structural investigation studies of the (90-x) Sb₂O₃-10WO₃-xNaPO₃ glasses. *Materials Today Communications*, 2022. **30**: p. 103226. <https://doi.org/10.1016/j.mtcomm.2022.103226>
11. Largot, H., et al., Spectroscopic investigations of Sm³⁺ doped phosphate glasses: Judd-Ofelt analysis. *Physica B: Condensed Matter*, 2019. **552**: p. 184-189. <https://doi.org/10.1016/j.physb.2018.10.010>

12. Jayasimhadri, M., et al., Spectroscopic characteristics of Sm³⁺-doped alkali fluorophosphate glasses. *Spectrochimica Acta Part A: Molecular and Biomolecular Spectroscopy*, 2006. **64**(4): p. 939-944. DOI: [10.1016/j.saa.2005.09.001](https://doi.org/10.1016/j.saa.2005.09.001)
13. Pawar, P., et al., Physical, thermal, structural and optical properties of Dy³⁺ doped lithium alumino-borate glasses for bright W-LED. *Journal of luminescence*, 2017. **183**: p. 79-88. <https://doi.org/10.1016/j.jlumin.2016.11.027>
14. Dimitrov, V. and T. Komatsu, An interpretation of optical properties of oxides and oxide glasses in terms of the electronic ion polarizability and average single bond strength. *J. Univ. Chem. Technol. Metall*, 2010. **45**(3): p. 219-250.
15. Zaid, M.H.M., et al., Effect of ZnO on the physical properties and optical band gap of soda lime silicate glass. *International journal of molecular sciences*, 2012. **13**(6): p. 7550-7558.
16. Elkhoshkhany, N., et al., Properties of tellurite glass doped with ytterbium oxide for optical applications. *Journal of Materials Science: Materials in Electronics*, 2019. **30**(7): p. 6963-6976. DOI :[10.1007/s10854-019-01013-9](https://doi.org/10.1007/s10854-019-01013-9)
17. Tasheva, T. and V. Dimitrov, Electronic polarizability, optical basicity and chemical bonding of zinc oxide-barium oxide-vanadium oxide glasses. *Bulg. Chem. Commun.*, 2017. **49**(F): p. 76-83.
18. Inaba, S., S. Oda, and K. Morinaga, Heat capacity of oxide glasses at high temperature region. *Journal of non-crystalline solids*, 2003. **325**(1-3): p. 258-266. [https://doi.org/10.1016/S0022-3093\(03\)00315-6](https://doi.org/10.1016/S0022-3093(03)00315-6)
19. Bhardwaj, S., et al., Spectroscopic properties of Sm³⁺ doped lead bismosilicate glasses using Judd–Ofelt theory. *Spectrochimica Acta Part A: Molecular and Biomolecular Spectroscopy*, 2014. **117**: p. 191-197.
20. Pawar, P., et al., Physical, structural, thermal and spectroscopic investigation of Sm₂O₃ doped LAB glasses for orange LED. *Journal of luminescence*, 2019. **208**: p. 443-452. <https://doi.org/10.1016/j.jlumin.2019.01.020>
21. Som, T. and B. Karmakar, Structure and properties of low-phonon antimony glasses and nano glass-ceramics in K₂O–B₂O₃–Sb₂O₃ system. *Journal of non-crystalline solids*, 2010. **356**(20-22): p. 987-999. DOI: [10.1016/j.jnoncrysol.2010.01.026](https://doi.org/10.1016/j.jnoncrysol.2010.01.026)
22. Poirier, G., *Nouveaux verres à base d'oxyde de tungstène*, 2003, Rennes 1.
23. Karmakar, B., P. Kundu, and R.N. Dwivedi, IR spectra and their application for evaluating physical properties of fluorophosphate glasses. *Journal of non-crystalline solids*, 2001. **289**(1-3): p. 155-162. [https://doi.org/10.1016/S0022-3093\(01\)00721-9](https://doi.org/10.1016/S0022-3093(01)00721-9)

24. Karmakar, B., et al., Effect of hydroxyl content on the physical properties of calcium metaphosphate glasses. *Bulletin of Materials Science*, 1999. **22**(2): p. 115-119. <http://doi.org/10.1007/BF02745563>
25. Arunkumar, S. and K. Marimuthu, Concentration effect of Sm³⁺ ions in B₂O₃–PbO–PbF₂–Bi₂O₃–ZnO glasses—structural and luminescence investigations. *Journal of alloys and compounds*, 2013. **565**: p. 104-114. <http://dx.doi.org/10.1016/j.jallcom.2013.02.151>
26. BAAZOUZI, M., Etude numérique de l'interaction sol-fondation superficielle située à proximité d'une pente, 2017, Université Mohamed Khider-Biskra.
27. Brow, R.K., et al., The short-range structure of sodium ultraphosphate glasses. *Journal of non-crystalline solids*, 1994. **177**: p. 221-228. [https://doi.org/10.1016/0022-3093\(94\)90534-7](https://doi.org/10.1016/0022-3093(94)90534-7)
28. Montagne, L., G. Palavit, and G. Mairesse, ³¹P MAS NMR and FT IR analysis of (50-x/2) Na₂O. xBi₂O₃.(50-x/2) P₂O₅ glasses. *Physics and chemistry of glasses*, 1996. **37**(5): p. 206-211.
29. Poirier, G., et al., Structural study of tungstate fluorophosphate glasses by Raman and X-ray absorption spectroscopy. *Journal of Solid State Chemistry*, 2005. **178**(5): p. 1533-1538. <https://doi.org/10.1016/j.jssc.2004.10.032>
30. Boudlich, D., et al., Infrared, Raman, and electron spin resonance studies of vitreous alkaline tungsten phosphates and related glasses. *Journal of the American Ceramic Society*, 2002. **85**(3): p. 623-630. <https://doi.org/10.1111/j.1151-2916.2002.tb00141.x>
31. Roy, J.S., Y. Messaddeq, and S.J. Ribeiro, Formation and optical properties of new glasses within Sb₂O₃–WO₃–ZnO ternary system. *Journal of Materials Science: Materials in Electronics*, 2019. **30**(18): p. 16798-16805. <http://doi.org/10.1007/s10854-019-01340-x>
32. Bartholomew, R.F., Structure and properties of silver phosphate glasses—Infrared and visible spectra. *Journal of non-crystalline solids*, 1972. **7**(3): p. 221-235. [https://doi.org/10.1016/0022-3093\(72\)90024-5](https://doi.org/10.1016/0022-3093(72)90024-5)
33. Leow, T.Q., et al., Study of structural and luminescence properties of lead lithium borophosphate glass system doped with Ti ions. *Sains Malaysiana*, 2014. **43**(6): p. 929-934.
34. Franco, D.F., et al., Glass formation and the structural study of the Sb₂O₃–SbPO₄–WO₃ system. *Eclética Química*, 2017. **42**: p. 51-59. <https://doi.org/10.26850/1678-4618eqj.v42.1.2017.p51-59>

35. Corbridge, D., Infra-red analysis of phosphorus compounds. *Journal of applied Chemistry*, 1956. **6**(10): p. 456-465. <https://doi.org/10.1002/jctb.5010061007>
36. Ali, A., Optical properties of Sm³⁺-doped CaF₂ bismuth borate glasses. *Journal of luminescence*, 2009. **129**(11): p. 1314-1319. <https://doi.org/10.1016/j.jlumin.2009.06.017>
37. Mott, N.F. and E.A. Davis, *Electronic processes in non-crystalline materials* 2012: Oxford university press.
38. Rao, V.H., et al., Influence of Sb₂O₃ on tellurite based glasses for photonic applications. *Journal of alloys and compounds*, 2016. **687**: p. 898-905. <http://dx.doi.org/10.1016/j.jallcom.2016.06.256>
39. Rani, P.R., et al., Structural, absorption and photoluminescence studies of Sm³⁺ ions doped barium lead alumino fluoro borate glasses for optoelectronic device applications. *Materials Research Bulletin*, 2019. **110**: p. 159-168. <https://doi.org/10.1016/j.materresbull.2018.10.033>
40. Thomas, S., et al., Optical properties of Sm³⁺ ions in zinc potassium fluorophosphate glasses. *Optical Materials*, 2013. **36**(2): p. 242-250. <https://doi.org/10.1016/j.optmat.2013.09.002>
41. Yamusa, Y., R. Hussin, and W.W. Shamsuri, Physical, optical and radiative properties of CaSO₄-B₂O₃-P₂O₅ glasses doped with Sm³⁺ ions. *Chinese Journal of Physics*, 2018. **56**(3): p. 932-943. <https://doi.org/10.1016/j.cjph.2018.03.025>
42. Prabhu, N.S., et al., Physical, structural and optical properties of Sm³⁺ doped lithium zinc alumino borate glasses. *Journal of non-crystalline solids*, 2019. **515**: p. 116-124. <https://doi.org/10.1016/j.jnoncrysol.2019.04.015>
43. Deopa, N. and A. Rao, Spectroscopic studies of Sm³⁺ ions activated lithium lead alumino borate glasses for visible luminescent device applications. *Optical Materials*, 2017. **72**: p. 31-39. <http://dx.doi.org/10.1016/j.optmat.2017.04.067>
44. Suhasini, T., et al., Absorption and fluorescence properties of Sm³⁺ ions in fluoride containing phosphate glasses. *Optical Materials*, 2009. **31**(8): p. 1167-1172. DOI:10.1016/j.optmat.2008.12.008
45. Jamalaiah, B., M.V. Kumar, and K.R. Gopal, Fluorescence properties and energy transfer mechanism of Sm³⁺ ion in lead telluroborate glasses. *Optical Materials*, 2011. **33**(11): p. 1643-1647. DOI:10.1016/j.optmat.2011.04.030

46. Kumar, J.S., et al., Photoluminescence and energy transfer properties of Sm³⁺ doped CFB glasses. *Solid state sciences*, 2011. **13**(8): p. 1548-1553. <https://doi.org/10.1016/j.solidstatesciences.2011.05.020>
47. Jamalaiah, B., et al., Photoluminescence properties of Sm³⁺ in LBTAf glasses. *Journal of luminescence*, 2009. **129**(4): p. 363-369. <https://doi.org/10.1016/j.jlumin.2008.11.001>
48. Naresh, V., B. Rudramadevi, and S. Buddhudu, Crossrelaxations and non-radiative energy transfer from (⁴G_{5/2}) Sm³⁺→(⁵D₀) Eu³⁺: B₂O₃–ZnO glasses. *Journal of alloys and compounds*, 2015. **632**: p. 59-67. <http://dx.doi.org/10.1016/j.jallcom.2015.01.138>
49. Sailaja, S., et al., Optical properties of Sm³⁺-doped cadmium bismuth borate glasses. *Journal of Molecular Structure*, 2013. **1038**: p. 29-34. <http://dx.doi.org/10.1016/j.molstruc.2013.01.052>
50. Rudramamba, K., et al., Optical properties of Sm³⁺ doped strontium bismuth borosilicate glasses for laser applications. *Optical Materials*, 2019. **89**: p. 68-79. <https://doi.org/10.1016/j.optmat.2018.12.048>
51. Rajagukguk, J., et al., Investigation of Sm³⁺-doped PBNaG glasses for orange LED applications. *Journal of the Korean Physical Society*, 2021. **78**(3): p. 177-181. <https://doi.org/10.1007/s40042-020-00034-6>
52. Som, T. and B. Karmakar, Efficient green and red fluorescence upconversion in erbium doped new low phonon antimony glasses. *Optical Materials*, 2009. **31**(4): p. 609-618. DOI: [10.1016/j.optmat.2008.06.018](https://doi.org/10.1016/j.optmat.2008.06.018)

General conclusion

General conclusion

Two new series of glasses were examined with the formula (90-x) glasses $\text{Sb}_2\text{O}_3-10\text{WO}_3-x\text{NaPO}_3$ (x ranging from 10 to 80) and (80-x) $\text{Sb}_2\text{O}_3-20\text{WO}_3-x\text{NaPO}_3$ (x ranging from 10 to 70). Certain thermal, physical, elastic, mechanical, optical and structural properties have been tested. The DSC curves confirmed the vitreous character as well as the thermal stability of our glasses. Vickers hardness and modulus of elasticity were tested. The increase in elastic moduli and physical characteristic parameters is associated with an increase in stiffness and a modification of the structural network of the glass system with the addition of NaPO_3 content by the formation of a P-O-M bridge (M=P, Sb or W), which increases network connectivity and contributes to an increase in glass transition temperature and modulus of elasticity. To establish the similarity between the theoretical and observed results of elastic moduli and Poisson's ratio in our glasses, Mackenzie's Makishima theory was used. Our system has many colors (yellow, blue, transparent), which are related to an increase or a decrease (reduction or oxidation) in the number of electrons in the atomic system of these materials.

In this glass, the transmitting edge shifts to lower wavelengths as NaPO_3 concentration increases, increasing the optical bandgap (E_g) and lowering the Urbach energy (E_u). To evaluate the dependence of these characteristics on the concentration of P^{5+} ions, optical parameters such as n, R_m and α_m were calculated. Based on the optical findings obtained, our SWN glasses can be employed in NLO applications. According to IR spectroscopic analysis, with the addition of NaPO_3 , the OH content increases, which increases non-radiative losses and lowers the quantum efficiency of the glass materials.

From Raman and IR spectroscopy, the average crosslink density and the number of network bonds per unit volume were increased. These results support the obtained results in the thermal, elastic and mechanical tests, which suggest the creation of a more linear chain of phosphate and the strong P-O-W linkage. Also, the optical and structural properties of these glasses have been found to be generally affected by structural changes in the composition of the glass due to the formation of linear phosphate chains with Sb_2O_3 and WO_3 , which increase the connectivity and stiffness of the glass network. In conclusion, these glasses are good candidates in photonics, which can be used in fiber optics, NLO applications, etc.

SWN glasses doped with Sm^{+3} ions in the chemical composition (40-x) $\text{Sb}_2\text{O}_3-10\text{WO}_3-50\text{NaPO}_3-x\text{Sm}_2\text{O}_3$ where x = 0.15, 0.3, 0.45, 0.60 and 0.75% in moles were prepared by the conventional melt annealing technique. The DSC curves highlight the good thermal stability of

General conclusion

these glasses. In addition, we calculated the Young's modulus (E_t) and Poisson's ratio (ν_t) of SWNSm glasses using the theory of Makishima and Mackenzie. The density is observed to increase with an increasing Sm_2O_3 concentration. The decrease in molar volume with the addition of the samarium content denotes the contraction of the vitreous network due to the decrease in the $d_{(\text{Sb}-\text{Sb})}$ separation. The vibrational mode of these materials is evaluated by FTIR transmission spectroscopy, and the addition of samarium ions boosted the increase in BO number. The bandgap values ($E_{g \text{ indirect}}$) for all these glass samples are in the range 2.84-2.87 eV, affirming the insulating nature of glass. Emission spectra showed a strong transition from $^4\text{G}_{5/2} \rightarrow ^6\text{H}_{5/2}$ (561 nm), $^4\text{G}_{5/2} \rightarrow ^6\text{H}_{7/2}$ (596 nm), $^4\text{G}_{5/2} \rightarrow ^6\text{H}_{9/2}$ (643 nm) and $^4\text{G}_{5/2} \rightarrow ^6\text{H}_{11/2}$ (707 nm) are recorded with 402 nm excitation. As Sm^{+3} content increases, the experimental lifetime of SWNSm glasses decreases from 1.846 ms to 1.734 ms. The decrease in lifetime value leads to cross-relaxation channels and an increase in OH groups in present glasses and may be due to the probability of non-radiative relaxations (presence quenching phenomena). The chromaticity coordinates (x, y) collected in the orange region make these Sm^{3+} doped SWN glasses suitable for orange LED applications.

Abstract

This study focuses on the synthesis of new SWN glasses designed primarily for photonic applications. Physical, thermal, mechanical, optical, and structural tests are performed on the two series $(90-x) \text{Sb}_2\text{O}_3-10\text{WO}_3-x\text{NaPO}_3$ and $(80-x) \text{Sb}_2\text{O}_3-10\text{WO}_3-x\text{NaPO}_3$. The DSC curves proved our glasses' glassy nature as well as their heat stability. Vickers hardness, modulus of elasticity, and Raman spectroscopy were all used to evaluate the materials. Enhanced stiffness and changes in the structural network of the glass system are connected to improvements in elastic moduli and physical characteristic parameters. By forming a P-O-M bridge (M=P, Sb, or W), the inclusion of NaPO_3 content improves network connectivity and increases T_g and elasticity modulus. This might be due to the glass network polymerizing as a result of the high concentration of PO_4 , which acts as a bridge between them, as shown by Raman spectroscopy. Chemical modifications in the glass composition caused by the creation of linear phosphate chains with Sb_2O_3 and WO_3 , which improved the connectivity and stiffness of the glass network. Sm^{3+} ions doped SWN glasses in the chemical composition $(40-x) \text{Sb}_2\text{O}_3-10\text{WO}_3-50\text{NaPO}_3-x\text{Sm}_2\text{O}_3$ where $x = 0.15, 0.3, 0.45, 0.60$ and 0.75 mol% were prepared by the conventional melt-quenching-annealing technique. Emission spectra which presented a prominent transition of ${}^4\text{G}_{5/2} \rightarrow {}^6\text{H}_{5/2}$ (561 nm), ${}^4\text{G}_{5/2} \rightarrow {}^6\text{H}_{7/2}$ (596 nm), ${}^4\text{G}_{5/2} \rightarrow {}^6\text{H}_{9/2}$ (643 nm) and ${}^4\text{G}_{5/2} \rightarrow {}^6\text{H}_{11/2}$ (707 nm) have been registered with excitation at 402 nm. As Sm^{3+} content increases, the experimental lifetime of SWNSm glasses decreases from 1.846 ms to 1.734 ms, which leads to an increase in OH groups and a probability of NR relaxations in these samples. The chromaticity coordinates (x, y) are collected in the orange region, making these Sm^{3+} ions doped SWN glasses suitable for orange LED and laser applications.

ملخص

تركز هذه الدراسة على صناعة زجاج SWN الجديد المصمم أساساً للتطبيقات الفوتونية. تم إخضاع السلسلتين $(90-x) \text{Sb}_2\text{O}_3-x\text{NaPO}_3$ و $(80-x) \text{Sb}_2\text{O}_3-20\text{WO}_3-x\text{NaPO}_3$ لمجموعة متنوعة من الاختبارات الفيزيائية والحرارية والميكانيكية والبصرية والبنوية. أثبتت منحنيات DSC الطبيعة الزجاجية بالإضافة إلى ثباتها الحراري. تم استخدام صلادة فيكرز ومعاملات المرونة ومطيف رامان لتقييم المواد. ترتبط الصلابة المحسنة والتغيرات في الشبكة الهيكلية للنظام الزجاجي بتحسينات في المعايير المرنة ومعاملات الخصائص الفيزيائية. من خلال تشكيل جسر P-O-M (M = P أو Sb أو W)، يعمل زيادة محتوى NaPO_3 على تحسين اتصال الشبكة، درجة حرارة الانتقال الزجاجي وزيادة معامل المرونة. قد يكون هذا بسبب بلورة شبكة الزجاج نتيجة للتركيز العالي لـ PO_4 ، والذي يعمل كجسر بينهما، كما هو موضح بواسطة مطيافية Raman. التغيرات الكيميائية في التركيب الزجاجي ناتجة عن إنشاء سلاسل فوسفات خطية مع Sb_2O_3 و WO_3 ، والتي أدت إلى تحسين اتصال وصلابة الشبكة الزجاجية. زجاج SWN المطعم بأيون Sm^{3+} في التركيب الكيميائي $(40-x) \text{Sb}_2\text{O}_3-10\text{WO}_3-50\text{NaPO}_3-x\text{Sm}_2\text{O}_3$ حيث $x = 0.15, 0.3, 0.45, 0.60$ و 0.75% مول تم تحضيرها بواسطة تقنية الذوبان-التلدين و الاحماء التقليدية. قدمت أطيف الانبعاث انتقالات بارزة ل (${}^4\text{G}_{5/2} \rightarrow {}^6\text{H}_{5/2}$ (561 nm), ${}^4\text{G}_{5/2} \rightarrow {}^6\text{H}_{7/2}$ (596 nm), ${}^4\text{G}_{5/2} \rightarrow {}^6\text{H}_{9/2}$ (643 nm) و ${}^4\text{G}_{5/2} \rightarrow {}^6\text{H}_{11/2}$ (707 nm)) المسجلة مع الإثارة عند 402 nm. مع زيادة محتوى Sm^{3+} ، ينخفض العمر التجريبي لزجاج SWNSm من 1.846 ms إلى 1.734 ms، هذا بسبب الزيادة في مجموعات OH و احتمالية لاسترخاء غير إشعاعية في هذه العينات. الإحداثيات اللونية (x, y) التي تم جمعها في المنطقة البرتقالية، تجعل زجاج SWN المطعم بأيون Sm^{3+} مناسب لتطبيقات LED البرتقالية والليزر.